UNIVERSITY OF Southampton

University of Southampton Research Repository

Copyright © and Moral Rights for this thesis and, where applicable, any accompanying data are retained by the author and/or other copyright owners. A copy can be downloaded for personal non-commercial research or study, without prior permission or charge. This thesis and the accompanying data cannot be reproduced or quoted extensively from without first obtaining permission in writing from the copyright holder/s. The content of the thesis and accompanying research data (where applicable) must not be changed in any way or sold commercially in any format or medium without the formal permission of the copyright holder/s.

When referring to this thesis and any accompanying data, full bibliographic details must be given, e.g.

Thesis: Author (Year of Submission) "Full thesis title", University of Southampton, name of the University Faculty or School or Department, PhD Thesis, pagination.

Data: Author (Year) Title. URI [dataset]

UNIVERSITY OF SOUTHAMPTON

FACULTY OF ENGINEERING AND PHYSICAL SCIENCES

National Center for Advanced Tribology at Southampton

Nanoscale Triboelectrification of Two-Dimensional Chemical Vapor Deposited Transition Metal Dichalcogenides

by

He Wang

Thesis for the degree of Doctor of Philosophy

December 2019

UNIVERSITY OF SOUTHAMPTON

ABSTRACT

FACULTY OF ENGINEERING AND PHYSICAL SCIENCES

Doctor of Philosophy

Nanoscale Triboelectrification of Two-Dimensional Chemical Vapor Deposited Transition Metal Dichalcogenides

He Wang

Triboelectrification, a contact-induced electrification where a material becomes electrically charged after brought into contact with a dissimilar one via friction [1], is an available, stable and efficient method to realize the mechanical-to-electrical energy conversion. Until now, this phenomenon has been investigated for insulators like polymers and silicon dioxide, and zero-bandgap semiconductor like graphene. For semiconductors with non-zero bandgaps, transition metal dichalcogenides have been paid much attention due to their distinctive optical, electrical and mechanical properties, and it has been reported that the performance of triboelectric nanogenerators can be dramatically enhanced by introducing single-layer MoS_2 into the friction layer as the triboelectric electron-accepter layer [2], but the theories behind are still poorly understood, so the aim of this investigation is to fill this research gap.

With this aim in mind, high-quality MoS_2, WS_2, $MoSe_2$, and WSe_2 nanoflakes were synthesized by chemical vapor deposition method and their triboelectric properties were characterized with atomic force microscopy and Kelvin force microscopy. Due to the various work functions of these four materials in reference to the conductive Pt-coated tip, the electrons are transferred from the samples to the tip during triboelectrification in the case of WS_2, $MoSe_2$, and WSe_2 whereas MoS_2 exhibits an opposite transfer direction. The densities of tribo-charges are different for these four materials but they can be modified by applying diverse biases to the conductive tip during the rubbing process. Impressively, these tribo-charges, tunneling to the interlayer between the nanoflakes and the underlying insulating substrate, show more than two orders of magnitude longer lifetime than conventional triboelectrification, and MoS_2 owns the longest lifetime while WSe_2 has the shortest among these four materials. In addition, the diffusion processes of WS_2 and $MoSe_2$ are alike thanks

to their similar work functions. The surface-adsorbed water molecules from the atmosphere can act as carrier trappers to affect the surface potential and charge distribution of 2D materials given the interaction with the environment nearby, but heat treatment can efficiently solve this problem. Besides, a positive correlation between the layer number and resistance to charge dissipation was observed, and there also exists the transfer of materials during the frictional process, which can be utilized for tuning the triboelectric properties of the rubbed material.

On these basis, applicable fields consisting of bandgap modification as well as tunable antenna have been investigated. For the bandgap modification, the in situ effect of strain was investigated and it exhibits that the bandgap decreases monotonically with the increase of applied force. The reason behind is the reduction of orbital overlapping and hybridization due to the weakened atomic bonds when localized strain appears. In addition, while the bandgap of MoS_2 is almost unchanged when an external perpendicular electric field is applied because of the very subtle band structure deformation, the bandgap of bilayer MoS_2 can be modified via the electric field generated by the underlying tribo-charges, and applying positive and negative biases has different effects on the bandgap thanks to the spontaneous polarization along the direction perpendicular to the nanoflakes plane. Meanwhile, a $MoSe_2$-based triboelectrically-controlled tunable antenna was proposed to apply to the upcoming 5G base station. As the tribo-charges can tunnel through the $MoSe_2$ nanoflakes and localize at the interlayer to act as a bias voltage, the conductive/insulating states $MoSe_2$ can be controlled, which results in the adjustable working frequency band from 28 GHz to around 38 GHz. In the meantime, a stable gain (less than 0.1 dBi variation in the whole range) is achieved for this omnidirectional antenna. Additionally, a unidirectional radiation can be reached with a metallic reflector placed at the back of the tunable antenna, and a broad beamwidth can still remain. Due to the long-term preservation of the tribo-charges, no extra bias is needed in this case and the energy can be saved to a large extent.

Contents

List of Figures ..... **v**

List of Tables ..... **xv**

Academic Thesis: Declaration of Authorship ..... **xvii**

Acknowledgements ..... **xix**

Definitions and Abbreviations ..... **xxi**

Chapter 1 Introduction **1**

1.1 Background and motivation 1

1.2 Aims and objectives 2

1.3 Thesis structure 3

Chapter 2 Literature review **5**

2.1 Triboelectrification 5

2.1.1 Triboelectric effect 5

2.1.2 Quantification of triboelectrification 6

2.1.3 Manipulation of triboelectrification 13

2.1.3.1 Extrinsically applied electric field 13

2.1.3.2 Chemical surface functionalization 16

2.1.4 Triboelectric applications 20

2.2 Classification of nanomaterials 23

2.2.1 Zero-dimensional nanomaterials 24

2.2.2 One-dimensional nanomaterials 24

2.2.3 Two-dimensional nanomaterials 25

2.2.4 Three-dimensional nanomaterials 25

2.3 Transition metal dichalcogenides 27

2.3.1 Structure and properties 27

2.3.2 Preparation methods 28

2.3.2.1 Top-down methods 29

2.3.2.2 Bottom-up methods 32

2.3.3 Transfer methods 38

2.3.4 Applications 40

2.4 Summary 45

Chapter 3 Chemical vapor deposition and characterization techniques 47

3.1 Chemical vapor deposition 47

3.1.1 A typical system 47

3.1.2 Factors affecting the coating characteristics 49

3.1.2.1 Temperature 49

3.1.2.2 Chamber pressure 49

3.1.2.3 Gas composition 50

3.1.2.4 Substrate 50

3.1.3 Advantages and disadvantages 50

3.2 Microstructural, physical and chemical analyses 51

3.2.1 Scanning Electron Microscope 51

3.2.2 Raman spectroscopy 52

3.2.3 X-ray photoelectron spectroscopy 54

3.2.4 Atomic force microscope and Kelvin force microscope 55

3.3 Summary 57

Chapter 4 Chemical vapor deposition for transition metal dichalcogenides 59

4.1 Temperature calibration 59

4.2 Effect of different factors 61

4.2.1 Precursors amount 61

4.2.2 Gas inlet 66

4.2.3 Temperature 67

4.2.4 Pre-treatment 68

4.3 Optimized transition metal dichalcogenides 69

4.3.1 MoS_2 69

4.3.2 WS_2 71

4.3.3 $MoSe_2$ 75

4.3.4 WSe_2 76

4.4 Summary 78

Chapter 5 Triboelectric properties of synthesized transition metal dichalcogenides 81

5.1 Initiation and detection of tribo-charges 81
5.2 Diffusion of tribo-charges 85
5.3 Manipulation of tribo-charges 90
5.4 Effect of multi-friction 93
5.5 Effect of layer number 95
5.6 Effect of material transfer 96
5.7 Summary 98

Chapter 6 Transition metal dichalcogenides-based applicable triboelectrification 101

6.1 Bandgap modification 101
6.1.1 Introduction 101
6.1.2 In situ strain-dependent bandgap modulation 101
6.1.3 Bandgap modification by tribo-charges 102
6.2 Triboelectrically-tunable antenna for 5G base station 105
6.2.1 Introduction 105
6.2.2 Omnidirectional antennas 106
6.2.3 Unidirectional antennas 109
6.3 Summary 112

Chapter 7 Conclusions and future work 113

7.1 Conclusions 113
7.2 Future work 115

Appendix 117
Bibliography 125

List of Figures

Figure 1 – Thesis structure. 3

Figure 2 – Macroscale triboelectrification measurement system [28]. 7

Figure 3 – The relationship between charges generated on the metal sphere and contact circles for various insulators. Test environment: 30% RH (Relative Humidity), 20 ℃ [28]. 7

Figure 4 – Average charges on metal sphere as a function of (a) relative humidity and (b) temperature for various tests [28]. 8

Figure 5 – Illustration of experiments to quantify nanoscale triboelectrification. (a) Generation of tribo-charges by contact-mode AFM. (b) The surface potential measured by KFM mode. (c) Surface topography after the rubbing process. (d) The surface potential of a larger area on SiO_2. (e) 3D image of the surface potential. (f) Cross-section profile of the potential distribution, corresponding to the dashed line in d [30]. 9

Figure 6 – Triboelectric charge accumulation process. (a) Surface potential images with the increase of cycles and (b) their corresponding potential profiles. (c) Derived surface charge density as a function of the number of friction cycles [30]. 10

Figure 7 – Charge diffusion over time. (a) Images of surface potential distribution as a function of time after triboelectrification and (b) their corresponding cross-sections [30]. 11

Figure 8 – Tunneling triboelectrification by friction of graphene with a Pt-coated AFM tip. (a) Schematic of the friction process and the KFM measurement system. (b) KFM image of graphene before rubbing. (c) KFM image of graphene after rubbing. (d) Potential difference generated by tunneling triboelectrification, ΔV_{TT}, along the blue dashed line in c after 0 and 72 h. (e) KFM images of graphene after rubbing the central area with different tip bias voltages of -10V, -5V, +5V and +10V [32]. 12

Figure 9 – Mechanism of triboelectrification between a triboelectrically-negative dielectric and metal. (a) Illustration of the contact electrification process. Energy band diagrams in the cases of (b) precontact, (c) contact with no bias, separation equilibrium with (d) no bias, (e) positive bias, and (f) negative bias [35]. 14

Figure 10 – Manipulation of triboelectrification by an applied electric field. (a) Surface potential maps of Parylene film rubbed with biases ranging from -2 to 5 V. (b) Cross-section profiles of the surface potential on Parylene film rubbed with biases from -10 to 10 V. The inset is the calculated surface charge density as a function of bias. [35]. 15

List of Figures

Figure 11 – Molecular structures of the thiols [36]. 16

Figure 12 – Chemical surface functionalization of SiO_2. (a) Fabrication process. Charge density of SiO_2 (b) with and (c) without functionalization [36]. 17

Figure 13 – Surface potentials of (a) unmodified and (b) modified PET samples [38]..... 18

Figure 14 – Triboelectric enhancement of PDMS by ultraviolet irradiation. (a) Measurement of triboelectrification. (b) A series of time-evolution contact potential difference (CPD) images with various ultraviolet treatment time. (c) CPD profiles at different times. A y-offset is assigned to each curve to avoid overlapping [39]. 18

Figure 15 – Charge density of various triboelectric materials (K-Kapton, PT-PTFE, PE-PET, and PD-PDMS) mixed with melamine [40]..... 19

Figure 16 – SEM images of PTFE before (a) and after (b) melamine mixture [40]..... 20

Figure 17 – Various triboelectric nanogenerators designed for harvesting sorts of energies: (a) finger tapping energy, (b) air-flow/wind energy, (c) relative in-plane sliding energy, (d) enclosed cage for harvesting oscillating/disturbing energy in water or mechanical vibration, (e) fabric for harvesting body motion energy, (f) energy in touchpad, (g) foot/hand pressing energy, (h) water impact energy, (i) cylindrical rotation energy, (j) shoe insole for walking energy, (k) flexible grating structure for harvesting energy, and (l) disc shape rotation energy [1]. 21

Figure 18 – Triboelectrification field-effect transistor. (a) Schematic diagram. (b) Equivalent circuit. (c) I_D-V_D output characteristics at different vertical distances (d) I_D-t output characteristics with the change of the vertical distance. The inset is I_D-d transfer characteristic [48]..... 22

Figure 19 – Resistance reduction of graphene by tunneling triboelectrification. (a) Optical image of the 4-wire graphene resistor (the yellow dashed box is rubbed by Pt-coated AFM tip). (b) Normalized resistance of the graphene resistor as a function of the tunneling triboelectric charge density [49]..... 22

Figure 20 – Images of some typical 0D nanomaterials: (a) quantum dots [56], (b) nanoparticles arrays [62], (c) core-shell nanoparticles [63], (d) hollow cubes [64], and (e) nanospheres [65]. 24

Figure 21 – Images of several typical 1D nanomaterials: (a) nanowires [67], (b) nanorods [68], (c) nanotubes [69], (d) nanobelts [70], (e) nanoribbons [71] and (f) hierarchical nanostructures [72]..... 25

Figure 22 – Images of some typical 2D nanomaterials: (a) junctions (continuous islands) [74], (b) branched structures [75], (c) nanoplates [76], (d) nanosheets [77], (e) nanowalls [78] and (f) nanodisks [79]. 26

Figure 23 – Images of some typical 3D nanomaterials: (a) nanocones [80], (b) nanoballs [81], (c) nanopillers [82], (d) nanocoils [83], (e) nanoflowers [84]. 26

Figure 24 – Various possible layered structure of TMDs [96]. 27

Figure 25 – The structure of MoS_2. The distance between adjacent layers is 6.5 Å [6]. 28

Figure 26 – Mechanically exfoliated MoS_2 nanosheets on 300 nm SiO_2/Si substrate. Optical (A-D) and topographic (E-H) images of single-layer (1L, thickness 0.8 nm; A and E), bi-layer (2L, thickness 1.5 nm; B and F), tri-layer (3L, thickness 2.1 nm; C and G), and quadruple-layer (4L, thickness 2.9 nm; D and H) MoS_2 nanosheets [12]. 29

Figure 27 – Monolayer MoS_2 prepared by thermal ablation. Optical images of a multi-layered MoS_2 flake deposited on the 285 nm SiO_2/Si substrate before (a) and after (b) laser-thinning process. The laser-scanned area is marked by a yellow dashed rectangle in (a). (c) Surface topography of the region marked by the square in (b) [120]. 30

Figure 28 – O_2 plasma treatment to control the thickness of mechanically exfoliated MoS_2. (a) The thickness of MoS_2 as a function of plasma treatment time. (b) Surface topographic images before and after plasma etching [125]. 30

Figure 29 – Lithium intercalation to fabricate 2D nanosheets from the layered bulk material [114]. 31

Figure 30 – Surface topographies of different TMDs on SiO_2 substrate prepared by liquid exfoliation method [96]. 32

Figure 31 – (a) Synthesis procedure for the ALD-based WS_2 nanosheets. Optical images of the transferred WS_2 nanosheet on the SiO_2 substrate for the (b) mono-, (c) bi- and (d) tetra-layered thicknesses. AFM images and height profiles (inset) of the transferred WS_2 nanosheet on the SiO_2 substrate for the (e) mono-, (f) bi- and (g) tetra-layered thicknesses [133]. 33

Figure 32 – A series of MoS_2 samples deposited on various substrates. (a) Single-layered MoS_2 fabricated by MoO_2 precursor on a range of substrates. Colored images are measured by optical microscopy, while black and white ones are SEM images. (b) Typical optical and SEM images of bilayer MoS_2 grown on SiO_2, showing diverse states of initiation and growth of the second layer. The last image in (b) is an SEM image indicating intricate

details of the bilayer structure. (c) Optical and SEM images of multi-layered samples at different stages of growth [149]. 35

Figure 33 – Single-layer WS_2 synthesized by CVD method. (a) Schematic illustration of CVD setup for the growth of WS_2. (b) Optical image of single-layer WS_2. (The scale bar is 50 μm). (c) AFM step height measurement to show the thickness of flakes (The scale bar is 10 μm) [150]. 36

Figure 34 – CVD-Growth of large-area single-layer $MoSe_2$. (a) Schematic of CVD growth system to fabricate $MoSe_2$. (b) Temperature profile. (c) Photo of large area $MoSe_2$. (d) Surface topography by AFM. (Inset: height profile along the dashed horizontal line in the map) [157]. 37

Figure 35 – CVD-fabricated WSe_2 on sapphire substrates. (a) The scheme for the growth of WSe_2 on sapphire substrates by the reaction of WO_3 and Se powders in a CVD furnace. (b) and (c) are optical images of the monolayer WSe_2 flakes and film grown at 850 and 750 °C, respectively. Scale bar is 10 μm. The inset in (c) is a uniform monolayer film grown on a sapphire substrate with both sides polished. (d) Surface topography of the monolayer grown at 850 °C [160]. 37

Figure 36 – Mechanism of molten-assisted-salt CVD reaction. Metal oxychlorides are formed to promote the reactions. (a-c) The addition of salt reduces the melting points of precursors. (d) SEM images of the Nb nucleus with (left) and without (right) salt addition. (e-g) The growth of 2D atomic layer with intermediate products. (h) Different single-crystalline monolayers [168]. 38

Figure 37 – Illustration of ultrasonic bubbling transfer of MoS_2. (a) Schematic illustration of the ultrasonic process used to detach PMMA/MoS_2 stack from the growth substrate. (b) Principles for the ultrasonic bubbling transfer of MoS_2 on insulating substrates. (c) PMMA/MoS_2/mica stack immersed in a beaker of water kept in an ultrasonic cleaner. (d) 5×5 cm^2 PMMA/MoS_2 stack floating on water. (e) Transfer of large-area MoS_2 onto SiO_2/Si substrate [171]. 39

Figure 38 – Electronic, optoelectronic and energy devices based on 2D TMDs [12], [181]–[185]. 41

Figure 39 – Creation of single-photon emitters with AFM tip in 2D WSe_2 [190]. 42

Figure 40 – (a) MoS_2-based X-band patch antenna: (left) top view with electrode configuration for DC bias. The letters D-G-S refer to drain-gate-source, respectively; (right) cross-section [191]. (b) Microwave switch based on MoS_2 thin-film [192]. 43

Figure 41 – (a) Illustration of the vertical contact-separation mode triboelectric nanogenerator with a MoS_2 monolayer. Rectified open-circuit voltage of the triboelectric nanogenerator (b) without and (c) with monolayer MoS_2. (d) Short-circuit current density and the amount of charge generated during a press-release cycle with and without monolayer MoS_2 [2]. 44

Figure 42 – Schematic diagram of a typical CVD equipment [139]. 47

Figure 43 – Different CVD reactor configurations: (a) horizontal; (b) vertical; (c) semi-pancake; (d) barrel; (e) multiple wafer [139]. 48

Figure 44 – (a) Column structure and (b) Imaging process of a SEM system (JSM-5410, courtesy of JEOL, USA) [203]. 51

Figure 45 – Diagram of Rayleigh, Stokes and anti-Stokes scattering processes. The lowest energy vibrational state *m* is displayed at the bottom with states of larger energy above it. Both the absorbed energy (upward arrows) and the scattered energy (downward arrows) have far more energies than a vibration [204]. 53

Figure 46 – (a) Raman spectrum of MoS_2 with different layers. (b) Peak frequencies (left vertical axis) and their difference (right vertical axis) as a function of thickness. (c) Schematic of $E2g1$ and $A1g$ modes [205]. 53

Figure 47 – A typical X-ray Photoelectron Spectrometer. 54

Figure 48 – Working principle of AFM system. 55

Figure 49 – Electronic energy levels of the sample and tip for three cases: (a) sample and tip are separated by distance *d* and not electrically connected, (b) sample and tip are in electrical contact, and (c) external bias is applied to nullify the contact potential difference [31]. 57

Figure 50 – (a) Photos and (b) schematic of tube furnace system. 60

Figure 51 – Temperature profile in the tube (Unit: ℃). 60

Figure 52 – Optical images of MoS_2 synthesized with different sulfur amounts: (a) 100 mg, (b) 150 mg and (c) 200 mg. The amount of MoO_3 is 15 mg; temperatures of MoO_3 and S are 700 and 200 ℃, respectively; ramping rate is 10 ℃/min; flow rate is 30 sccm. Scale bar is 50 μm. 62

Figure 53 – (a) Raman and (b) PL spectra of MoS_2 synthesized with 100, 150 and 200 mg sulfur. (c) XPS spectrum for Mo 3d and S 2s orbitals. 62

List of Figures

Figure 54 – Schematic illustration of the relationship between the Mo:S atom ratio and the domain shape. The ball-and-stick models in the central part show the top view microstructure of the monolayer MoS_2 crystal in different shapes, while the ball models on the left show two kinds of MoS_2 termination structures. The schematic diagram on the right illustrates the domain shape changing procedure depending on the growing rates of two different terminations [214]. 64

Figure 55 – Optical images of MoS_2 synthesized with the same S:MoO_3 ratio: (a) 150:15 and (b) 250:25 (unit: mg). Temperatures of MoO_3 and S are 700 and 200 ℃, respectively; ramping rate is 10 ℃/min; flow rate is 30 sccm. Scale bar is 50 μm. 64

Figure 56 – (a) Raman and (b) PL spectra of MoS_2 synthesized with the same S:MoO_3 ratio: 150:15 and 250:25 (unit: mg). 65

Figure 57 – Optical images of MoS_2 at different locations: the distances from MoO_3 are (a) 3 cm, (b) 5 cm and (c) 7 cm. $WSulphur$ = 150 mg, $TSulphur$ = 200 ℃, $WMoO3$ = 15 mg, $TSubstrate$ = 700 ℃, ramping rate = 10 ℃/min, flow rate = 30 sccm. Scale bar is 50 μm. 65

Figure 58 – Optical images of MoS_2 synthesized with (a) pure Ar and (b) Ar mixed with 6% H_2. The amounts of MoO_3 and S are 15 and 150 mg, respectively; temperatures of MoO_3 and S are 700 and 200 ℃, respectively; ramping rate is 10 ℃/min; flow rate is 30 sccm. Scale bar is 50 μm. 66

Figure 59 – Optical images of MoS_2 synthesized with (a) 30 sccm, (b) 40 sccm and (c) 50 sccm Ar flow. The amounts of MoO_3 and S are 15 and 150 mg, respectively; temperatures of MoO_3 and S are 700 and 200 ℃, respectively; ramping rate is 10 ℃/min. Scale bar is 50 μm. 67

Figure 60 – Optical images of MoS_2 synthesized with different MoO_3 temperatures: (a) 650 ℃, (b) 700 ℃ and (c) 750 ℃. The amounts of MoO_3 and S are 15 and 150 mg, respectively; temperature of S is 200 ℃; ramping rate is 10 ℃/min; flow rate is 30 sccm. Scale bar is 50 μm. 67

Figure 61 – Surface topographies of SiO_2/Si substrate before and after piranha solution treatment. 68

Figure 62 – Optical images of MoS_2 deposited on SiO_2/Si substrate (a) without and with (b) piranha solution treatment. The amounts of MoO_3 and S are 15 and 150 mg, respectively; temperatures of MoO_3 and S are 700 and 200 ℃, respectively; ramping rate is 10 ℃/min; the flow rate is 30 sccm. Scale bar is 50 μm. 68

Figure 63 – Temperature profile of MoO_3 (black line) and S (red line) for the growth of MoS_2. 69

Figure 64 – Characterization of MoS_2 on SiO_2/Si substrate by CVD method. (a) Optical image. (b) Surface topography by AFM in tapping mode. (c) Raman spectrum and (d) PL spectrum excited by 532 nm laser. (e) Mo 3d, S 2s orbitals and (f) S 2p orbitals demonstrated by XPS spectra. 70

Figure 65 – Temperature profile of WO_3 (black line) and S (red line) for the growth of WS_2..... 72

Figure 66 – Characterization of WS_2 nanoflakes synthesized on SiO_2/Si substrate by CVD method. (a) Optical image and (b) Surface topographic map of a monolayer. (c) Raman spectrum and (d) PL spectrum with 532 nm laser excitation. XPS spectra of (e) W 4f and (f) S 2p orbitals of a monolayer. 72

Figure 67 – (a) Optical image and (b) Surface topography of few layers (5 layers) and multilayers (9 layers) WS_2. 73

Figure 68 – XPS spectra of (a) W 4f, (b) S 2p and (c) C 1s orbitals of few layers (5 layers)..... 74

Figure 69 – XPS spectra of (a) W 4f, (b) S 2p and (c) C 1s orbitals of multilayers (9 layers). 74

Figure 70 – Temperature profile of MoO_3 (black line) and Se (red line) for the growth of $MoSe_2$. 75

Figure 71 – Characterization of chemical vapor deposited $MoSe_2$ nanoflakes on SiO_2/Si substrate. (a) Optical image and (b) Surface topographic map of a monolayer. (c) Raman spectrum and (d) PL spectrum with 633 nm laser excitation. XPS spectra of (e) Mo 3d and (f) Se 3d orbitals. 76

Figure 72 – Temperature profile of WO_3 (black line) and Se (red line) for the growth of WSe_2. 77

Figure 73 – Characterization of WSe_2 nanoflakes synthesized on SiO_2/Si substrate by CVD method. (a) Optical image and (b) Surface topographic map of a monolayer. (c) Raman spectrum and (d) PL spectrum with 532 nm laser excitation. XPS spectra of (e) W 4f and (f) Se 3d orbitals of a monolayer. 78

Figure 74 – Schematic illustration of triboelectric experiments of MoS_2 based on AFM and KFM. (a) Surface potential characterizations in KFM mode before and after charge generation by triboelectrification with contact-mode AFM. (b) Surface topography images before and after triboelectric charge generation. (c) Surface potential image and cross-section profile of the potential distribution along the red line before the rubbing process (the rubbed area is marked with the blue square). (d) Surface potential image and cross-section profile of the potential distribution along the red line after the rubbing process. 83

List of Figures

Figure 75 – Triboelectric characterization of WS_2. (a) Surface topographic images and (b) surface potential maps of WS_2 monolayer before and after triboelectrification. 84

Figure 76 – Triboelectric characterization of $MoSe_2$. (a) Surface topographic images and (b) surface potential maps of $MoSe_2$ monolayer before and after triboelectrification. 84

Figure 77 – Triboelectric characterization of WSe_2. (a) Surface topographic images and (b) surface potential maps of WSe_2 monolayer before and after triboelectrification. 85

Figure 78 – Diffusion of triboelectric charges on MoS_2 over time. (a) Surface potential images after 0, 24, 36 and 48 hours. (b) Cross-section profiles between the lines in a. (c) The surface potential difference as a function of time and its fitted curve. (d) The schematic diagram for tunneling triboelectrification. 86

Figure 79 – KFM images and Cross-section profile of MoS_2 monolayer on (a) gold, (b) sapphire and (c) polyimide substrates before and after triboelectrification. 87

Figure 80 – Diffusion of tribo-charges on WS_2. (a) Surface potential maps after 12, 24, 36 and 48 hours. (b) The surface potential difference as a function of time and its fitted curve.89

Figure 81 – Diffusion of tribo-charges on $MoSe_2$. (a) Surface potential maps after 12, 24, 36 and 48 hours. (b) The surface potential difference as a function of time and its fitted curve.89

Figure 82 – Diffusion of tribo-charges on WSe_2. (a) Surface potential maps after 12, 24, 36 and 48 hours. (b) The surface potential difference as a function of time and its fitted curve.90

Figure 83 – Manipulation of polarity and density of tunneling triboelectric charges on MoS_2. (a) Surface potential images after rubbing the central region with -10, -5, +5 and +10 V biases. (b) Charge density and surface potential difference as a function of tip bias.91

Figure 84 – Controllable density of tribo-charges on WS_2 via bias voltage. (a) Surface potential maps after the triboelectric process with different biases: -10, -5, +5 and +10 V. (b) Charge density and surface potential difference with tip bias. 92

Figure 85 – Controllable density of tribo-charges on $MoSe_2$ via bias voltage. (a) Surface potential maps after the triboelectric process with different biases: -10, -5, +5 and +10 V. (b) Charge density and surface potential difference with tip bias..... 92

Figure 86 – Controllable density of tribo-charges on WSe_2 via bias voltage. (a) Surface potential maps after the triboelectric process with different biases: -10, -5, +5 and +10 V. (b) Charge density and surface potential difference with tip bias..... 93

Figure 87 – Accumulation of triboelectric charges on MoS_2 with rubbing cycles increased. (a) Surface potential images after rubbing with 0, 4, 8 and 12 cycles. (b) Cross-section

profiles between the lines in a. (c) Charge density and surface potential difference as a function of frictional cycle number. 94

Figure 88 – Surface potentials as a function of WS_2 with different layer numbers before and after thermal treatment. 95

Figure 89 –The surface potential difference as a function of time and its fitted curve for monolayer, 5-layer and 9-layer WS_2 nanoflakes. 96

Figure 90 – Material transfer during the triboelectric process for WS_2. (a) Surface potentials with different applied normal forces. Monolayer (1 layer), few-layer (5 layers) and multilayer (9 layers). (b) EDX map of the rubbed area for monolayer WS_2 applied with 25 nN normal force to show the Pt peak. 97

Figure 91 – PL spectra of MoS_2 monolayer on different substrates rubbed with 0, 20, 40 and 60 nN normal force applied: (a) SiO_2/Si, (b) gold, (c) sapphire and (d) polyimide. 102

Figure 92 – PL spectra of MoS_2 monolayer on different substrates rubbed with -10, 0 and +10 V bias voltages applied: (a) SiO_2/Si, (b) gold, (c) sapphire and (d) polyimide. 103

Figure 93 – PL spectra of MoS_2 bilayer on different substrates rubbed with -10, 0 and +10 V bias voltages applied: (a) SiO_2/Si, (b) gold, (c) sapphire and (d) polyimide. 104

Figure 94 – Drawing schemes of five bilayer MoS_2 stacking structures: (a) A-A, (b) A-A', (c) A'-B, (d) A-B' and (e) A-B. Here, one pair of S atoms is represented by one yellow circle for a concise scheme [268]. 104

Figure 95 – Structure of tunable 5G omnidirectional antenna. 106

Figure 96 – Return loss characteristic of proposed antenna with (a) total length *Ld+ L_MoSe₂* and (b) width *Wd* of dipole, length of feeding parts (c) *Lf* and (d) *Lt*. 107

Figure 97 – Return loss of tunable 5G omnidirectional antenna when $MoSe_2$ is in conducting and insulating states. 108

Figure 98 – Radiation patterns (E-plane and H-plane) of tunable 5G unidirectional antenna working at (a) 28 GHz (b) 37 GHz and (c) 39 GHz. 108

Figure 95 – Structure of tunable 5G unidirectional antenna. 110

Figure 99 – Return loss of tunable 5G unidirectional antenna when $MoSe_2$ is in conducting and insulating states. 111

Figure 100 – Radiation patterns (E-plane and H-plane) of tunable 5G unidirectional antenna working at (a) 28 GHz (b) 37 GHz and (c) 39 GHz. 111

List of Figures

Figure 101 – Characterization of MoS_2 transferred on gold substrate. (a) Optical image. (b) Surface topography by AFM in tapping mode. (c) Raman spectrum and (d) PL spectrum excited by 532 nm laser. (e) Mo 3d, S 2s (f) S 2p and (g) C 1s orbitals demonstrated by XPS spectra. 118

Figure 102 – Characterization of MoS_2 transferred on sapphire substrate. (a) Optical image. (b) Surface topography by AFM in tapping mode. (c) Raman spectrum and (d) PL spectrum excited by 532 nm laser. (e) Mo 3d, S 2s (f) S 2p and (g) C 1s orbitals demonstrated by XPS spectra. 119

Figure 103 – Characterization of MoS_2 transferred onto polyimide substrate. (a) Optical image. (b) Surface topography by AFM in tapping mode. (c) Raman spectrum and (d) PL spectrum excited by 532 nm laser. (e) Mo 3d, S 2s (f) S 2p and (g) C 1s orbitals demonstrated by XPS spectra. 120

Figure 104 – XPS spectra of C 1s orbital for (a) MoS_2, (b) WS_2, (c) $MoSe_2$ and (d) WSe_2..... 121

Figure 105 – CVD tube furnace glovebox. 122

Figure 106 – Characterization of WS_2/MoS_2 heterostructure deposited on SiO_2/Si substrate by CVD method. (a) Optical image. (b) Surface topography by AFM in tapping mode. (c) Raman spectrum and (d) PL spectrum excited by 532 nm laser. (e) Mo 3d, S 2s, (f) W 4f, (g) S 2p as well as (h) C 1s orbitals demonstrated by XPS spectra. 124

List of Tables

Table 1 – Triboelectric series for some common materials [1].....6

Table 2 – Experimental setups for the optimized MoS_2, WS_2, $MoSe_2$, and WSe_2.....79

Table 3 – Characterizations of the optimized MoS_2, WS_2, $MoSe_2$, and WSe_2.....79

Table 4 – Surface potential differences compared to the unrubbed area for TMDs monolayers.82

Table 5 – Parameters of fitted tribo-charge diffusion function for MoS_2 monolayer. 88

Table 6 – Parameters of fitted tribo-charge diffusion function for WS_2, $MoSe_2$ and WSe_2 monolayers. 90

Table 7 – Parameters of fitted functions. 96

Table 8 – Atomic ratios of elements on monolayer WS_2 with various normal forces. 97

Table 9 – Triboelectric parameters for MoS_2, WS_2, $MoSe_2$ and WSe_2 monolayers 98

Table 10 – Parameters for tunable 5G omnidirectional antenna.....109

Table 11 – Parameters for tunable 5G unidirectional antenna.....110

Academic Thesis: Declaration of Authorship

I, He Wang, declare that the thesis entitled "**Nanoscale Triboelectrification of Two-Dimensional Chemical Vapor Deposited Transition Metal Dichalcogenide Films**" and the work presented in it are my own and has been generated by me as the result of my own original research.

I confirm that:

1. This work was done wholly or mainly while in candidature for a research degree at this University;
2. Where any part of this thesis has previously been submitted for a degree or any other qualification at this University or any other institution, this has been clearly stated;
3. Where I have consulted the published work of others, this is always clearly attributed;
4. Where I have quoted from the work of others, the source is always given. With the exception of such quotations, this thesis is entirely my own work;
5. I have acknowledged all main sources of help;
6. Where the thesis is based on work done by myself jointly with others, I have made clear exactly what was done by others and what I have contributed myself;
7. Parts of this work have been published as:

Journal Publications

- H. Wang, C.-C. Huang, and T. Polcar, "Controllable Tunneling Triboelectrification of Two-Dimensional Chemical Vapor Deposited MoS_2," Sci. Rep., vol. 9, no. 1, p. 334, 2019.
- H. Wang, C.-C. Huang, and T. Polcar, "Triboelectrification of Two-Dimensional Chemical Vapor Deposited WS_2 at Nanoscale," Sci. Rep., vol. 9, no. 1, pp. 1–8, 2019

Conference

- H.Wang, C. –C Huang, and T. Polcar, "Nanoscale Triboelectrification of Two-Dimensional Chemical Vapour Deposited $MoSe_2$". Presented at: International Tribology Conference in Sendai, Japan 2019.

Signed: .....

Date: .....

Acknowledgements

First and foremost, I would like to thank my PhD supervisors, Professor Tomas Polcar and Dr Chung-Che Huang, who have provided invaluable support and encouragement throughout my PhD. My background was electronic engineering but Tomas trusted me and offered this opportunity even without any interview with me. This project challenged me from now and then, but Tomas and Chung-Che always inspired me and the guidance as well as advice from them were of the utmost importance to accomplish this PhD project. I sincerely thank you both for the enjoyable PhD experience.

This PhD project was funded by Faculty of Engineering and Physical Sciences jointed with my supervisor Tomas, for which I am greatly thankful. I want to express my gratitude to China Scholarship Council for covering my living expenses over my four-year study in UK. I would also like to convey my appreciation to Peter Jost Charitable Foundation, who made me a grant towards the costs of attending the International Tribology Conference 2019 in Sendai, and Engineering and Physical Sciences Research Council to cover publication fees.

Great thanks must go to colleagues and friends who have stood by my side in their individual ways for the past years. I am grateful for the patient training provided by Neil Session, Ruomeng Huang, Sasha Buchnev, Jurgita Zekonyte, and Simon Watson. Special thanks go to Professor Yunqi Fu and Hu Yang, for their patient guidance during my academic life. Particularly, I sincerely thank Tian Bai for the crucial assistance since I started to apply for my PhD, Taolin Liu whose selfless helping hand made my trips to Portugal and Japan, and Ales Rapuc for the coffee times and discussions about our old but productive AFM. Anqi Liang, Guoqiang Yu, Kuo Huang, Ningxin Zhao, Songsong Lu and Yuanguo Tan, our board game nights are unforgettable. Additional thanks should go to Haosheng Qian for the companion of the Portugal journey and Japanese study in Southampton, Tengjiao He for the movie times as well as the ‘Hi He’ greeting every time, Mu Li for the meals and gossips we shared, and Shenglong Zhou as well as Maruti for the gym workouts almost every day. There are too many to mention but you know who you are, I wish you all the best for the future.

Last but not least, I must thank my parents for offering countless support, care, and positivity all my life. It is your unwavering love that keeps me conquering every obstacle and marching fearlessly.

Definitions and Abbreviations

0D	Zero-dimensional
1D	One-dimensional
2D	Two-dimensional
3D	Three-dimensional
1L	Single layer
2L	Bi-layer
3L	Tri-layer
4L	Quadruple-layer
AFM	Atomic force microscope
ALD	Atomic layer deposition
APTES	3-aminopropyl triethoxysilane
CVD	Chemical vapor deposition
CPD	Contact potential difference
FETs	Field effect transistors
FEP	Fluorinated ethylene propylene
KFM	Kelvin force microscopy
LED	Light emitting diode
Mo-zz	Mo zigzag
MOSFET	Metal-oxide semiconductor field effect transistors
PET	Polyethylene terephthalate
PDMS	Polydimethylsiloxane
PI	Polyimide
PL	Photoluminescence
PMMA	Polymethyl methacrylate
PTFE	Polytetrafluoroethylene
RMS	Root mean squared

Sccm	Standard cubic centimeters per minute
SEM	Scanning electron microscope
S-zz	S-zigzag
TENG	Triboelectric nanogenerator
TMD	Transition metal dichalcogenide
XPS	X-ray photoelectron spectroscopy

Chapter 1 Introduction

The basic information of my PhD project, containing the background and motivation, aims and objectives, is introduced in this chapter, and the layout of this thesis is provided as well.

1.1 Background and motivation

Nowadays, energy consumption is very huge considering the thousands of devices integrated into a single system. Taking smartphones as an example, innumerable sensors need to be distributed around the globe to implement communication networks worldwide. To power such a gigantic network, batteries are not a suitable candidate because of the inconvenience brought by scattered locations, regular replacement and inspections. Consequently, it is of great essence to develop techniques related to energy harvesting, especially mechanical energy, which can meet the demands for the maintain-free, self-powered and sustainable operation of micro/nano- systems [3].

Due to the availability, stability, and efficiency of mechanical-to-electrical energy conversion, triboelectrification, a contact-induced electrification where a material becomes charged after brought into contact with another dissimilar one via friction [1], has attracted great attention recently.

To make the best of triboelectrification, suitable materials need to be selected. Based on the number of dimensions at the nanoscale, materials can be classified into zero-dimension (0D), one-dimension (1D), two-dimension (2D) and three-dimension (3D). Among them, 2D materials, whose only one dimension is strictly in the nanometer range, exhibit distinctive shape-dependent and high energy density properties, so they are desirable candidates for various nanodevices, including transistors, sensors, nano-reactors and nanogenerators.

However, there are uncountable 2D materials, which one to choose? Recently, the investigation on 2D transition metal dichalcogenides (TMDs) has been a hot topic. Thanks to their natural abundance and distinctive optical [4][5], electrical [6], and mechanical [7][8] properties, TMDs have become the driving force behind a range of applications, including optoelectronics [9][10], sensors [11][12], electronics [13][14], energy storage devices [15][16], and triboelectric nanogenerators in particular [2]. For instance, monolayer MoS_2 was introduced into the friction layer of a triboelectric nanogenerator as the triboelectric electron-acceptor layer in an attempt to dramatically enhance the output performance, where

the peak power density is 120 times larger than that of the device without monolayer MoS_2 [2]. Even though the principles behind the performance enhancement was discussed, studies concerning the mechanism of triboelectrification are still very limited. Therefore, four typical TMDs including MoS_2, WS_2, $MoSe_2$, and WSe_2 were chosen for a better understanding of triboelectrification.

1.2 Aims and objectives

The goal of this project is to investigate the nanoscale triboelectrification of 2D chemical vapor deposited TMDs films for their triboelectric applications.

As triboelectric behaviors of TMDs produced by chemical vapor deposition (CVD) method have been poorly observed and consequently weakly understood, more research is required and six main objectives of this investigation are depicted as follows:

- Triboelectrification is one of the keywords in this project, so a comprehensive review about this concept is imperative, including its background, mechanism, applicable materials, quantification, manipulation as well as applications.
- As the studied materials for triboelectrification, TMDs are another crucial part of this project, so their structures and properties, preparation and transfer methods, and current applications need to be reviewed at depth.
- CVD methods have been practiced in a diversity of formats according to the initiation of chemical reactions. For example, it can be divided into atmospheric pressure CVD, low-pressure CVD and ultrahigh vacuum CVD by the operating pressure. Resultantly, the appropriate CVD method should be chosen to produce desired 2D TMDs, including MoS_2, WS_2, $MoSe_2$ and WSe_2 in this project.
- Various parameters such as precursors, gas flow, reaction pressure, and temperature, are incorporated in a single CVD experiment, so the effects of different parameters need to be evaluated for the optimization of high-quality materials.
- Microstructural, physical-chemical nature and triboelectric properties of 2D chemical vapor deposited TMDs films need to be characterized and analyzed systematically with the assistance of optical microscope, scanning electron microscope, Raman spectroscopy, X-ray photoelectron spectroscopy, atomic force microscope and Kelvin force microscopy.
- Based on the nanoscale triboelectrification investigated in this project, triboelectric applications need to be considered for TMDs, which may provide a guidance for the development of novel 2D TMDs-based nanodevices.

1.3 Thesis structure

The structure of this thesis is demonstrated by the flow chart in Figure 1. The thesis is split into seven chapters and a brief description of each chapter is explained.

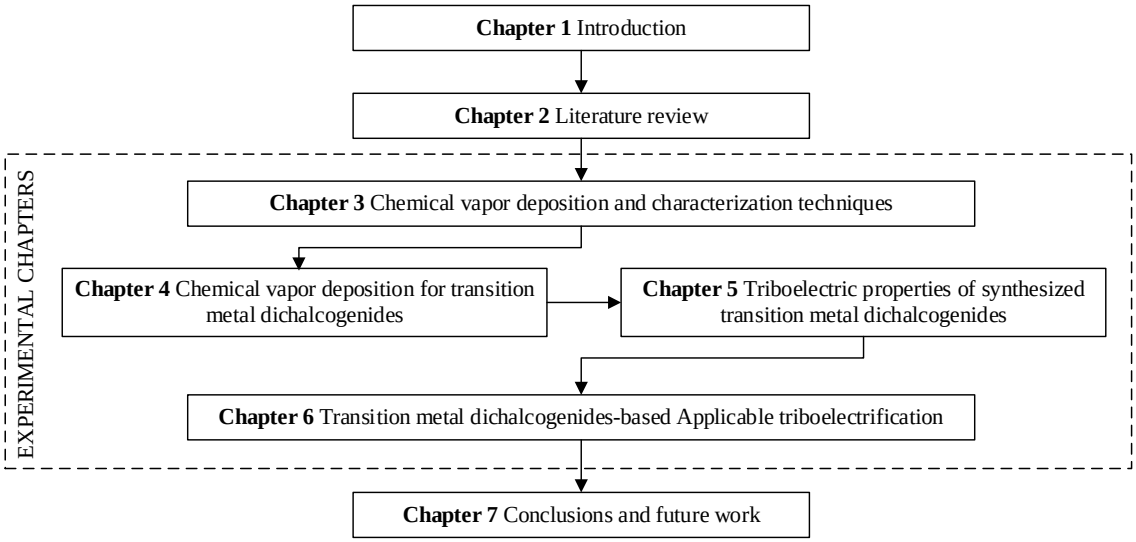

Figure 1 – Thesis structure.

Chapter 1 details the project background and motivation, aims and objectives, and provides an outline of the thesis structure.

Chapter 2 reviews the literature relevant to this project at length. It covers triboelectrification, consisting of the effort to disclose its mechanism, quantification, manipulation as well as applications. Parallelly, insights have been gained on work published in the last decades about the structure and properties, fabrication and transfer methods, and applications of TMDs.

Chapter 3 provides a detailed introduction to chemical vapor deposition, and various instruments including SEM, Raman spectroscopy, XPS, AFM as well as KFM are also reviewed for the structural, physical, chemical and triboelectric characterizations of fabricated materials

Chapter 4 starts with the temperature calibration of the tube furnace used in this research and then examines the effects of various reaction parameters within the chemical vapor deposition process, including amount and temperature of precursors, gas flow, precursor temperature and pre-treatment via piranha solution. Furthermore, optimized MoS_2, WS_2, $MoSe_2$, and WSe_2 have been synthesized and their high-qualities were also confirmed.

Chapter 5 evaluates the triboelectric properties of MoS_2, WS_2, $MoSe_2$, and WSe_2, including initiation and detection, diffusion, and control of tribo-charges, effects of multi-friction, layer number as well as material transfer. On these basis, the mechanism behind triboelectrification is explained based on these four materials.

Chapter 6 presents two TMDs-based applicable triboelectric fields: bandgap modification and tunable antenna for 5G base station, and their working principles along with the performance are examined.

Chapter 7 summarizes the key results of the thesis and proposes the future work needed to continue this investigation.

Chapter 2 Literature review

This chapter provides an introduction to triboelectrification in the first place, including its background, mechanics, quantification and applications. Classification of nanostructured materials are subsequently discussed on a dimensional basis, and it is followed by the review on structure, synthesis and transfer methods, applications of 2D layered TMDs. Afterward, the chemical vapor deposition method and relevant characterization techniques employed in this project are discussed.

2.1 Triboelectrification

2.1.1 Triboelectric effect

Triboelectric effect, contact-induced electrification where material becomes charged after brought into contact with another dissimilar one through friction [1], is one of the most frequently experienced phenomena in our daily life. For instance, it can be extremely challenging to comb our hair in the morning due to the accumulated triboelectric charges; charges induced by air friction can be formed on an airplane when flying, and it can interfere with the radio frequency communication, or even cause the plane to be hit by lightning.

However, the mechanism behind this phenomenon is still being observed possibly with debate. Generally, it is suggested that when two different materials come into contact, a chemical bond, named as adhesion, is formed between some parts of the two surfaces, and charges (electrons, ions or molecules) will transfer from one material to the other to make the electrochemical potential balanced. Once separated, some bonded atoms have a tendency to retain extra electrons, and some tend to lose them, forming the triboelectric charges on the surfaces.

Materials, from metal to semiconductors and insulators, all exhibit triboelectric effect, and the strength of triboelectrification is dependent on their polarity, namely the intrinsic attribute to gain or lose electrons. To describe the triboelectrification of materials, triboelectric series, which is a list of materials behavior regarding their general trend of triboelectric properties without numerical data in the current existing form [17], was proposed and such a series for some common materials are listed in Table 1. For example, when Aluminum and PVC are brought into contact, electrons will transfer from Aluminum to PVC since Aluminum is more positive than PVC in the triboelectric series.

Table 1 – Triboelectric series for some common materials [1].

Positive			Negative
	Polyformaldehyde 1.3-1.4	(continued)	
	Etylcellulose	Polyester (Dacron)	
	Polyamide 11	Polyisobutylene	
	Polyamide 6-6	Polyuretane flexible sponge	
	Melanime formol	Polyethylene Terephthalate	
	Wool, knitted	Polyvinyl butyral	
	Silk, woven	Polychlorobutadiene	
	Aluminum	Natural rubber	
	paper	Polyacrilonitrile	
	Cotton, woven	Acrylonitrile-vinyl chloride	
	Steel	Polybisphenol carbonate	
	Wood	Polychloroether	
	Hard rubber	Polyvinylidine chloride (Saran)	
	Nickel, copper	Polystyrene	
	Sulfur	Polyethylene	
	Brass, silver	Polypropylene	
	Acetate, Rayon	Polyimide (Kapton)	
	Polymethyl methacrylate (Lucite)	Polyvinyl Chloride (PVC)	
	Polyvinyl alcohol	Polydimethylsiloxane (PDMS)	
	(continued)	Polytetrafluoroethylene (Teflon)	

2.1.2 Quantification of triboelectrification

Although the design and operation conditions for triboelectric applications are distinctive, one common factor that can be used to evaluate their performance is the charge density on the surface, whose saturated value may be insensitive to the triggering configurations. Resultantly, triboelectric charge density or relative charge density in reference to a standard material can be chosen as a parameter to characterize triboelectric performance, and quantitative methods are required to assure the accuracy of measurement [1].

Until now, a variety of measurements have been conducted to study the triboelectric charges induced by the contact and separation of charging partners [18]–[27]. For example, the measurement system in Figure 2 has been used for the characterization of triboelectrification at macroscale: tribo-charges on a stainless steel ball, which is in rolling-contact with the inner surface of an insulating tube, was measured by a Faraday cup and an electrometer [27]. The insulating materials consist of glass, quartz, acrylic, polytetrafluoroethylene (PTFE), polycarbonate and nylon.

The effect of contact cycles on the charge transferred from/to the metal sphere was determined in the first place. A contact cycle was defined as an end-to-end rolling of a sphere, and the results for six insulator tubes are depicted in Figure 3. Each data point represents the average of five measurements for the contact cycle number of specific insulator tested. It is noteworthy that the signs of charges on metals are positive for all the insulating tubes, and the magnitude of charge increases in the following rank: acrylic, nylon, quartz, Pyrex, polycarbonate, PTFE. Besides, an obvious saturation effect can be seen in all cases.

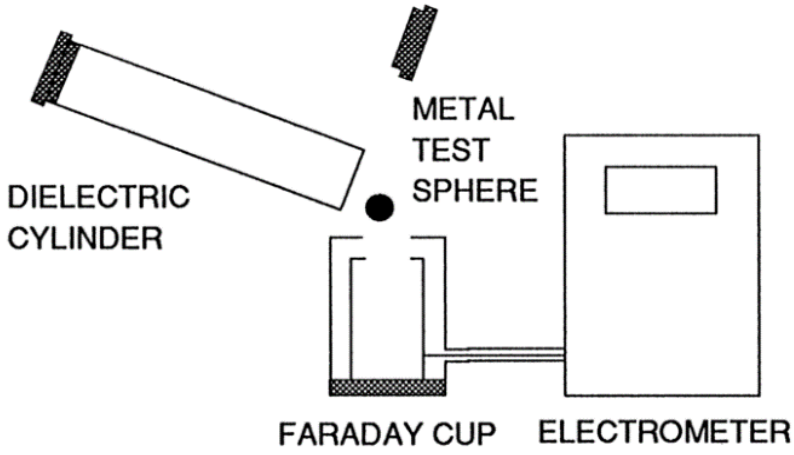

Figure 2 – Macroscale triboelectrification measurement system [28].

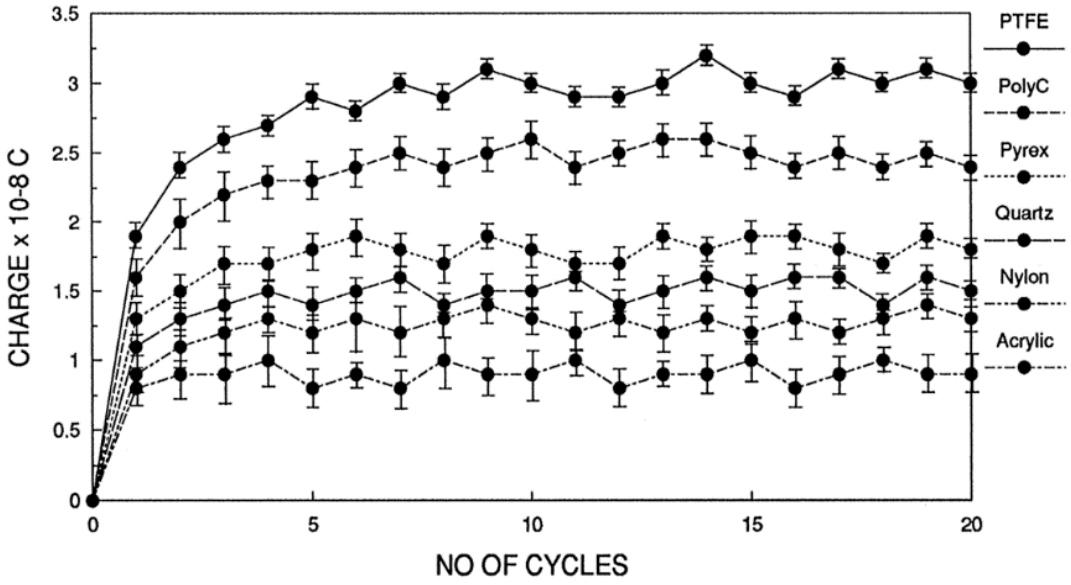

Figure 3 – The relationship between charges generated on the metal sphere and contact circles for various insulators. Test environment: 30% RH (Relative Humidity), 20 ℃ [28].

The effects of humidity and temperature were then studied by averaging the data of all six insulators on a given condition. As shown in Figure 4, each data point represents the overall average of three measurements carried out for each insulator at specific relative humidity and temperature. It is worth noting that the increase of relative humidity leads to a decrease in the net charges at a given temperature, and there is a decrease in the net charge with the increase of temperature at a given relative humidity. However, these conclusions on the impacts of relative humidity and temperature are not solid, since the charge values were averaged from six different materials.

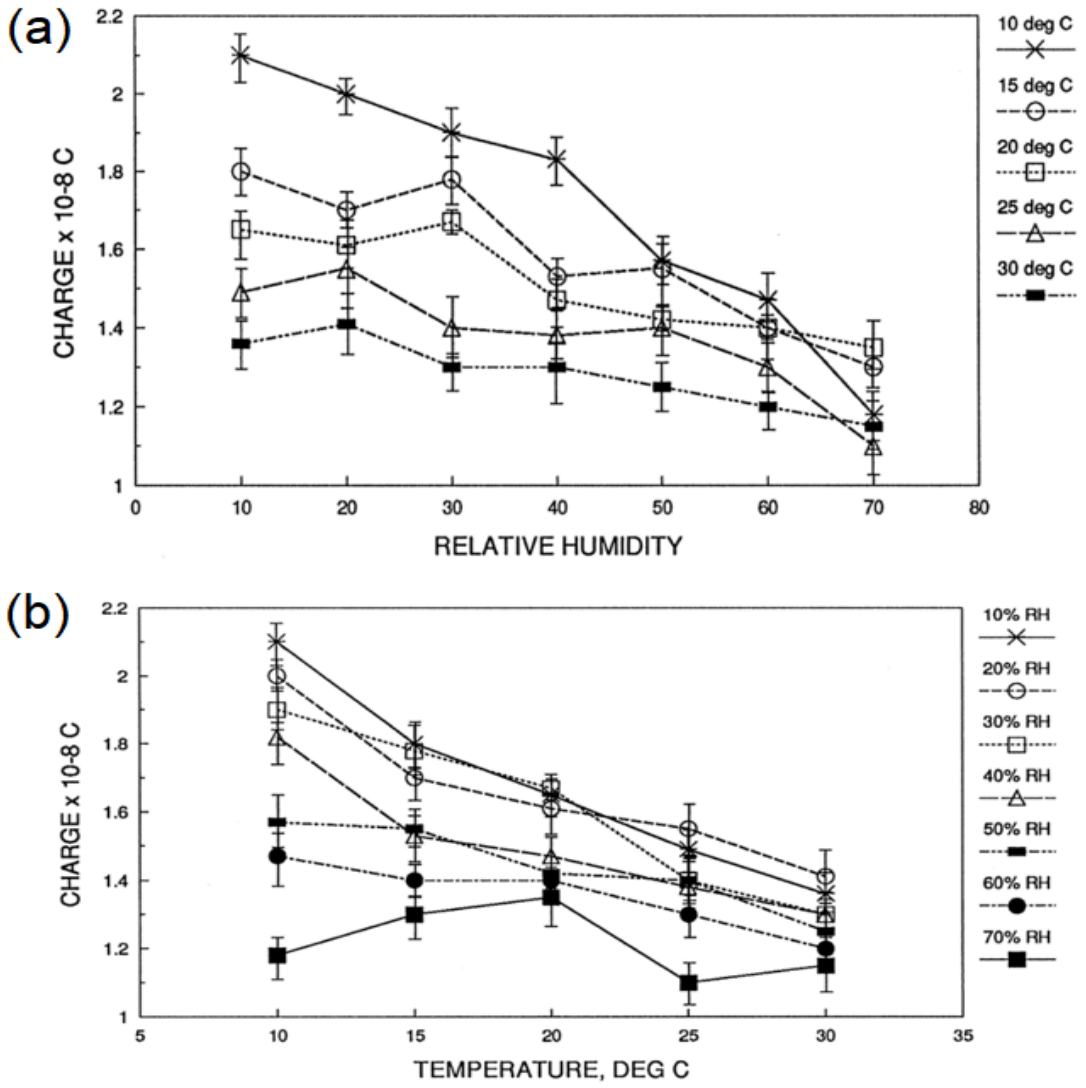

Figure 4 – Average charges on metal sphere as a function of (a) relative humidity and (b) temperature for various tests [28].

In [29], this system was also employed to investigate the triboelectrification of wood and PTFE, so this approach is suitable for the macroscale quantification of triboelectrification.

In order to characterize triboelectrification at the micro/nano-scale, an in situ method combining contact-mode AFM and KFM was proposed in [30]. As the applied normal force, area, speed as well as cycles of the frictional process can be precisely adjusted by AFM system, triboelectric properties, including triboelectric charge distribution, multi-friction effect and charge diffusion, were obtained.

As demonstrated in Figure 5a and b, a 4×4 μm^2 area on SiO_2 was rubbed by contact-mode AFM tip under a 120 nN normal load, and, subsequently, its surface potential was measured by KFM mode with the underlying silicon wafer grounded. As can be seen in Figure 5c, d,

e and f, there is no obvious topographic distinction between the rubbed and unrubbed regions, but the potential of the unrubbed region is 0.167 V higher than that of the rubbed one, which means that some electrons were transferred during the rubbing process thereby reducing the surface potential of the central region.

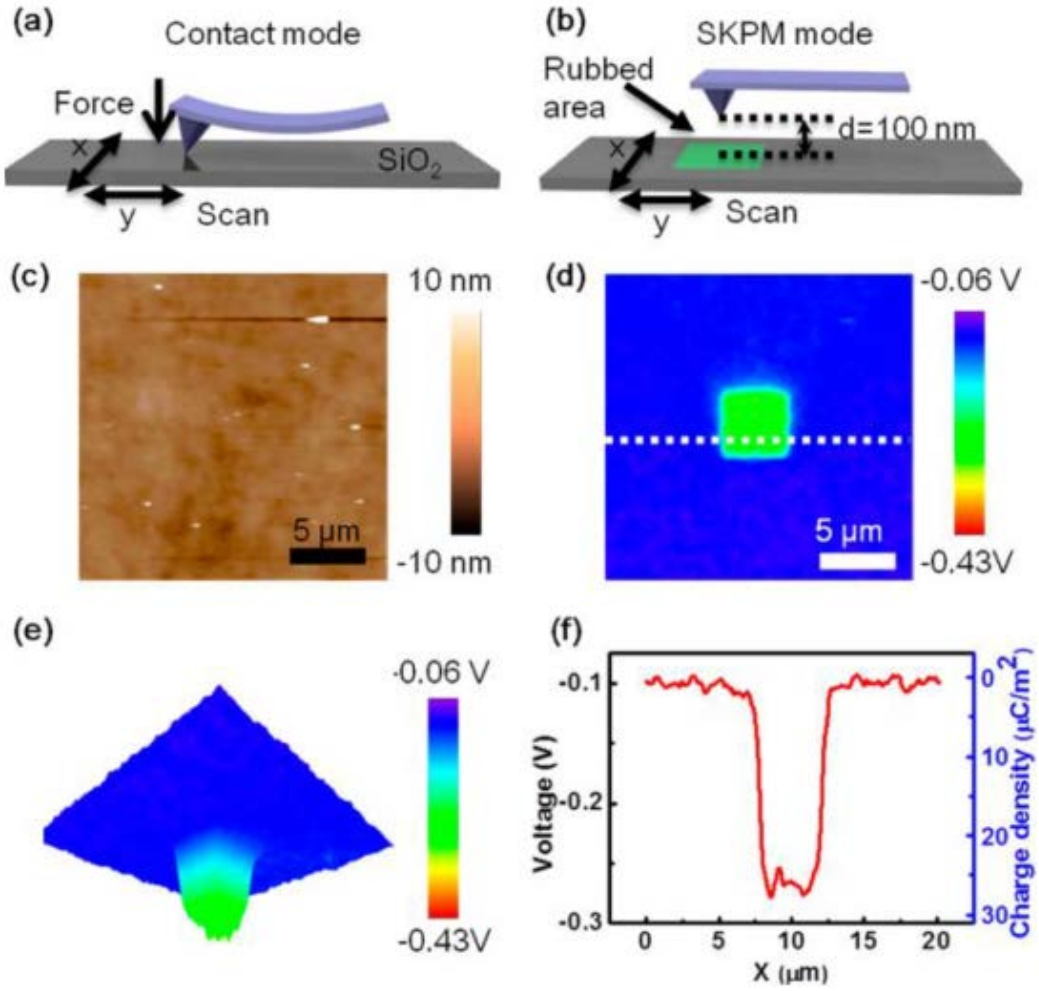

Figure 5 – Illustration of experiments to quantify nanoscale triboelectrification. (a) Generation of tribo-charges by contact-mode AFM. (b) The surface potential measured by KFM mode. (c) Surface topography after the rubbing process. (d) The surface potential of a larger area on SiO_2. (e) 3D image of the surface potential. (f) Cross-section profile of the potential distribution, corresponding to the dashed line in d [30].

With regard to the determination of triboelectric charge density, the relationship between surface potential difference and charge density was investigated. Theoretically, Kelvin force microscopy is to match the tip bias with the tip-sample contact potential difference to negate the vibration of the tip, and the contact potential difference is mainly determined by two elements: electrostatic potential difference and effective work functions of two materials [30]. The former is dependent on the surface charge and applied bias, while the latter is

governed by the surface properties of two materials [31]. Provided that the effective work function is almost identical across the sample surface, the distinction of surface potential between the rubbed and unrubbed regions is ascribed to the triboelectric process.

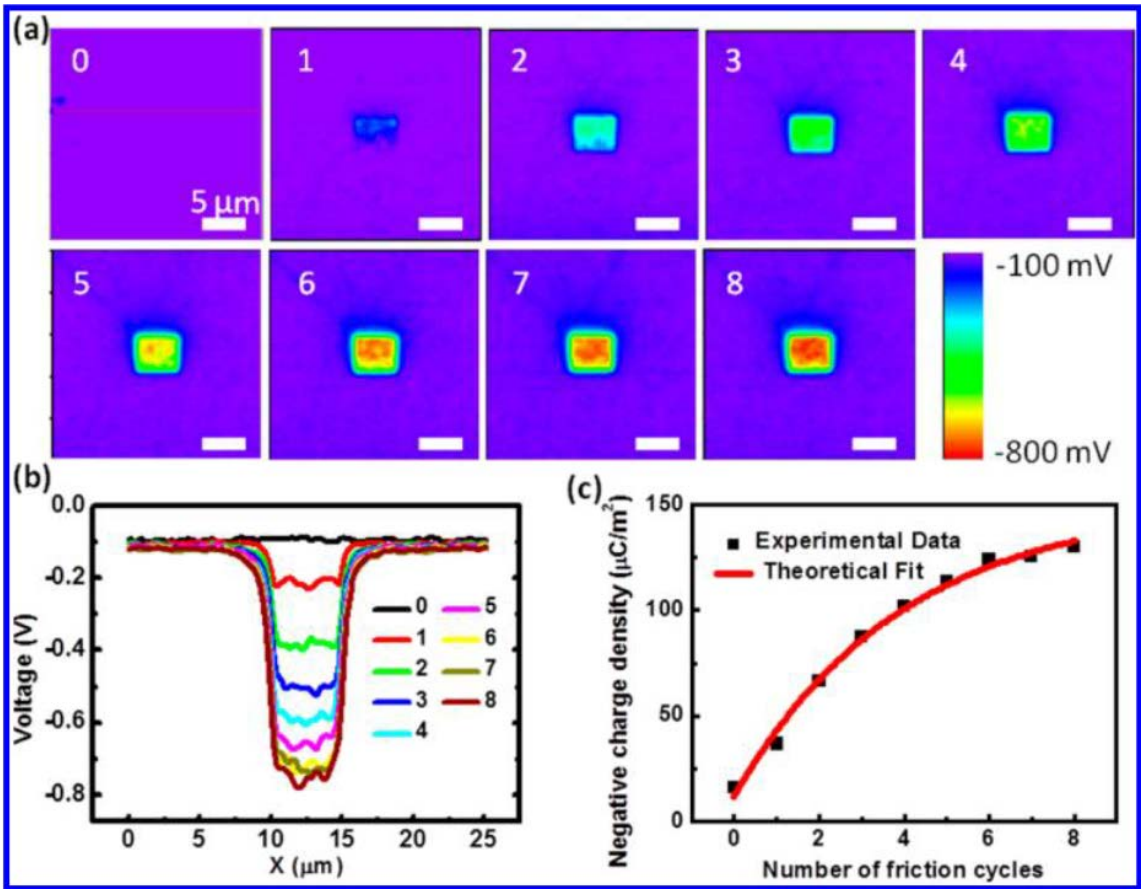

Figure 6 – Triboelectric charge accumulation process. (a) Surface potential images with the increase of cycles and (b) their corresponding potential profiles. (c) Derived surface charge density as a function of the number of friction cycles [30].

As the scale of charged region is far bigger than the thickness of SiO_2, the charge-induced potential change of SiO_2 can be associated with its surface charge density σ by the parallel capacitor model, as described in (2-1) [30].

$$\sigma = \frac{\Delta V \varepsilon_0 \varepsilon_{SiO2}}{t_{SiO2}} \tag{2-1}$$

where ΔV is the potential change; ε_{SiO2} and t_{SiO2} are the relative permittivity and thickness of SiO_2, respectively; ε_0 is the vacuum permittivity. On the condition of $\Delta V = -0.167\ V$, σ can be calculated as -29 μC/m^2. At the same time, a 2D numerical calculation for potential distribution with the surface charge density of -29 μC/m^2 and the presence of AFM tip was simulated to verify the accuracy of this model [30]. The simulation shows that there is no potential gradient between the tip and sample surface of the charged area when tip bias is set

to be -0.168 V, suggesting that the electrostatic force on the tip is canceled. So the simulated tip bias (-0.168 V) is in agreement with the measured potential difference (-0.167 V).

In addition, multi-friction effect was investigated by rubbing the same area for multiple cycles with a constant load [30]. The corresponding KFM images after 0-8 frictional cycles are displayed in Figure 6a, and the extracted potential profiles are demonstrated in Figure 6b. According to equation (2-1), the surface charge density was calculated (Figure 6c), and it can be seen that there is a clear tendency for accumulation and saturation of the surface charge.

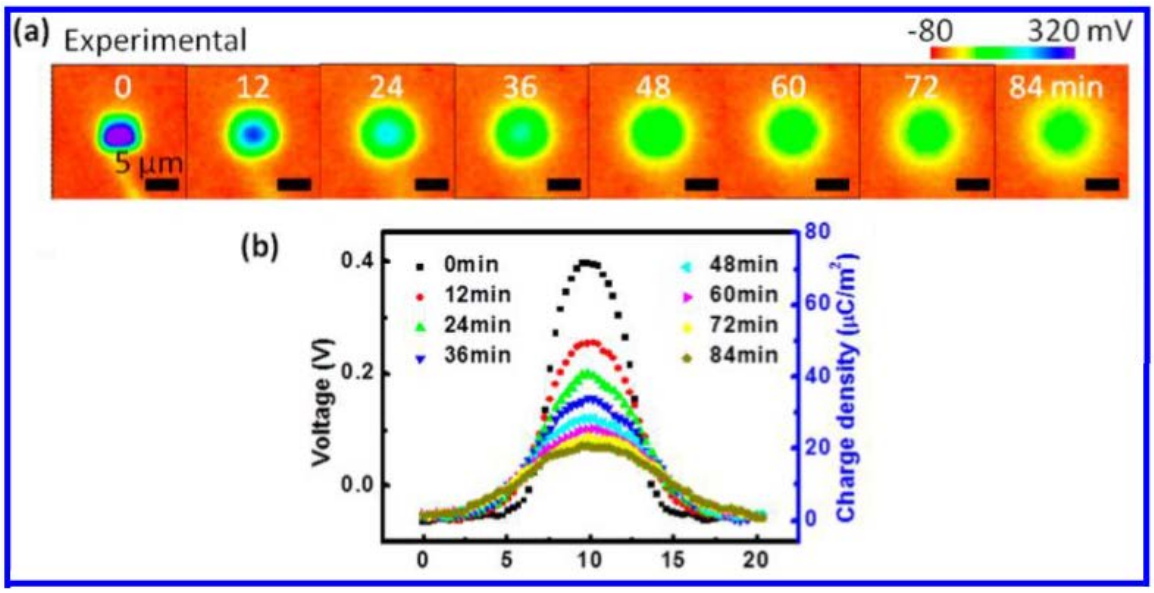

Figure 7 – Charge diffusion over time. (a) Images of surface potential distribution as a function of time after triboelectrification and (b) their corresponding cross-sections [30].

Benefiting from the nanometer resolution of AFM and KFM, the in situ approach can also be adapted to give an insight on the diffusion of tribo-charges by monitoring the surface potential distribution within a period of time after the rubbing process [30]. In the experiment, a 4×4 μm^2 area of SiO_2 surface was scanned over by a Pt-coated AFM tip working in contact mode with a 120 nN load to initiate tribo-charges, surface potential distribution was then measured by KFM every 12 min. As depicted in Figure 7a, the charged region becomes larger and the peak voltage becomes smaller with the passage of time. As evident from the profiles in Figure 7b, positive charges can be transferred to SiO_2 surface by rubbing with Pt-coated Si-based tip, the potential peak reduces from 0.4 to -0.06 V, and the half-width at full maximum of potential distribution profiles increases from 5.1 to 8.6 μm, which indicates the diffusion of surface charges to adjacent regions.

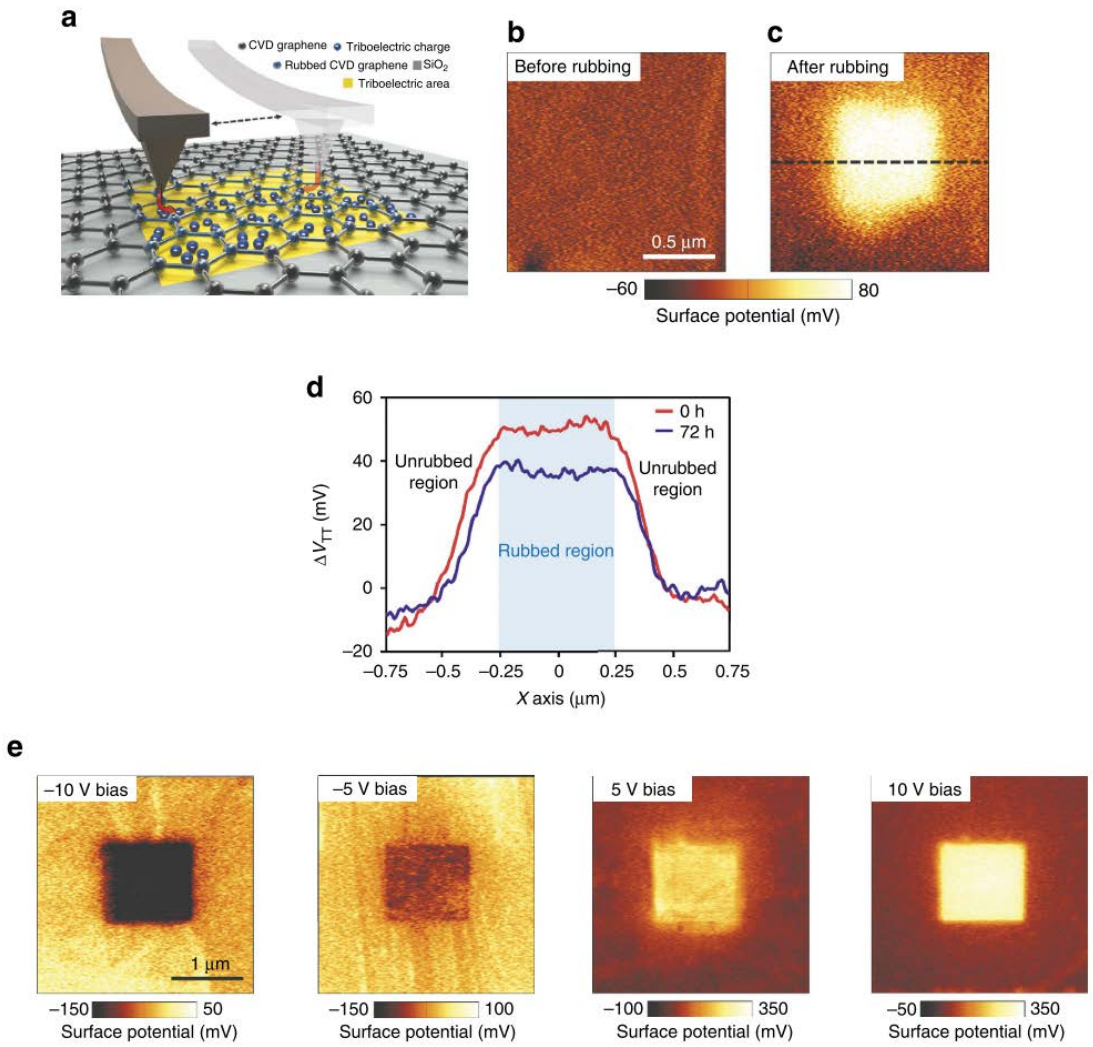

Figure 8 – Tunneling triboelectrification by friction of graphene with a Pt-coated AFM tip. (a) Schematic of the friction process and the KFM measurement system. (b) KFM image of graphene before rubbing. (c) KFM image of graphene after rubbing. (d) Potential difference generated by tunneling triboelectrification, ΔV_{TT}, along the blue dashed line in c after 0 and 72 h. (e) KFM images of graphene after rubbing the central area with different tip bias voltages of -10V, -5V, +5V and +10V [32].

This method has also been employed for the triboelectric characterization of graphene [32]. As demonstrated in Figure 8a, a 0.5×0.5 μm^2 area of chemical vapor deposited graphene on SiO_2/Si substrate was rubbed using a Pt-coated AFM tip in contact mode, with a force of 15 nN and the Si connected to the ground. The surface potential maps shows that the rubbed region has a ~50mV higher surface potential than the unrubbed region (Figure 8b and c). As electric charges may be localized for long times only in insulating materials, it is suggested that some of the charges generated during rubbing tunnel through the monolayer graphene and are locally trapped on the underlying insulator. Figure 8d shows the ΔV_{TT}, the net

variations of the surface potential between the rubbed an unrubbed regions due to tunneling triboelectrification, as a function of position (along the black dashed line of Figure 8c) taken immediately after rubbing and after 72 h. As evident, the potential variation is very well preserved even after 72 h. Similar to the SiO_2 case, both the density and polarity of the tribo-charges can be controlled by changing the tip biasing voltage, as shown in Figure 8e.

Therefore, triboelectrification can be quantified as triboelectric charge density at macro- and micro/nano-scale.

2.1.3 Manipulation of triboelectrification

After unveiling the quantitative analysis of triboelectrification, researchers have been engaged in the study to modulate triboelectrification, mainly the polarity and magnitude of transferred charges.

So far, physical surface engineering ways have been widely employed to boost the tribo-charge density [33][34]. For instance, the surface morphologies can be altered by physical techniques with the creation of pyramids-, square- or hemisphere-based patterns, which are effective to enlarge the contact area and thereby enhancing triboelectrification. Here are also other approaches: extrinsically applied electric field and chemical surface functionalization.

2.1.3.1 Extrinsically applied electric field

The mechanism of triboelectrification between metal and a triboelectrically-negative dielectric is illustrated in Figure 9a. It is worth noting that the Fermi level of the top metal is higher than the highest filled surface energy states of the dielectric material (Figure 9b), so when they are in physical contact, electrons will flow from the top metal to the dielectric surface until an identical level to the Fermi level of metal is reached (Figure 9c). Once they are separated, an electric field is formed thanks to the transferred charges (Figure 9d), and its intensity is proportional to the induced charge density of metal σ_1. In the meantime, an energy barrier obstructing the further movement of electrons is created by the separation. To simplify, a critical tunneling distance z is defined, which means that electrons can move freely to maintain a constant Fermi level when the distance is below z, but the tunneling will be hindered when the distance is above z.

Using the parallel-plate model, the dielectric surface charge density σ consists of σ_1 on the top metal and σ_2 on the bottom one, and the following equation should be satisfied when the distance is equal to z [35].

$$\sigma_1 + \sigma_2 + \sigma = 0 \tag{2-2}$$

According to the built-up electric field σ_1/ε_0, the vacuum energy level E_{VCC} between the metal and dielectric surface will be altered by ΔE_{VCC}:

$$\Delta E_{VCC} = ze\sigma_1/\varepsilon_0 \tag{2-3}$$

where ΔE_{VCC} is ,e is the electron charge [35].

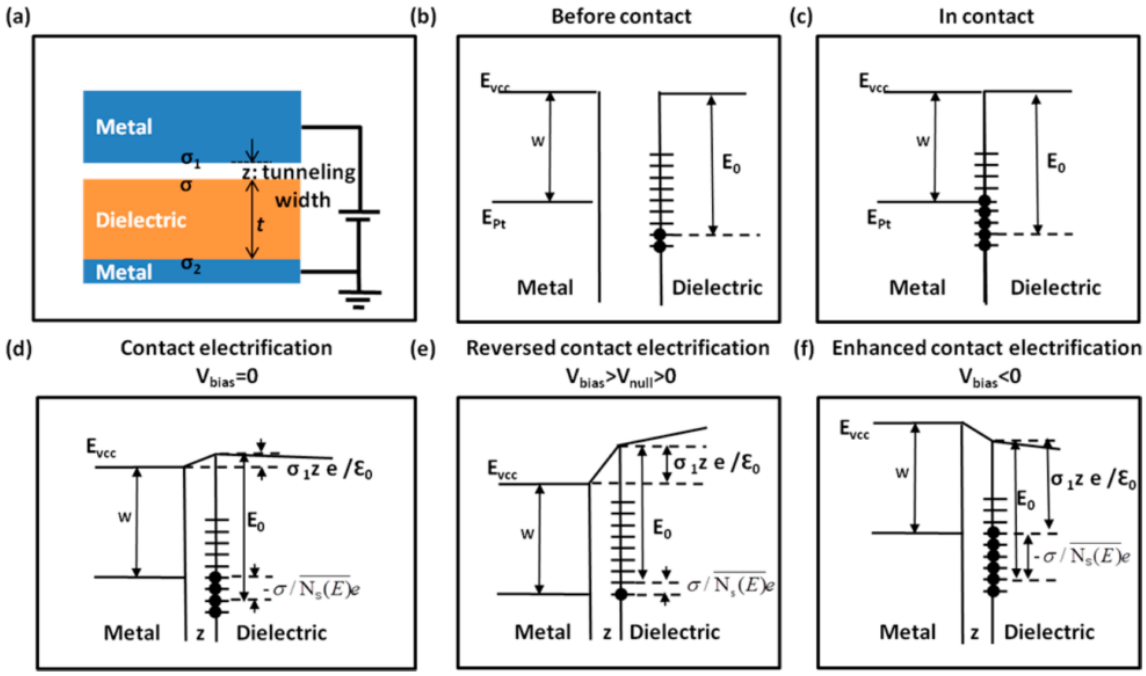

Figure 9 – Mechanism of triboelectrification between a triboelectrically-negative dielectric and metal. (a) Illustration of the contact electrification process. Energy band diagrams in the cases of (b) precontact, (c) contact with no bias, separation equilibrium with (d) no bias, (e) positive bias, and (f) negative bias [35].

The dielectric surface state is filled from the initial E_0 to the same energy level as the Fermi energy level of metal when the system reaches equilibrium again. Assuming that the range of filled surface state is ΔE_S and the surface density of state is $N_s(E)$, σ can be expressed as follows [35]:

$$\sigma = -e\int_{E_0}^{E_0+\Delta E_S} N_s(E)dE \tag{2-4}$$

The average surface density of state $\overline{N_s(E)}$ can be obtained as below [35]:

$$\overline{N_s(E)} = \frac{\int_{E_0}^{E_0+\Delta E_S} N_s(E)dE}{\Delta E_S} \tag{2-5}$$

Consequently, the range of filled surface state ΔE_S can be written as [35]:

$$\Delta E_S = -\sigma/\overline{N_s(E)}e \tag{2-6}$$

By combining (2-3) and (2-6), the following relationship can be obtained [35]:

$$E_0 - W = \Delta E_{VCC} + \Delta E_S = ze\sigma_1/\varepsilon_0 - \sigma/\overline{N_s(E)}e \tag{2-7}$$

where W is the initial surface state of metal.

Under this circumstance, the relative energy band height can be changed by applying an external electric field between two electrodes, which can also modulate the charge transfer process accordingly. For example, a positive bias applied to the top electrode can reduce its Fermi energy level, so there is a decrease in the number of transferred electrons from the top metal electrode to the dielectric surface. It is noticed that the Fermi energy level of top metal can equate to the highest filled surface states of the dielectric at a certain bias, where there will be no charge transfer between the top metal and the dielectric. If the bias is more positive than the nullified bias, electrons will flow in the opposite direction instead (from dielectric to metal), resulting in a positive-charged dielectric surface (Figure 9e). On the other hand, if a negative bias is applied to the metal, its Fermi level will be increased and more electrons will be driven to the dielectric to fill up the higher surface energy states, leaving a more negative-charged dielectric surface (Figure 9f).

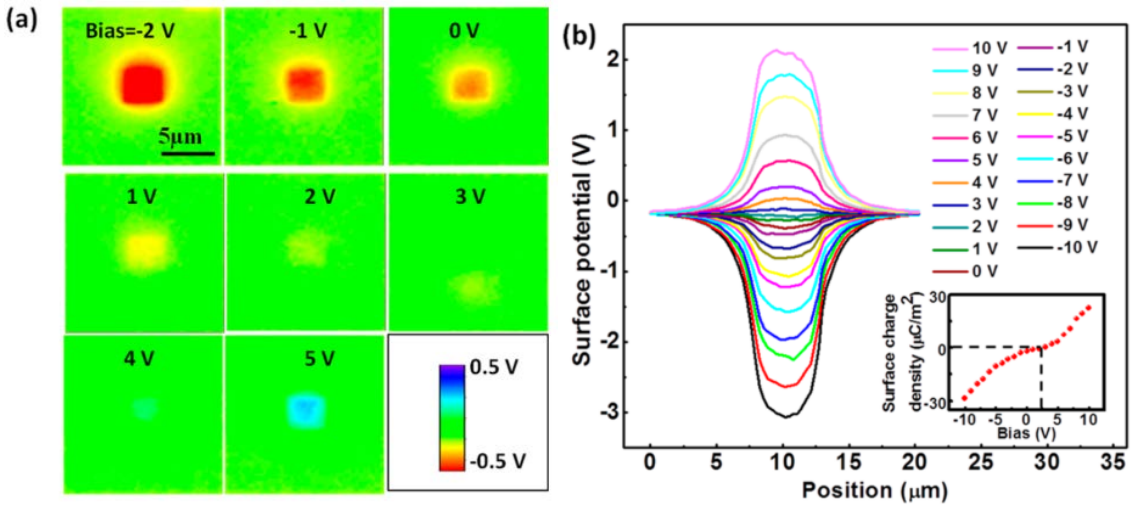

Figure 10 – Manipulation of triboelectrification by an applied electric field. (a) Surface potential maps of Parylene film rubbed with biases ranging from -2 to 5 V. (b) Cross-section profiles of the surface potential on Parylene film rubbed with biases from -10 to 10 V. The inset is the calculated surface charge density as a function of bias. [35].

To quantify the effect of applied bias on triboelectric process, different regions of a 2 μm thick Parylene film was rubbed with biases varying from -10 to 10 V, and the surface potential distributions were recorded. It is noteworthy in Figure 10a that a negative charge density can be enhanced by a negative bias; charges can be offset when bias is about 2 V; a bias above 2 V can bring positive charges to the rubbed region. As evident in Figure 10b, surface potential changes monotonically with applied bias, so does the surface charge density.

As a consequence, triboelectrification, including the polarity and magnitude of transferred charges, can be manipulated by an externally-applied electric field between the tip and sample.

2.1.3.2 Chemical surface functionalization

Another direct and effective approach to alter triboelectrification is chemical surface functionalization, where diverse nanostructures are embedded on the surface of the contact materials or even inside [1]. Due to the modification of work function via various functional head groups, triboelectric properties can be adjusted correspondingly since it is closely relevant to the work functions of two contact surfaces.

In [36], thiols was used to make alterations to the surfaces of conductive gold (Au). As can be seen from Figure 11, four different functional head groups were attached to Au surface: hydroxyl (-OH), ester (-$COOCH_3$), amine (-NH_2) and chloro (-Cl). And the functionalization of amine was revealed by 4-aminothiophenol and cysteamine hydrochloride, respectively. It is found that functional groups of hydroxyl, ester, and amine can enhance the surface potential compared with the bare Au surface; the smallest enhancement is brought by hydroxyl while the largest is by amine. As for two amine thiol molecules, cysteamine hydrochloride results in a larger improvement in the surface potential, which may be attributed to the lower electronegativity of ethylene (-CH_2-) group than phenylene (-C_6H_4-) group [37]. Therefore, it can be concluded that triboelectric properties of gold can be altered by surface functionalization.

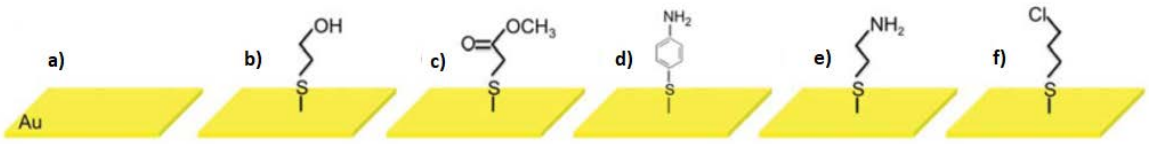

Figure 11 – Molecular structures of the thiols [36].

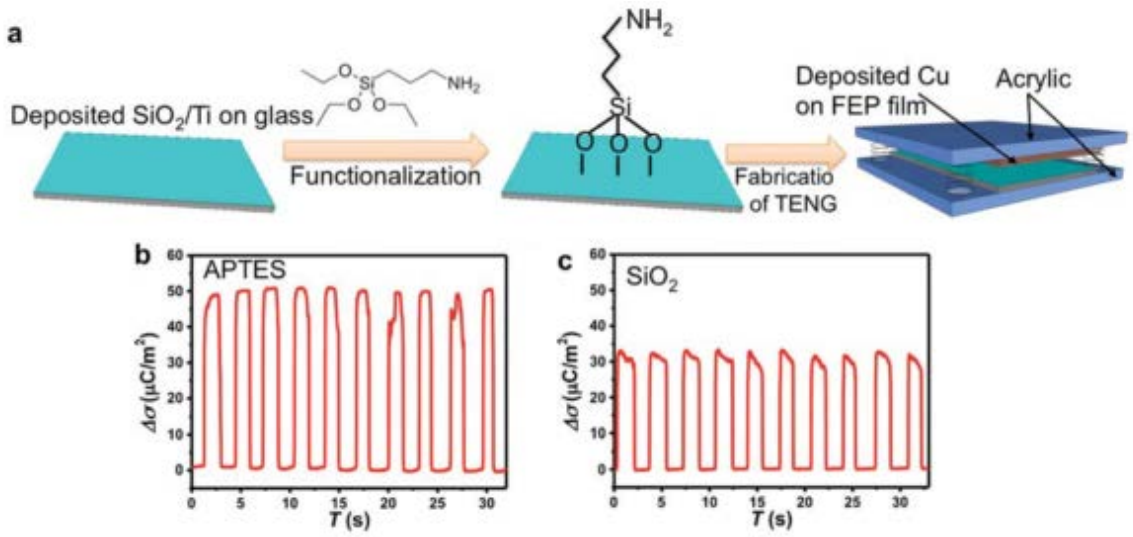

Figure 12 – Chemical surface functionalization of SiO_2. (a) Fabrication process. Charge density of SiO_2 (b) with and (c) without functionalization [36].

Apart from the functionalization of the conductive surface, the applicability of this method for insulating surfaces was demonstrated by inorganic SiO_2 [36]. As evident in Figure 12, SiO_2 was deposited on the top of a glass slide with a titanium film in between as the electrode and adhesion layer. A silane molecule (3-aminopropyl triethoxysilane, APTES), which has amine as the head group, was then exploited, and it was followed by the fabrication of triboelectric nanogenerator (TENG), with copper-deposited fluorinated ethylene propylene (FEP) film on a glass slide as the counter material. In comparison to the results of unfunctionalized SiO_2, the surface charge density of functionalized SiO_2 increases by ~17 $\mu C/m^2$, indicating that the triboelectric performance of insulating SiO_2 can be improved by chemical surface functionalization method.

As for organic materials, it is reported in [38] that the triboelectric charge density of polyethylene terephthalate (PET) film can be intensified significantly by surface modification. In the experiment, PET surface was modified by the inductive-coupled plasma etching method utilizing a mixture of oxygen (O_2) and carbon tetrafluoride (CF_4) gases, which was followed by the surface potential characterization by KFM. As can be seen from Figure 13, the averaged surface potential of modified PET (105 mV) is ~2.5 times as much as that of the unmodified one (41 mV).

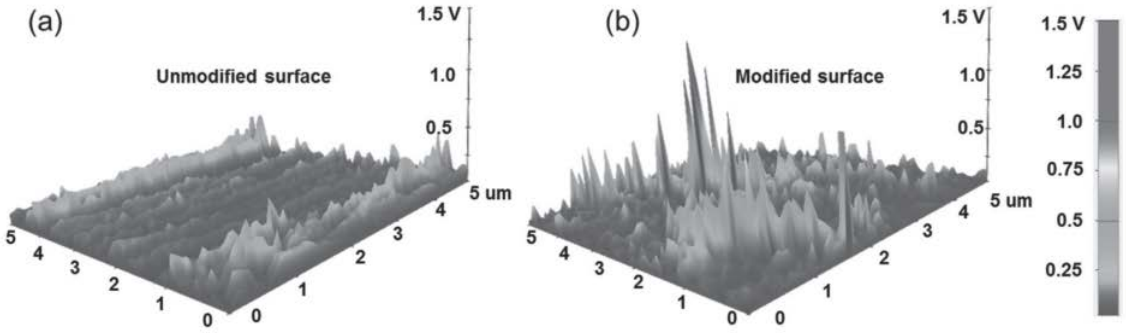

Figure 13 – Surface potentials of (a) unmodified and (b) modified PET samples [38].

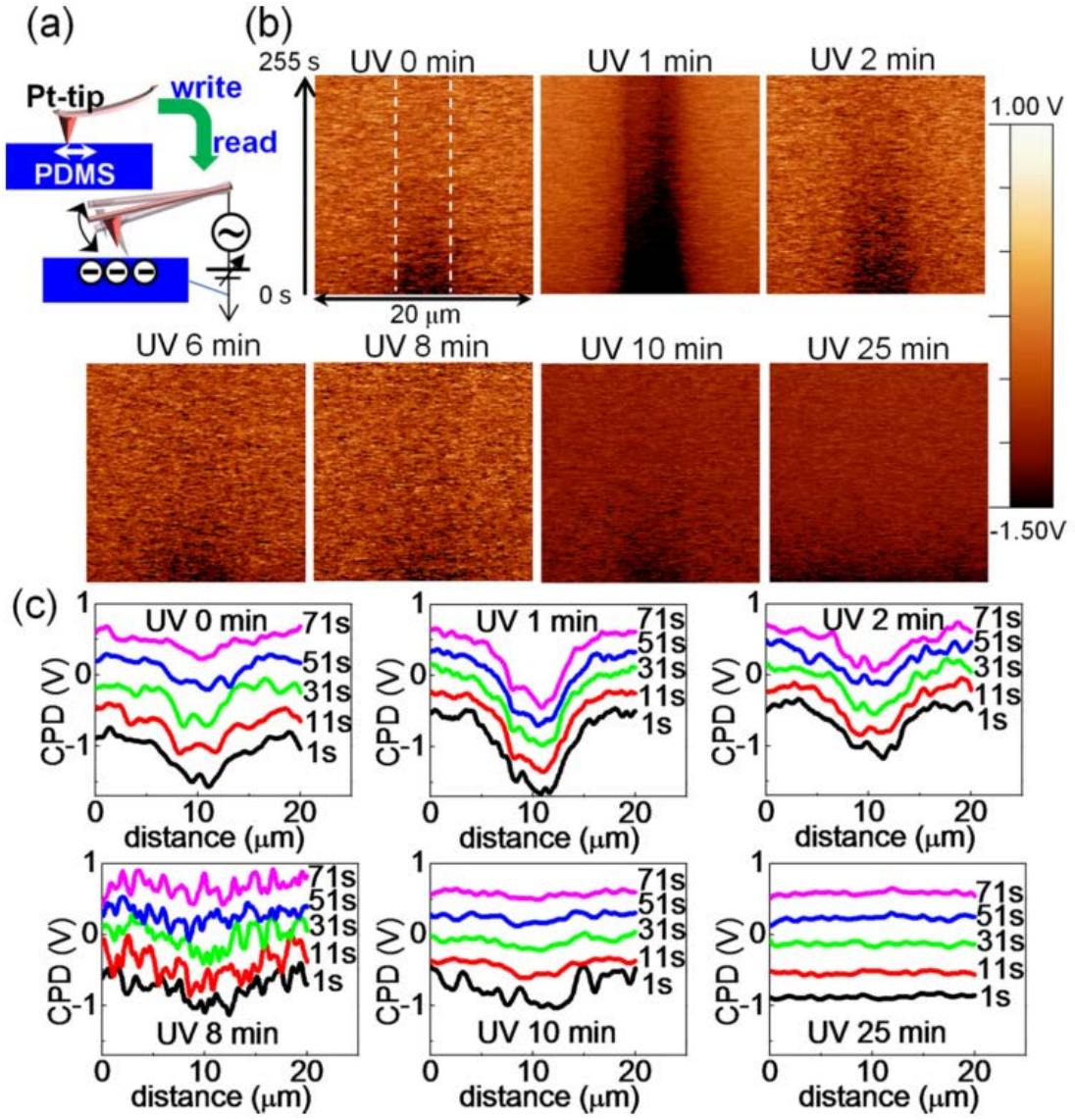

Figure 14 – Triboelectric enhancement of PDMS by ultraviolet irradiation. (a) Measurement of triboelectrification. (b) A series of time-evolution contact potential difference (CPD) images with various ultraviolet treatment time. (c) CPD profiles at different times. A y-offset is assigned to each curve to avoid overlapping [39].

Kim et al reported that triboelectric performance of transparent polydimethylsiloxane (PDMS) film could be signified by ultraviolet irradiation [39]. In the experiment, PDMS film was rubbed by Pt-coated AFM tip, which was followed by the KFM measurement for surface potential (Figure 14a). The lower row of each image in Figure 14b shows the earlier time and dashed lines represent the rubbed region. According to the extracted profiles in Figure 14c, negative charges are formed on the surface via rubbing operation, which is consistent with the triboelectric series in which PDMS owns a stronger affinity for negative charge than platinum. The surface potential difference between the rubbed and unrubbed regions diminishes over time for the film without exposure to ultraviolet. When these films were exposed to ultraviolet light for 1 or 2 minutes, not only is the contact potential difference enhanced, but the diffusion rate of triboelectric charges also becomes slower. However, the contact potential difference disperses with the increase of exposure time, and the surface potential of the whole area moves to a more negative value gradually when the exposure time reaches 25 minutes.

In addition, it has been verified that the triboelectric properties of Kapton, PTFE, PET, and PDMS can be improved by mixing melamine [40], and charge densities of all these composites increase to different degrees, as displayed in Figure 15.

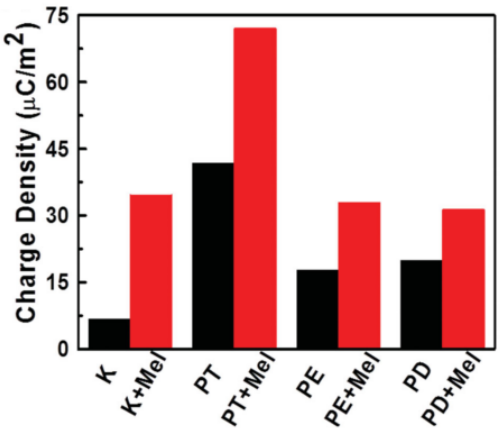

Figure 15 – Charge density of various triboelectric materials (K-Kapton, PT-PTFE, PE-PET, and PD-PDMS) mixed with melamine [40].

The effect mainly results from two aspects. Firstly, the surface morphology of the layer materials is changed by mixing melamine. The increase in the surface roughness and effective surface area of PTFE (Figure 16) boosts the triboelectric charge density. Secondly, the relative permittivity of materials can be modified by the addition of melamine. As melamine has smaller molecules, the permittivity value increases gradually with the mixing

procedure, and reach a maximum at a proper mixing concentration due to the improvement in the porosity of the nanocomposite films [40].

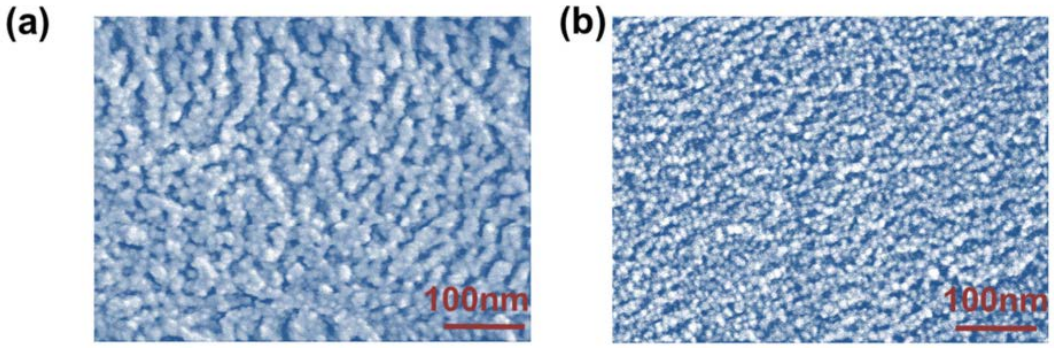

Figure 16 – SEM images of PTFE before (a) and after (b) melamine mixture [40].

2.1.4 Triboelectric applications

To date, various triboelectric applications have been invented, and one of the most popular kinds is triboelectric nanogenerators, which consist of the traditional Wimshurst machine as well as Van de Graaff generator, and the cutting-edge systems designed to harvest small scale mechanical energy by functioning in four modes: vertical contact-separation mode [41], lateral sliding mode [42], single-electrode mode [43] and freestanding triboelectric-layer mode [44].

Built on the aforementioned four working modes, a broad range of triboelectric nanogenerators have been fabricated to harvest sorts of mechanical energies that are available but wasted in our daily life, such as human motion, walking, vibration, mechanical triggering, rotating tire, wind, flowing water and more [1], [45], as illustrated in Figure 17. As of today, the area power density produced by a triboelectric nanogenerator has reached as high as 500 W/m^2, volume power density reaches 15 MW/m^3, and an instantaneous conversion efficiency of ~70% has been realized [46]. If the energy generated by all the residual vibrations are acquired, a total energy conversion efficiency of up to 85% can be experimentally achieved for low frequency [47].

The discovery of triboelectric nanogenerator is a milestone in the field of converting mechanical energy into electricity. As an extension of triboelectric nanogenerators, tribotronics have been developed by coupling triboelectrification with semiconductors, where the electrostatic potential is created by triboelectrification as a gate voltage to tune the electrical transport and transformation in semiconductors.

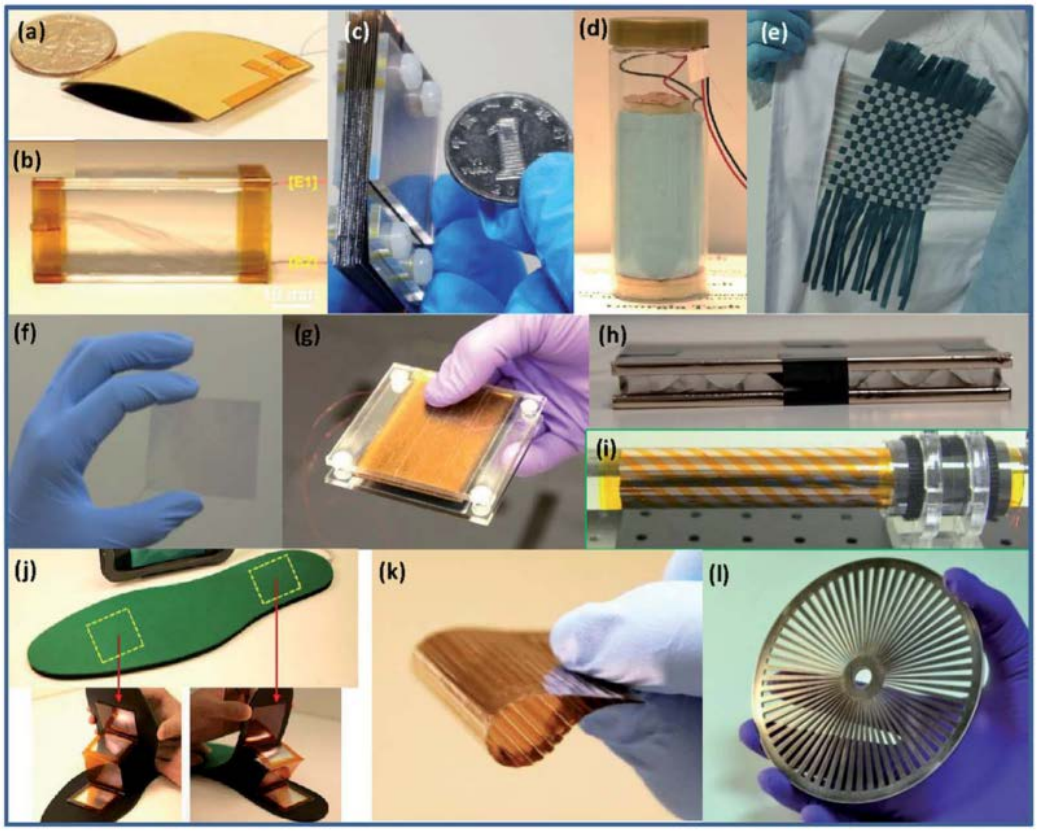

Figure 17 – Various triboelectric nanogenerators designed for harvesting sorts of energies: (a) finger tapping energy, (b) air-flow/wind energy, (c) relative in-plane sliding energy, (d) enclosed cage for harvesting oscillating/disturbing energy in water or mechanical vibration, (e) fabric for harvesting body motion energy, (f) energy in touchpad, (g) foot/hand pressing energy, (h) water impact energy, (i) cylindrical rotation energy, (j) shoe insole for walking energy, (k) flexible grating structure for harvesting energy, and (l) disc shape rotation energy [1].

Based on the idea of tribotronics, the triboelectrification field effect transistor was invented, which is composed of a back-gate silicon-on-insulator metal–oxide–semiconductor field-effect transistor (MOSFET) and a mobile layer [48]. Different from the conventional back gate MOSFET, the externally applied gate voltage source is replaced by the mobile layer, which consists of a Kapton film and an aluminum electrode and can contact and separate from the gate electrode vertically by an external force (Figure 18a). When the Kapton film touches the gate electrode, the aluminum is positively charged while the Kapton negatively. When the mobile layer is gradually separated, electrons will flow from the mobile aluminum to the source electrode by electrostatic induction, leaving a positive inner gate voltage for the back-gated MOSFET. The contact electrification field-effect transistor can be considered as the coupling of the MOSFET and triboelectric nanogenerators (Figure 18b), in which the inner gate voltage can be generated and the carrier transport between drain and source can

be tuned/controlled by the external contact instead of the conventional gate voltage (Figure 18c). With the mobile layer vertically separated by 80 μm, the drain current is decreased from 13.4 to 1.9 A at a drain voltage of 5V (Figure 18d).

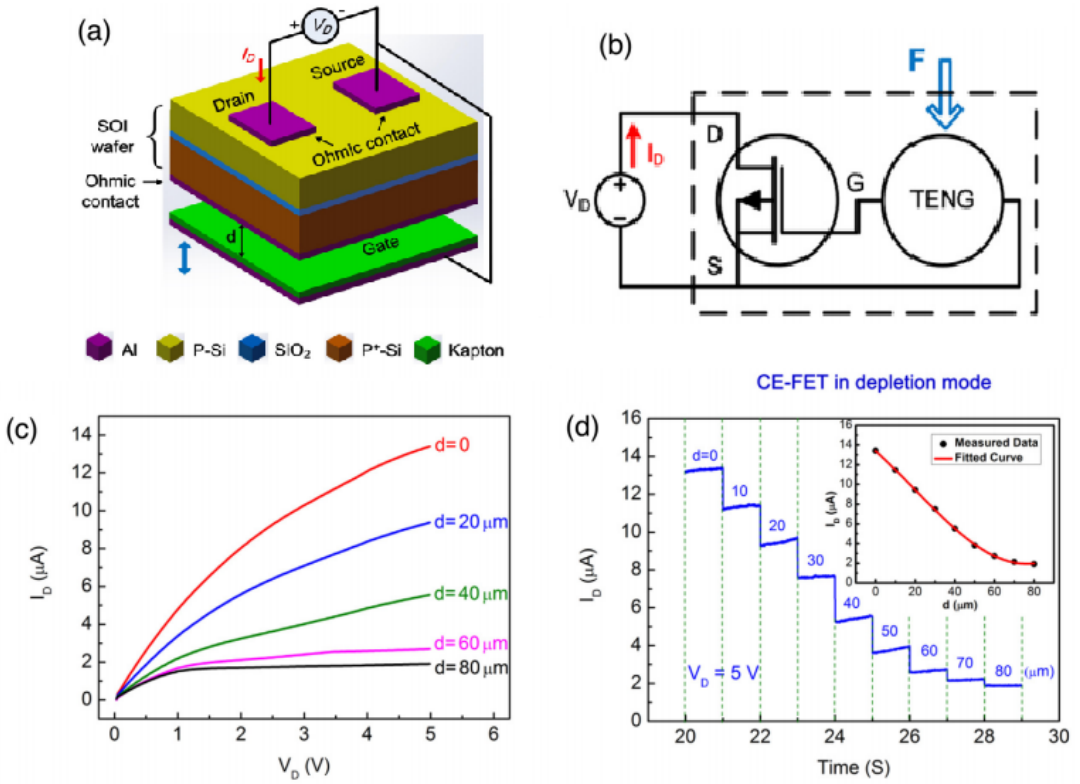

Figure 18 – Triboelectrification field-effect transistor. (a) Schematic diagram. (b) Equivalent circuit. (c) I_D-V_D output characteristics at different vertical distances (d) I_D-t output characteristics with the change of the vertical distance. The inset is I_D-d transfer characteristic [48].

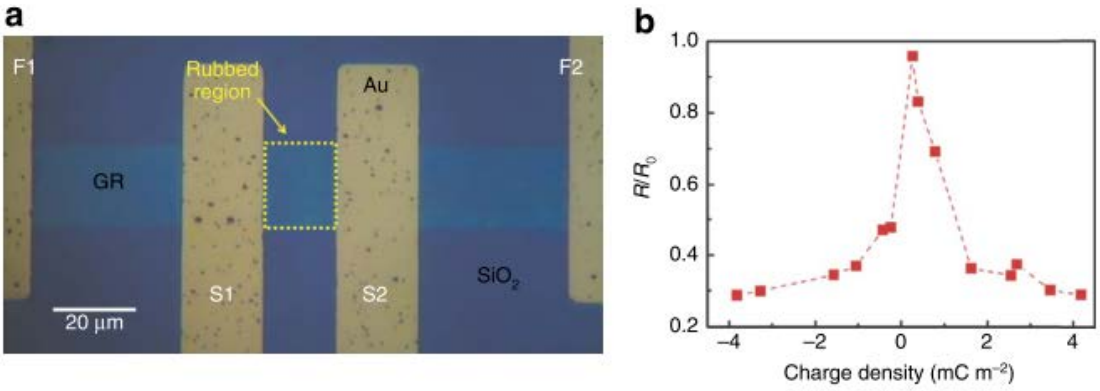

Figure 19 – Resistance reduction of graphene by tunneling triboelectrification. (a) Optical image of the 4-wire graphene resistor (the yellow dashed box is rubbed by Pt-coated AFM tip). (b) Normalized resistance of the graphene resistor as a function of the tunneling triboelectric charge density [49].

Furthermore, Seongsu Kim's group introduced the concept of tunneling triboelectrification, which is the friction-induced tunneling of charges through a 2D material and their accurate localization on the insulator underneath the 2D material, to effectively create, modify or destroy the gate by controlling the properties of 2D materials with the spatial resolution of AFMs [49]–[51]. Figure 19a shows the fabricated 4-contacts monolayer graphene resistor, whose middle area (yellow dashed box, 17×20 mm^2, between the sense electrodes S1 and S2) was rubbed by a Pt-coated tip. The voltage difference of the single-layer graphene between the inner electrodes S1 and S2 was measured in vacuum by applying a constant current through the external force electrodes F1 and F2. During the measurements, the current was kept at a very low level (100nA) to prevent any perturbation to the stored charges. In fact, the tunneling triboelectric charges stored under graphene can be removed at sufficiently high currents. Although the threshold current depends on the sample, it is found that the trapped charges can survive even under current up to the mA range for widths of only 20mm. Figure 19b shows the normalized resistance R/R_0 (where R_0 and R are the resistances of graphene before and after rubbing, respectively) as a function of the tunneling triboelectric charge density. As expected, the resistivity can be electrostatically reduced by the tunneling of tribo-charges. The dependence of the resistance on the tip voltage is obviously similar to the gate bias-dependent resistance in graphene field-effect devices with conventional gates [52], [53].

2.2 Classification of nanomaterials

To observe the triboelectric phenomena in depth, it is of crucial essence to select appropriate materials for the investigation. Recently, nanomaterials, defined as solid materials characterized by at least one dimension in the nanometer range, have attracted much more attention and gained prominence in technological advancements thanks to their tunable physical, chemical and biological properties with enhanced performance over their bulk counterparts. In this situation, how to classify nanomaterials is an inevitable question. The first classification of nanomaterials was raised by Gleiter [54] but this arrangement was incomplete due to the ignorance of dimensionality. The scheme was further developed by Skoroknod and Pokropivny, with 0D, 1D, 2D and 3D nanostructured materials included [55]. This categorization is highly subject to the movement of electrons along the dimensions inside the nanomaterials. For instance, 0D nanomaterials have electrons entrapped in a dimensionless space while electrons in 1D can move along one dimension. Likewise,

electrons in 2D and 3D nanomaterials can move along two and three dimensions, respectively.

2.2.1 Zero-dimensional nanomaterials

Zero-dimensional nanomaterials behave like atomic or molecular clusters with well-discrete energy states since the excited electrons are confined by three dimensions. Significant progress has been made over the past decade and a variety of physiochemical methods have been developed to fabricate such materials with well-controlled dimension. For instance, heterogeneous particles arrays, uniform particles arrays (quantum dots), onions, core-shell quantum dots, nanolenses as well as hollow spheres have been synthesized by several research groups [56][57], as shown in Figure 20. Until now, 0D nanostructured materials have been applied to light-emitting diodes (LEDs) [58], single-electron transistors [59], lasers [60], and solar cells [61].

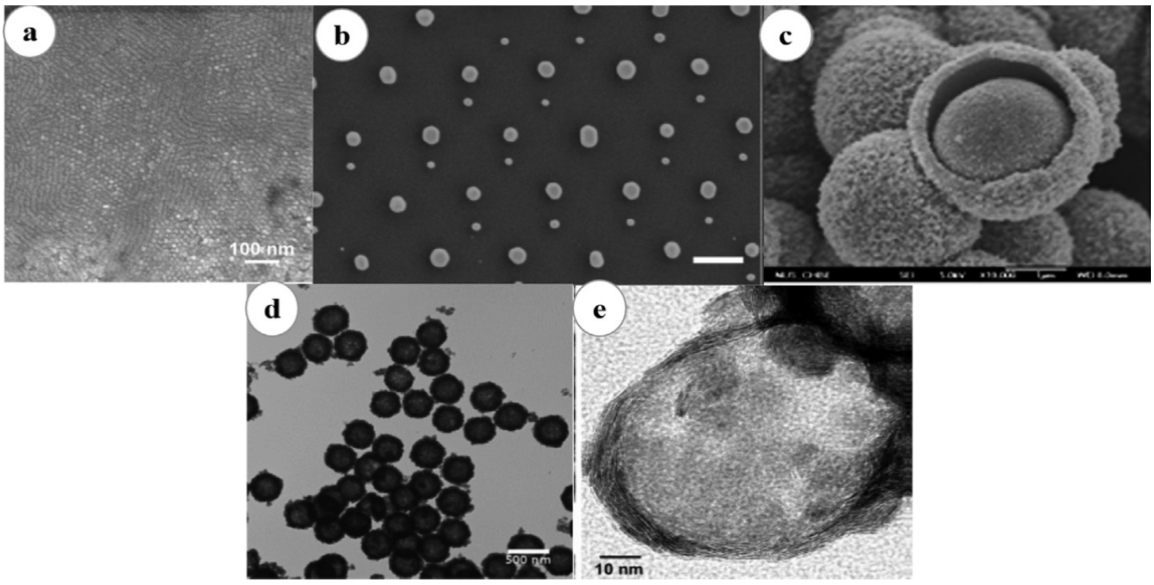

Figure 20 – Images of some typical 0D nanomaterials: (a) quantum dots [56], (b) nanoparticles arrays [62], (c) core-shell nanoparticles [63], (d) hollow cubes [64], and (e) nanospheres [65].

2.2.2 One-dimensional nanomaterials

One-dimensional nanomaterials, which own nanoscale size along two dimensions and a wire or rod-like appearance, are a promising tool to explore the dependence of dimensionality as well as size on functional properties, and a diversity of novel phenomena at the nanoscale. Therefore, they have shown a collection of potential applications, such as nano-systems,

nanocomposites, nanoelectronics, alternative energy resources and national security systems [66]. Figure 21 demonstrates the images of nanowires, nanorods, nanotubes, nanobelts, nanoribbons, and hierarchical nanostructures.

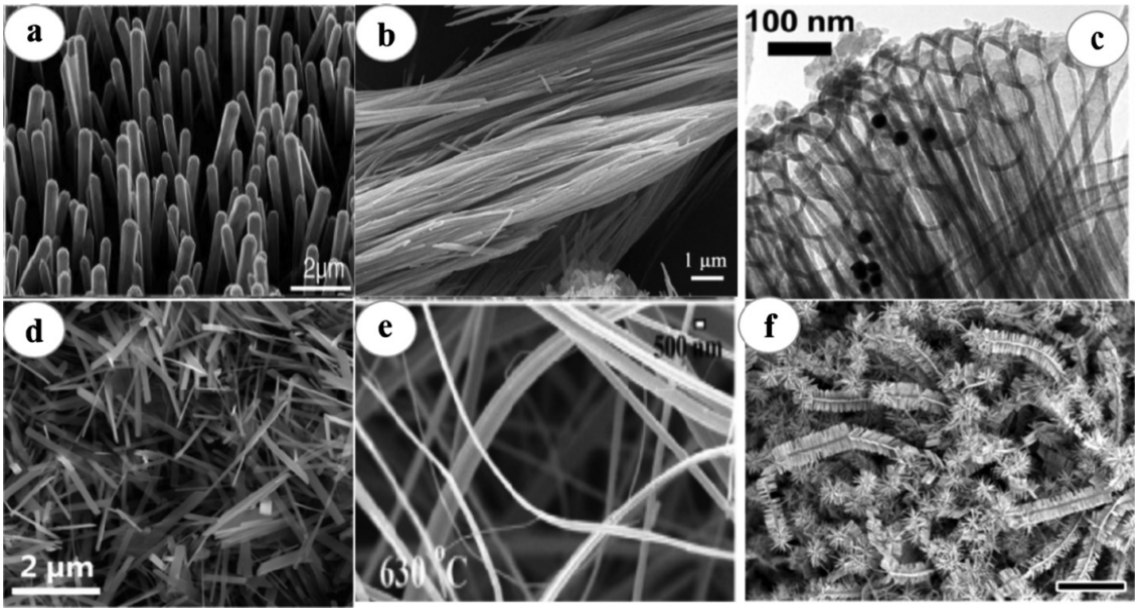

Figure 21 – Images of several typical 1D nanomaterials: (a) nanowires [67], (b) nanorods [68], (c) nanotubes [69], (d) nanobelts [70], (e) nanoribbons [71] and (f) hierarchical nanostructures [72].

2.2.3 Two-dimensional nanomaterials

Two-dimensional nanomaterials, whose only one dimension is strictly in the nanometer range, have become a focal point in the material field recently. These materials exhibit distinctive shape-dependent properties and high energy density, making them the building blocks for the key components of many nanodevices, including photocatalysts, nanoreactors, nanocontainers, sensors and templates for other 2D structured materials [73]. Some typical 2D nanomaterials like junctions (continuous islands), branched structures, nanoprisms, nanoplates, nanosheets, nanowalls and nanodisks, are displayed in Figure 22.

2.2.4 Three-dimensional nanomaterials

Three-dimensional nanomaterials possess large surface area and unique physicochemical features since sizes, shapes, dimensionality and morphologies play a crucial role in their performance. Resultantly, an increasing number of researchers have concentrated on synthesizing 3D nanomaterials with a well-controlled structure. These ordered nanomaterials have been employed for various applications, consisting of catalysis, batteries

and magnetic materials. Images of several typical 3D nanomaterials are presented in Figure 23.

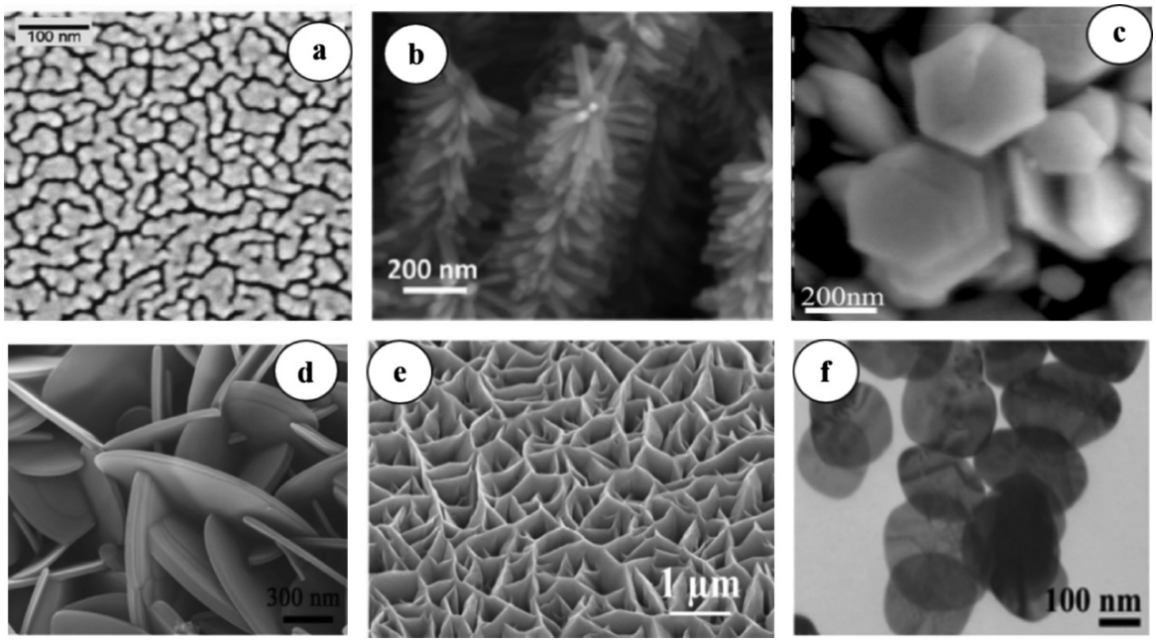

Figure 22 – Images of some typical 2D nanomaterials: (a) junctions (continuous islands) [74], (b) branched structures [75], (c) nanoplates [76], (d) nanosheets [77], (e) nanowalls [78] and (f) nanodisks [79].

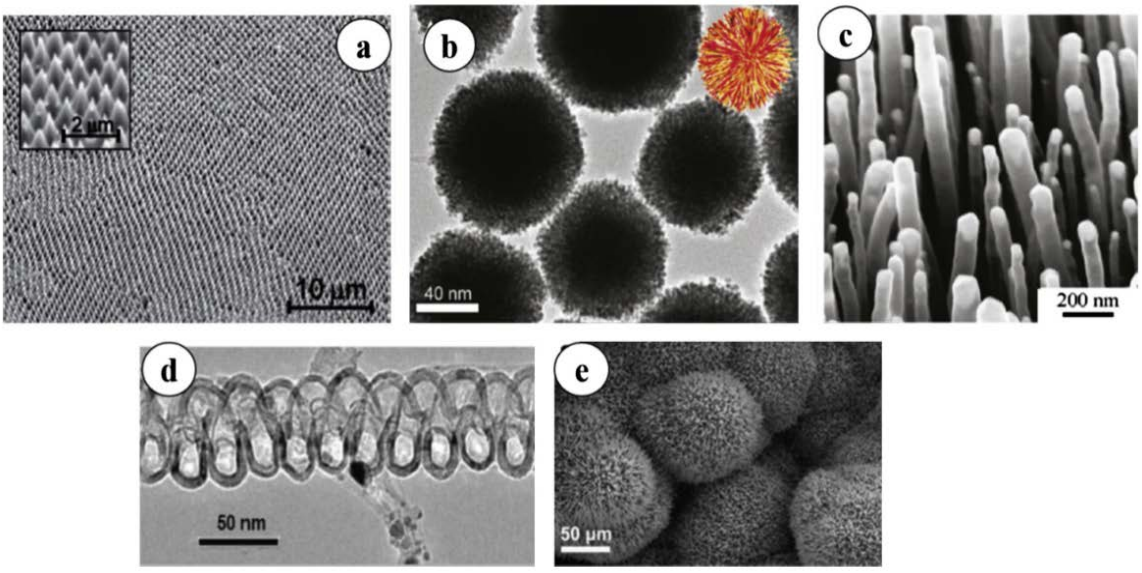

Figure 23 – Images of some typical 3D nanomaterials: (a) nanocones [80], (b) nanoballs [81], (c) nanopillers [82], (d) nanocoils [83], (e) nanoflowers [84].

2.3 Transition metal dichalcogenides

To date, 2D materials have received great interest since the discovery of graphene in 2004 [85]. Graphene shows potential prospects in both basic and applied research [86][87] due to its distinctive properties such as ultrahigh electron mobility [88], integral quantum Hall effect [89][90][91] to name a few. Its rapid development also sheds new light on the discovery of more 2D materials [89], [92]–[94].

2.3.1 Structure and properties

Transition metal dichalcogenides are a family of materials consisting of over 40 compounds with the generalized formula of MX_2, where M is a transition metal like Mo and W, and X is a chalcogen such as S, Se or Te (Figure 24). A single layer of TMDs contains three atomic layers where the transition metal is sandwiched by two chalcogens with strong intralayer covalence, while 3D crystals are formed by weak interlayer van der Waals interaction, as the structure of MoS_2 displayed in Figure 25.

The chalcogens in TMDs are not highly reactive because of their saturation, which allows for the fabrication of monolayer via exfoliation or vapor deposition approaches. The isolated individual layer exhibit dramatic property changes compared to their bulk counterparts since the charge carriers are strictly confined in two dimensions and the interactions in the out-of-plane direction is absent. One of the attractive features is the indirect-to-direct bandgap transition when some TMDs like MoS_2, WS_2, $MoSe_2$ and WSe_2 are thinned to monolayer [95].

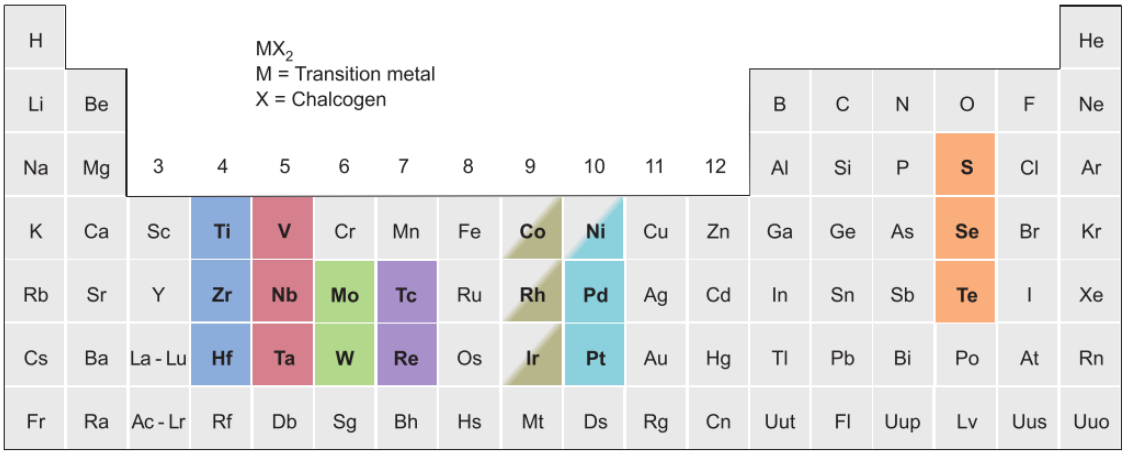

Figure 24 – Various possible layered structure of TMDs [96].

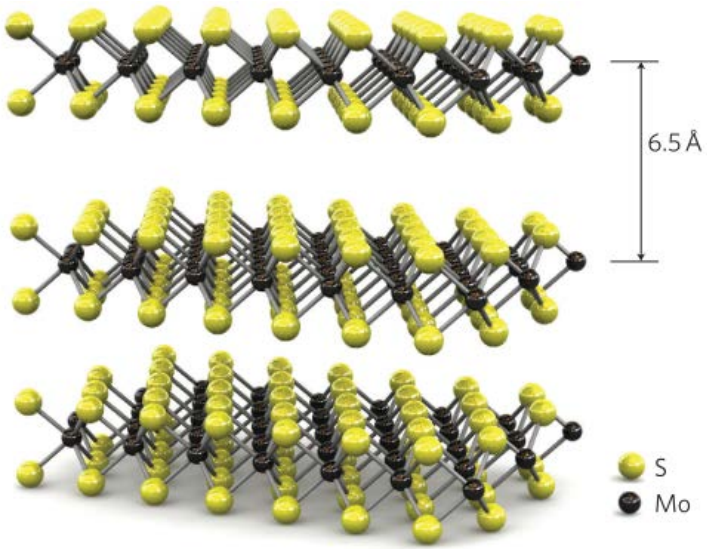

Figure 25 – The structure of MoS_2. The distance between adjacent layers is 6.5 Å [6].

Most TMDs have both metallic (1T, one layer per trigonal unit cell) and semiconductive (2H, 2 layers per hexagonal unit cell) phases [97]. The stable phase of TMDs is 2H phase at room temperature, while 1T phase can be achieved by Li-intercalation [98] or electron beam irradiation [99]. The chemically exfoliated 1T MoS_2 is known to be 10^7 times more conductive than the semiconductive 2H phase [100]. But in the case of WTe_2, 1T or 1T' (one layer per distorted trigonal unit cell) phase is more stable than 2H phase at room temperature [101]. Both 2H and 1T' phase in $MoTe_2$ can be easily modulated to each other in that the cohesive energy difference between both phases is similar. Besides, the dichalcogenides of titanium (Ti), chromium (Cr), nickel (Ni), zinc (Zn), vanadium (V), niobium (Nb), and tantalum (Ta) simply exhibit metallic behavior [102]. Additionally, some TMDs can exhibit high mobility with an appropriate substrate and metal contacts. For example, MoS_2 gives a mobility of 700 $cm^2 V^{-1} s^{-1}$ on SiO_2/Si substrate with scandium contact and 33~151 $cm^2 V^{-1} s^{-1}$ on BN/Si substrate at room temperature [103], [104].

Apart from excellent electrical transport properties, TMDs are mechanically flexible and strong. An exceptionally high Young's modulus of ~0.33 ± 0.07 TPa has been reported in suspended few-layer MoS_2 nanosheets [7]. Bertolazzi et al. reported high in-plane stiffness (~180 ± 60 N/m) and Young's modulus of single-layer MoS_2 (~270 ± 100 GPa) [105].

2.3.2 Preparation methods

So far, a diversity of approaches has been utilized for preparing 2D TMDs, and, generally, they can be categorized into top-down and bottom-up methods. Top-down methods refer to

approaches to obtain TMDs nanosheets from their bulk counterparts, whereas bottom-up methods are to obtain single- or multi-layers of TMDs nanosheets from atom or molecules.

2.3.2.1 Top-down methods

Mechanical exfoliation is one of the most common methods in this category. A typical process follows three steps: appropriate thin TMDs films are firstly peeled off from their bulk materials by adhesive Scotch tapes; freshly cleaved thin films on the Scotch tape are brought onto the target substrate and further cleaved by tools such as plastic tweezers; single- or few-layer TMDs are left on the substrate after the removal of Scotch tape. Until now, a variety of monolayer 2D TMDs crystals, including MoS_2, $MoSe_2$, WS_2 and WSe_2, have been successfully prepared by this method [106], [107], [116], [117], [108]–[115]. Optical and topographic images of mechanically exfoliated single- and few-layer MoS_2 nanosheets are depicted in Figure 26. Samples produced by this method are of high quality and can be employed for investigation about their basic properties with the help of various facilities like the transmission electron microscope, scanning tunneling microscopy, optical microscopy, Raman spectroscopy and so forth [118][119]. Nevertheless, it is a challenge to scale up the size of TMDs materials through this method, and its reproducibility is relatively low.

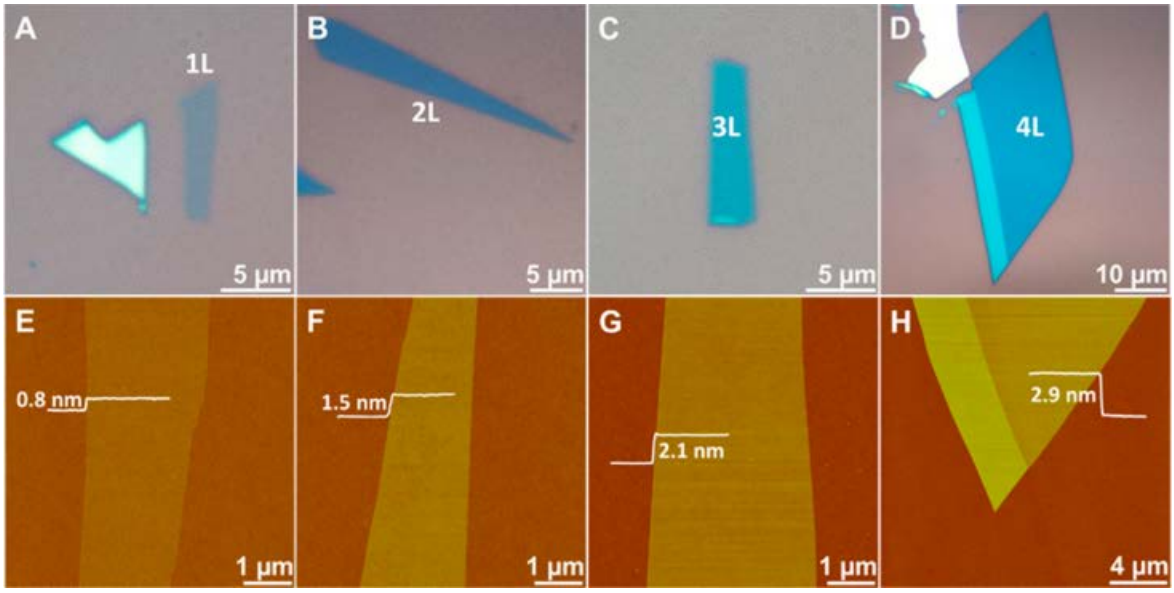

Figure 26 – Mechanically exfoliated MoS_2 nanosheets on 300 nm SiO_2/Si substrate. Optical (A-D) and topographic (E-H) images of single-layer (1L, thickness 0.8 nm; A and E), bi-layer (2L, thickness 1.5 nm; B and F), tri-layer (3L, thickness 2.1 nm; C and G), and quadruple-layer (4L, thickness 2.9 nm; D and H) MoS_2 nanosheets [12].

Thermal ablation is another method to prepare monolayer TMDs. In [120], the laser from Raman microscope was utilized to thin the multi-layered MoS_2 deposited on SiO_2/Si by

scanning over the film with high power (Figure 27a and b), in a similar way to the procedure used to locally oxidize graphene and reduce graphene oxide [121][122][123]. It can be obviously seen that the MoS_2 nanosheet of 0.9 ± 0.3 nm thickness remains on the surface (Figure 27c), which is consistent with the expected thickness of monolayer [124][12]. However, the laser-thinning procedure relies on the heat-induced sublimation of upper layers, which cannot be easily dissipated overs the sample due to the poor van der Waals force between layers. So the accurate control of laser power poses a threat to the practical application of this method.

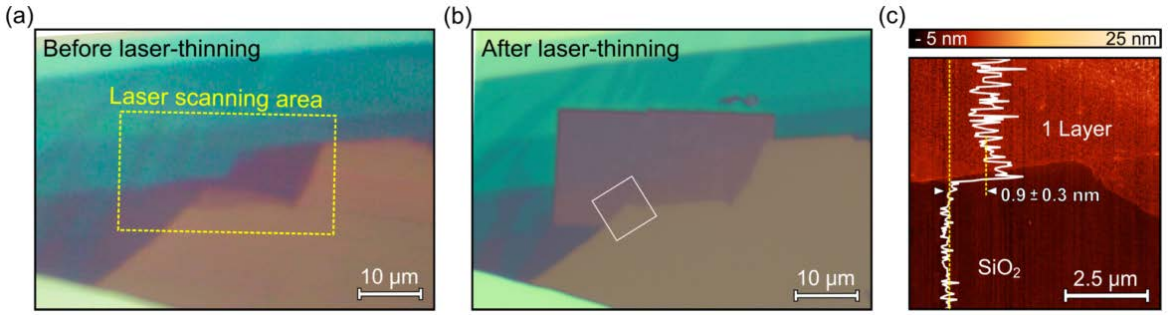

Figure 27 – Monolayer MoS_2 prepared by thermal ablation. Optical images of a multi-layered MoS_2 flake deposited on the 285 nm SiO_2/Si substrate before (a) and after (b) laser-thinning process. The laser-scanned area is marked by a yellow dashed rectangle in (a). (c) Surface topography of the region marked by the square in (b) [120].

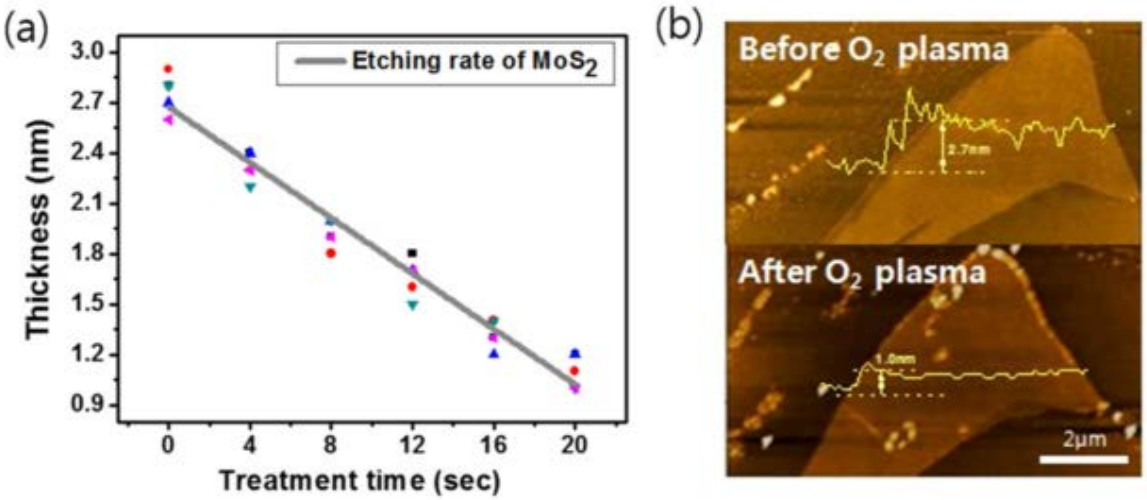

Figure 28 – O_2 plasma treatment to control the thickness of mechanically exfoliated MoS_2. (a) The thickness of MoS_2 as a function of plasma treatment time. (b) Surface topographic images before and after plasma etching [125].

Suhhyun Kim et al explored O_2 plasma treatment to control the thickness of mechanically exfoliated MoS_2. The MoS_2 sample was atomically-etched in 4 s intervals during the total 20 s treating time, and there is a linear decrease in the thickness measured by AFM in Figure 28. Possibly, this method is able to etch a small portion of MoS_2, such as S and Mo atoms or Mo-S bonds, since the thickness of each 4 s etching is 0.3 ~ 0.4 nm whereas the monolayer MoS_2 is ~0.7 nm. Nevertheless, MoO_3 can be easily formed in the meantime due to the high-reactivity of O_2 plasma, and it is difficult to remove the undesirable MoO_3 considering its high melting point (795 ℃) [126] and distorted lattice structure [125], [127].

Lithium intercalation is another top-down method, and its history can be traced back to 1970s [128]. Hitherto, various single-layered TMDs with high yield have been produced by this approach [129][130]. Although the semiconductor properties are lost by the change of metallic phase, they can be recovered by heating at 300 ℃. Considering the time-consuming reaction, an electrochemical cell is optimized to make it more efficient (Figure 29) [112]. On the other hand, its feasibility is still limited by the requirement of an inert atmosphere and the hazard by the use of flammable lithium.

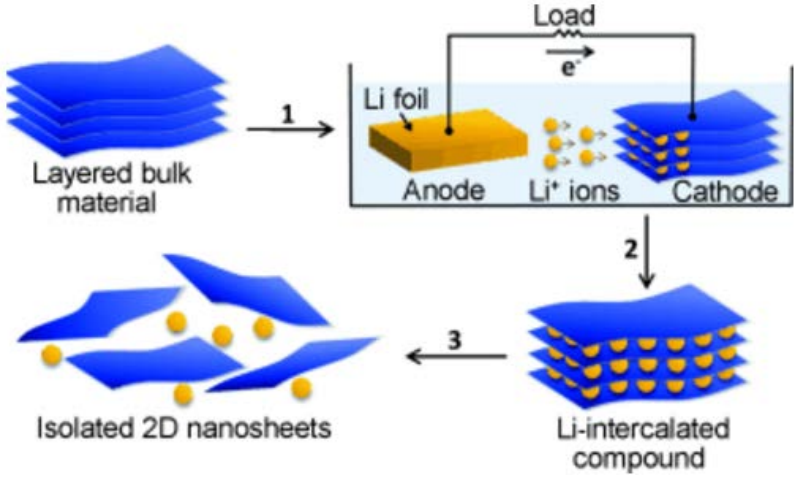

Figure 29 – Lithium intercalation to fabricate 2D nanosheets from the layered bulk material [112].

In order to prepare large quantities of single- or few-layer TMDs nanosheets, liquid exfoliation by direct sonication in various solvents has been observed (Figure 30), including in aqueous surfactant solutions, organic solvents, mixed solvent of ethanol and water, a mixture of polymer and solvent and so on [111], [113], [116]. Nevertheless, the yield of this method is relatively low [131].

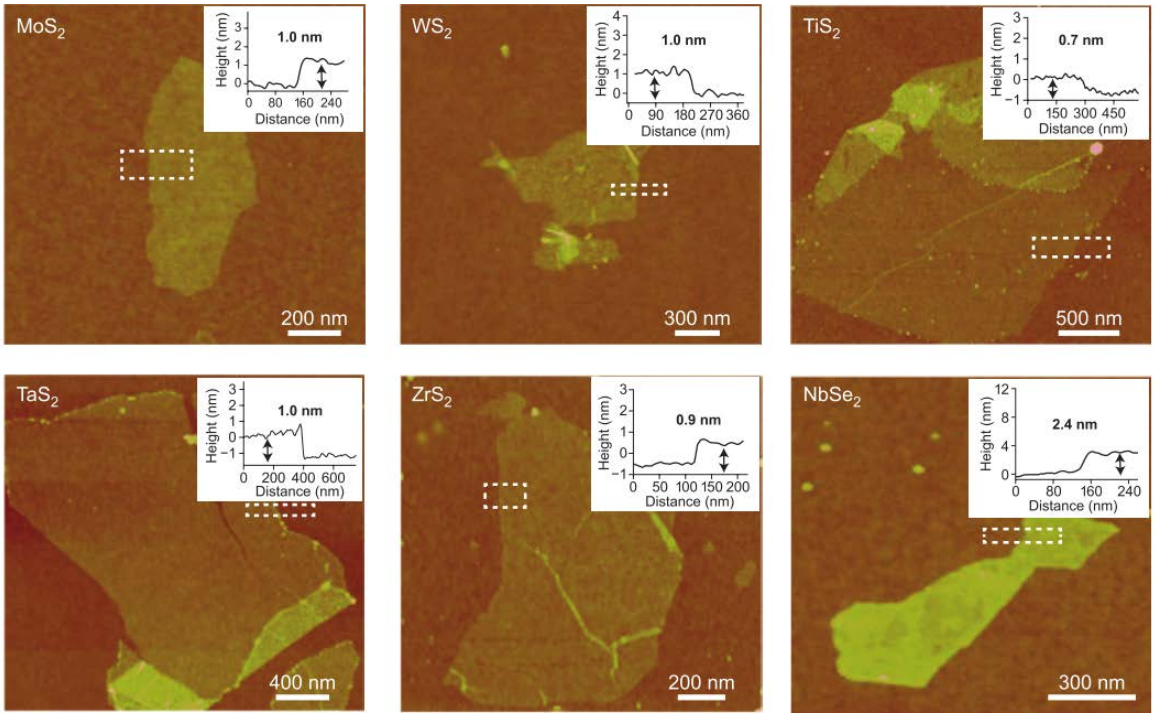

Figure 30 – Surface topographies of different TMDs on SiO_2 substrate prepared by liquid exfoliation method [96].

2.3.2.2 Bottom-up methods

In opposition to the abovementioned top-down methods, there are various bottom-up methods to obtain single- or multi-layers of TMDs nanosheets from atom or molecules, such as hydrothermal synthesis [132], atomic layer deposition [133], pulsed laser deposition [134], [135], physical vapor deposition [136] and chemical vapor deposition [137]–[141].

Yiya Peng et al have prepared single-layer MoS_2 and $MoSe_2$ by hydrothermal synthesis method [132]. In a typical process, ammonium molybdate ($(NH_4)_6Mo_7O_{24}\cdot 4H_2O$), sulfur (or selenium) as well as hydrazine monohydrate were loaded into a 25 mL Teflon-line stainless steel autoclave, which was then filled with distilled water to 80% of its capacity. The autoclaves were held at 150-180 ℃ for 48 hours and then cooled naturally. The dark-grey powders left were filtered and washed with distilled water, diluted hydrochloric acid and ethanol successively, and the final products were dried in vacuum at 40 ℃ for 3 hours. It is evident that this method is time-consuming though monolayer TMDs can be successfully produced.

WS_2 nanosheets have been synthesized on SiO_2/Si substrate by the sulfurization of the atomic layer deposited WO_3 film as shown in Figure 31 [133]. For the atomic layer deposition (ALD) of WO_3, a newly synthesized precursor $WH_2(iPrCp)_2$ was vaporized by

maintaining the bubbler temperature at 95 ℃, and it was delivered to the atomic layer deposition chamber by pure Ar (99.999%). Subsequently, O_2 plasma was introduced for the reaction and it was followed by the purging of Ar gas. As to the sulfurization procedure, the prepared WO_3 was loaded to a tube furnace and heated to 470 ℃ for 1 hour with 25 sccm Ar mixed with 25 sccm H_2 to remove organic contaminants in the first place. Afterward, the temperature was targeted to 1000 ℃ gradually over 90 minutes and held for half an hour with 50 sccm Ar flow mixed with 5 sccm H_2S. Finally, the sample was cooled to room temperature with 50 sccm Ar flow. WS_2 nanoflakes grown by this method can preserve the advantages of atomic layer deposition, such as controllable thickness, reproducibility, uniformity and high-conformity [142], [143]. However, it is inconvenient to operate two separate procedures and hazardous gas like H_2S is used in the sulfurization process.

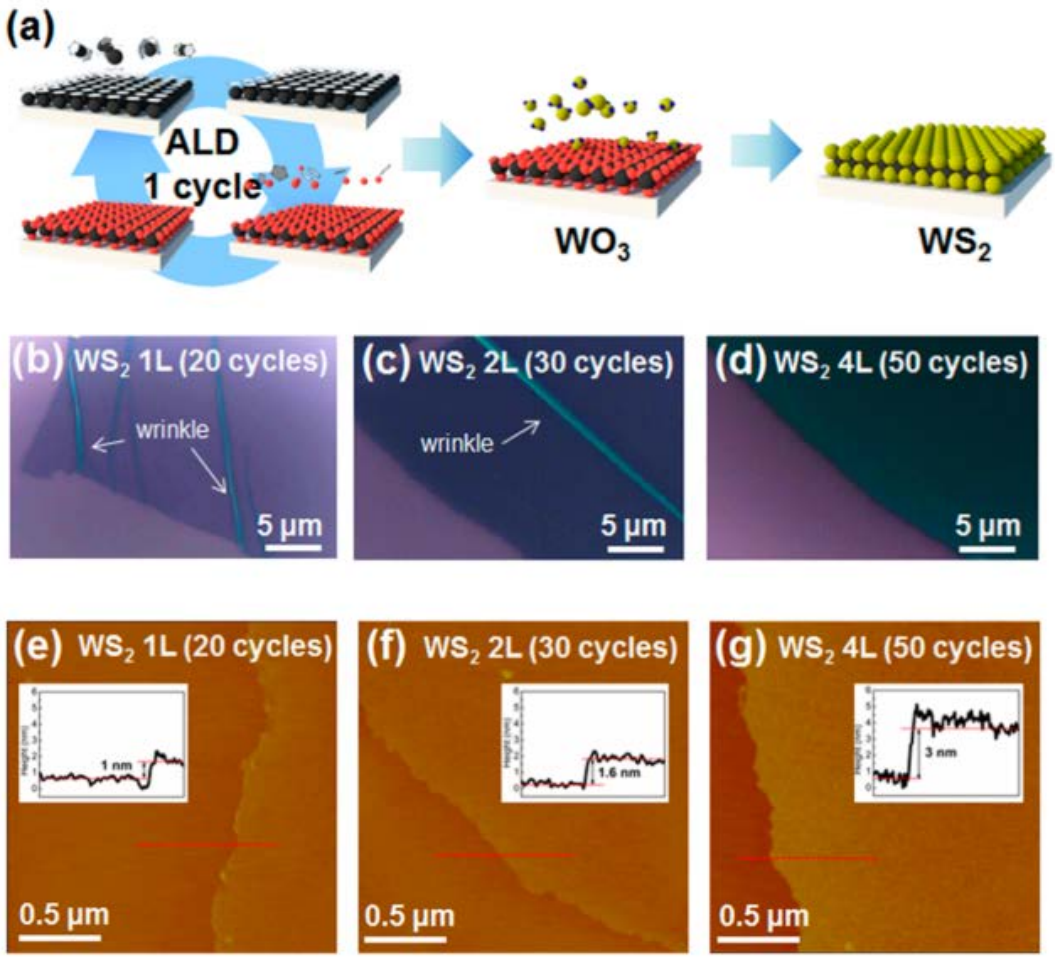

Figure 31 – (a) Synthesis procedure for the ALD-based WS_2 nanosheets. Optical images of the transferred WS_2 nanosheet on the SiO_2 substrate for the (b) mono-, (c) bi- and (d) tetra-layered thicknesses. AFM images and height profiles (inset) of the transferred WS_2 nanosheet on the SiO_2 substrate for the (e) mono-, (f) bi- and (g) tetra-layered thicknesses [133].

Additionally, the pulsed laser deposition method has been utilized for the preparation of MoS_2 thin film. In [134], MoS_2 was synthesized from commercial MoS_2 powder (99.95%, Aldrich Sigma Chemicals) with polyvinyl alcohol as a binder, applying a pressure of 75 kN/cm^2 followed by sintering under Ar atmosphere at 800 ℃ for 12 hours. Similar method has been reported in [135] and the whole process can take more than 8 hours. Apparently, it is a time-consuming bottom-up method to synthesize TMDs by pulsed laser deposition.

Another common synthesis method is physical vapor deposition, during which the material changes from a condensed phase to the gaseous phase and then back to the condensed phase again, so coatings or thin films can be produced. For example, C. Muratore et al selected magnetron sputtering to synthesize MoS_2 since the low temperature enables the scalable growth of very thin TMDs films over a large area (>1 m^2) on various substrates [136]. On the other hand, it is a challenge to control the layer number with guaranteed uniformity.

Recently, the chemical vapor deposition method has been widely used to grow large-area TMDs films. In a typical process, precursors are heated to evaporate and the products are deposited on substrates. The purity, uniformity, conformity as well as reproducibility of thin films can be guaranteed by this approach. Until now, direct sulfurization or selenization of different metal oxides or chlorides has been extensively reported to prepare MoS_2 [144]–[149], WS_2 [150]–[154], $MoSe_2$ [155]–[158] and WSe_2 [159]–[163] by many research groups.

Ismail Bilgin's group fabricated mono- and multi-layered MoS_2 samples by direct sulfurization of MoO_2 instead of commonly used MoO_3 or Mo [149]. As evident from Figure 32, the lateral size of monolayer MoS_2 fabricated on amorphous, crystalline, transparent and conductive substrates ranges from 10 to 50 μm. Importantly, there is no treatment of either the substrates [144] or precursors [164], [165] before reaction, making it convenient for applications such as catalytic and nanodevices. Furthermore, these MoS_2 samples are free from contamination induced by the transfer process, so they are potentially more suitable for varieties of cutting edge metrology tools, including transmission electron microscopy, scanning tunneling microscopy and different optical spectroscopies, to name a few. In addition, the growth of bi-, tri- or even multi- layers can be triggered by changing the synthesis conditions.

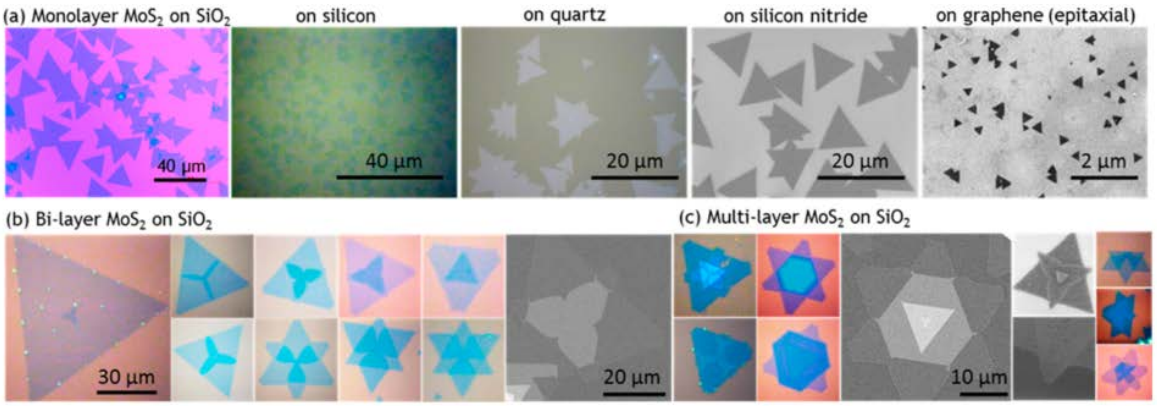

Figure 32 – A series of MoS_2 samples deposited on various substrates. (a) Single-layered MoS_2 fabricated by MoO_2 precursor on a range of substrates. Colored images are measured by optical microscopy, while black and white ones are SEM images. (b) Typical optical and SEM images of bilayer MoS_2 grown on SiO_2, showing diverse states of initiation and growth of the second layer. The last image in (b) is an SEM image indicating intricate details of the bilayer structure. (c) Optical and SEM images of multi-layered samples at different stages of growth [149].

The schematic of the CVD setup of WS_2 preparation is shown in Figure 33a. SiO_2/Si substrate was placed face-down on the WO_3 crucible at the center of the furnace during the growth, and S powder was loaded in a separate crucible in the upstream region of the quartz tube. The temperature was controlled to rise up to 950 ℃ at 50 ℃/min ramping rate and then held for 3 min. After that, the furnace was turned off and cooled in air. As evident from the optical image in Figure 33b, the lateral size of the triangle-shaped flakes is more than 150 μm; the AFM step height on the edge of the flake is ~0.8 nm (Figure 33c), verifying the single-layer nature of the as-grown WS_2 sample.

Rudresh Ghosh's group successfully prepared large-area single-layer $MoSe_2$ by CVD method. The experimental setup and temperature profile are shown in Figure 34a and b, respectively. It is remarkable from Figure 34c that the produced sample is of high optical uniformity, and the AFM line profile shown in the inset of Figure 34d presents a step height of ~0.8 nm, corresponding to monolayer $MoSe_2$. Besides, the overall root mean squared (RMS) roughness of ~0.140 nm for produced $MoSe_2$ nanosheet is provided by the AFM scanning result, which is comparable to the roughness of SiO_2 (0.199 nm RMS), indicating the uniformity of $MoSe_2$ film at nanoscale.

The schematic of the experimental setup to fabricate WSe_2 by selenization of WO_3 powder in a CVD chamber is illustrated in Figure 35a. The morphologies of the films grown on

sapphire substrates vary with the substrate temperature. As can be seen from the optical images in Figure 35b, WSe_2 deposited at 850 ℃ shows a triangular shape, and the lateral size is between 10 and 50 μm. Besides, the sparsely distributed triangles exhibit the low nucleation density of WSe_2. According to Figure 35c, many small WSe_2 domains merge to a continuous film when grown at 750 ℃, since a lower growth temperature can lead to a higher nucleation density. Meanwhile, it is noted from Figure 35d that the thickness of film grown at 850 ℃ is ~0.73 nm, which is in accordance with the reported thickness for monolayer WSe_2 by mechanical exfoliation method [166][167]. Importantly, it should be pointed that hydrogen gas is added as a reducing agent together with Se to further reduce the metal oxides and help with the selenization reaction since the thermodynamic condition cannot be met without hydrogen gas. The shape of monolayer WS_2 can be also tailored from jagged to straight edge triangles by using hydrogen gas as a minor carrier [9].

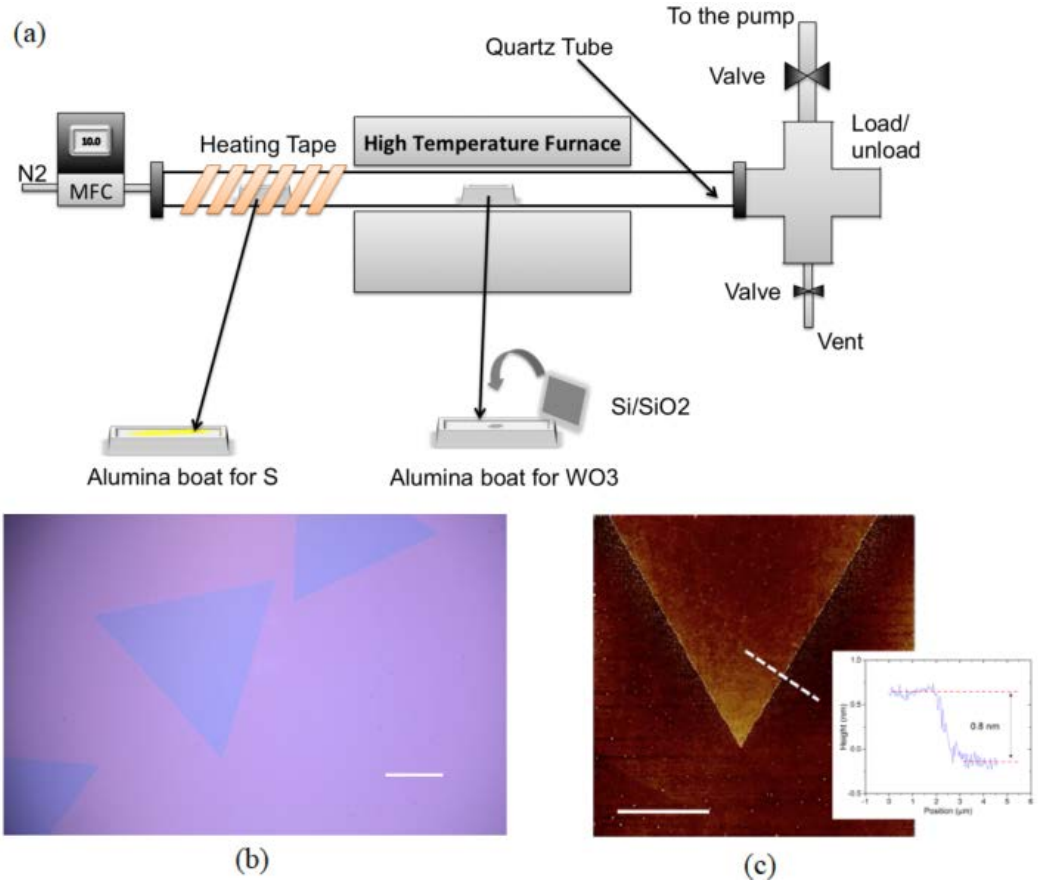

Figure 33 – Single-layer WS_2 synthesized by CVD method. (a) Schematic illustration of CVD setup for the growth of WS_2. (b) Optical image of single-layer WS_2. (The scale bar is 50 μm). (c) AFM step height measurement to show the thickness of flakes (The scale bar is 10 μm) [150].

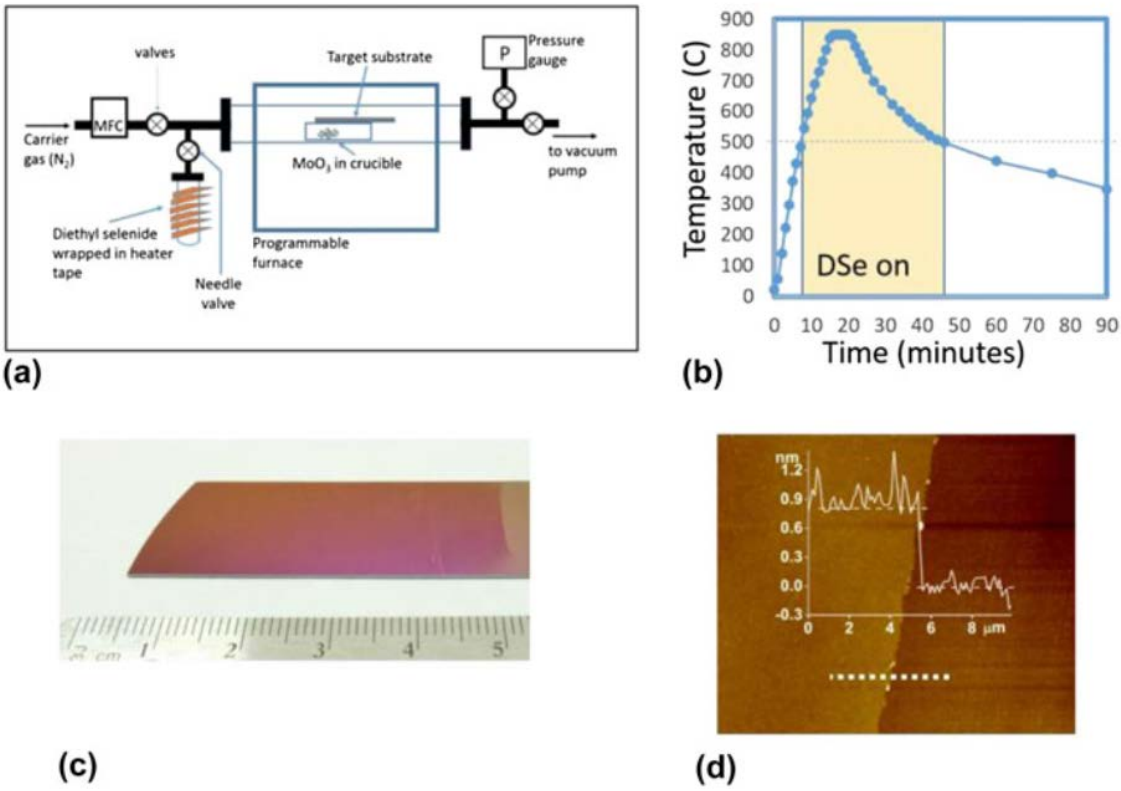

Figure 34 – CVD-Growth of large-area single-layer $MoSe_2$. (a) Schematic of CVD growth system to fabricate $MoSe_2$. (b) Temperature profile. (c) Photo of large area $MoSe_2$. (d) Surface topography by AFM. (Inset: height profile along the dashed horizontal line in the map) [157].

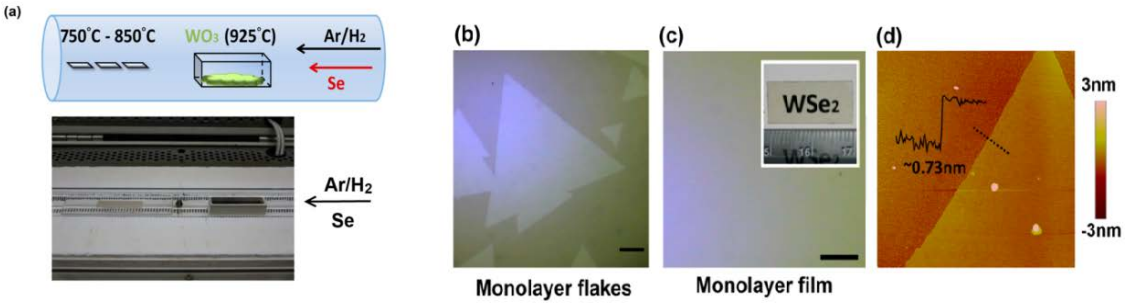

Figure 35 – CVD-fabricated WSe_2 on sapphire substrates. (a) The scheme for the growth of WSe_2 on sapphire substrates by the reaction of WO_3 and Se powders in a CVD furnace. (b) and (c) are optical images of the monolayer WSe_2 flakes and film grown at 850 and 750 °C, respectively. Scale bar is 10 μm. The inset in (c) is a uniform monolayer film grown on a sapphire substrate with both sides polished. (d) Surface topography of the monolayer grown at 850 °C [160].

However, the growth rate of WS_2 and WSe_2 by sulfurization and selenization of metals or metal compounds is still limited due to the high melting points of their metal or metal oxide

precursors. In this situation, molten-salt-assisted methods have been developed to facilitate their synthesis, as shown in Figure 36. Jiangdong Zhou et al elaborated its working principles and demonstrated that the melting point of reactants could be decreased by salt, since intermediate products, such as metal oxychlorides with an appropriate temperature to vaporize, could be formed through the reaction with salt [168].

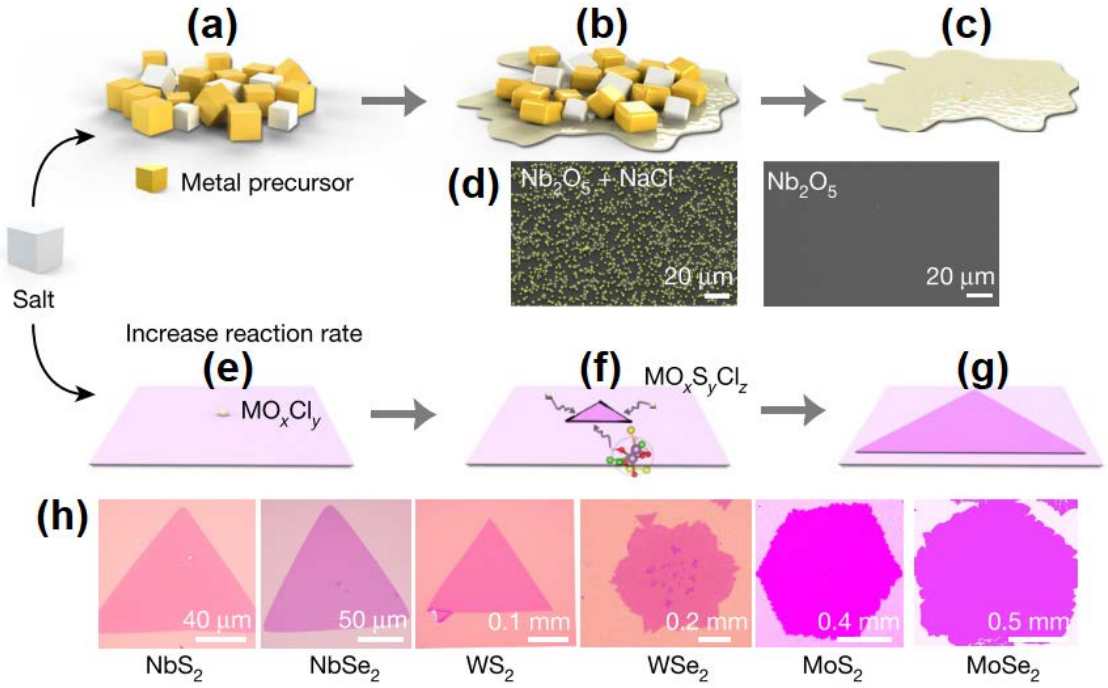

Figure 36 – Mechanism of molten-assisted-salt CVD reaction. Metal oxychlorides are formed to promote the reactions. (a-c) The addition of salt reduces the melting points of precursors. (d) SEM images of the Nb nucleus with (left) and without (right) salt addition. (e-g) The growth of 2D atomic layer with intermediate products. (h) Different single-crystalline monolayers [168].

2.3.3 Transfer methods

For further characterization and device fabrication, it is a critical issue to transfer TMDs films from growth substrates onto target ones with intact morphological and physicochemical properties. Currently, wet-etching transfer method is the most widely adopted for TMDs. Typically, polymethyl methacrylate (PMMA) is coated on the TMDs nanoflakes as a support film, and the composite stack is separated from the substrate via chemical etching [146], [165], [169], [170], where hydrogen fluoride or strong alkali is normally used, which can lead to sample degradation and substrate destruction.

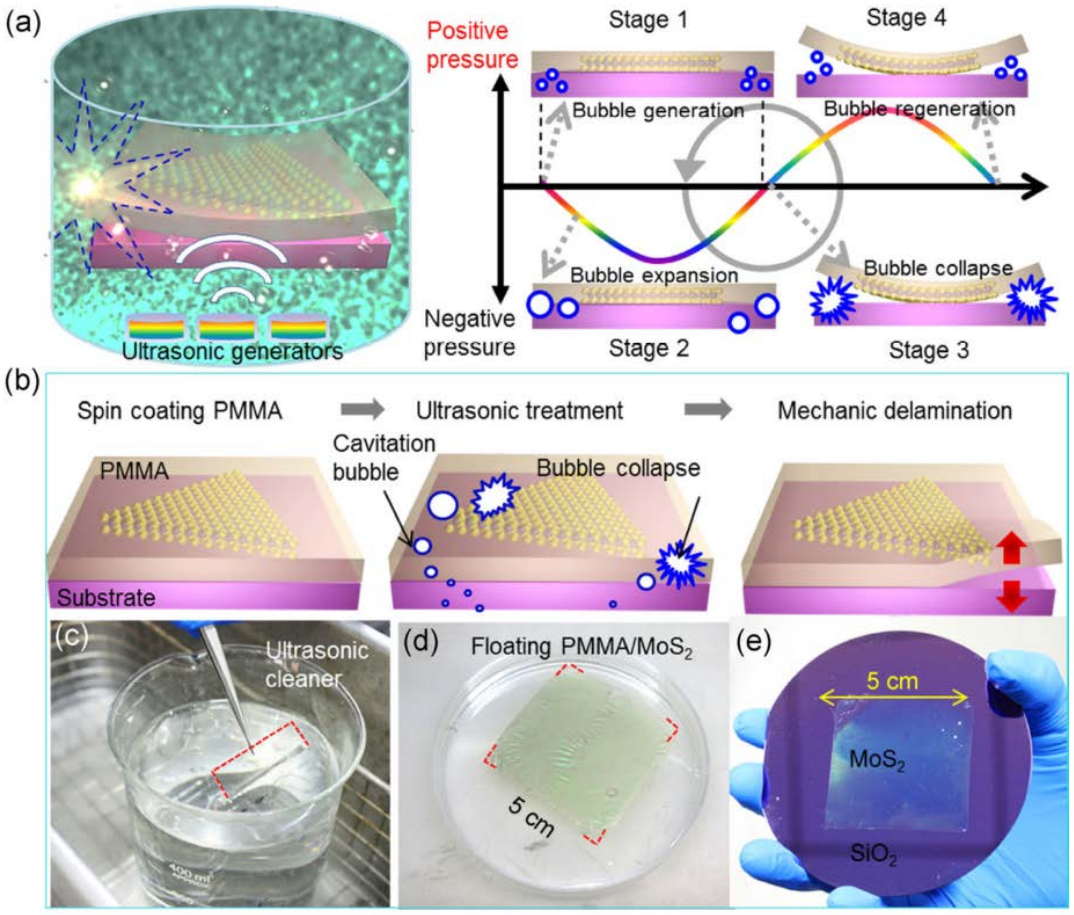

Figure 37 – Illustration of ultrasonic bubbling transfer of MoS_2. (a) Schematic illustration of the ultrasonic process used to detach PMMA/MoS_2 stack from the growth substrate. (b) Principles for the ultrasonic bubbling transfer of MoS_2 on insulating substrates. (c) PMMA/MoS_2/mica stack immersed in a beaker of water kept in an ultrasonic cleaner. (d) 5×5 cm^2 PMMA/MoS_2 stack floating on water. (e) Transfer of large-area MoS_2 onto SiO_2/Si substrate [171].

Donglin Ma's group proposed an ultrasonic bubbling transfer method with high efficiency, environmental friendliness and recyclable use of the substrate. This process is realized by an ultrasonic process to generate micron-sized cavitation bubbles, whose collapse can produce sufficient force at the interface between the PMMA-coated TMDs and the substrate to drive delamination. A typical bubbling cycle is demonstrated in Figure 37a, with the middle sine curve showing the pressure change as a function of ultrasonication time. During the negative-pressure period of the ultrasonic wave at the initial stage (stage 1), a massive number of cavitation bubbles are formed, and these bubbles expand rapidly (stage 2) until the pressure suddenly switches from negative to positive at stage 3, when these bubbles are compressed and collapse with the rise of positive-pressure in a short time, providing considerable force at the interface between the PMMA/MoS_2 stack and the substrate. Over

many bubbling cycles (stage 4), the bubble-induced force repeatedly separates the stack from the growth substrate. Thanks to the water penetration arising from the hydrophilic nature of growth substrates like mica, sapphire, SiO_2/Si, the adhesion at the interface is weak, thereby facilitating the ease of delamination. In the meantime, the PMMA/MoS_2 stack is quite stable under the ultrasonication process, which is possibly attributed to a relatively strong interface adhesion from the dense contact and similar hydrophobic nature of PMMA and MoS_2 as proposed in [172].

As evident from the key steps illustrated in Figure 37b, the MoS_2 on growth substrate is firstly spin-coated with PMMA at a relatively low speed to yield a thin film, which is then annealed to completely remove the residual solvent. The PMMA/MoS_2/substrate stack is subsequently immersed in a beaker of water kept in an ultrasonic cleaner (Figure 37c). Within a few seconds, the edge of the PMMA/MoS_2 film can be detached from the substrate, eventually causing the PMMA/MoS_2 floating on the water surface (Figure 37d). The detached PMMA/MoS_2 film can then be transferred onto the target substrates (like SiO_2/Si in Figure 37e), and the PMMA layer can be removed using acetone. It is worth noting that the entire process only involves water and no chemical etchants or hazardous pollutants, such as hydrogen fluoride or potassium hydroxide, so it is relatively safer and more environmentally friendly than the wet-etching method.

2.3.4 Applications

So far, more than 40 types of TMDs have been under investigation [173]–[175]. Many 2D TMDs, thanks to their semiconductive nature, possess great potential for low-power and miniaturized transistors which may be more efficient than the currently utilized Si-based ones [6]. Aside from the similar high carrier mobility, on/off ratio, TMDs can be deposited onto flexible substrates and survive the strain and stress which is a still a challenge for Si. For example, back-gated FETs have been fabricated on ultra-thin $MoSe_2$ films recently, and its ON/OFF ratio reaches the magnitude of 10^6 and the intrinsic mobility is up to ~50 $cm^2V^{-1}S^{-1}$ at ambient temperature [156].

The van der Waals interaction between adjacent layers and large surface area originating from the film structure make 2D TMDs promising for sensing and energy storage (such as batteries and super-capacitors) applications [176], [177]. The large surface-to-volume ratio grants 2D TMDs-based sensors with excellent selectivity, sensitivity, and low-power consumption, and there is no physical gate for these TMDs-based sensors to react selectively to the targeted molecules [178].

Due to the weakly bonded atomic layers, 2D TMDs can be delaminated and stacked with other TMDs so diversity of van der Waals heterostructures can be constructed without the limitation of lattice matching [94]. For instance, vertically stacked dissimilar 2D TMDs heterostructure can acquire distinctive properties that cannot be achieved separately. Based on the brand new functions like band alignment, tunneling transport and strong interlayer coupling, a class of novel devices including photodetectors, LEDs, tunneling transistors and flexible electronics can be manufactured [179].

The unique indirect-to-direct bandgap transition when TMDs monolayers are scaled down from its bulk counterpart makes TMDs a desirable candidate for diverse optoelectronics such as photo-detectors, LEDs, photo-transistors and solar cells [180].

Figure 38 displays various electronic, optoelectronic and energy storage devices fabricated by 2D TMDs [12], [181]–[185].

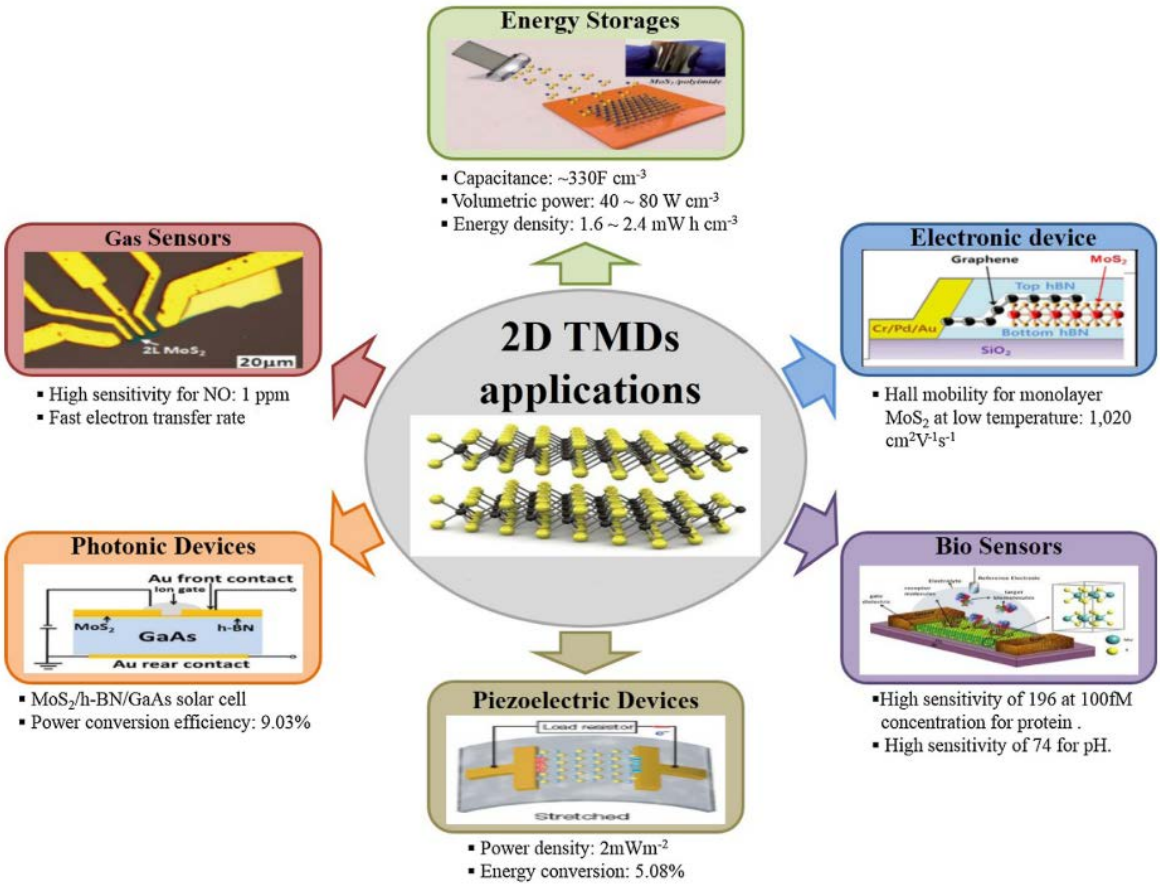

Figure 38 – Electronic, optoelectronic and energy devices based on 2D TMDs [12], [181]–[185].

Apart from the scale-down and gate bias methods, the strain can also be employed to adjust the electronic structures thereby the bandgap of 2D TMDs. For example, it is expected that

a relatively small tensile strain can induce a direct-to-indirect gap transition or even a semiconductor-to-metal transition in the case of single-layer MoS_2, whose indirect gap is only slightly higher than its direct one in energy [186]. Until now, a massive number of simulations have been reported and the results show a redshift of the gap energy with tensile strain and a decrease of effective carrier masses with tensile strain, which may enhance the carrier mobility and the transport characteristics [187]. The strain-induced bandgap modification has also been studied experimentally and their results are consistent with the calculated ones [188]. On this basis, 2D TMDs have been applied for single-photon emitters, which can generate one photon ideally indistinguishable from another at a high rate and thereby suitable for a range of quantum-based techniques like communications, computing, metrology and sensing [189], since 2D TMDs can be coupled to photonic waveguides, cavities and plasmonic structures, and their single-photon emitters can be electrically driven. The single-photon emitter behavior recently identified in 2D TMDs is from random sites, which results from defects whose existence and position are difficult to manipulate with the nanoscale precision and reliability. However, these sites are normally correlated with high-strain regions. Matthew R. Rosenberger et al used AFM to localize nanometer-scale single-photon emitters in single-layer WSe_2 deposited on a deformable polymer, which can impart strain to WSe_2, as shown in Figure 39 [190].

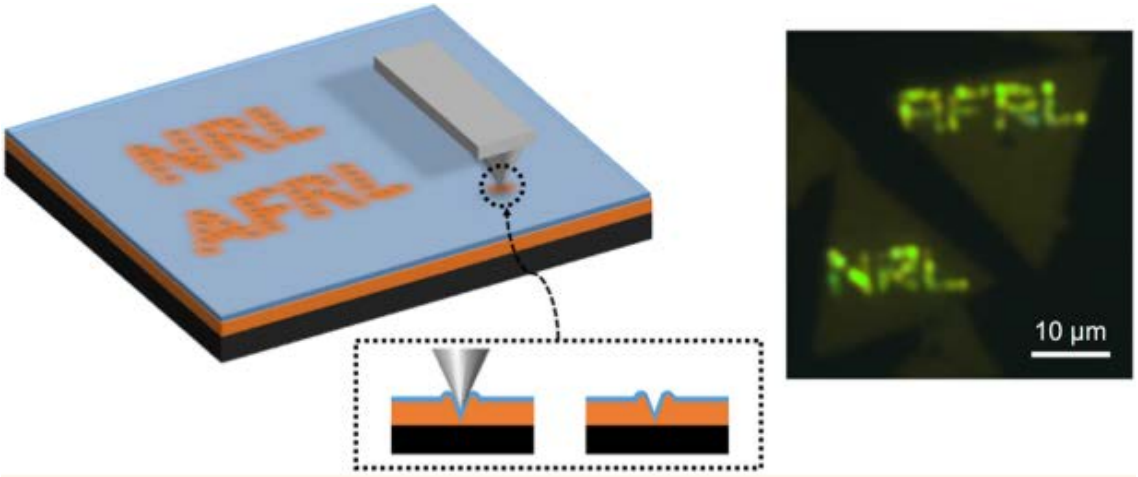

Figure 39 – Creation of single-photon emitters with AFM tip in 2D WSe_2 [190].

Like graphene, 2D TMDs are electrically tunable materials whose sheet resistance can be modified by incident light or applying a gate bias [149]. Until now, MoS_2-based X-band patch antenna has been proposed (Figure 40a), which exhibits a 560 MHz frequency shift from 9.56 GHz to 10.12 GHz and a gain difference of more than 18 dB when the bias of MoS_2 changes from -2 V to +5 V [191]. Besides, microwave switches have also been

designed (Figure 40b), and its ON/OFF states can be controlled by the bias applied onto MoS_2 thin film [192].

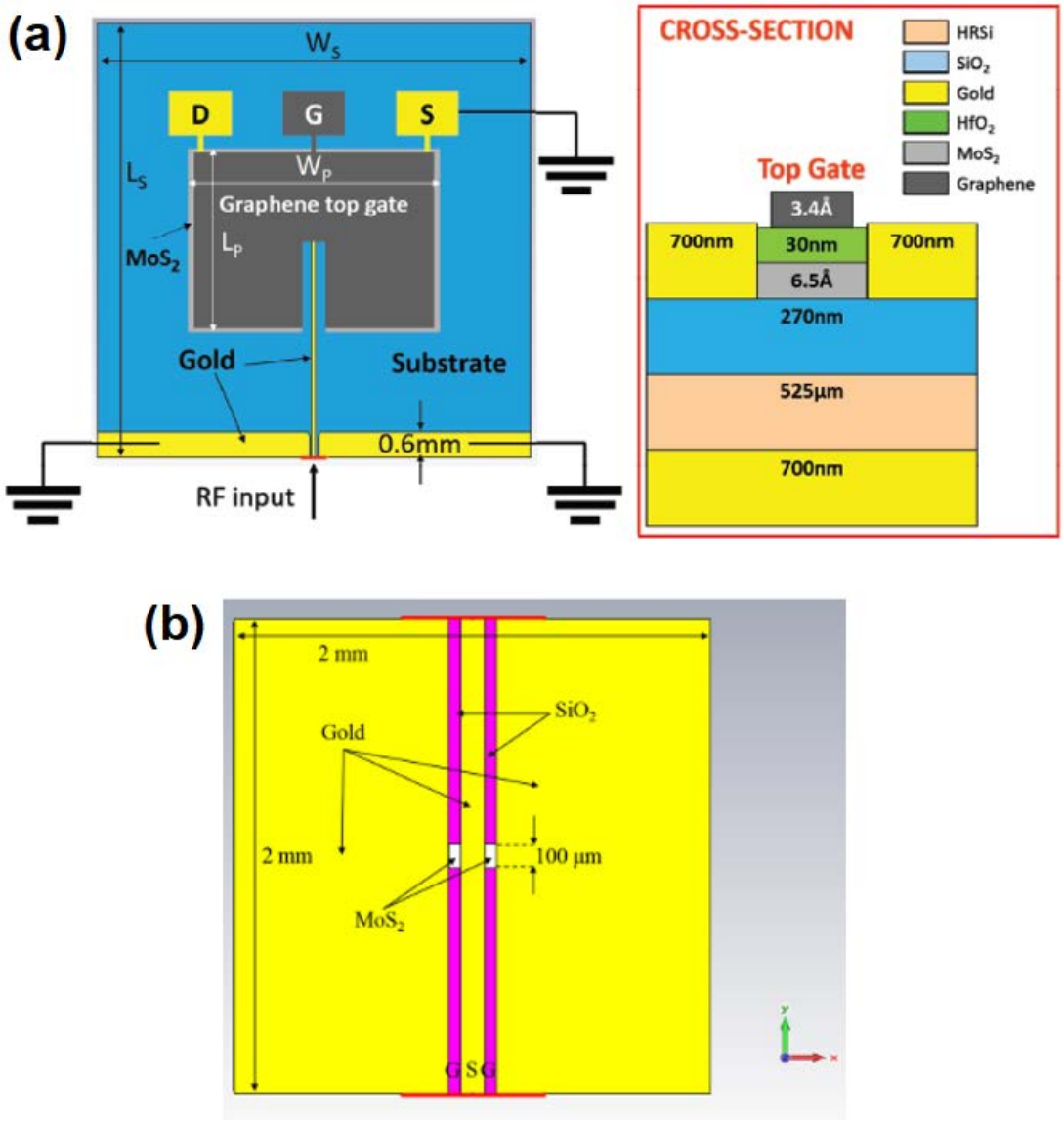

Figure 40 – (a) MoS_2-based X-band patch antenna: (left) top view with electrode configuration for DC bias. The letters D-G-S refer to drain-gate-source, respectively; (right) cross-section [191]. (b) Microwave switch based on MoS_2 thin-film [192].

Additionally, monolayer MoS_2 has been introduced into the friction layer of a triboelectric nanogenerator as the triboelectric electron-acceptor layer to enhance its output performance [2]. A schematic view of a vertical contact-separation mode triboelectric nanogenerator based on the MoS_2:polyimide (abbreviated as PI) layer is illustrated in Figure 41a. The bottom part of the device is made of a glass substrate onto which an Al electrode and a negative friction layer with a PI (Kapton)/MoS_2:PI/PI stacked structure are deposited. The top part is made of a PET substrate onto which an Al electrode is deposited. The top PI layer

in the friction layer acts as the negative friction material and can attract electrons from the top Al electrode during the triboelectric process. The monolayer MoS_2 embedded into the PI layer act as the triboelectric electron acceptors. Parallelly, a triboelectric nanogenerator without monolayer MoS_2 was fabricated with a friction layer structure of PI (Kapton) film/PI film to investigate the effect monolayer MoS_2. As evident in Figure 41b and c, the open-circuit voltage of the triboelectric nanogenerator without MoS_2 is ~30 V, while the value for the one with monolayer MoS_2 is as high as 400 V. Furthermore, the short-circuit (SC) current density of the triboelectric nanogenerator with monolayer MoS_2 is obviously higher than that of the one without MoS_2 (Figure 41d). As the electricity generated by triboelectric nanogenerator needs to be stored in an energy-storage device before powering electronic devices, the total amount of charge is the key to the efficient. The total amount of charge generated by a press-release cycle for the triboelectric nanogenerator with monolayer MoS_2 reached approximately 0.2 μC, which was much larger than that (0.05 μC) produced by using a triboelectric nanogenerator without MoS_2, as shown in Figure 41d.

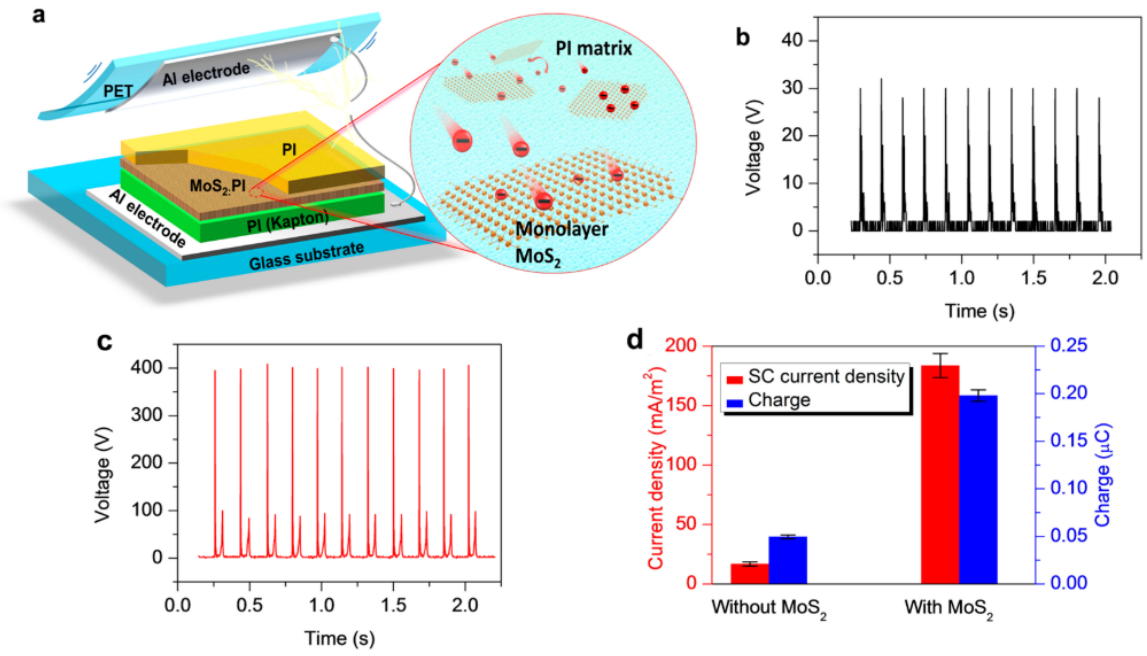

Figure 41 – (a) Illustration of the vertical contact-separation mode triboelectric nanogenerator with a MoS_2 monolayer. Rectified open-circuit voltage of the triboelectric nanogenerator (b) without and (c) with monolayer MoS_2. (d) Short-circuit current density and the amount of charge generated during a press-release cycle with and without monolayer MoS_2 [2].

2.4 Summary

Triboelectrification, a most frequently experienced phenomenon, is an ideal candidate to achieve the available, stable and efficient mechanical-to-electrical energy conversion. Materials all exhibit triboelectric effect and their intensity depends on the intrinsic attribute to gain/lose electrons, and the triboelectric series has been proposed to describe their relative triboelectric abilities. To quantify triboelectrification in depth, the charge density on contact surfaces is chosen as the evaluation parameter for triboelectric performance and macro- as well as micro/nano-scale methods have been developed for its characterization. Furthermore, it has been proved that physical surface engineering, extrinsically applied electric fiend and chemical surface functionalization approaches are capable of modulating triboelectrification, mainly the polarity and magnitude of tribo-charges. Built on it, diverse triboelectric applications such as triboelectric nanogenerators as well as tribotronics, have been invented.

Appropriate materials are required for the investigation of triboelectrification in this project, so the classification of materials (0D, 1D, 2D and 3D) is introduced based on the number of dimensions at nano-range. As for 0D or 1D materials, it is still a challenge to generate and collect the triboelectric charges given their very limited dimensionality with respect to 2D and 3D materials. Although triboelectrification of 3D materials such as SiO_2 and various polymers has been studied, the tribo-charge density is relatively low compared with the reported results for 2D materials like graphene, and the wear is a problem for practical use, so 2D materials are considered for this project.

Among numerous 2D materials, TMDs exhibit distinctive optical, electrical and mechanical properties, thereby having become the driving force behind a range of applications, including optoelectronics, sensors, electronics, energy storage devices and triboelectric nanogenerators. However, the mechanism of triboelectrification is still poorly understood, so four typical 2D TMDs (MoS_2, WS_2, $MoSe_2$, and WSe_2) are selected for the investigation of triboelectrification at nanoscale.

To date, a massive number of top-down and bottom-up methods have been utilized to synthesize TMDs, but CVD approach is favored since the purity, uniformity, conformity and reproducibility of thin films can be guaranteed, so the materials in this study were produced by this method.

Chapter 3 Chemical vapor deposition and characterization techniques

As all of the materials utilized in this project were synthesized by chemical vapor deposition, a detailed introduction is provided in this chapter. In addition, various instruments including SEM, Raman spectroscopy, XPS, AFM as well as KFM are also reviewed for the structural, physical, chemical and triboelectric characterizations of fabricated materials.

3.1 Chemical vapor deposition

As a relatively mature technique, chemical vapor deposition is a method by which volatile molecular chemicals are delivered in the gaseous phase to a heated substrate where reaction and/or adsorption occurs to form a solid film. Various metals and compounds from sub-micrometer to several millimeters in thickness can be deposited by this method.

3.1.1 A typical system

Considering the different reaction environments, such as precursors and product properties, substrate geometry, temperature and pressure, diverse CVD equipment has been designed. The schematic diagram of a typical CVD process is displayed in Figure 42.

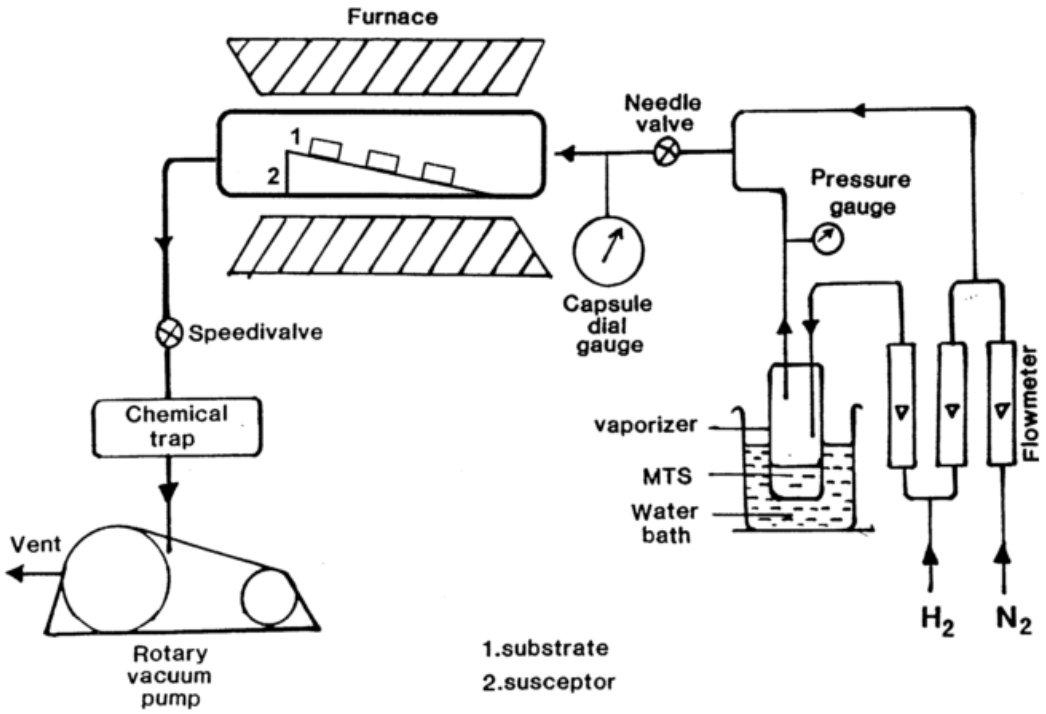

Figure 42 – Schematic diagram of a typical CVD equipment [139].

Once the gaseous precursors are vaporized and transported to the reactor by the gas carrier, homogeneous or heterogeneous chemical reactions in the vapor phase can take place on/in the vicinity of the substrate at/above/below atmospheric pressure.

The reactor can be classified as hot-wall and cold-wall types. In the hot-wall reactor, resistively or radioactively heating furnace is utilized to maintain a uniform temperature profile. Although temperature can be controlled precisely in the central deposition zone, deposition can occur not only on the substrate but also on the reactor walls, resulting in a lower deposition efficiency and maintenance problems. As for the cold-wall reactor, electrical resistance, inductive coupling or infrared is employed to heat substrates instead of the reactor wall [193], so the deposition on cold-wall is negligible in this case. Nevertheless, the cold-wall reactor cannot be applied in all systems and the deposited films may be non-uniform since the temperature cannot be controlled adequately all the time, particularly for large substrates with complex shapes. A range of reactor configurations are depicted in Figure 43.

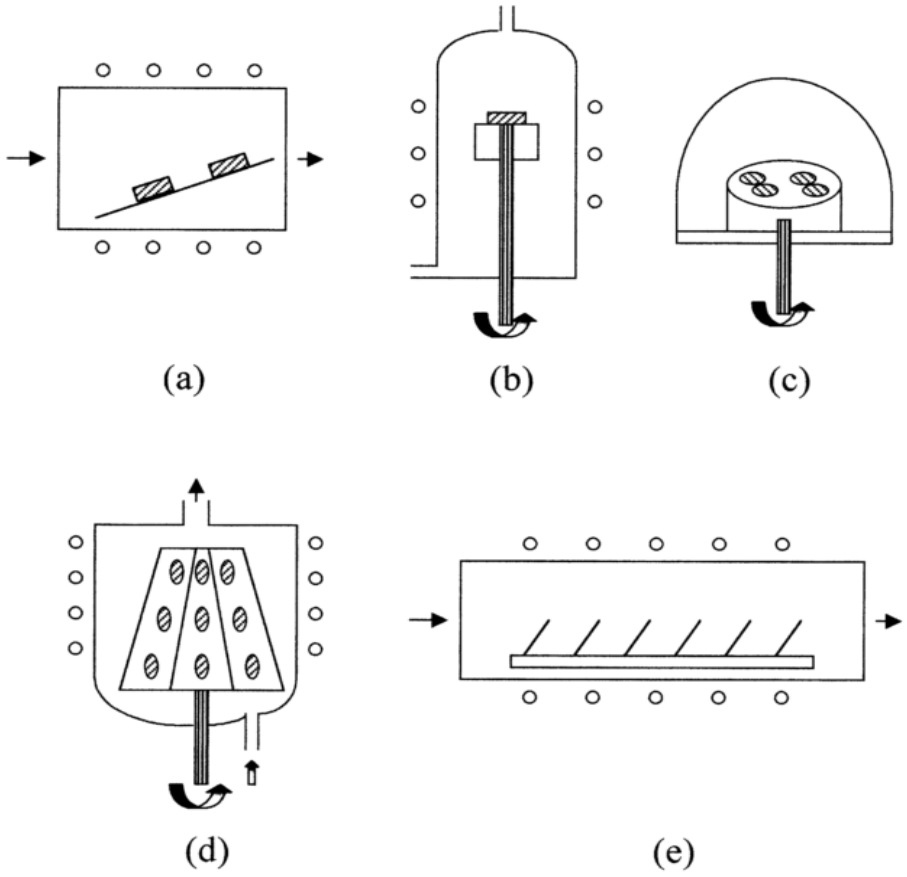

Figure 43 – Different CVD reactor configurations: (a) horizontal; (b) vertical; (c) semi-pancake; (d) barrel; (e) multiple wafer [139].

The exhaust extract system normally contains a vacuum pump to provide required pressure environment for deposition and other components responsible for the removal of hazardous by-product and toxic unreacted precursors. The corrosive by-products and unreacted precursors are neutralized or trapped by a liquid nitrogen trap, inflammable gases are burned off, and unreacted expensive precursors are collected at the outlet and recycled. Owing to the wide range of chemicals used as precursors, reactions and disposal/recycle problems are different and therefore, the exhaust extract system needs to be tailored for individual situations as well.

3.1.2 Factors affecting the coating characteristics

Factors like temperature, substrate chemistry, and chamber pressure together with carrier gas composition have a great impact on the characteristics of CVD-grown films. There is no doubt that a relatively high degree of flexibility is conferred by the combination of different parameters, enabling a wide range of film microstructures to be obtained. On the other hand, the optimization process can be complicated, so the influences of these factors are discussed in this section.

3.1.2.1 Temperature

Temperature is an important factor to affect the kinetics and thermodynamics of CVD reactions. If the temperature is too low, deficiencies such as unfavorable amorphous surface and impurity may occur on deposited films [194][195]. With the rise of temperature, the diffusion rate can be higher thereby accelerating the growth of films, but this trend does not continue infinitely and a reduction in deposition rate may occur in that the thermodynamic driving force is reduced by further heating [194][196]. Consequently, the optimization of substrate temperature can make the reaction thermodynamically favorable and economically viable.

3.1.2.2 Chamber pressure

CVD can take place under different chamber pressures, such as low pressure, atmospheric pressure, and high pressure. As reduced pressures tend to limit undesired gas-phase reactions, enhanced quality and uniformity can be realized on the prepared coatings, and deposition can be carried out at lower temperatures. Therefore, many CVD experiments have been conducted below atmospheric pressure [197][198][199].

3.1.2.3 Gas composition

Precursor gases are often diluted by carrier gases in CVD reaction, and plentiful reactant gases in the gas flow can help with the deposition on substrates. But excessive reactant gases may result in poor adhesion and large microstructural variations on the surface, since needle-shaped or dendritically-branched crystals, and whiskers can be formed in the film [200][201]. As a consequence, an appropriate concentration of precursors is required.

3.1.2.4 Substrate

The substrate properties exert a strong influence on the properties of CVD films. A mismatch of thermal expansion coefficients between substrate and film can lead to excessively high residual stresses in the products, thereby promoting buckling or cracking. In some extreme matters, spontaneous delamination of films from the substrate can happen during the cooling procedure [196][202].

3.1.3 Advantages and disadvantages

CVD method is capable of producing materials with high purity and density, and the synthesized films usually own excellent adhesion, uniformity. Its reproducibility is at a relatively high rate, and coating with conformal coverage can be achieved regardless of complex shape. In the meantime, the deposition process can be adjusted by optimizing reaction parameters, including pressure, temperature, gas inlet and precursors. As a consequence, CVD method can manipulate the crystal structure, surface morphology and orientation of products, which cannot be easily reached by the commonly used physical vapor deposition method (a process where the target material is vaporized from a condensed phase and then deposit onto the substrate as a thin film in condensed phase). Importantly, the cost for the conventional CVD method is reasonable, making it suitable for industrial applications.

However, the high deposition temperature renders the choice of substrate materials. Chemical and safety hazards can be formed by the exploitation of corrosive, flammable, toxic and explosive precursors. Moreover, it is a challenge to deposit multi-component films with manipulated stoichiometry owing to the different vaporization rates of precursors.

In order to overcome these drawbacks, environmental-friendly methods like electrostatic spray assisted vapor deposition have been proposed. But their utilization of sophisticated reactors and/or vacuum systems leads to a higher cost, so other CVD processes without

complex systems, such as aerosol assisted chemical vapor deposition and combustion chemical vapor deposition, can provide alternatives for cost-effective applications.

3.2 Microstructural, physical and chemical analyses

The structural, physical, chemical and triboelectric properties of TMDs can be characterized by the use of SEM, Raman microscopy, XPS, AFM, and KFM, so their working principles are reviewed in this section.

3.2.1 Scanning Electron Microscope

The scanning electron microscope is one of the most versatile instruments suitable for the measurement and analysis of morphology at a micro-scale.

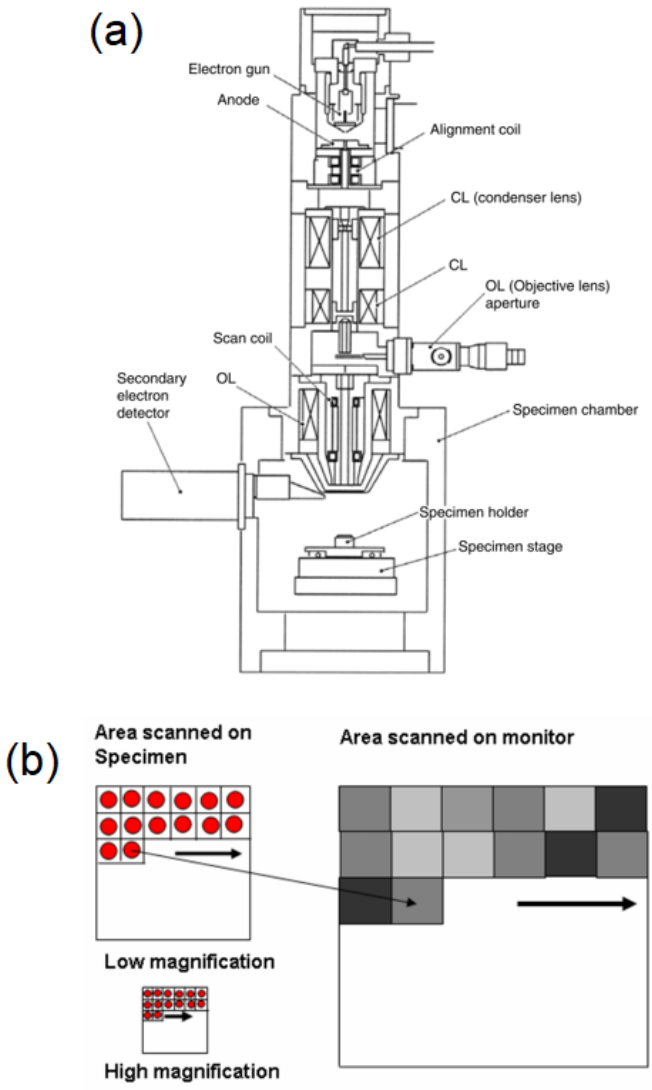

Figure 44 – (a) Column structure and (b) Imaging process of a SEM system (JSM-5410, courtesy of JEOL, USA) [203].

The schematic diagram of a typical SEM is presented in Figure 44a. On the top of the column is the electron gun, which can emit and accelerate electrons to an energy level ranging from 0.1 to 30 keV. The large diameter of the electron beam makes the image resolution limited, so a series of electromagnetic lenses (condenser lens and objective lens) and apertures are utilized to tune the electron beam, thereby forming a focused electron spot on the specimen. This process can decrease the size of the electron source from ~50 μm (for a tungsten filament) to the final required spot size of 1~100 nm. The environment is maintained at a high-vacuum level to make an electron move without scattering caused by the air. In the specimen chamber, specimen stage, electron beam scanning coils, signal detector and the processing system act to provide real-time observation, images or spectra of the specimen surface. As evident in Figure 44b, the specimen is scanned from left to right and top to bottom, and the beam-specimen interaction signal (secondary electrons emitted by atoms excited by the electron beam) within each pixel on the specimen is then derived and collected by the secondary electron detector. Finally, the intensity of the signal can be converted to a grayscale value of the corresponding monitor pixel by the processing system, and the information of the measured sample can be provided.

3.2.2 Raman spectroscopy

In Raman spectroscopy, a single frequency of radiation is employed to irradiate the sample, and the light interacts with a molecule and polarizes (distorts) the cloud of electrons around the nuclei to build a short-lived unstable state named as “virtual state” and the photon is re-radiated quickly. While most re-emitted light owns the same wavelength as the incident light (Rayleigh scattering), the wavelength of a small portion is shifted from the original one. This inelastic scattering can be divided into two sorts: Stokes scattering and anti-Stokes scattering, as presented in Figure 45. The frequency of stokes scattering is smaller than that of the incident light, whereas the frequency of anti-stokes scattering is greater. As the frequency difference contains fingerprints of materials, namely vibrational modes, Raman spectroscopy can be exploited to identify substances from the characteristic spectral patterns, provide information on physical forms and chemical structures, and determine the amount of a specific substance in the sample.

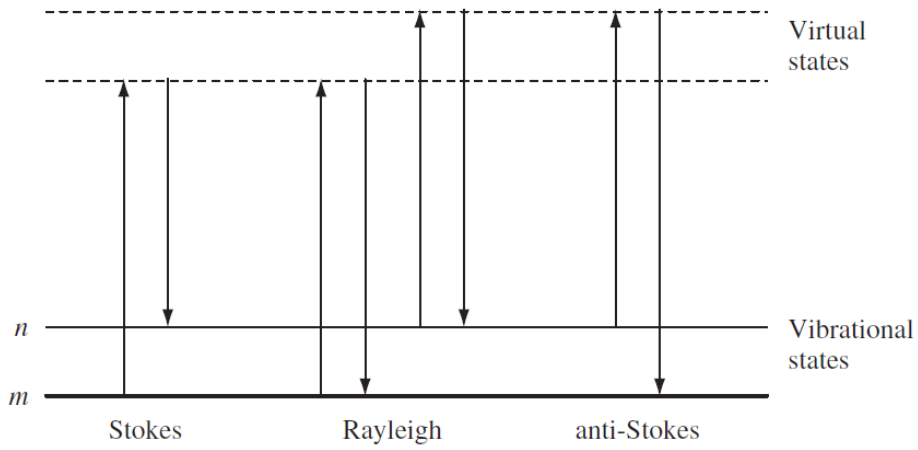

Figure 45 – Diagram of Rayleigh, Stokes and anti-Stokes scattering processes. The lowest energy vibrational state *m* is displayed at the bottom with states of larger energy above it. Both the absorbed energy (upward arrows) and the scattered energy (downward arrows) have far more energies than a vibration [204].

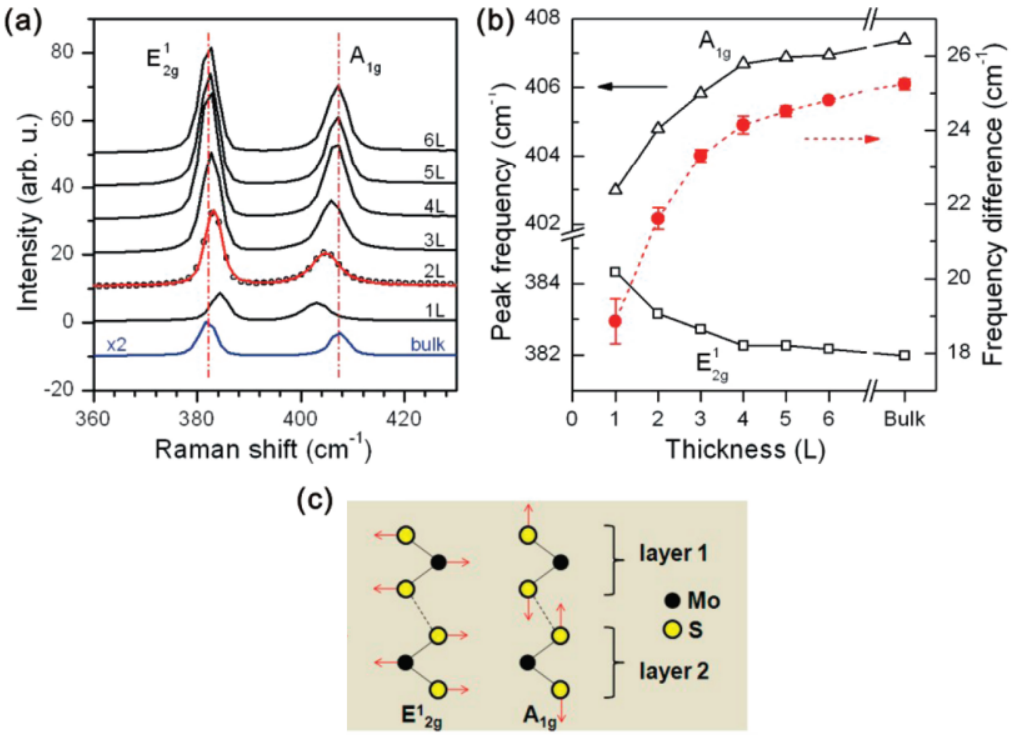

Figure 46 – (a) Raman spectrum of MoS_2 with different layers. (b) Peak frequencies (left vertical axis) and their difference (right vertical axis) as a function of thickness. (c) Schematic of E^1_{2g} and A_{1g} modes [205].

MoS_2, from bulk to monolayer, has two distinct characteristic peaks in the range of 300~450 cm^{-1}: E^1_{2g} and A_{1g} peaks, which are dependent on the layer number of MoS_2 [206] [205], as presented in Figure 46. The E^1_{2g} peak corresponds to the in-plane vibration of Mo and S

atoms parallel to the layer, and a redshifts from 385 to 382 cm^{-1} can be observed with the increase of layer number. The reason behind is that the short-range van der Waals force is stronger than dielectric shielding of the long-range Coulomb interaction [207]. The A_{1g} peak corresponds to the out-of-plane vibration of S atom perpendicular to the layer, and it exhibits a blue shift from 403 to 407 cm^{-1} with the gradual decrease of van der Waals force , which can suppress the atom vibration perpendicular to the layer [208]. Apart from MoS_2, the layer number can also be identified via the Raman spectra for WS_2, $MoSe_2$ and WSe_2 [209]–[211].

3.2.3 X-ray photoelectron spectroscopy

For the characterization by X-ray photoelectron spectroscopy, a specimen is illuminated by low energy X-rays in an ultra-high vacuum environment, which can cause the photo-ionization of atoms on the specimen's surface and photoelectrons are emitted at energy levels determined by the structure and chemical state of the specimen. The XPS analysis technique can examine the kinetic energy of the emitted photoelectrons and uses it to determine their binding energy as equation (3-1):

$$E_{binding} = E_{source} - E_{kinetic} \tag{3-1}$$

where $E_{binding}$ is the binding energy, E_{source} is the enrgy of X-ray source, and $E_{kinetic}$ is the detected kinetic energy of the emitted photoelectrons. Therefore, the chemical states and quantities of elements can be inferred.

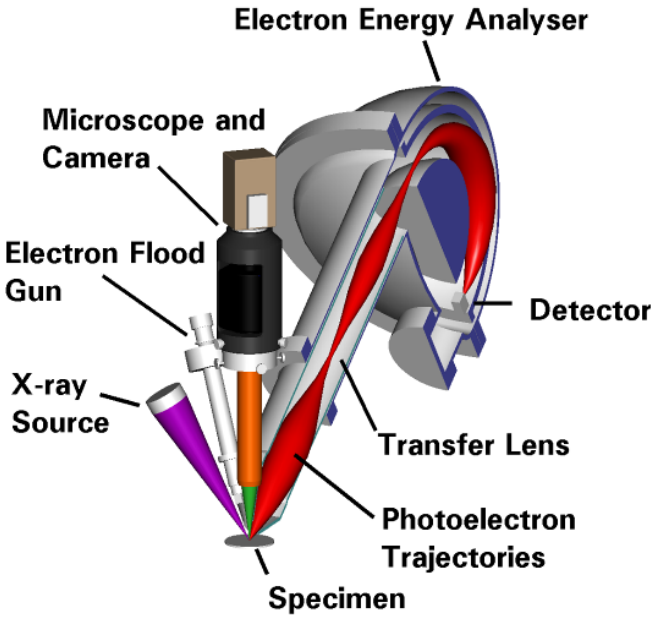

Figure 47 – A typical X-ray Photoelectron Spectrometer.

A typical XPS system, demonstrated in Figure 47, consists of an X-ray source, electron energy analyzer, optical microscope, and electron flood gun. The X-ray monochromator in this system is based on an aluminum anode and use Al Kα radiation (photon energy = 1486.68 eV). The photoelectrons emitted from the specimen are collected by the transfer lens and focused onto the electron energy analyzer. The microscope is fitted to assist in locating the areas of interest on the specimen. The electron flood gun is required to control the surface charging when analyzing insulating surfaces. The ion gun is also installed to etch the specimen in situ for depth analysis.

3.2.4 Atomic force microscope and Kelvin force microscope

Currently, tip-based microscopes and surface force apparatus have been extensively developed for micro/nanotribological studies. One of them is an atomic force microscope, which is capable of resolving features as small as an atomic lattice, for either conductive or non-conductive samples. With little sample preparation, AFM can provide high-resolution and three-dimensional information, so this technique makes it possible to image in situ, in fluid, under controlled temperature and on other diverse conditions, and the potential of AFM extends to applications in life science, materials science, electrochemistry, polymer science, biophysics, nanotechnology, and biotechnology.

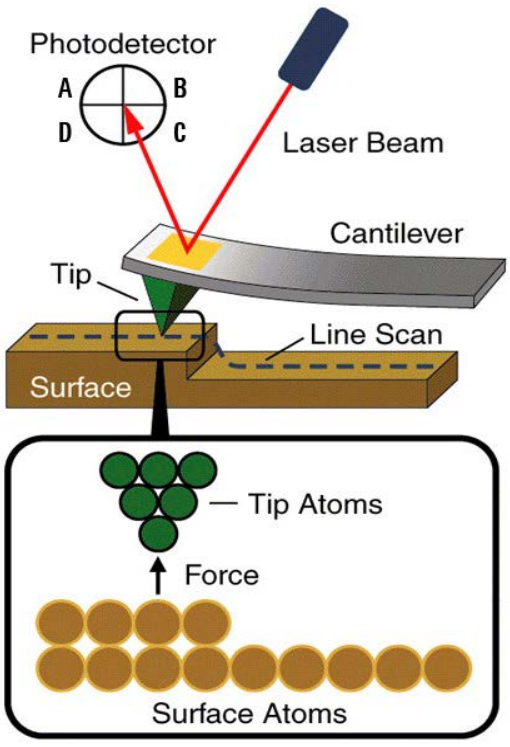

Figure 48 – Working principle of AFM system.

In an AFM system (shown in Figure 48), a sharp tip at the free end of a cantilever (the "probe") is brought into contact with the sample surface, so it can interact with the surface, causing the cantilever to bend. In the meantime, a laser beam is reflected from the cantilever onto a position-sensitive photodiode detector, so the change of the laser spot position can be monitored as the cantilever bends, which includes the information of the sample surface.

Based on the force interaction between the tip and sample, AFM is commonly operated in two modes: non-contact mode and contact mode. The former mode can be utilized to view the surface topography, so surface defects can be identified at the nanoscale; the latter mode aims to study nanotribological properties, such as adhesion, coefficient of friction to name a few. Both modes are able to measure soft/hard surfaces in liquid and air [212].

To date, applications of AFM have been expanded to multi-frequency measurement of electric and mechanical sample-tip force interactions. As for local electric properties, KFM mode is one of the relative advances.

To describe the mechanism of KFM, energy diagrams of the tip and sample with varied work functions are illustrated in Figure 49. The vacuum levels of tip and sample are aligned when there is no electrical contact between them. As they approach each other and the distance between them is close enough for electron tunneling, their Fermi levels will line up at a steady-state via an electron current flow while the vacuum energy levels are different, so a tip-sample contact potential difference is generated as:

$$V_{CPD} = \frac{\varphi_{tip} - \varphi_{sample}}{-e} \tag{2-8}$$

where φ_{tip} and φ_{sample} are the work functions of tip and sample, respectively; e is the electronic charge.

This contact potential difference can result in an electrical force acting on the contact area. However, if a voltage V_{DC}, which owns the identical magnitude to V_{CPD} is applied, the electrical force can be offset, and the surface potential maps obtained by KFM just exhibit the offset voltage V_{DC}. Once the material of tip is given, the work function of the sample can be estimated with the surface potential images measured by KFM. In [125], the work function of the gold-coated tip (work function of gold is 4.91 eV) was used to measure the work function of tri-layered and bi-layered pristine MoS_2 after oxygen plasma treatment.

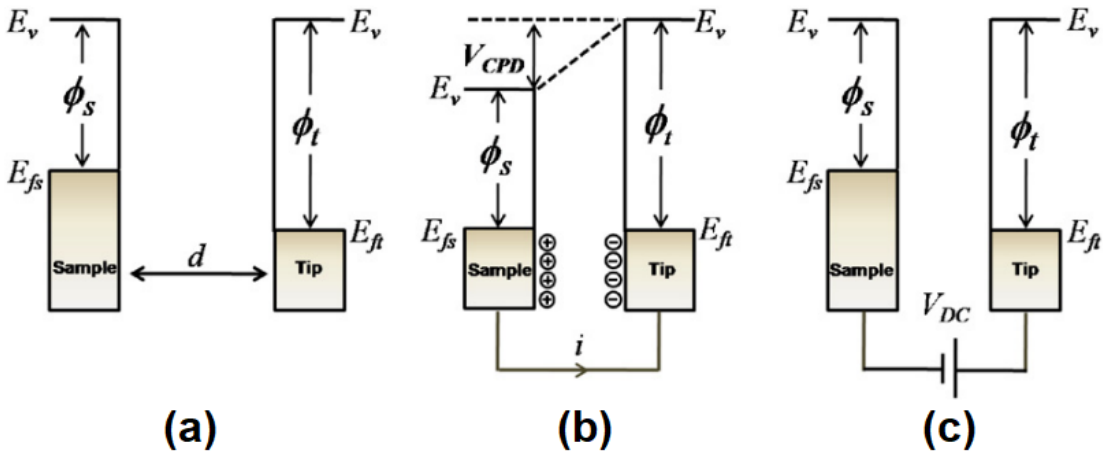

Figure 49 – Electronic energy levels of the sample and tip for three cases: (a) sample and tip are separated by distance *d* and not electrically connected, (b) sample and tip are in electrical contact, and (c) external bias is applied to nullify the contact potential difference [31].

3.3 Summary

Until now, numerous methods have been developed to grow TMDs but CVD approach is favored considering that the purity, uniformity, conformity as well as reproducibility of thin films can be guaranteed. Meanwhile, various parameters including precursors and product properties, substrate geometry, temperature and pressure are controllable in a single CVD process, so diverse crystal structure, surface morphology and orientation of products can be achieved. Although the high deposition temperature and the use of hazardous chemicals are the main drawbacks of this method, alternatives like electrostatic spray assisted vapor deposition and aerosol assisted chemical vapor deposition have been proposed.

To evaluate the structural, physical, chemical and triboelectric properties of CVD-synthesized TMDs, a range of facilities, consisting of optical microscope, scanning electron microscope (SEM, Zeiss EVO50XVP, with EDX system of Oxford Instruments INCA 250), Raman spectroscopy (InVia Raman Spectrometer), X-ray photoelectron spectroscopy (XPS, Thermo Scientific Theta Probe XPS System MC03), atomic force microscope (AFM, Scanning Probe Microscopy 5500, Agilent Technologies) and Kelvin force microscopy (KFM, a mode integrated within the AFM system).

Chapter 4 Chemical vapor deposition for transition metal dichalcogenides

In this chapter, the tube furnace system for chemical vapor deposition in this whole project is introduced in the first place: a temperature profile was obtained, and the effects of diverse parameters such as precursors, carrier gas and temperature were studied. On these basis, high-quality 2D TMDs including MoS_2, WS_2, $MoSe_2$, and WSe_2 were successfully prepared. It should be mentioned that all the chemical vapor deposition experiments were performed, for convenience and economic concern, at atmospheric pressure.

4.1 Temperature calibration

The tube furnace system for chemical vapor deposition during the investigation is shown in Figure 50. In this system, parameters consisting of temperatures of precursors and substrates, pressure, carrier gas, and the amounts of precursors can be controlled independently. Precursors, substrates, and boats were placed in a 115 cm long and 3 cm outer-diameter quartz tube, which was surrounded and heated by the furnace. One end of the tube was linked to a series of gas inlets, through which gases like nitrogen (N_2), hydrogen (H_2), argon (Ar), and hydrogen disulfide (H_2S) can be introduced into the system; the other end was connected to the exhaust extract component. All the TMDs films were grown on Si substrates covered with 300 nm SiO_2.

Before the reaction, boats and substrates were cleaned with acetone, isopropanol and deionized water for 10 minutes, and then blow-dried by a nitrogen gun. Subsequently, substrates were placed on the cleaned boat containing a certain amount of MoO_3 (WO_3), which was pushed to a certain location in the tube. Then, another boat containing specific amount of sulfur (selenium) was loaded at the upstream, and it was heated by a heating tape, so the temperatures of different precursors could be manipulated separately. 300 standard cubic centimeters per minute (sccm) Ar gas (or mixed with 6% hydrogen) was then introduced by mass flow controller to purge for 10 min. After that, the furnace was programed to heat the substrate and vaporize MoO_3 (WO_3) precursor. When the target temperature was reached, S (Se) was heated and its vapor was delivered to the substrates, where the reaction took place and TMDs were deposited. Once the deposition was completed, the system was switched off to cool down naturally.

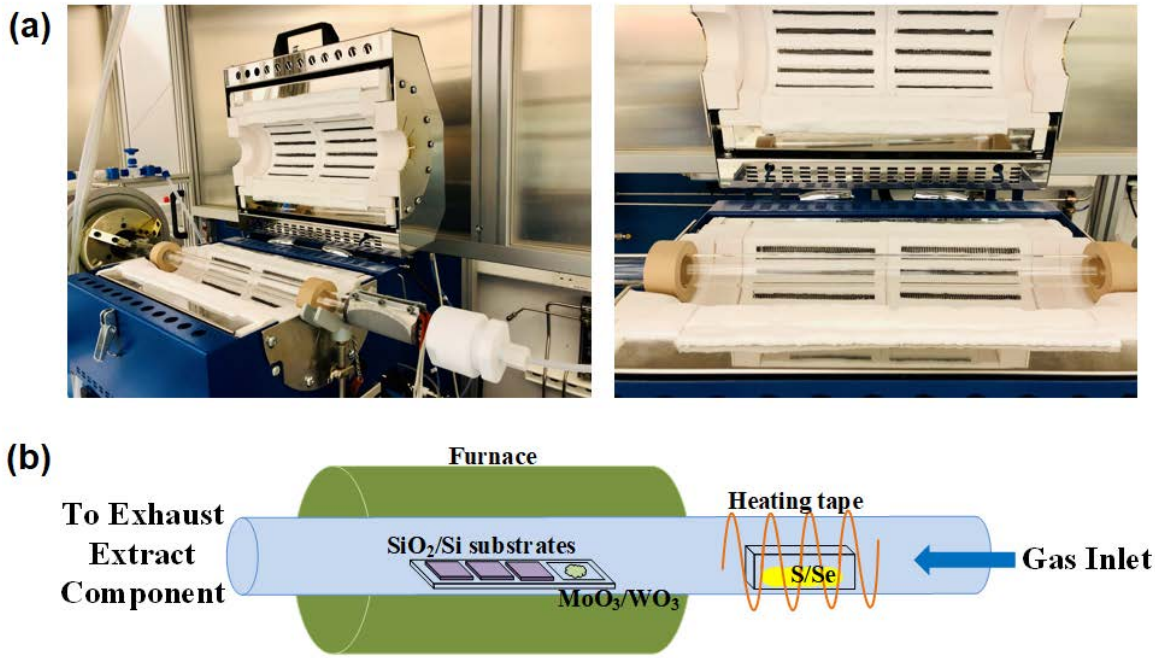

Figure 50 – (a) Photos and (b) schematic of tube furnace system.

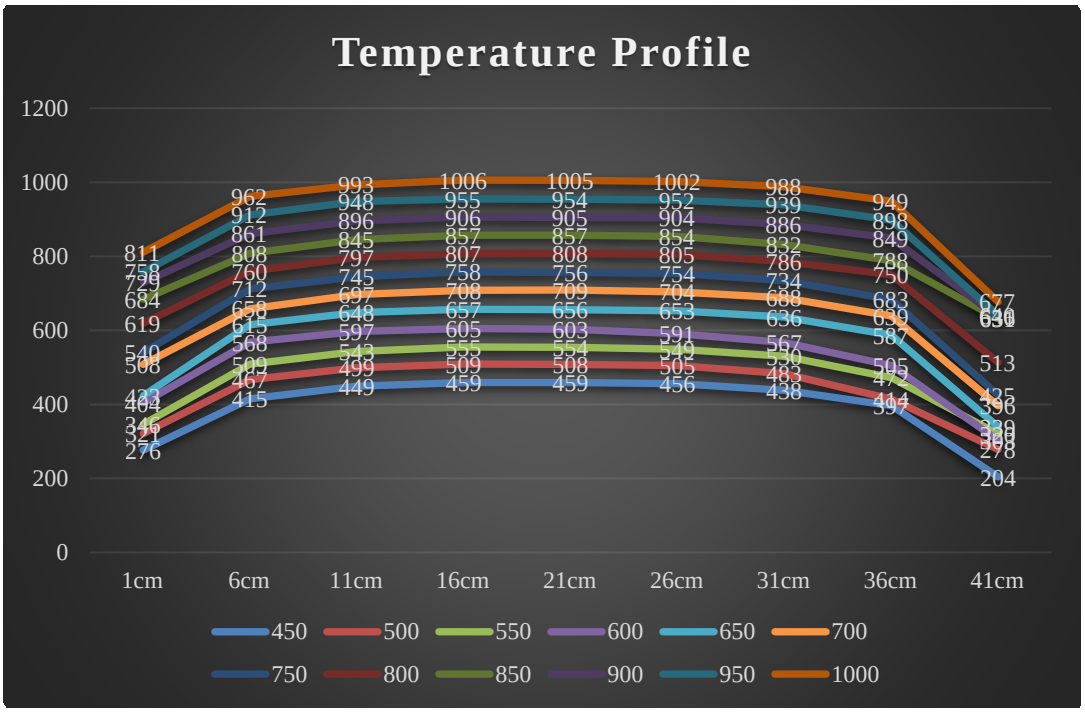

Figure 51 – Temperature profile in the tube (Unit: ℃).

As thermodynamics play a key role in CVD reaction, it is of essence to calibrate the temperature profile in the tube, and the proposed methods up to now can be divided into two kinds: physical probes (e.g. thermometer) and optical devices (e.g. pyrometer). In general, physical probes are easily operative and low-cost, but the measurement is confined to localized places and the reaction near the substrate surface may be influenced by the probe.

On the contrary, optical devices will not disturb the reaction, and high spatial resolution can be reached even in a rapidly changing environment, moreover, desired species can be detected selectively. But its shortcoming is that CVD reactors need to be modified to tailor the devices. As the calibration was performed prior to the CVD reaction, K-type thermocouple, which covers a wide temperature range from −200°C to 1260°C, was used to calibrate the tube temperature profile instead of optical devices, which tend to be more complex and expensive.

Figure 51 shows the temperature profile in the tube system under set-up temperatures ranging from 450 to 1000 ℃. It is noteworthy that the measured temperatures of the central area (between 11 and 26 cm) approach the setup value, and the maximum deviation is less than 10 ℃. Outside this area, there is a dramatic reduction in temperature with the increase of distance from the tube center. Under this circumstance, temperatures of substrate and precursors can be tuned by placing them at specific locations.

4.2 Effect of different factors

In order to determine the optimal conditions for the growth of TMDs layers, effects of parameters including amount and temperature of precursors, gas inlet and pre-treatment to substrate, have been investigated with regard to MoS_2.

4.2.1 Precursors amount

To investigate the effect of precursors amount, MoS_2 samples were prepared with 15 mg MoO_3 and different amounts (100, 150 and 200 mg) of sulfur. As evident from the optical images in Figure 52, MoS_2 flakes experience a morphology transformation as well as a size change. With the increase of sulfur amount, these flakes transform from small-sized regular triangle (~25 μm) to slightly larger three-point stars (~40 μm); some dark-colored chemicals can be clearly seen on the substrate in the case of 100 and 150 mg sulfur.

To confirm that the flakes in these three images are exactly monolayer MoS_2, flakes squared in Figure 52 were characterized via Raman spectroscopy. Raman spectrum in Figure 53a shows two characteristic vibrational modes: E_{2g}^1 at 383.2 cm^{-1} and A_{1g} at 404.2 cm^{-1}, and their frequency difference is ~21 cm^{-1} for these three cases; photoluminescence (PL) spectrum in Figure 53b exhibits one peak at ~675.7 nm for these flakes. All of these results agree with the reported values for single-layer MoS_2 [149]. It should be mentioned that the measured results here are shifted from the provided data in section 3.2.2, since a ~20%

variation in the frequency difference between E^1_{2g} and A_{1g} modes for single-layer MoS_2 grown on SiO_2/Si substrate can appear due to the substrate-induced effects such as doping due to impurities and trapped charges, substrate-sample interactions, strain and even sample background noise, which may play a measurable role in the Raman spectroscopic features of 2D-MoS_2 [149].

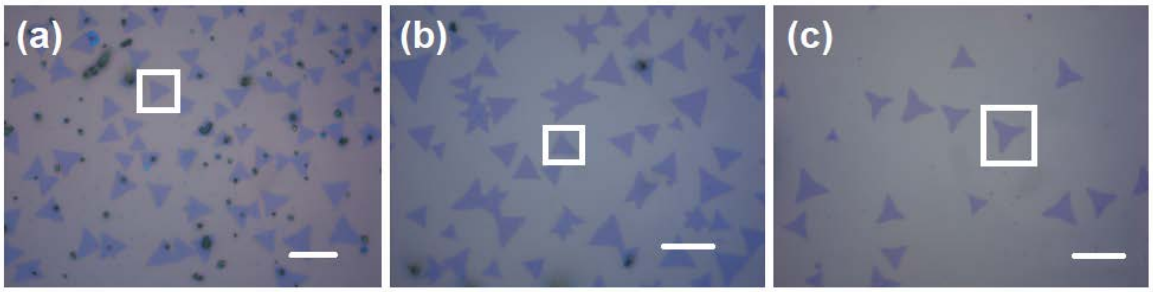

Figure 52 – Optical images of MoS_2 synthesized with different sulfur amounts: (a) 100 mg, (b) 150 mg and (c) 200 mg. The amount of MoO_3 is 15 mg; temperatures of MoO_3 and S are 700 and 200 °C, respectively; ramping rate is 10 °C/min; flow rate is 30 sccm. Scale bar is 50 µm.

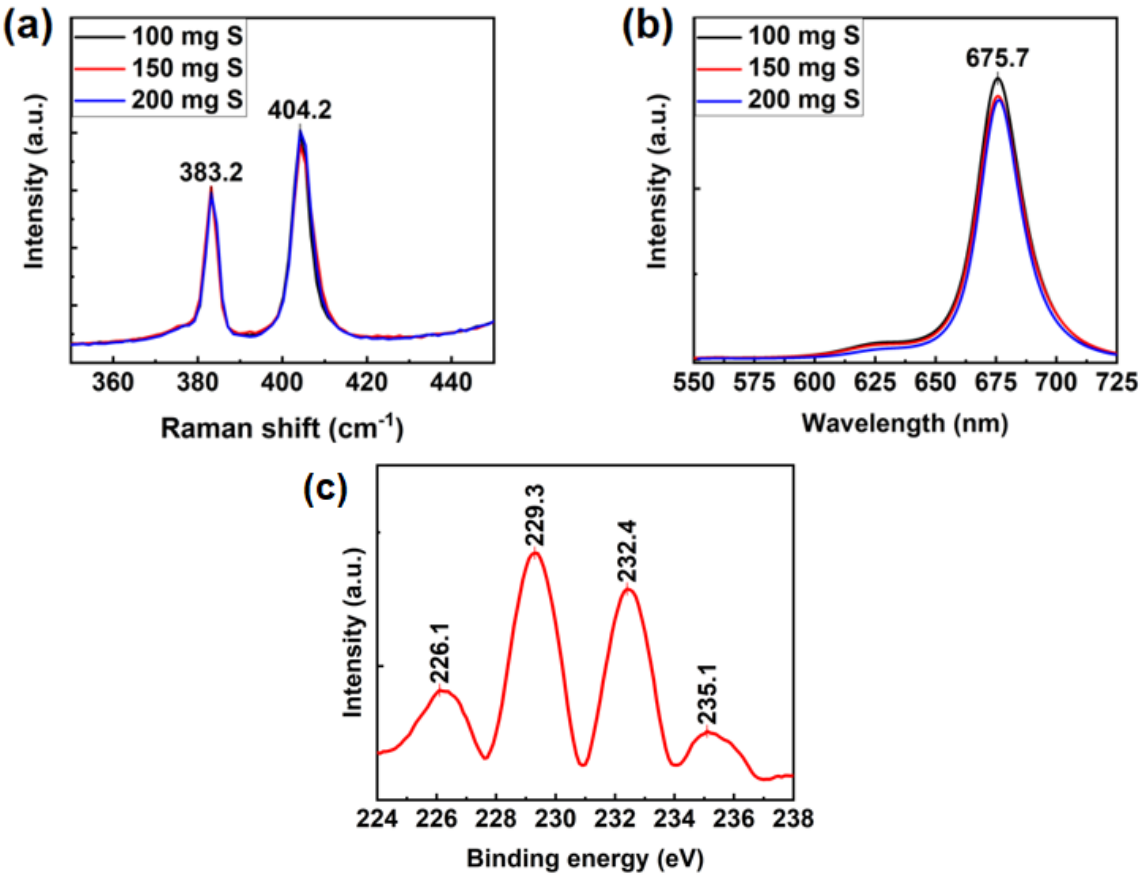

Figure 53 – (a) Raman and (b) PL spectra of MoS_2 synthesized with 100, 150 and 200 mg sulfur. (c) XPS spectrum for Mo 3d and S 2s orbitals.

As for the dark-colored chemicals, their nature has been confirmed by XPS as illustrated in Figure 53c. Apart from the S 2s orbital at 226.1 eV, the Mo 3d orbits exhibit three peaks at 229.3, 232.4 and 235.1 eV. The first two peaks belong to the Mo $3d_{5/2}$ and Mo $3d_{3/2}$, respectively, correlating to Mo^{4+} state in MoS_2. The third peak of Mo 3d core level peak at 235.1 eV originates from the Mo^{6+} state of MoO_3. Resultantly, these dark-colored chemicals are unreacted MoO_3 or partially reduced molybdenum oxysulfide, whose existence results from the sulphur deficiency during the growth.

The final crystal shape is determined by the growth rate of different crystal faces based on the principles of crystal growth [213]. In the end, the rapid growth faces either become smaller or disappear altogether, and the slowest growing faces become the largest. The growing rate of faces is dependent on the surface free energy, and the low-energy faces have the tendency to grow slower compared with the high-energy ones. For monolayer MoS_2, its final shape is related to the growth rate of different edge terminations, and the most commonly observed edge structures are Mo zigzag (Mo-zz) terminations and S zigzag (S-zz) terminations due to their energetically stable structures [165]. Their structural difference gives them distinctive chemical activity on varied Mo:S ratio conditions, which can influence the growth rate and domain shape of MoS_2.

Figure 54 illustrates the relationship between the Mo:S atom ratio and the domain shape. When the Mo:S ratio is larger than 1:2, S-zz terminations grow faster than Mo-zz terminations since S-zz terminations have a higher probability to meet and bond with free Mo atoms in the Mo-rich situation, so a triangular shape with three sides of Mo-zz terminations can be formed. Under S-rich circumstance (Mo:S < 1:2), Mo-zz terminations grow faster than S-zz terminations and the sides of triangular MoS_2 flakes are S-zz terminations. When the Mo:S ratio corresponds to the stoichiometric ratio (1:2), termination stability and probability for the meeting of two terminations are similar and so are their growth rates, and the final shape will be hexagon in this case [146].

In the situation where the growth rate of Mo edge is at least three times faster than that of S edge, MoS_2 flakes with a three-point star shape are more likely to grow, since the growth of S-zz terminations cannot keep pace with the growth of Mo-zz terminations, and S-zz terminations can only form a curved edge instead of a straight one, which looks like a three-point star. Moreover, this shape often transforms into several-point stars due to the imperfect curved structure of S-zz edge.

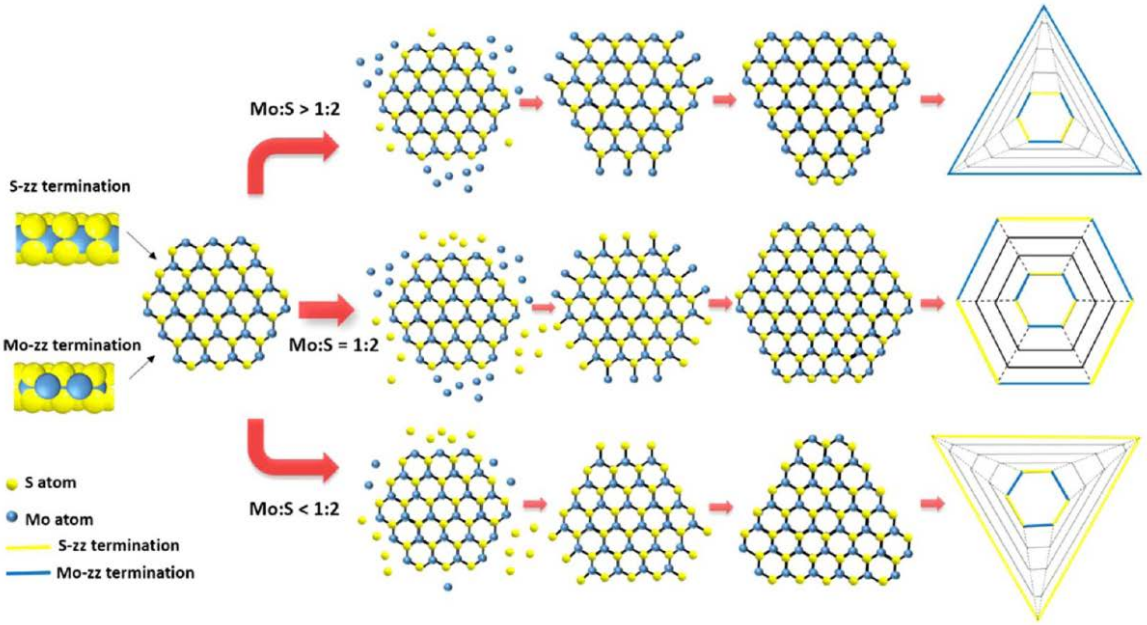

Figure 54 – Schematic illustration of the relationship between the Mo:S atom ratio and the domain shape. The ball-and-stick models in the central part show the top view microstructure of the monolayer MoS_2 crystal in different shapes, while the ball models on the left show two kinds of MoS_2 termination structures. The schematic diagram on the right illustrates the domain shape changing procedure depending on the growing rates of two different terminations [214].

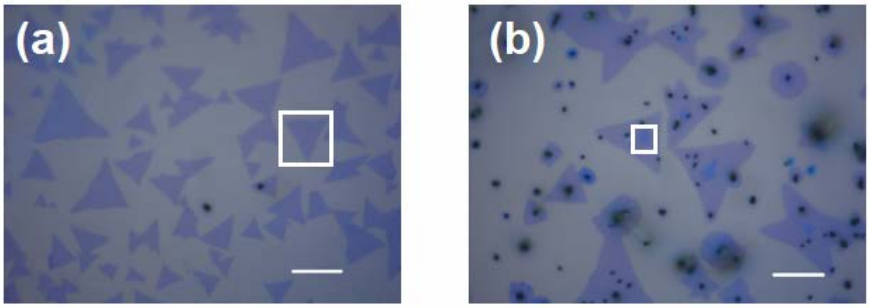

Figure 55 – Optical images of MoS_2 synthesized with the same S:MoO_3 ratio: (a) 150:15 and (b) 250:25 (unit: mg). Temperatures of MoO_3 and S are 700 and 200 °C, respectively; ramping rate is 10 °C/min; flow rate is 30 sccm. Scale bar is 50 μm.

Aside from the investigation of various Mo:S ratios, experiments with the same Mo:S ratio, $W_{Sulphur}$: W_{MoO_3} = 150:15 and 250:25 (unit: mg), were also conducted (Figure 55). It can be noticed that some brighter flakes have been deposited with more precursors, and the Raman spectrum Figure 56a shows that the frequency difference between E^1_{2g} (381.9 cm^{-1}) and A_{1g} (408.1 cm^{-1}) modes is 26.2 cm^{-1}, and the PL spectrum in Figure 56b has two obvious emission peaks at 635.9 and 683.3 nm, corresponding to B and A excitons, respectively. At

room temperature, the absorptive optical response close to the band edges in TMDs is strongly dominated by excitons, particularly A and B excitons, which originate from transitions at the K-point. The energy difference between A and B is caused by valence band splitting due to spin–orbit coupling [215]. All evidence confirms that the squared area in Figure 55b is multi-layered MoS_2 [207]. Additionally, many unreacted MoO_3 or partially reduced molybdenum oxysulfide are left on the substrate (Figure 55b), whose presence indicates the excess of precursors.

In general, the number of layers can be roughly estimated via the variation in the color of nanoflakes on the substrate: monolayer is almost transparent and shows a dark blue color, whereas a multilayer is brighter and yellow color can even be seen for much thicker flakes, as reported in [216].

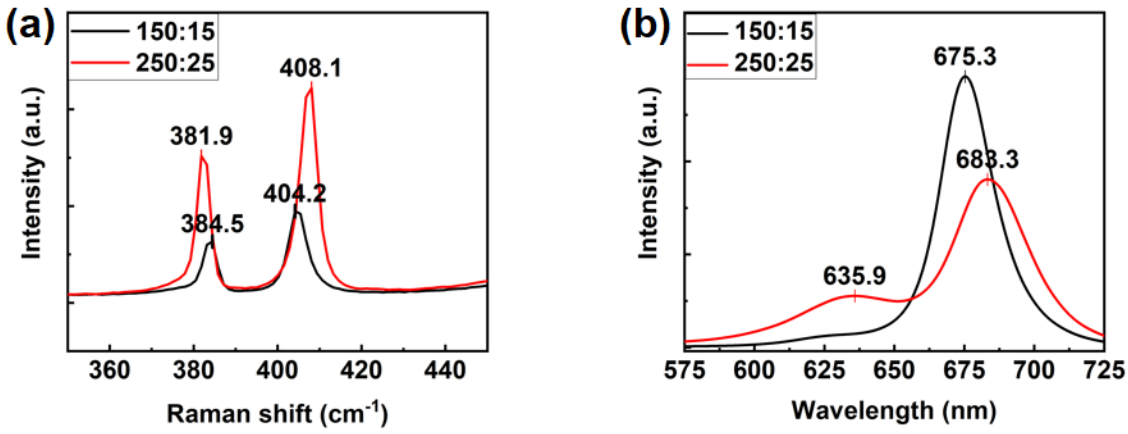

Figure 56 – (a) Raman and (b) PL spectra of MoS_2 synthesized with the same S:MoO_3 ratio: 150:15 and 250:25 (unit: mg).

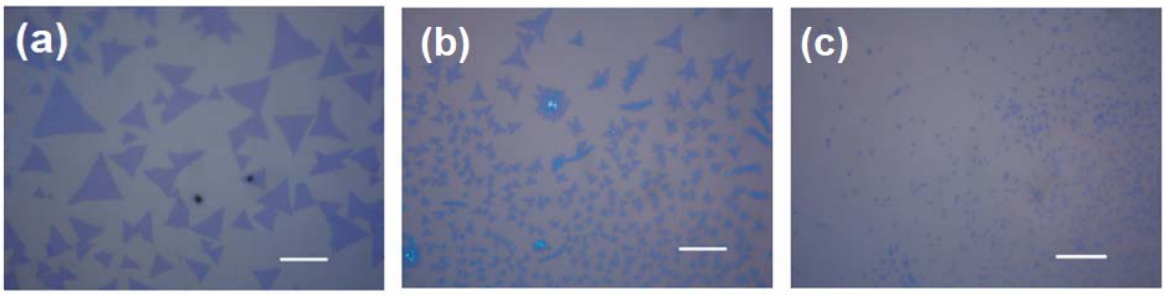

Figure 57 – Optical images of MoS_2 at different locations: the distances from MoO_3 are (a) 3 cm, (b) 5 cm and (c) 7 cm. $W_{Sulphur}$ = 150 mg, $T_{Sulphur}$ = 200 °C, W_{MoO_3} = 15 mg, $T_{Substrate}$ = 700 °C, ramping rate = 10 °C/min, flow rate = 30 sccm. Scale bar is 50 µm.

Figure 57 displays the optical images of MoS_2 at different locations on the substrate. As evident from the temperature profile measured in section 4.1, the temperatures at these three

locations are almost the same within the CVD chamber. It is noteworthy that the size and density of MoS_2 flakes decrease with the increasing distance from MoO_3 on the substrate, and the regular triangles transform to three-point stars due to the reduction of MoO_3 precursor concentration.

4.2.2 Gas inlet

In the CVD process, gaseous precursors are usually diluted by the carrier gas and some gases can also act as the source of precursors, for example, H_2S can be used as the precursor and carrier gas for the growth of MoS_2 and WS_2. In some cases, reactant gases like H_2 are mixed in the gas flow to assist the reaction, here, MoS_2 was prepared by pure Ar gas and Ar mixed with 6% H_2 to observe its effect. As shown in Figure 58, single-layer triangular MoS_2 was deposited with pure Ar and thicker nanoflakes were grown with a mixture of H_2 gas, and most multilayers are irregular triangle-shaped. So the excessive reactant gas can accelerate the growth of the product but may also lead to various microstructures on the surface.

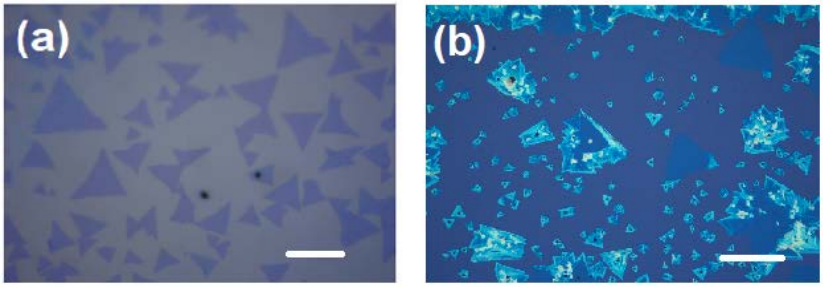

Figure 58 – Optical images of MoS_2 synthesized with (a) pure Ar and (b) Ar mixed with 6% H_2. The amounts of MoO_3 and S are 15 and 150 mg, respectively; temperatures of MoO_3 and S are 700 and 200 ℃, respectively; ramping rate is 10 ℃/min; flow rate is 30 sccm. Scale bar is 50 μm.

In addition, MoS_2 samples have been synthesized with 30, 40 and 50 sccm Ar flow to investigate the effect of gas flow rate. It is noticed that triangular MoS_2 flakes were deposited on the substrate with 30 sccm Ar flow (Figure 59a). When the flow rate was increased to 40 sccm, many MoS_2 flakes were formed in bulk and some dendritic structures can be obviously seen (Figure 59b). As the flow rate reached 50 sccm, the SiO_2/Si substrate is covered by bulkier MoS_2 flakes and only a few small-sized MoS_2 monolayers are left (Figure 59c).

Theoretically, both the mass transfer process and crystal growth rate can be improved with the increase of Ar flow rate. In this case, precursor atoms may not have enough time to move to the right lattice location, where crystal domains have the lowest surface free energy, so

instability and defect may occur and MoS_2 seems to grow more kinetically than thermodynamically under high flow rate.

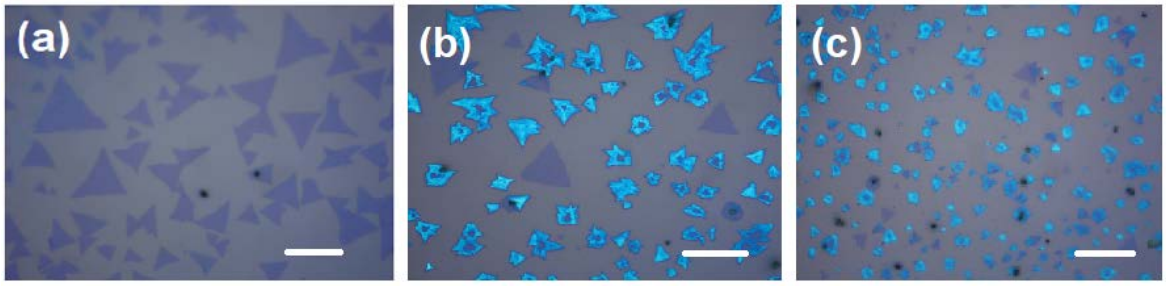

Figure 59 – Optical images of MoS_2 synthesized with (a) 30 sccm, (b) 40 sccm and (c) 50 sccm Ar flow. The amounts of MoO_3 and S are 15 and 150 mg, respectively; temperatures of MoO_3 and S are 700 and 200 ℃, respectively; ramping rate is 10 ℃/min. Scale bar is 50 μm.

4.2.3 Temperature

Owing to the fact that temperature plays a key role in kinetics and thermodynamics of CVD reactions, MoO_3 precursor was heated to 650 ℃, 700 ℃ and 750 ℃ to evaluate its influence (Figure 60). As the temperature can control the evaporation rate of MoO_3, a MoO_3 precursor concentration gradient can be created in the gaseous phase, resulting in various Mo:S ratio conditions within the tube. When the temperature of MoO_3 was increased from 650 ℃ to 750 ℃, MoS_2 flakes grew from small-sized three-point stars to medium-sized regular triangles, and then to thicker large-sized dendritic-like shape. Similarly, the temperature of S precursor can be controlled to adjust the S concentration inside the system, thereby influencing the growth of products. Resultantly, it is necessary to optimize the precursor temperature to obtain favorable flakes.

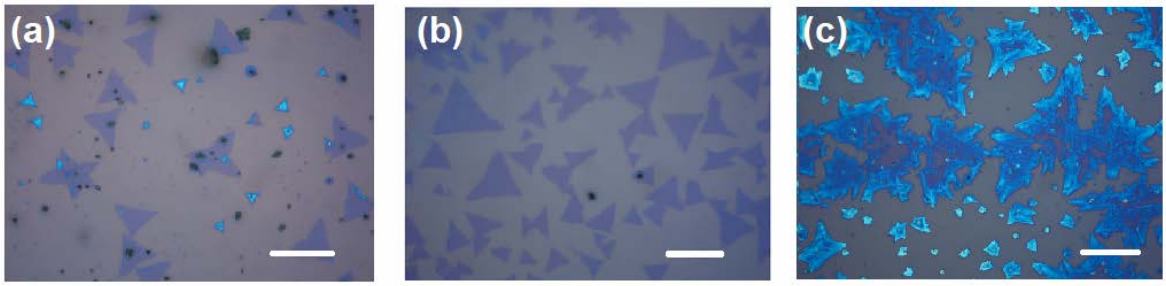

Figure 60 – Optical images of MoS_2 synthesized with different MoO_3 temperatures: (a) 650 ℃, (b) 700 ℃ and (c) 750 ℃. The amounts of MoO_3 and S are 15 and 150 mg, respectively; temperature of S is 200 ℃; ramping rate is 10 ℃/min; flow rate is 30 sccm. Scale bar is 50 μm.

4.2.4 Pre-treatment

In previous experiments, only acetone and isopropanol were used to clean substrates prior to the CVD process. To estimate the impact of substrate cleanliness, piranha solution (a mixture of sulfuric acid and hydrogen peroxide, H_2SO_4:H_2O_2=3:1) was also employed to clean the organic residues off further.

To characterize the cleanliness of the substrate, its surface topographies were measured before and after the treatment by piranha solution (Figure 61), and the RMS roughness reduces from 0.35 to 0.29 nm by the utilization of piranha solution, indicating that a cleaner SiO_2/Si substrate surface is achieved. As can be seen from Figure 62, there is an increase in size and density of MoS_2 flakes on SiO_2/Si substrate with the pre-treatment by piranha solution, and more multi-layered MoS_2 can be found on the pre-treated substrate. Consequently, it can be concluded that the utilization of piranha solution makes it easier for the growth of MoS_2 flakes.

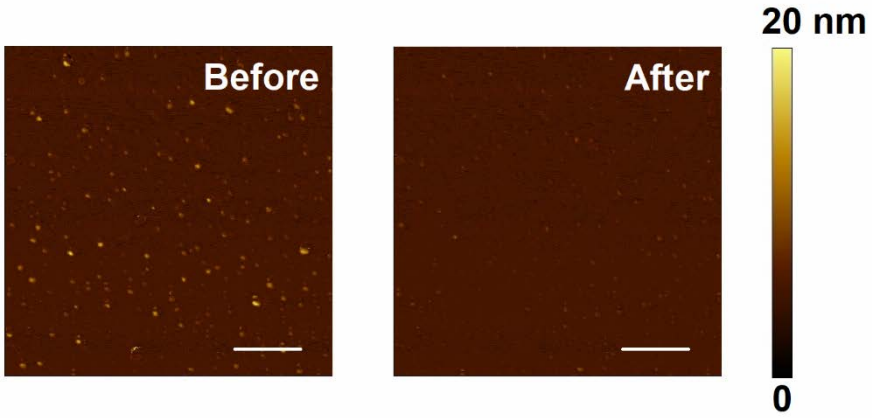

Figure 61 – Surface topographies of SiO_2/Si substrate before and after piranha solution treatment.

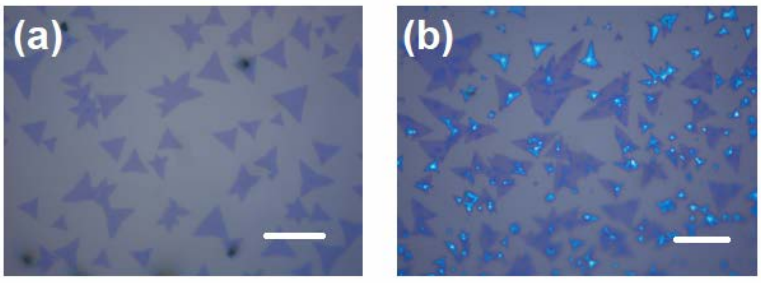

Figure 62 – Optical images of MoS_2 deposited on SiO_2/Si substrate (a) without and with (b) piranha solution treatment. The amounts of MoO_3 and S are 15 and 150 mg, respectively; temperatures of MoO_3 and S are 700 and 200 ℃, respectively; ramping rate is 10 ℃/min; the flow rate is 30 sccm. Scale bar is 50 μm.

4.3 Optimized transition metal dichalcogenides

Based on the published recipes in section 2.3.2.2 and effects of various parameters within CVD operation in 4.2, optimized MoS_2, WS_2, $MoSe_2$, and WSe_2 have been synthesized, and their qualities were evaluated by techniques introduced in 3.2, including optical microscope, AFM, Raman spectroscopy as well as XPS.

4.3.1 MoS_2

Before the reaction, boats and substrates were cleaned with acetone, isopropanol, and deionized water, and then blow-dried by the nitrogen gun. Subsequently, SiO_2/Si substrates were placed on a boat containing 10 mg MoO_3 (Alfa Aescar 99.9995%), and the boat was then pushed into the tube center. After that, another boat containing 100 mg sulfur (Alfa Aescar 99.9995%) was loaded at the upstream, whose temperature was separately controlled by the heating tape instead of the furnace. Later on, 300 sccm Ar gas (BOC, 99.999% pure with additional purifications) was introduced to purge the tube for 10 minutes. Afterward, Ar flow was decreased to 30 sccm, and the furnace temperature was programmed to heat substrates and vaporize MoO_3 to 550 ℃ at 25 ℃/min ramping rate. After holding this temperature for 5 minutes, it was set to 700 ℃ at 10 ℃/min ramping rate, and sulfur was heated to 200 ℃ so its vapor could be transported to the tube center, where CVD reaction occurred and MoS_2 was deposited. After 15 minutes deposition at 700 ℃, the heating system was turned off to cool down naturally. The temperature profile of this process is plotted in Figure 63.

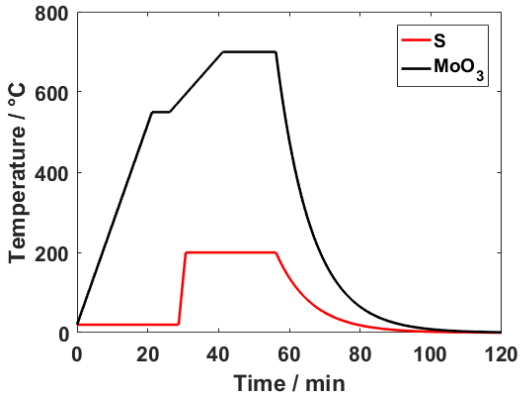

Figure 63 – Temperature profile of MoO_3 (black line) and S (red line) for the growth of MoS_2.

Figure 64a displays the optical image of MoS_2 synthesized on SiO_2/Si substrate by CVD method. It is noteworthy that the fabricated MoS_2 sample exhibits a triangular shape, and the

lateral size can reach up to ~120 µm, whose limitation may result from the lattice mismatch between the MoS_2 and SiO_2/Si substrate. As evident from the surface topography measured by tapping-mode AFM in Figure 64b, the step height of monolayer MoS_2 from the substrate is ~0.8 nm, which is consistent with the reported thickness of mechanically exfoliated MoS_2 monolayers [170], [217]–[221].

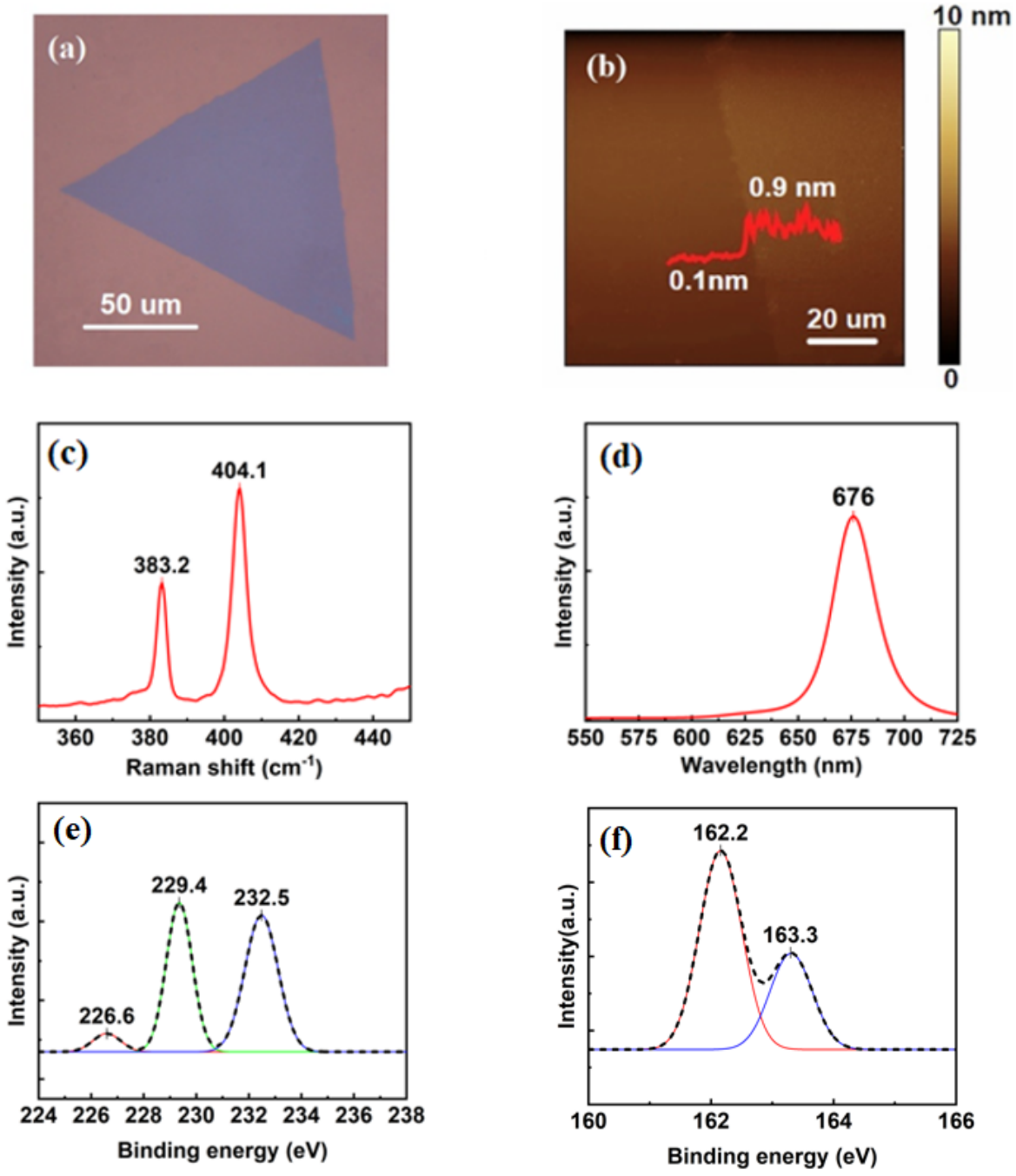

Figure 64 – Characterization of MoS_2 on SiO_2/Si substrate by CVD method. (a) Optical image. (b) Surface topography by AFM in tapping mode. (c) Raman spectrum and (d) PL spectrum excited by 532 nm laser. (e) Mo 3d, S 2s orbitals and (f) S 2p orbitals demonstrated by XPS spectra.

As can be seen in Figure 64c, there are two characteristic peaks in the Raman spectrum: 383.2 cm^{-1} peak (E_{2g} mode) and 404.1 cm^{-1} peak (A_{1g} mode) [208], [222]. The frequency difference between E_{2g} and A_{1g} modes is calculated to be 20.9 cm^{-1} in this study, corresponding to monolayer MoS_2 [12], [223], [224]. Besides, the obvious emission peak at 676 nm in the PL spectrum (Figure 64d) is also indicative of the single-layer nature of the as-fabricated MoS_2 [165], [225].

XPS was performed with Al Kα source to determine the chemical composition of the film. Considering that the TMDs nanoflakes characterized in the project are very thin (2D materials), only flood gun was used to clean the sample surface prior to the operation of X-ray gun. Importantly, the carbon 1s spectra were scanned for the calibration of results, and all the C 1s orbitals are demonstrated in appendix. It can be noted from Figure 64e that the Mo 3d peaks at 232.5 and 229.4 eV are the $3d_{3/2}$ and $3d_{5/2}$ orbitals of MoS_2, respectively; the peak at 226.6 eV belongs to the S 2s orbital. Figure 64f shows the S 2p peaks at 163.3 and 162.1eV corresponding to the $2p_{1/2}$ and $2p_{3/2}$ doublets of S [226]. All these binding energies are in agreement with the reported values for MoS_2 crystal [227], [228], and the atomic ratio of Mo and S is close to the stoichiometric 1:2.

4.3.2 WS_2

Prior to the reaction, SiO_2/Si substrates were loaded on a boat containing 30 mg WO_3 (Alfa Aescar 99.9995%) and 10 mg NaCl (Alfa Aescar 99.9995%, its addition can reduce the melting point of WO_3 to facilitate the vaporization [168]), and then placed to the tube center. Afterward, another boat with 150 mg sulfur (Alfa Aescar 99.9995%) was placed at the upstream. After a 10-minute purge with 300 sccm Ar gas (BOC, 99.999% pure with additional purifications), the flow rate was decreased to 30 sccm, and the furnace was subsequently programmed to 900 ℃ to heat substrates and vaporize WO_3. In the meantime, sulfur was heated up to 200 ℃ by the heating tape so its vapor could be transported to the substrate. After 15 minutes of deposition, the furnace and heating tape were switched off for natural cooling-down. The temperature profile of the whole process is plotted in Figure 65.

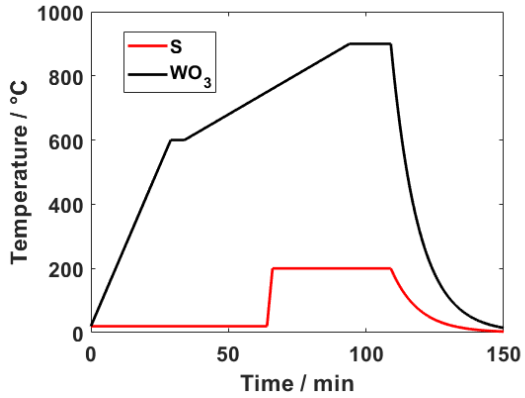

Figure 65 – Temperature profile of WO_3 (black line) and S (red line) for the growth of WS_2.

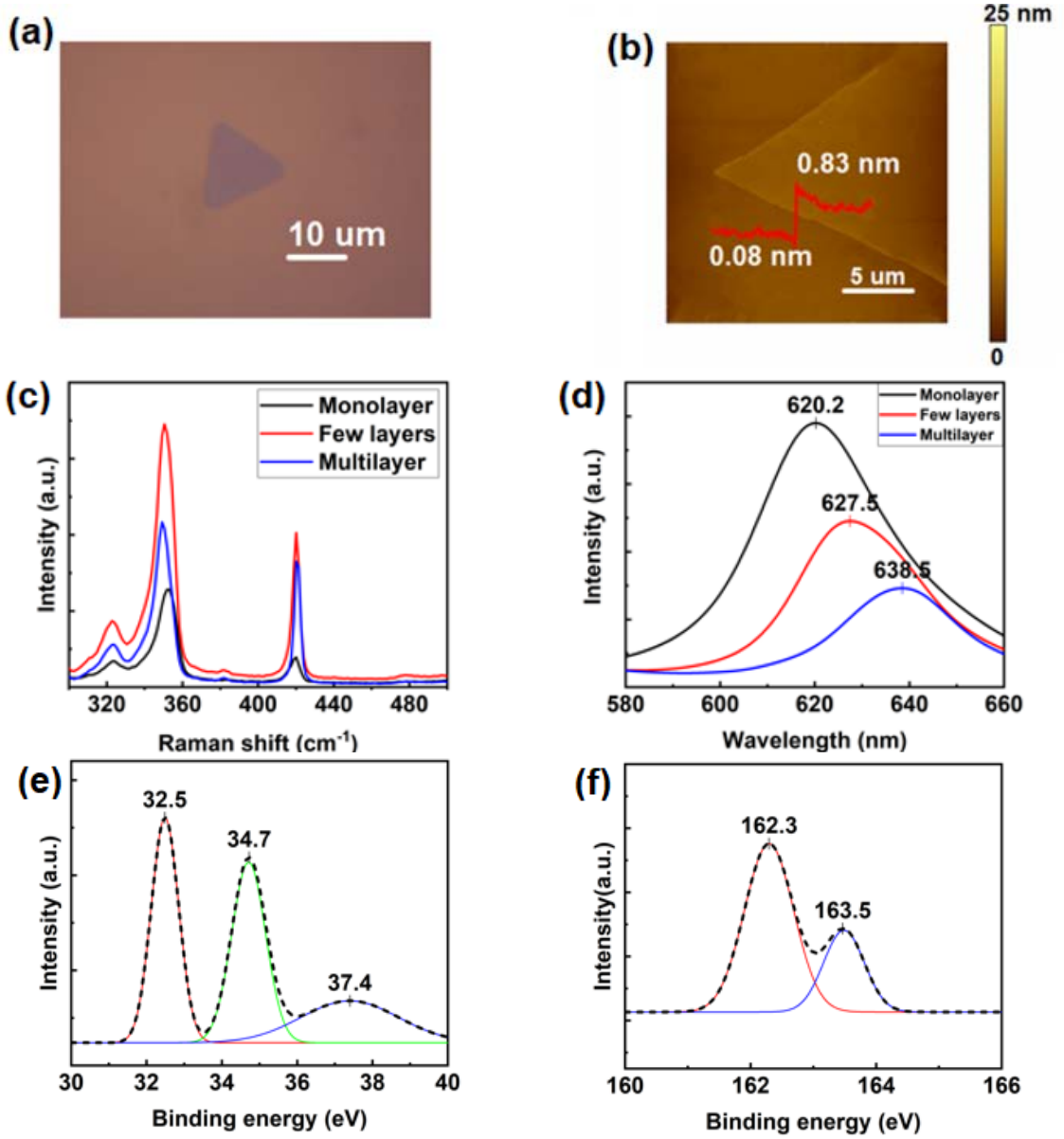

Figure 66 – Characterization of WS_2 nanoflakes synthesized on SiO_2/Si substrate by CVD method. (a) Optical image and (b) Surface topographic map of a monolayer. (c) Raman spectrum and (d) PL spectrum with 532 nm laser excitation. XPS spectra of (e) W 4f and (f) S 2p orbitals of a monolayer.

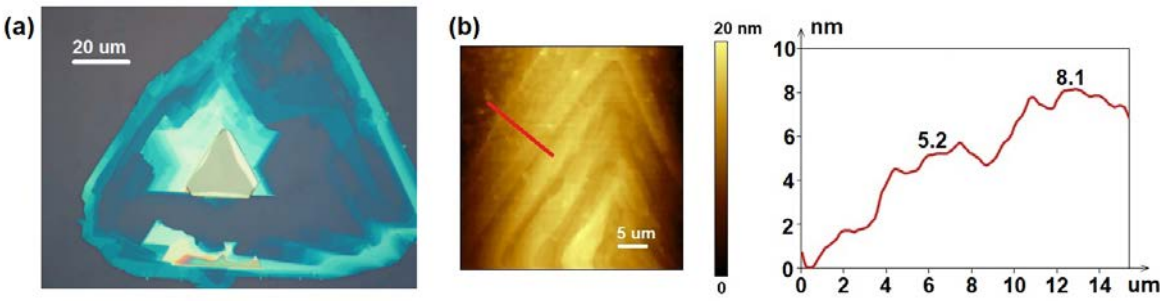

Figure 67 – (a) Optical image and (b) Surface topography of few layers (5 layers) and multilayers (9 layers) WS_2.

The WS_2 nanoflakes deposited on SiO_2/Si substrate by CVD method were observed by optical microscopy, and their lateral size can reach up to ~100 µm as shown in Figure 66a and Figure 67a. Besides, the number of layers can be generally estimated via the variation in the color of nanoflakes on the substrate: while WS_2 monolayer is almost transparent and shows a dark cyan color, a multilayer is brighter and yellow color can be seen for much thicker flakes.

To specify the exact layer number of different areas, surface topographies have been mapped by tapping-mode AFM, and the thickness is ~0.75 nm (Figure 66b), which agrees with the reported thickness of monolayer WS_2 [229]–[231]. Apart from it, the surface topographic image of few layers and multilayers in Figure 67b shows that their thicknesses are ~4.2 and ~7.1 nm corresponding to 5 layers and 9 layers, respectively. Besides, Raman spectrum was measured with 532 nm laser excitation for further characterization. As displayed in Figure 66c, the 352.4 cm^{-1} 2LA and 419.6 cm^{-1} A_{1g} peaks are obvious for monolayer, while a slight red shift of 2LA and a blue shift of A_{1g} mode were observed with the increase of layer number [140], [232]. In addition, PL spectrum in Figure 66d shows an obvious shift of emission peak from 620.2 to 638.5 nm, indicating the layer number of WS_2 nanoflakes.

According to the XPS spectra of monolayer WS_2 nanoflakes in Figure 66e and f, the W 4f peaks at 34.7 and 32.5 eV are assigned to the $4f_{5/2}$ and $4f_{7/2}$ orbitals of WS_2, respectively [233], [234]; the W 5p core level at 37.6 eV suggests the existence of W^{6+}, likely residual WO_3 on the as-deposited sample [235]. 163.5 and 162.3 eV peaks belong to the S doublets: $2p_{1/2}$ and $2p_{3/2}$ [233]. All the binding energies are indicative of WS_2 crystal, and the atomic ratio of S and W is ~2:1. Additionally, the XPS spectra of a few layers and multilayers are shown in Figure 68 and Figure 69.

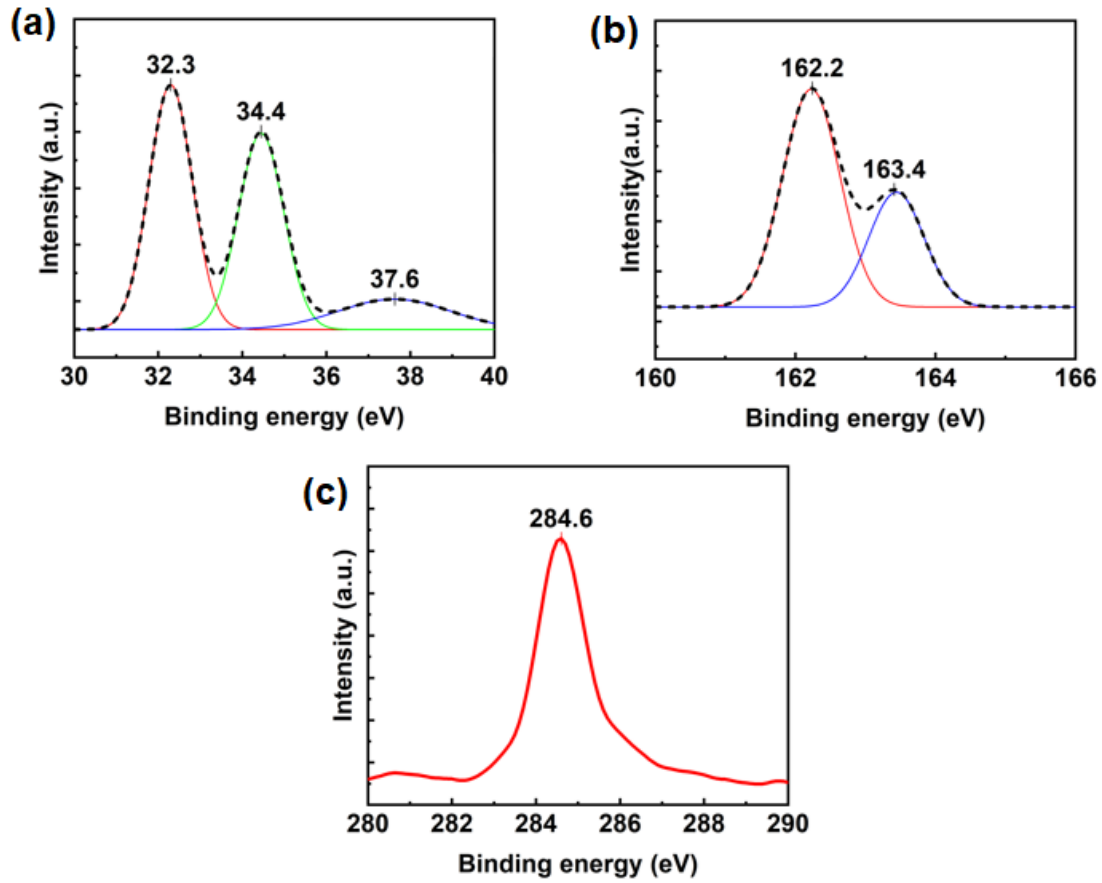

Figure 68 – XPS spectra of (a) W 4f, (b) S 2p and (c) C 1s orbitals of few layers (5 layers).

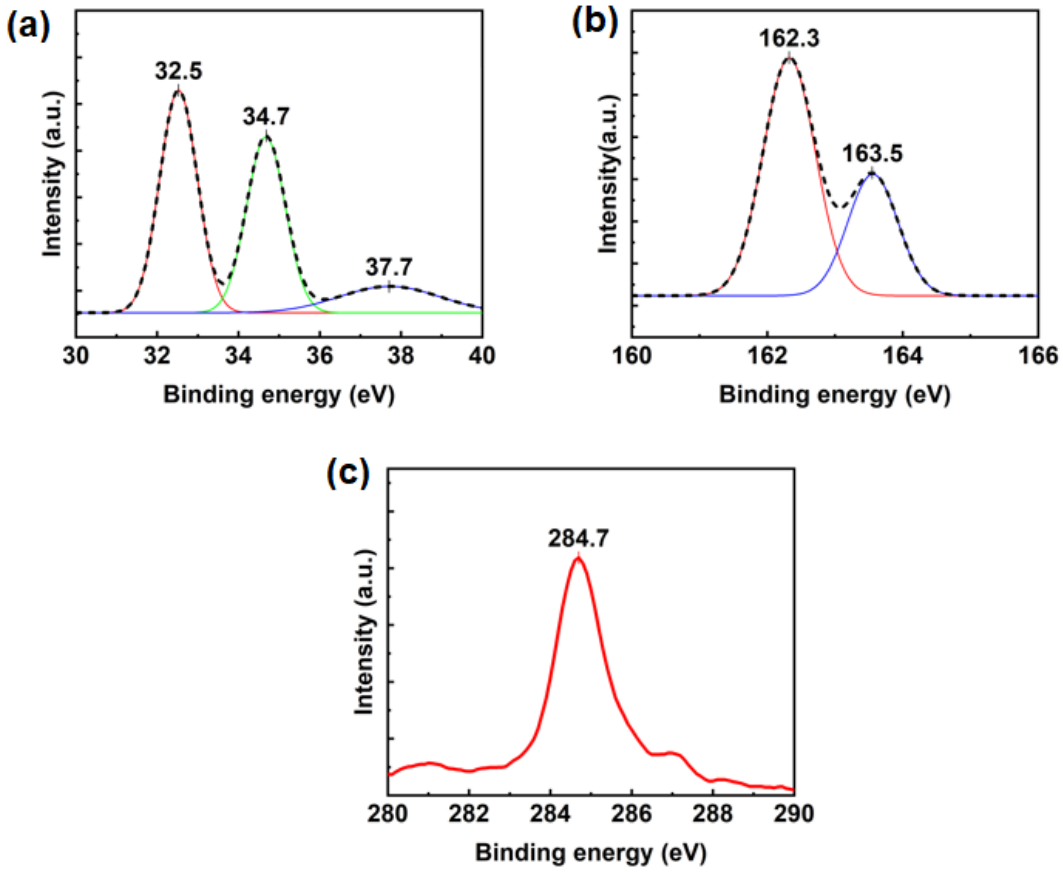

Figure 69 – XPS spectra of (a) W 4f, (b) S 2p and (c) C 1s orbitals of multilayers (9 layers).

4.3.3 $MoSe_2$

All the $MoSe_2$ nanoflakes used in this project were produced in a quartz tube (1.2-inch diameter) by a chemical vapor deposition approach under atmospheric pressure. MoO_3 (Alfa Aescar 99.9995%) and Se (Alfa Aescar 99.9995%) were selected as the sources of Mo and Se, respectively; Si wafer coated with 300 nm SiO_2 was utilized as the substrate for the growth of $MoSe_2$; Ar gas mixed with 6% H_2 (BOC, 99.999% pure with additional purifications) was employed as the carrier gas. After the precursors and substrates were in place, the tube was purged with 300 sccm gas flow for 10 minutes, and the gas flow rate was set to 30 sccm for the synthesis of $MoSe_2$. 10 mg MoO_3 as well as the SiO_2/Si was heated to 750 ℃ while the temperature of 100 mg Se was targeted at 300 ℃. After a 15-minute deposition, the whole heating system was shut down to cool off naturally. The temperature profile of the entire process is plotted in Figure 70.

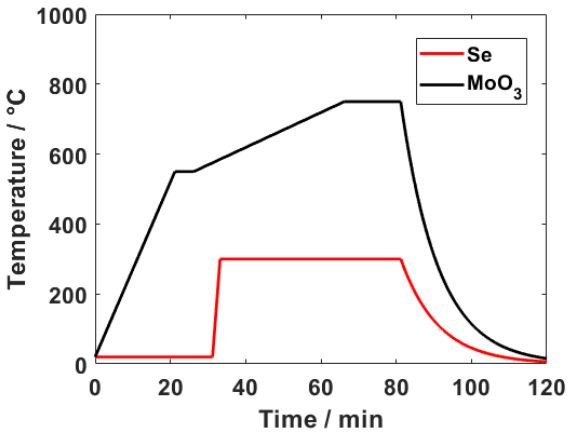

Figure 70 – Temperature profile of MoO_3 (black line) and Se (red line) for the growth of $MoSe_2$.

As the optical image displayed in Figure 71a, the lateral size of the chemical vapor deposited $MoSe_2$ nanoflake is ~10 μm, and the thickness measured by tapping-mode AFM is ~0.78 nm (Figure 71b), which confirms the monolayer nature of $MoSe_2$ nanofilm [157], [236]. For further characterization, Raman spectroscopy was performed and the peaks at 239.8 cm^{-1} and 288.1 cm^{-1} in the Raman spectrum (Figure 71c) are assigned to A_{1g} and E_{2g} modes, respectively [237], [238]; the 794.1 nm peak in the PL spectrum (Figure 71d) belongs to single-layer $MoSe_2$ [239], [240]. As evident from the XPS spectra in Figure 71e and f, the 232 and 228.8 eV peaks correspond to the Mo $3d_{3/2}$ and $3d_{5/2}$ orbitals, respectively; the Se 3d peaks at 54.9 and 54 eV originate from the $3d_{3/2}$ and $3d_{5/2}$ doublets [156], [241]. An atomic ratio of 1:2.05 is extracted for Mo and Se under this circumstance.

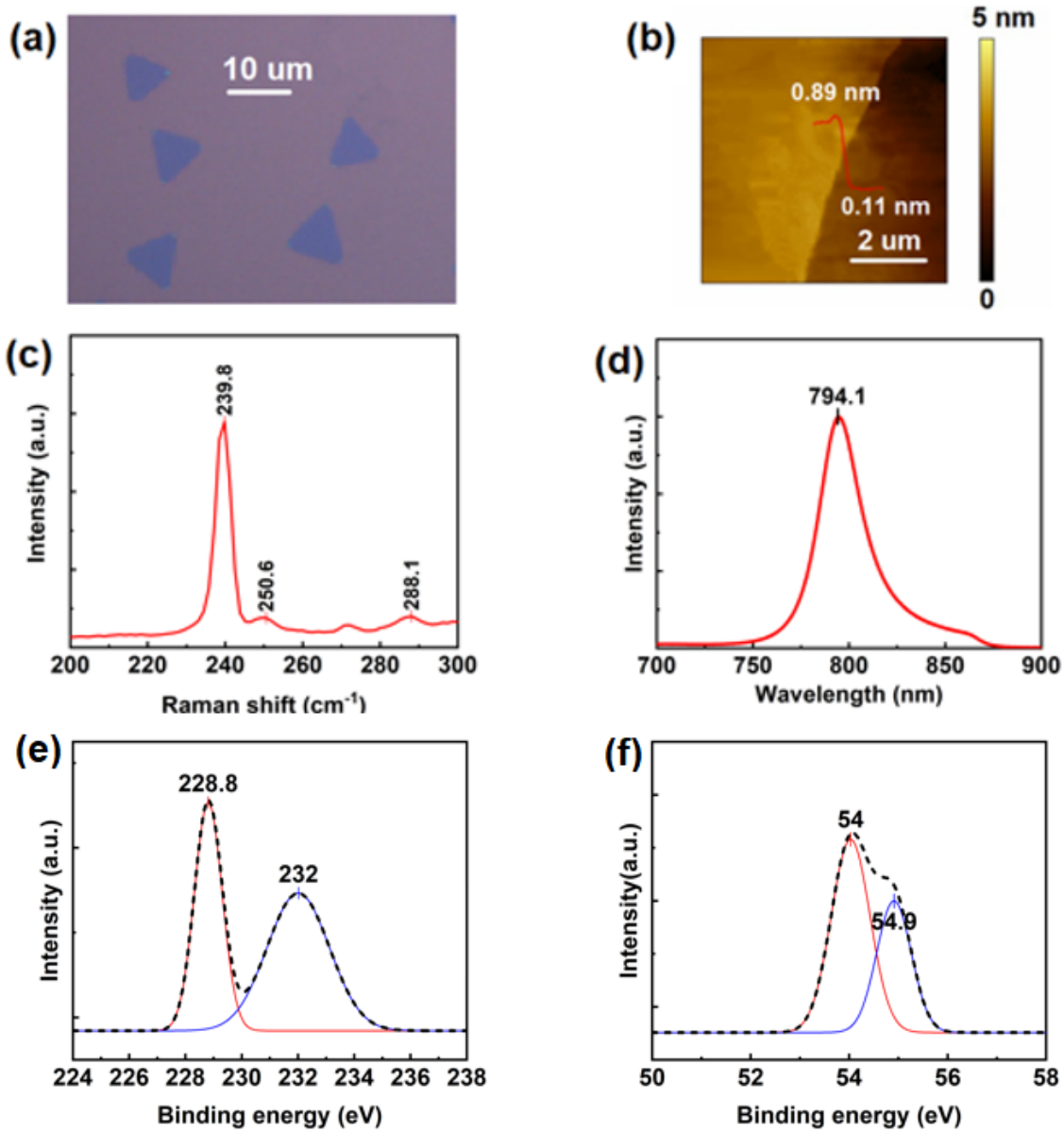

Figure 71 – Characterization of chemical vapor deposited $MoSe_2$ nanoflakes on SiO_2/Si substrate. (a) Optical image and (b) Surface topographic map of a monolayer. (c) Raman spectrum and (d) PL spectrum with 633 nm laser excitation. XPS spectra of (e) Mo 3d and (f) Se 3d orbitals.

4.3.4 WSe_2

The cleaned SiO_2/Si substrates and 30 mg WO_3 precursor (Alfa Aescar 99.9995%) were placed at the tube center, and 150 mg selenium (Alfa Aescar 99.9995%) was loaded at the upstream and surrounded by the heating tape. After purging the tube system for 10 minutes with 300 sccm Ar gas mixed with 6% H_2 (BOC, 99.999% pure with additional purifications), the flow rate was reduced to 30 sccm and the furnace system was programmed for the growth of WSe_2. The WO_3 was targeted to 850 ℃ while the Se was heated to 300 ℃. After a

deposition for 15 minutes, the system was shut down to cool down naturally. The temperature profile of this process is displayed in Figure 72.

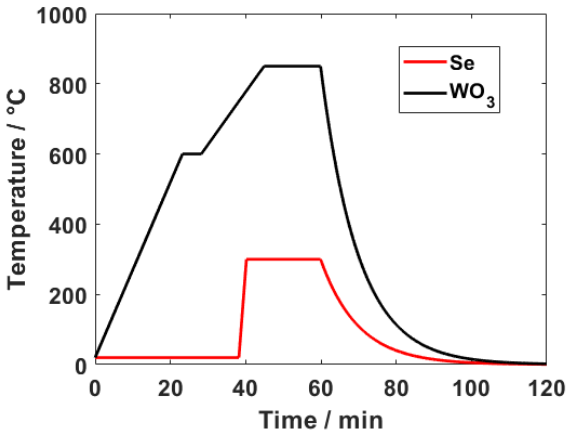

Figure 72 – Temperature profile of WO_3 (black line) and Se (red line) for the growth of WSe_2.

The lateral size of chemical vapor deposited triangular WSe_2 nanofilms is ~20 μm as displayed in Figure 73a, and a thickness of ~0.76 nm was measured by tapping mode AFM (Figure 73b), which confirms that the synthesized WSe_2 nanofilm is indeed monolayer [242], [243]. Two Raman peaks at 249.2 and 258.9 cm^{-1} belong to the E_{2g} and A_{1g} modes of WSe_2, respectively. As the van der Waals force can induce the interactions between neighboring layers, a peak at ~308 cm^{-1} can be detected for multi-layered WSe_2, and this special peak has been used to confirm the single-layer nature of WSe_2 instead of the frequency difference between E_{2g} and A_{1g} modes [242], [244]. Apparently, there is no B_{2g}^{1} peak at ~308 cm^{-1} as demonstrated by the inset of Figure 73c, so the as-grown WSe_2 is only one layer. Additionally, the emission peak at 752.5 nm also indicates the single-layer nature of the WSe_2 sample (Figure 73d) [242]. As for the XPS spectra in Figure 73e and f, the peaks at 32.5 and 34.7 eV are the W $4f_{7/2}$ and W $4f_{5/2}$ doublets; the weak peak at 37.4 eV may result from the WO_3 residues on the sample surface; the 54.8 and 55.7 eV peaks are ascribed to the Se $3d_{5/2}$ and Se $3d_{3/2}$ orbits; the atomic ratio of W and Se was calculated to be 1:1.98, which is close to the stoichiometric 1:2 [245].

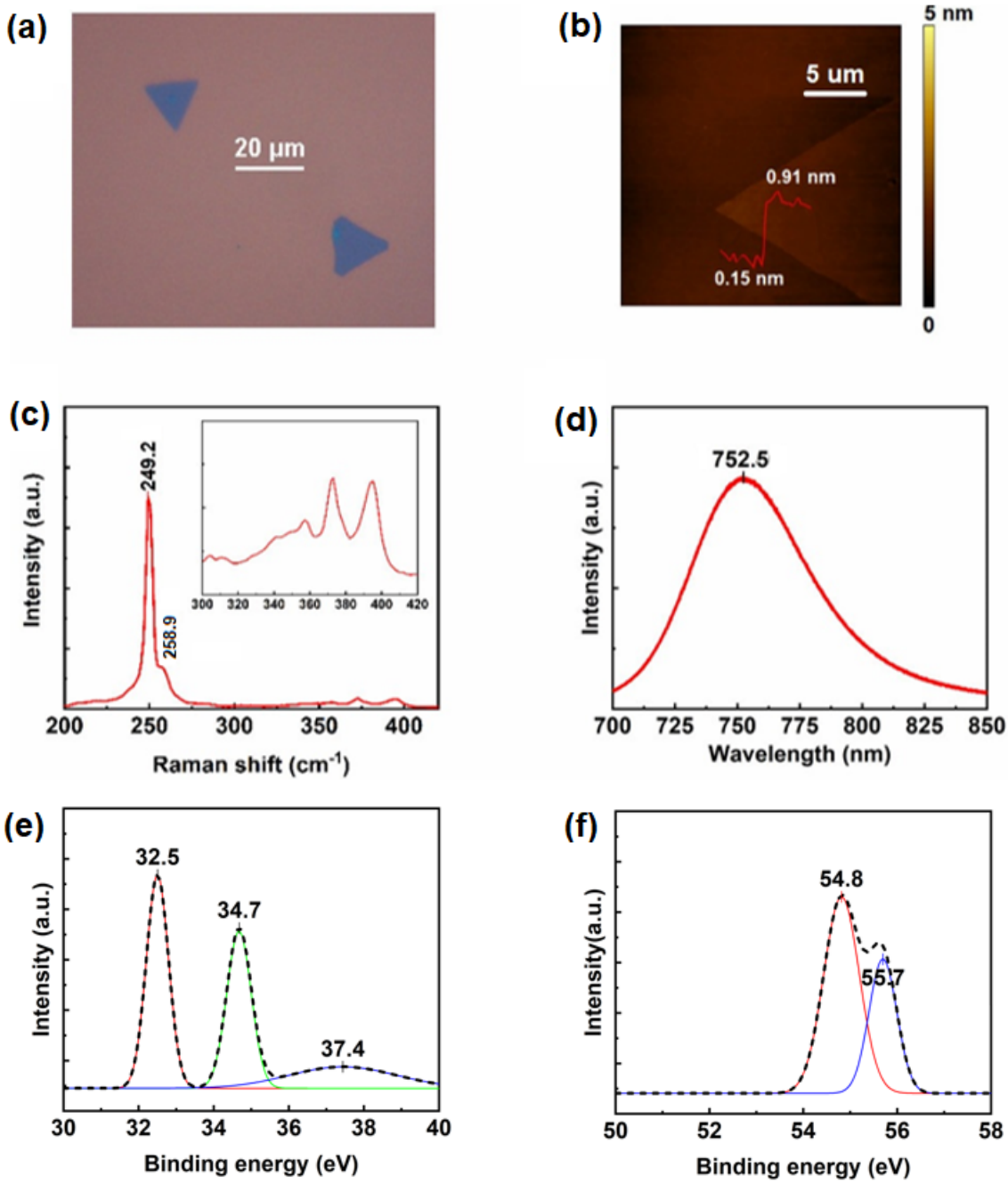

Figure 73 – Characterization of WSe_2 nanoflakes synthesized on SiO_2/Si substrate by CVD method. (a) Optical image and (b) Surface topographic map of a monolayer. (c) Raman spectrum and (d) PL spectrum with 532 nm laser excitation. XPS spectra of (e) W 4f and (f) Se 3d orbitals of a monolayer.

4.4 Summary

Prior to all the deposition operation, the temperature profile within the tube furnace system was calibrated by a K-type thermocouple, so the temperatures of substrate and precursors can be tuned by placing them at specific locations. Subsequently, the effects of precursors amount (different and the same precursors ratios, deposition locations), gas flow, precursors

temperature and the pre-treatment by piranha solution, were investigated to facilitate the preparations of TMDs via CVD method. Here are some tips for the successful synthesis:

- Precise amount of precursors should be used so their concentrations are suitable for the preparation of desirable materials, otherwise the precursors may not be fully turned into the products and defects can show up at the same time.
- Proper carrier gas should be introduced for the reaction, since it can speed up the deposition to grow unfavorable microstructures. It should be pointed out that the growth of $MoSe_2$ and WSe_2 requires the mixture of H_2 to meet the thermodynamic condition. Additionally, the gas flow rate needs to be optimized since it can affect the concentration of precursors within the tube, thereby having an influence on the synthesized products.
- As the temperature can control the amount of vaporized precursors, it is crucial to optimize this parameter to adjust the concentration of precursors inside the reaction system, only in this way can favorable products be obtained.
- A cleaner substrate surface can be achieved by the use of piranha solution, and it can facilitate the growth of desirable products.

Table 2 – Experimental setups for the optimized MoS_2, WS_2, $MoSe_2$, and WSe_2.

Materials	**Precursors**	**Gas inlet**	**Flow rate**	**Temperature**
MoS_2	10 mg MoO_3, 100 mg S	Ar	30 sccm	MoO_3: 700 ℃, S: 200 ℃
WS_2	30 mg WO_3, 150 mg S	Ar		WO_3: 900 ℃, S: 200 ℃
$MoSe_2$	10 mg MoO_3, 100 mg Se	6% H_2/Ar		MoO_3: 750 ℃, Se: 300 ℃
WSe_2	30 mg WO_3, 150 mg Se	6% H_2/Ar		WO_3: 850 ℃, Se: 300 ℃

Table 3 – Characterizations of the optimized MoS_2, WS_2, $MoSe_2$, and WSe_2.

Materials	**Size**	**Thickness**	**Raman peaks**	**PL peaks**	**Atomic ratio**
MoS_2	>120 μm	~0.8 nm	383.2 and 404.1 cm^{-1}	676 nm	Mo:S = ~1:2
WS_2 (1 layer)	>120 μm	~0.75 nm	352.4 and 419.6 cm^{-1}	620.2 nm	W:S = ~1:2
WS_2 (5 layers)		~4.2 nm	350.5 and 420.1 cm^{-1}	627.5 nm	
WS_2 (9 layers)		~7.1 nm	349.2 and 420.2 cm^{-1}	638.5 nm	
$MoSe_2$	~10 μm	~0.78 nm	239.8 and 288.1 cm^{-1}	794.1 nm	Mo:Se = ~1:2
WSe_2	~20 μm	~0.76 nm	249.2 and 258.9 cm^{-1}	752.6 nm	W:Se = ~1:2

Based on the published growth recipes and abovementioned investigation on various parameters for CVD process, optimized transition metal dichalcogenides including MoS_2, WS_2, $MoSe_2$, and WSe_2 have been synthesized in the same CVD system, whose experimental setups are listed in Table 2, and their high-quality have been confirmed by optical microscope, AFM, Raman spectroscopy as well as XPS, as summarized in Table 3. It can be obviously seen that the sizes of $MoSe_2$ and WSe_2 are smaller than those of MoS_2 and WS_2, which results from the limited control of H_2 gas inlet. The accuracy of gas controller utilized in this project cannot guarantee a stable flow rate below 30 sccm, and the H_2 gas is already mixed with Ar to realize a 6% proportion. Based on the publications for the chemical vapor deposited $MoSe_2$ and WSe_2, a smaller H_2 flow rate is favored for their growth but it cannot be realized via the CVD system employed in this project. However, these materials are still large enough for the characterization of triboelectrification, since the measurement operated by AFM and KFM is just within an area of $5\times5\ \mu m^2$.

Chapter 5 Triboelectric properties of synthesized transition metal dichalcogenides

High-quality 2D TMDs including MoS_2, WS_2, $MoSe_2$, and WSe_2 have been successfully synthesized and characterized, the next task is to evaluate their triboelectric performance via AFM and KFM, so the mechanism behind can be unveiled.

5.1 Initiation and detection of tribo-charges

To unveil the mechanism of triboelectrification, the surface potential before and after triboelectric operation was monitored by combining contact-mode AFM and KFM, as illustrated in Figure 74a. Contact-mode AFM was operated to rub a 1×1 μm^2 square area of the TMD samples (MoS_2, WS_2, $MoSe_2$, and WSe_2) by a conducting tip under a normal force of 25 nN, with the underlying Si grounded. KFM mode was carried out to image the tip-sample contact potential difference of a larger area (5×5 μm^2) with the rubbed area centered. As evident in Figure 74c, the MoS_2 surface is equipotential except for random fluctuations (probably induced by the absorbed charges from air or contamination) before triboelectrification. After rubbing, the topographic change is undetectable (Figure 74b) but the distinction in the surface potential image is obvious between the rubbed and unrubbed regions (Figure 74d). The cross-section profile in Figure 74d demonstrates that the surface potential of the rubbed section in the center is ~20 mV lower than that of the other region.

During the surface potential measurements, an AC voltage and a DC bias are applied between the tip and sample surface. The electrostatic forces acting on the conductive tip can be detected by a lock-in technique to monitor its oscillating amplitude within the system. The amplitude signal comprises the DC bias as well as the work function difference between the tip and sample, and the contact potential difference V_{CPD} is canceled by the DC bias via a feedback circuit [246], so their relationship can be described as equation (5-1):

$$V_{CPD} = \frac{1}{e}\left(\varphi_{tip} - \varphi_{sample}\right) \tag{5-1}$$

where φ_{tip} and φ_{sample} represent the work functions of the tip and sample, respectively; e is the electronic charge.

As a result, the contact potential difference between the rubbed and surrounding intact areas, ΔV_{CPD}, can be computed as equation (5-2):

$$\Delta V_{CPD} = V_{CPD}(\text{rubbed}) - V_{CPD}(\text{unrubbed})$$

$$= \frac{1}{e}\left(\varphi_{tip} - \varphi_{rubbed}\right) - \frac{1}{e}\left(\varphi_{tip} - \varphi_{unrubbed}\right)$$

$$= \frac{1}{e}\left(\varphi_{unrubbed} - \varphi_{rubbed}\right) \quad (5\text{-}2)$$

where φ_{rubbed} and $\varphi_{unrubbed}$ represent the work functions of the rubbed and unrubbed areas of the sample surface, respectively.

As the Fermi levels of two materials are aligned when brought into contact, their work functions (the minimum energy needed to remove an electron from Fermi level to the vacuum immediately outside the solid surface) would be changed correspondingly. In this case, a fraction of negative charges were transferred to the sample surface via triboelectrification, which lowered the surface potential of the central region.

The same experiments have also been conducted for WS_2, $MoSe_2$ as well as WSe_2, whose surface topographic and potential maps before and after triboelectrification are illustrated in Figure 75, Figure 76, and Figure 77, respectively. It is noticed that the electrons are transferred from the samples to the AFM tip during triboelectrification in the case of WS_2, $MoSe_2$ and WSe_2, whereas MoS_2 exhibits an opposite transfer direction, and the surface potential differences in reference to the unrubbed area are different for all of them, as summarized in Table 4. The reason behind this phenomenon is the diverse work functions of these four TMDs materials (Table 4). For the Pt-coated conductive tip used in the project, few nanometers thick titanium (Ti) layer is placed between Si and Pt to improve the adhesion, and the silicon tip itself is doped with antinomy (Sb) though the influence on KFM is minor. Provided that the work functions of Pt, Ti, Si and Sb are 5.65, 4.33, 4.85 and 4.55 eV, respectively [247], the work function of the tip is the contributions from all of these materials and a value of ~5.1 eV is obtained according to the measured surface potential difference data. Based on the working principles of KFM described in this section, especially the equations (5-1) and (5-2), the results match well for all of these four TMDs.

Table 4 – Surface potential differences compared to the unrubbed area for TMDs monolayers.

Materials	MoS_2	WS_2	$MoSe_2$	WSe_2
Potential difference	~20 mV lower	~0.5 V higher	~0.5 V higher	~0.9 V higher
Work functions	5.15 eV [248]	4.6 eV [249]	4.57 eV [250]	4.21 eV [249]

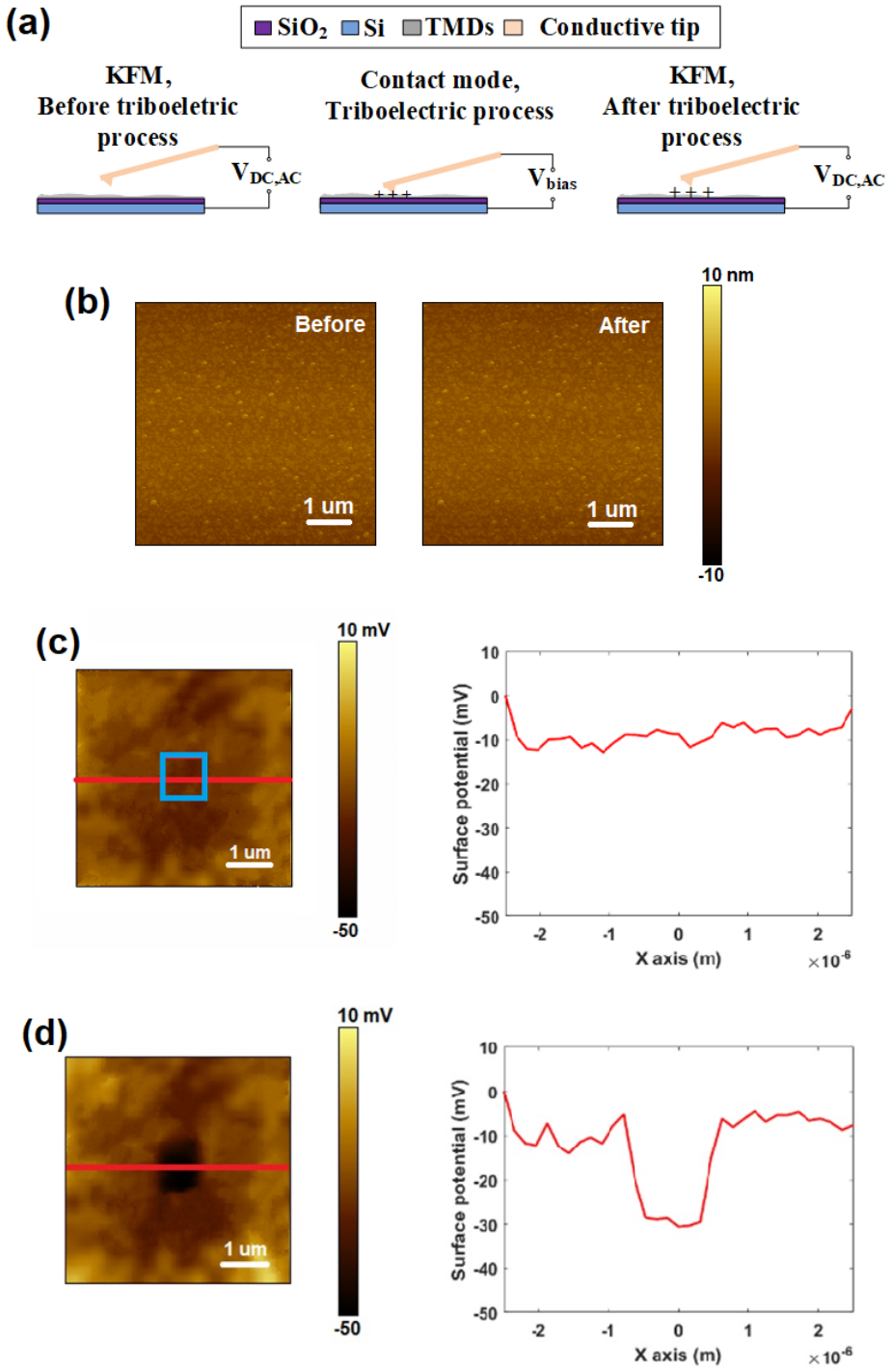

Figure 74 – Schematic illustration of triboelectric experiments of MoS_2 based on AFM and KFM. (a) Surface potential characterizations in KFM mode before and after charge generation by triboelectrification with contact-mode AFM. (b) Surface topography images before and after triboelectric charge generation. (c) Surface potential image and cross-section profile of the potential distribution along the red line before the rubbing process (the rubbed area is marked with the blue square). (d) Surface potential image and cross-section profile of the potential distribution along the red line after the rubbing process.

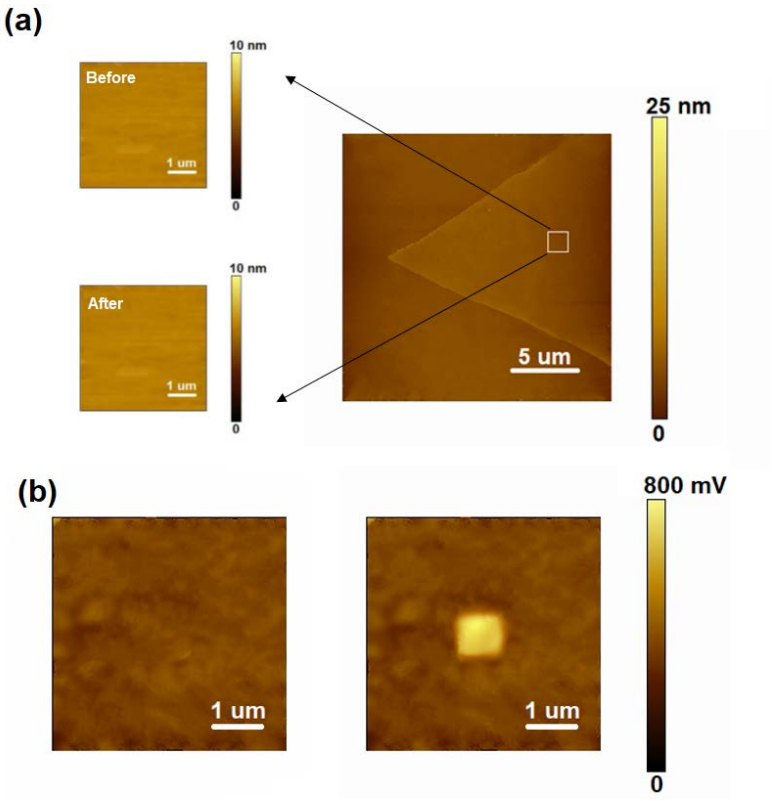

Figure 75 – Triboelectric characterization of WS_2. (a) Surface topographic images and (b) surface potential maps of WS_2 monolayer before and after triboelectrification.

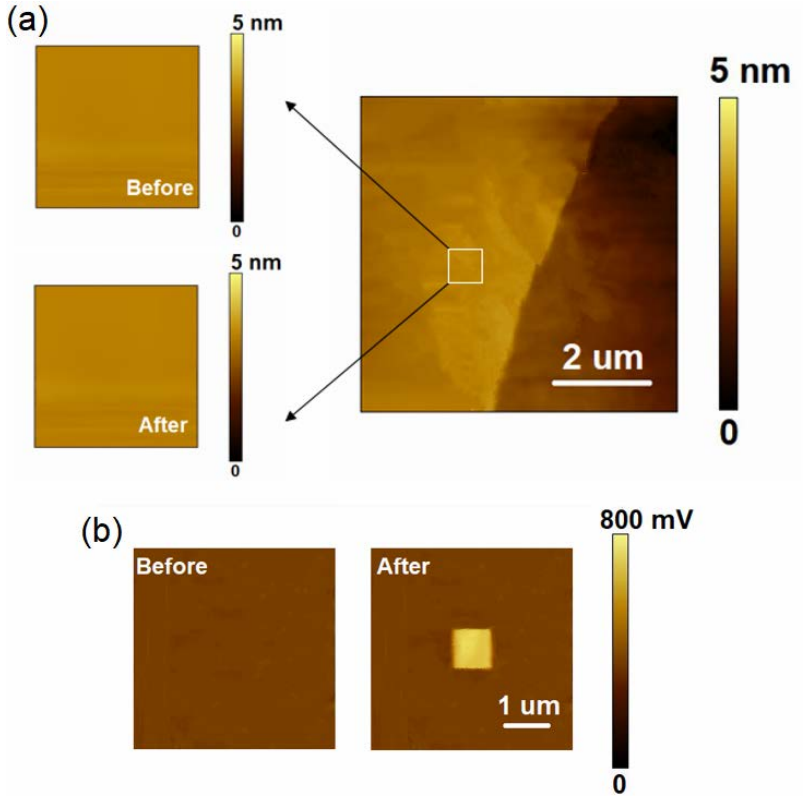

Figure 76 – Triboelectric characterization of $MoSe_2$. (a) Surface topographic images and (b) surface potential maps of $MoSe_2$ monolayer before and after triboelectrification.

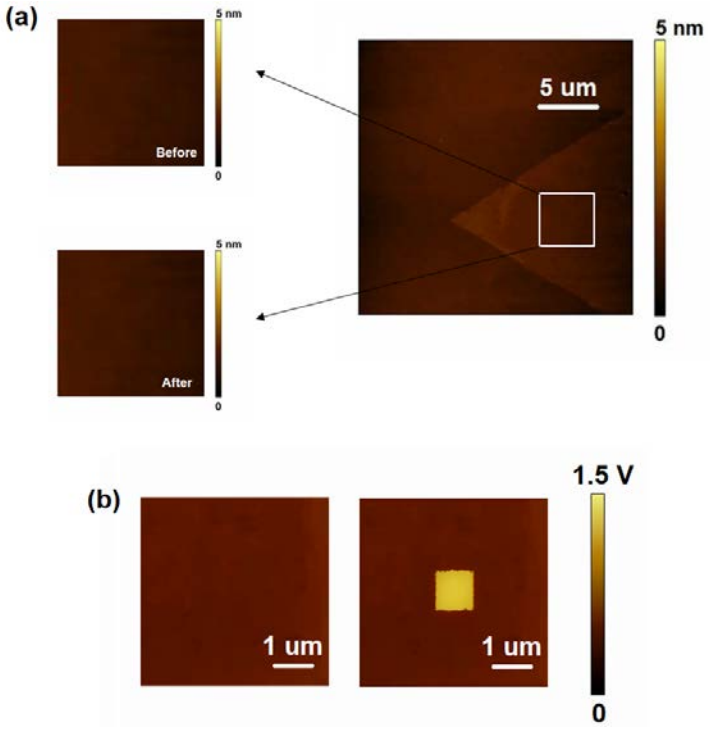

Figure 77 – Triboelectric characterization of WSe_2. (a) Surface topographic images and (b) surface potential maps of WSe_2 monolayer before and after triboelectrification.

5.2 Diffusion of tribo-charges

To evaluate the lifetime of tribo-charges, Figure 78a and b show the surface potential maps and their cross-section profiles of single-layer MoS_2 (corresponding to the stripy region confined by the two red lines in Figure 78a, the surface potentials were averaged to reduce the influence of random fluctuations) after triboelectrification for up to 48 hours. It is noteworthy that the potential difference remains detectable even after two days. As charges can be kept for a long time only on insulating materials, such variation cannot originate from the charges on MoS_2. Here we suggest that some triboelectric charges generated by triboelectrification tunnel through the single-layer MoS_2 and localize on the insulator underneath, as the reported results for graphene in [32].

Additional experiments have also been conducted with monolayer MoS_2 on other substrates, consisting of conductive gold as well as insulators like sapphire and polyimide (Figure 79, their preparations and characterizations were provided in Appendix). Similar to the case of SiO_2, triboelectric charges are stored at the air-insulator interface after tunneling through MoS_2 for sapphire and polyimide. However, there are no detectable localized charges in the rubbed section with gold as the substrate. As the surface potential of the whole area is slightly

lower after triboelectrification, it is suggested that the transferred charges spread across the whole MoS_2 or gold substrate due to the excellent conductivity of gold.

The surface potential differences of the rubbed versus unrubbed regions on sapphire and polyimide decreased by ~10 mV after 12 hours, but in the case of SiO_2 substrate, ~5 mV decrease was observed (Figure 78c), which indicates better preservation of tunneling triboelectric charges. Therefore, we used MoS_2 monolayers on SiO_2 substrate for further investigation.

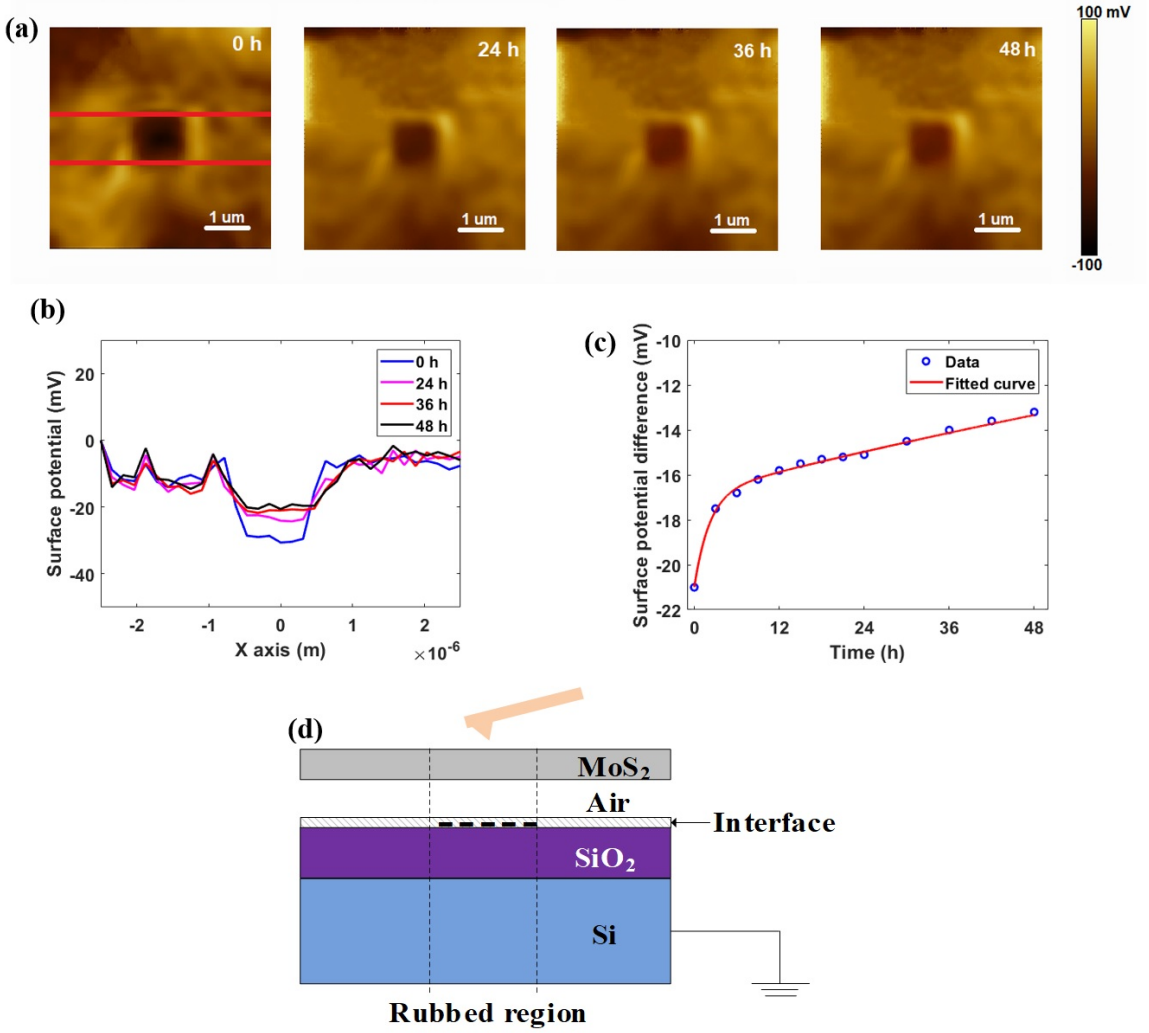

Figure 78 – Diffusion of triboelectric charges on MoS_2 over time. (a) Surface potential images after 0, 24, 36 and 48 hours. (b) Cross-section profiles between the lines in a. (c) The surface potential difference as a function of time and its fitted curve. (d) The schematic diagram for tunneling triboelectrification.

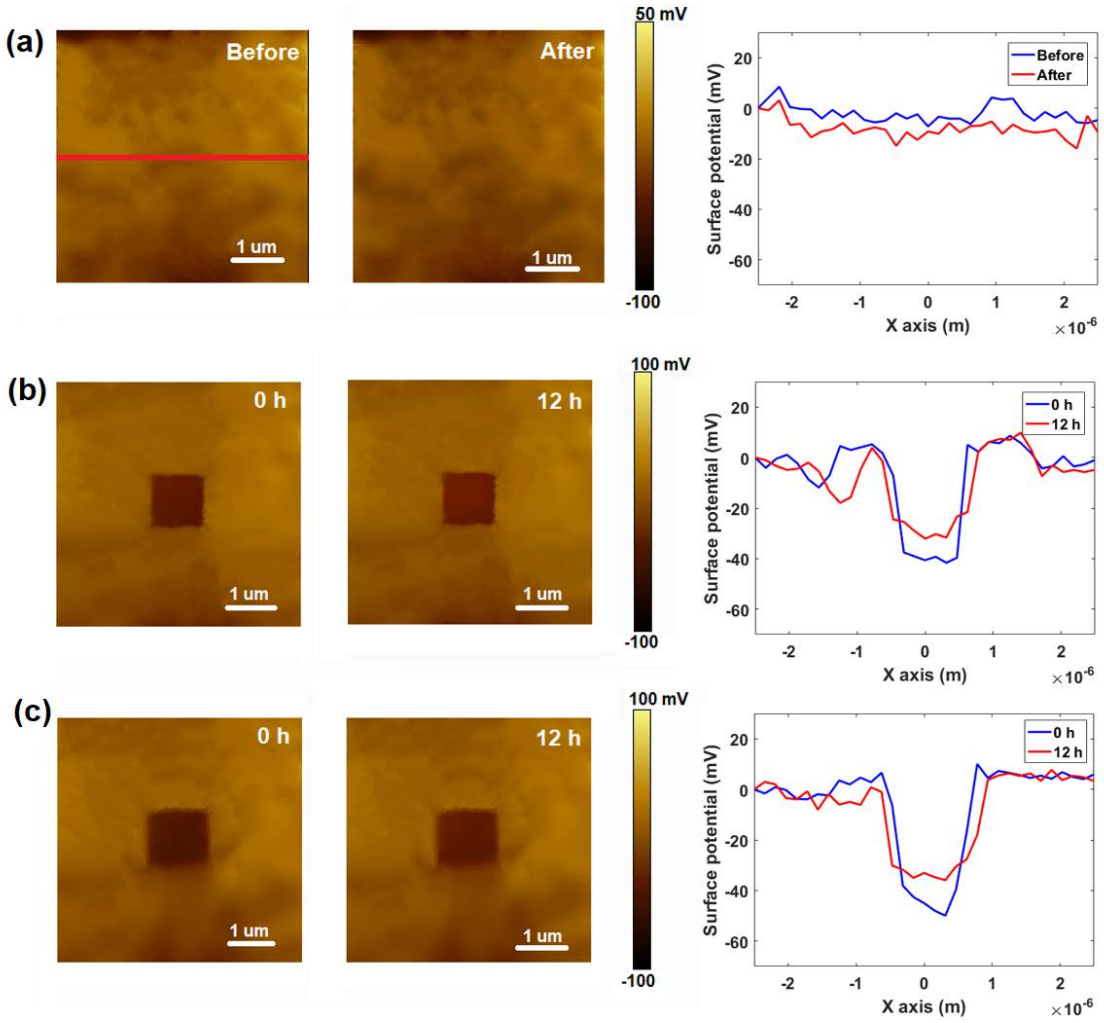

Figure 79 – KFM images and Cross-section profile of MoS_2 monolayer on (a) gold, (b) sapphire and (c) polyimide substrates before and after triboelectrification.

As charges cannot diffuse through insulators like air and SiO_2, these tunneling tribo-charges are localized on the air-SiO_2 interface, and attract opposite charges from MoS_2 and/or Si underneath SiO_2, as the schematic diagram shown in Figure 78d. Considering the 0.3 nm thickness of S-Mo-S sandwich structure of MoS_2 single-layer [251]–[254], the air gap between the MoS_2 monolayer and SiO_2 substrate is estimated as 0.5 nm, which is far smaller than that of the SiO_2 (300 nm). Under this circumstance, the capacitance of air is even larger, and almost all the opposite charges are donated by MoS_2 and accumulate across the air gap, while the stored charges on SiO_2 layer are almost unvaried. Therefore, the measured surface potential difference across MoS_2 is almost identical to the voltage change through the air gap.

After the triboelectric process, there should be no detectable current flow in MoS_2 once the equilibrium is reached, therefore, the discharge will only originate from leakage currents. As the diffusion of charges happens to both air and SiO_2, two voltage magnitudes (V_1, V_2) and

two-time constants (τ_1, τ_2) are developed. Figure 78c shows the relationship between the surface potential difference (ΔV) with time and its fitted function is depicted below:

$$\Delta V = V_1 \times e^{\frac{-t}{\tau_1}} + V_2 \times e^{\frac{-t}{\tau_2}} \quad (5\text{-}3)$$

Table 5 – Parameters of fitted tribo-charge diffusion function for MoS_2 monolayer.

Parameters	V_1/mV	V_2/mV	τ_1/h	τ_2/h
Single-layer MoS_2	-4.2	-16.8	2.17	207.8

All the parameters are listed in Table 5. It is obvious that apart from a term with a small magnitude (V_1) and a short time constant (τ_1), the other one has a larger initial amplitude (V_2) and time constant (τ_2), which is significantly longer than the ~1 h decay time of tribo-charges on SiO_2 with an identical thickness of 300 nm [30]. The dominant term is attributed to the small-area air gap: the initial amplitude is greater since most of the charges are attracted from MoS_2 and trapped across the air gap; the longer time constant originates from the great insulating nature of air and the protection of MoS_2 film.

Additionally, the diffusion of tribo-charges has also been characterized for WS_2, $MoSe_2$ and WSe_2 monolayers, and the relationship between the surface potential differences with time are demonstrated in Figure 80, Figure 81 and Figure 82, respectively. Similarly, these tribo-charges can remain for at least 48 hours in these three cases, which is ascribed to the tunneling of tribo-charges through the TMDs nanoflakes and localize onto the underlying SiO_2/Si substrate. Utilizing the fitted function in (5-3), the parameters are summarized in Table 6. There are still two terms: one has a small magnitude (V_1) and a short time constant (τ_1), and the other one owns a larger initial amplitude (V_2) and time constant (τ_2). Since the air gap is considerably thinner than the SiO_2 substrate, most charges are offered by TMDs nanoflakes and trapped at the interlayer, and a larger initial amplitude V_2 is presented. The excellent insulation of air and the shield of TMDs nanofilms lead to a longer time constant τ_2.

To sum up, MoS_2 has the longest lifetime for tribo-charges while WSe_2 owns the shortest among these four materials, and the diffusion processes of WS_2 and $MoSe_2$ are alike. This can be explained by their work functions, since a lower work function indicates an easier electron transition from the valence band to the conductive band, making the material neutralize the abundant charges with the surrounding environment fluently.

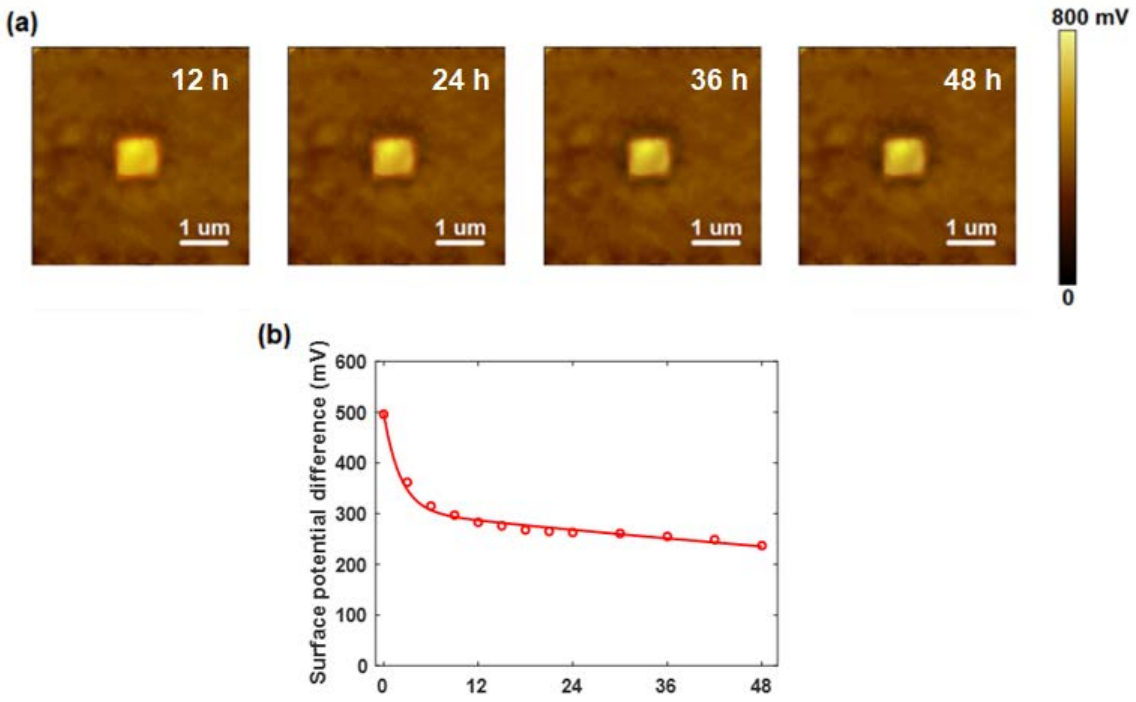

Figure 80 – Diffusion of tribo-charges on WS_2. (a) Surface potential maps after 12, 24, 36 and 48 hours. (b) The surface potential difference as a function of time and its fitted curve.

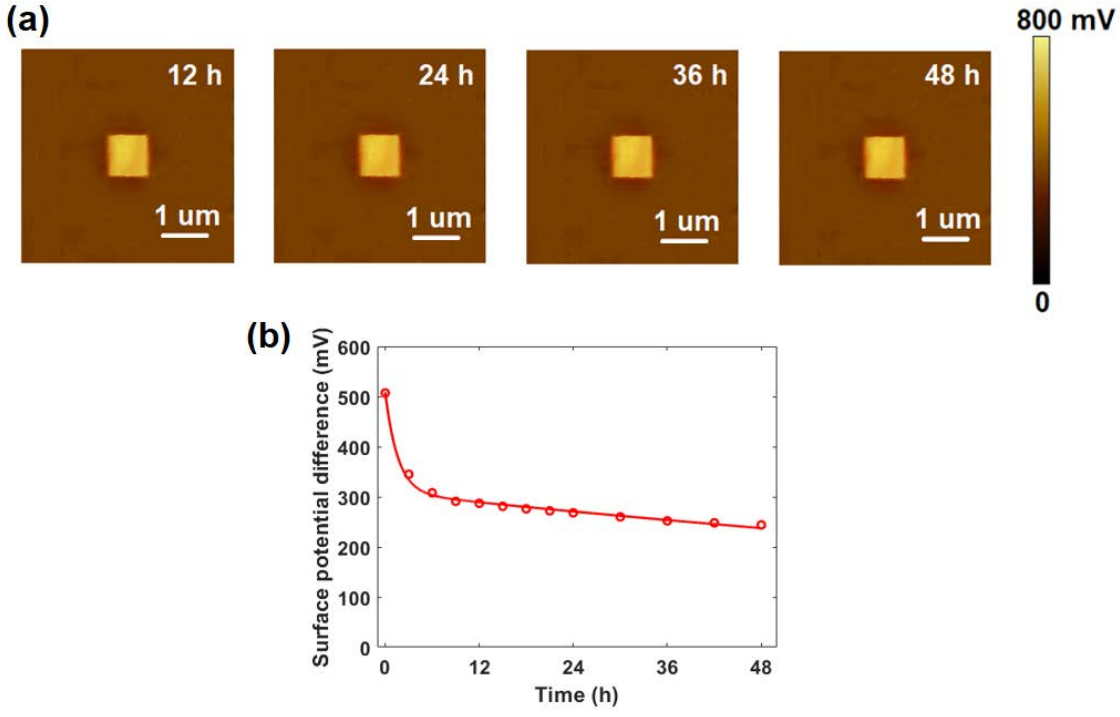

Figure 81 – Diffusion of tribo-charges on $MoSe_2$. (a) Surface potential maps after 12, 24, 36 and 48 hours. (b) The surface potential difference as a function of time and its fitted curve.

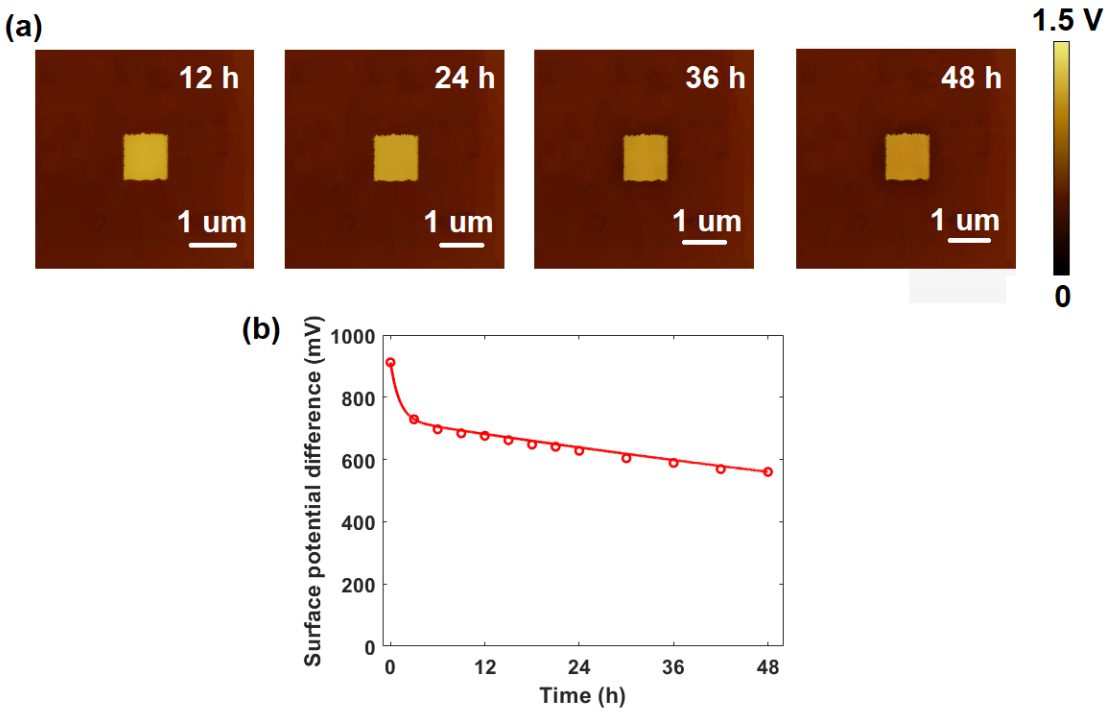

Figure 82 – Diffusion of tribo-charges on WSe_2. (a) Surface potential maps after 12, 24, 36 and 48 hours. (b) The surface potential difference as a function of time and its fitted curve.

Table 6 – Parameters of fitted tribo-charge diffusion function for WS_2, $MoSe_2$ and WSe_2 monolayers.

Materials	V_1/mV	V_2/mV	τ_1/h	τ_2/h
WS_2	194.1	305.2	2.1	184.0
$MoSe_2$	191.7	297.9	2.0	183.6
WSe_2	114.8	236.5	1.3	164.5

5.3 Manipulation of tribo-charges

The polarity and density of tunneling triboelectric charges on MoS_2 can be controlled by applying different bias voltages to the conducting Pt-coated AFM tip during the triboelectric process. As can be seen from the surface potential images after rubbing with biases ranging from -10 to +10 V in Figure 83a, positive charges are trapped at the interface and electrons are attracted in the central region of MoS_2 at positive bias voltages, resulting in an n-type MoS_2; in contrast, negative charges are injected across the air gap and holes are attracted in the rubbed section with negative biases, so a p-type MoS_2 is formed. As the surface potential difference between the intact and rubbed sections is almost identical to the voltage drop through the air gap, charge density σ of tunneling triboelectrification can be calculated based on the capacitor model as:

$$\sigma = \frac{\Delta V\, \varepsilon_0 \varepsilon_{Air}}{t_{Air}} \tag{5-4}$$

where ΔV is the voltage drop through the air gap, ε_0 is the vacuum dielectric constant, ε_{Air} and t_{Air} are the relative dielectric constant and thickness of the air gap, respectively.

As evident from the surface potential differences and corresponding charge densities in Figure 83b, the surface potential difference increases with the applied voltage non-linearly, which results from the different energy state densities within the bandgap.

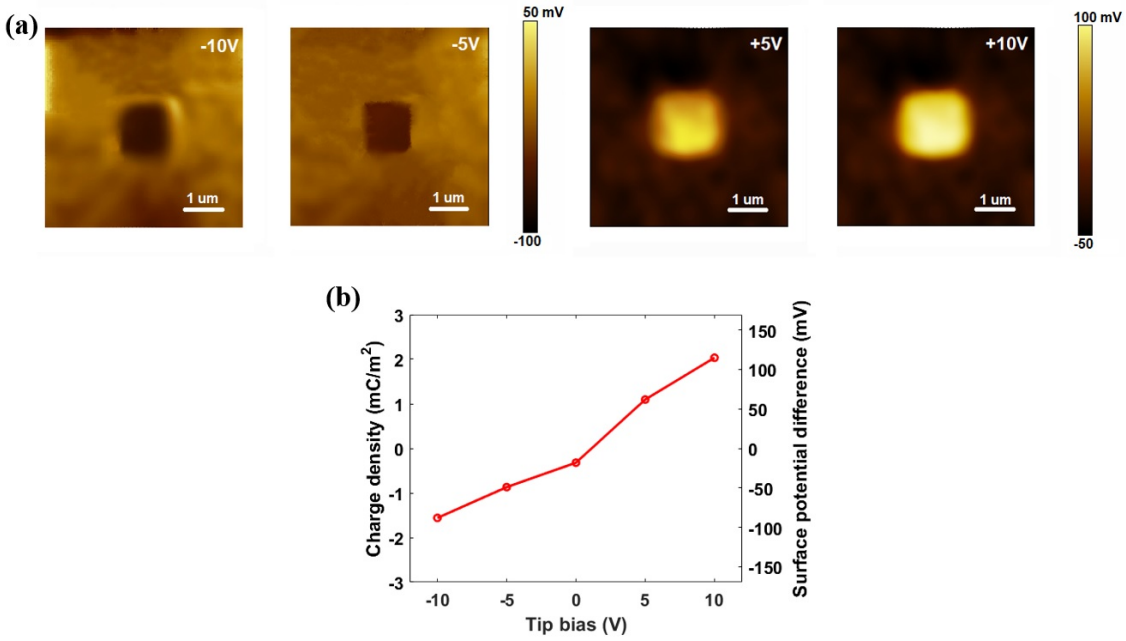

Figure 83 – Manipulation of polarity and density of tunneling triboelectric charges on MoS_2. (a) Surface potential images after rubbing the central region with -10, -5, +5 and +10 V biases. (b) Charge density and surface potential difference as a function of tip bias.

Akin to MoS_2, the density of tribo-charges on WS_2, $MoSe_2$ and WSe_2 monolayers can be tuned via various biases onto the conductive tip during the sliding process as well, as shown in Figure 84, Figure 85 and Figure 86, respectively. Here, it can be noticed that the controllable range narrows down in the following rank: WSe_2, $MoSe_2$, WS_2, MoS_2 when -10 ~ +10 V biases are applied. This may result from the varying carrier mobility and the capacity to accept/lose charges of these materials.

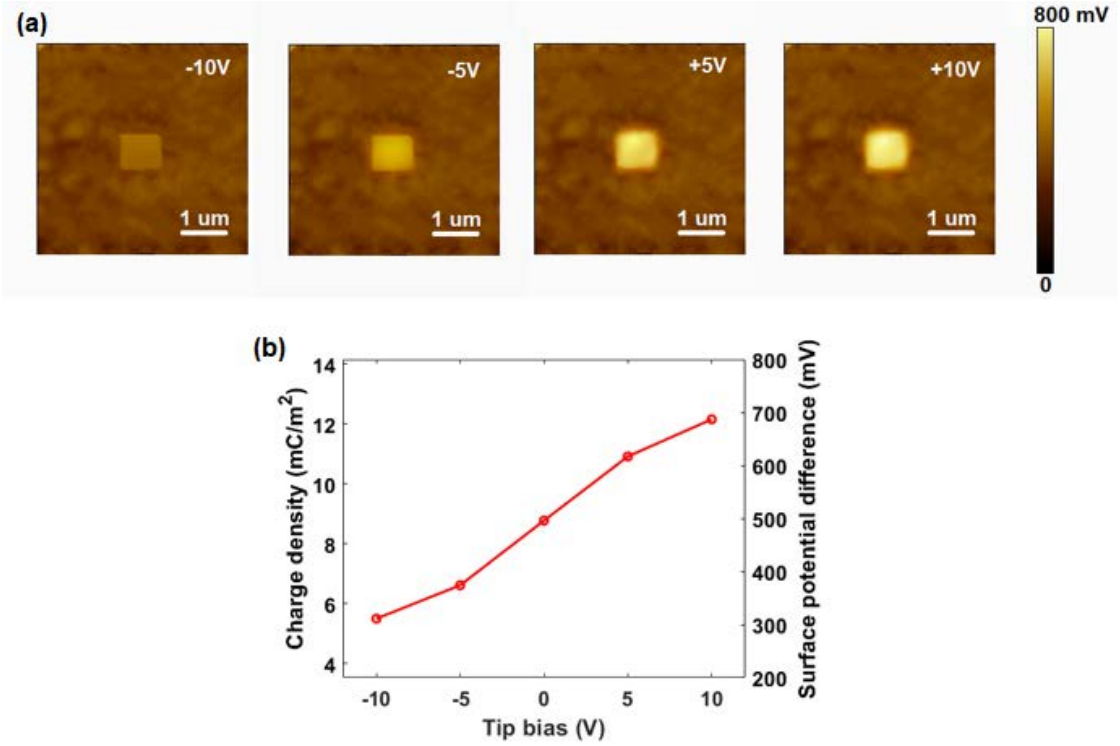

Figure 84 – Controllable density of tribo-charges on WS_2 via bias voltage. (a) Surface potential maps after the triboelectric process with different biases: -10, -5, +5 and +10 V. (b) Charge density and surface potential difference with tip bias.

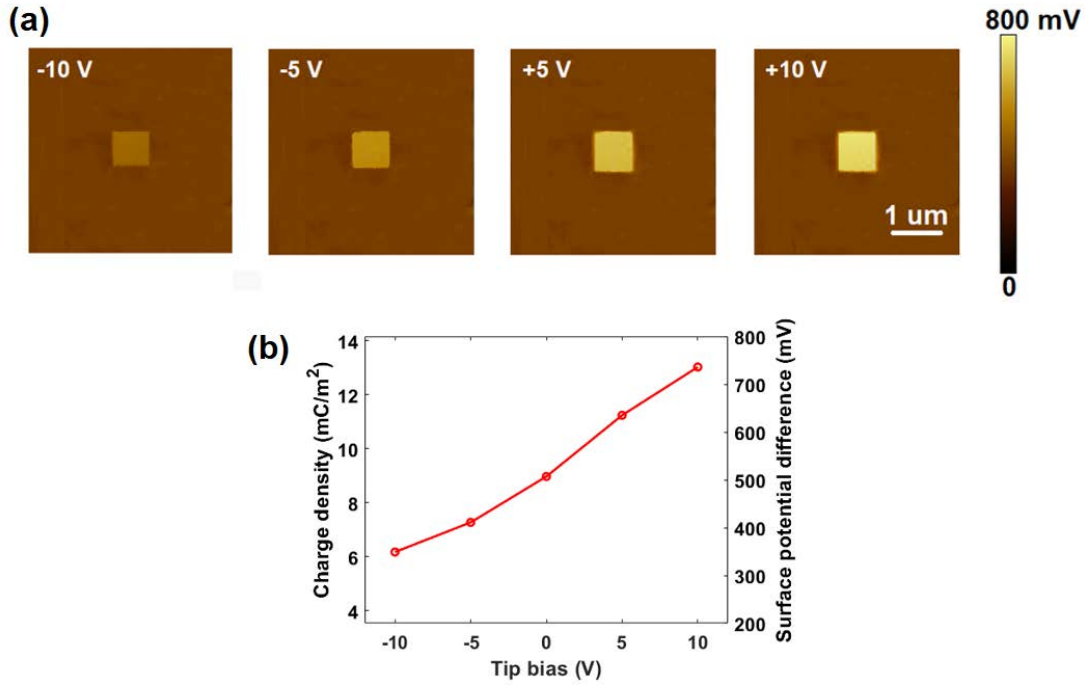

Figure 85 – Controllable density of tribo-charges on $MoSe_2$ via bias voltage. (a) Surface potential maps after the triboelectric process with different biases: -10, -5, +5 and +10 V. (b) Charge density and surface potential difference with tip bias.

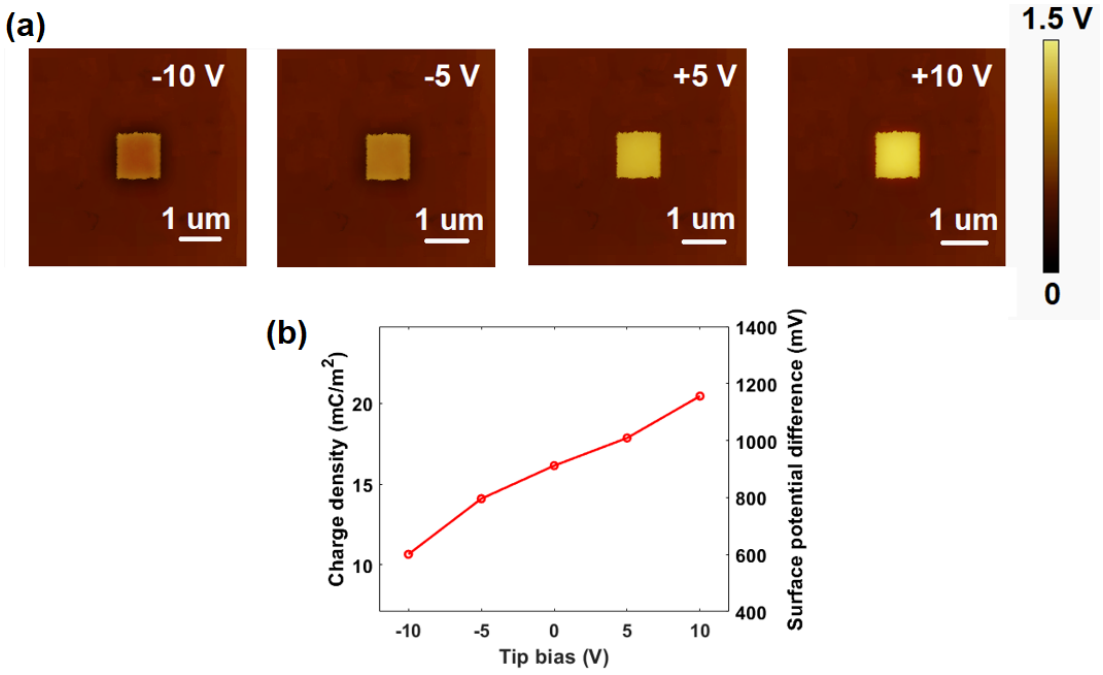

Figure 86 – Controllable density of tribo-charges on WSe_2 via bias voltage. (a) Surface potential maps after the triboelectric process with different biases: -10, -5, +5 and +10 V. (b) Charge density and surface potential difference with tip bias.

5.4 Effect of multi-friction

Now we explore the ability of AFM system to provide multiple scans of a selected area to increase the accumulated charge. Taking single-layer MoS_2 for example, The as-deposited sample was rubbed for multiple cycles with a constant contact force of 25 nN and bias voltage of +10 V; corresponding surface potential images are shown in Figure 87a. As the whole measurement was completed within 30 minutes, the influence of charge diffusion can be neglected considering the good preservation of tunneling triboelectric charges. Figure 87b displays the averaged surface potential differences and relevant charge densities within these 12 cycles, and an obvious accumulation and saturation trend for the triboelectric charge can be seen.

Based on previous reports [255], [256], the mechanism of triboelectric process can be described by the assumption of effective work function: the amount of transferred charges in each cycle is linked with the difference of effective work functions between the tip and sample. The difference will reduce with the charge accumulation process until saturation is reached. A phenomenological model can be used to fit the experimental data as illustrated in equation (5-5) [30]:

$$\frac{d\sigma}{dn} = \mathrm{k}V_c - pV_e\sigma \tag{5-5}$$

where σ and n are the surface charge density and the number of rubbing cycles, respectively, k is the charge efficiency coefficient, V_c is representative of the work function difference between the tip and sample, p is the charge impedance coefficient, and V_e is the charge-induced potential on the measured surface.

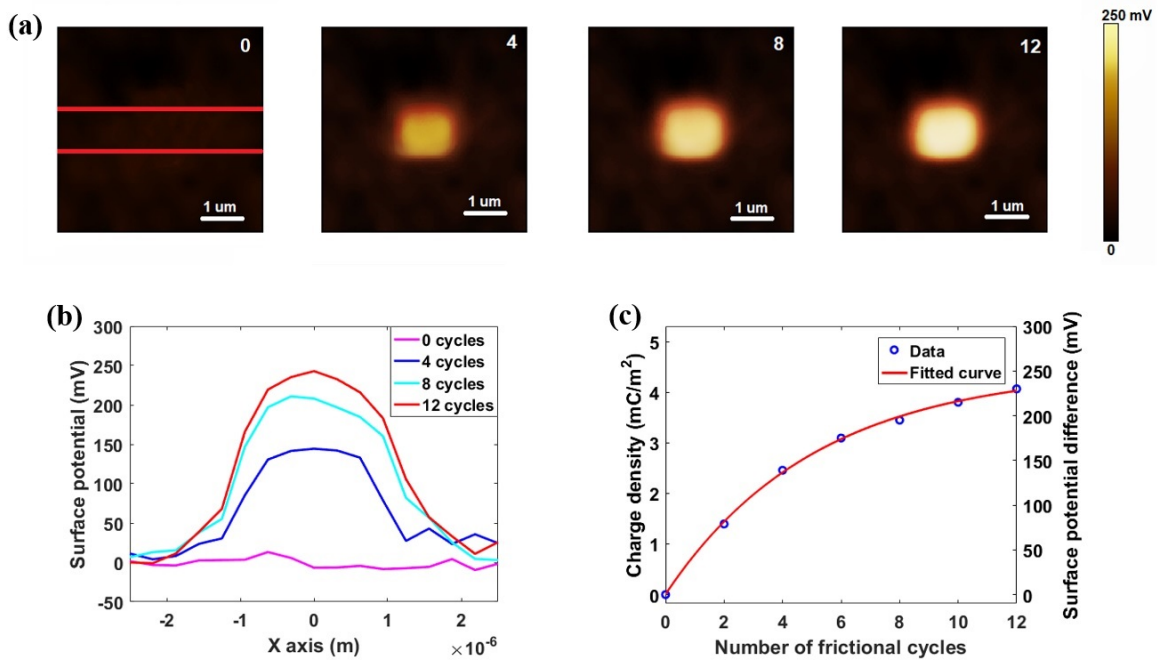

Figure 87 – Accumulation of triboelectric charges on MoS_2 with rubbing cycles increased. (a) Surface potential images after rubbing with 0, 4, 8 and 12 cycles. (b) Cross-section profiles between the lines in a. (c) Charge density and surface potential difference as a function of frictional cycle number.

Considering the boundary conditions for equation (5-5), the following relationship can be obtained [30]:

$$\sigma = \sigma_0 \exp\left(-\frac{n}{n_0}\right) + \sigma_\infty[1 - \exp\left(-\frac{n}{n_0}\right)] \tag{5-6}$$

where σ_0 and σ_∞ are the surface charge densities at $n = 0$ and $n = \infty$, respectively. n_0 is a constant indicating the speed of charge saturation.

By fitting the experimental data for different rubbing cycles (Figure 87c), all the parameters can be extracted: $\sigma_0 = (8.01 \pm 0.01)$ μC/m^2, $\sigma_\infty = (4.46 \pm 0.01)$ mC/m^2, $n_0 = (5.14 \pm 0.01)$. Compared with the recently published results, the saturated tunneling triboelectric charge density of MoS_2 (~4.46 mC/m^2) is significantly higher than that of SiO_2 (~150 μC/m^2) [30]. As for the enhancement of charge density, it mainly results from the tunneling of triboelectric charges, which are kept at the interlayer between the MoS_2 monolayer and the underlying

SiO_2/Si substrate. Under this circumstance, the MoS_2 layer, as well as the thin air gap, protect these charges from being neutralized by charges or ions in the air, thereby improving the charge density compared with the case of SiO_2.

5.5 Effect of layer number

Here, the effects of layer number were investigated with WS_2 nanoflakes. As evident from the surface potential curve before annealing in Figure 88, it becomes smaller with the increase of layer number, which can be explained by an interlayer screening effect, since the surface potential of a nanofilm is screened by the external electric field induced by the defects in the SiO_2/Si substrate [257], [258].

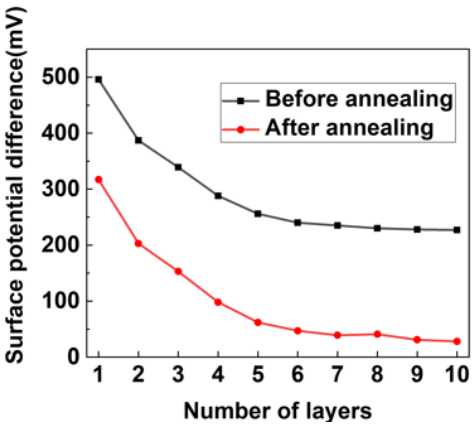

Figure 88 – Surface potentials as a function of WS_2 with different layer numbers before and after thermal treatment.

Besides, it has also been reported that the surface potential and the charge distribution of 2D materials, such as graphene and h-BN nanoflakes [259], [260], are extremely sensitive to the ambient atmosphere. For WS_2, the water molecules adsorbed from the atmosphere may act as carrier trappers. It is suggested that defects on the SiO_2/Si substrate mainly involve surface-adsorbed water molecules, so efficient heat treatment can reduce the presence of undesired adsorbents, thereby the effect of the external electric field from the substrate. To eliminate the effect of water, 10 minutes annealing at 100 ℃ was further performed on the rubbed WS_2 nanoflakes, followed by immediate measurement of surface potential by KFM. As illustrated in Figure 88, while the surface potential difference still shows a similar descending tendency with the increase of layer number, the thermal treatment caused a decrease of ~0.2 mV. The reason behind is that the work function of unrubbed area ($\varphi_{unrubbed}$) is lowered due to the removal of moisture via annealing, but the water molecules were already removed during the triboelectric process for the rubbed central area, so the

annealing has less influence on the work function of this area (φ_{rubbed}). Based on equation (5-2), the difference of the contact potential between these two regions (ΔV_{CPD}) is reduced.

As for the diffusion of tribo-charges, Figure 89 shows the surface potential difference (ΔV) with time for monolayer, 5-layer and 9-layer WS_2 nanoflakes. Using the fitted tribo-charge diffusion function depicted in equation (5-3), the parameters are listed in Table 7. Considering the poor conductivity (higher work function) as well as better protection (more layers to shield the tunneling charges from the atmosphere) of multilayers, a larger time constant is observed as the thickness of nanoflakes increases.

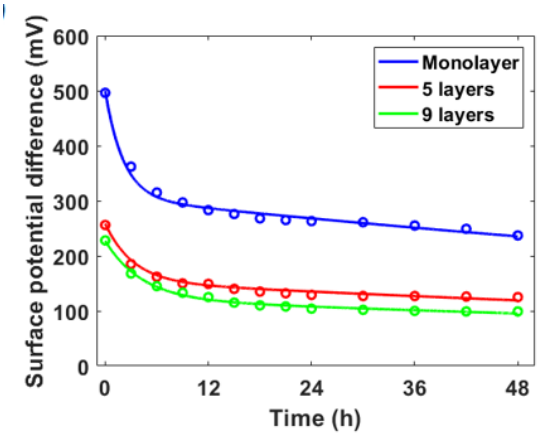

Figure 89 –The surface potential difference as a function of time and its fitted curve for monolayer, 5-layer and 9-layer WS_2 nanoflakes.

Table 7 – Parameters of fitted functions.

	V_1/mV	V_2/mV	τ_1/h	τ_2/h
Monolayer	194	305	2	184
5 layers	105	153	3	191
9 layers	106	121	4	199

5.6 Effect of material transfer

As AFM system is capable of scanning with varied normal forces, the as-grown WS_2 nanoflakes were rubbed with 25, 50, 75 and 100 nN to investigate the effect of load. As evident from the surface potential difference shown in Figure 90a, there is a slight reduction in the surface potential differences for monolayer, few-layer, and multilayer with the increase of applied normal force. However, the work function should be identical for the measured nanoflakes with the same thickness, so it is suggested that some materials may be transferred during the rubbing process. Then, the elemental composition of the rubbed areas

was analyzed by EDX, and an energy peak at 2.06 keV, belonging to Pt, is detected in Figure 90b.

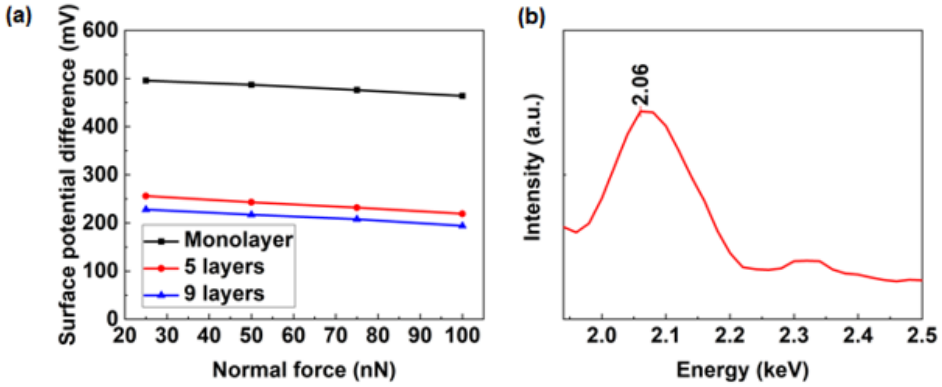

Figure 90 – Material transfer during the triboelectric process for WS_2. (a) Surface potentials with different applied normal forces. Monolayer (1 layer), few-layer (5 layers) and multilayer (9 layers). (b) EDX map of the rubbed area for monolayer WS_2 applied with 25 nN normal force to show the Pt peak.

The chemical composition of rubbed WS_2 monolayer with various applied normal forces is listed in Table 8. The Pt content increased with applied force. Note that low values of chemical composition related to Pt, W and S are due to EDX interaction volume (max. depth approx. 1 µm for acceleration voltage 20 kV).

Table 8 – Atomic ratios of elements on monolayer WS_2 with various normal forces.

Normal force/nN	Pt	Si	C	O	W	S
25	0.24	31.55	1.18	66.73	0.10	0.20
50	0.33	31.24	1.01	67.14	0.09	0.19
75	0.39	30.97	0.98	67.37	0.09	0.20
100	0.44	30.80	0.91	67.58	0.08	0.19

Obviously, there is a slight rise in Pt ratio with the increase of the applied forces. Considering the negative correlation between the surface potential difference and applied force, we suppose that it is Pt that has been transferred from the tip to the WS_2 nanoflakes, since the transfer of Pt (with a larger work function) can enhance the work function of WS_2, thereby lowering the surface potential difference as depicted by equation (5-2).

5.7 Summary

The triboelectric characterizations of MoS_2, WS_2, $MoSe_2$ and WSe_2 have been conducted in this chapter and some key parameters for their monolayers are summarized in Table 9.

Table 9 – Triboelectric parameters for MoS_2, WS_2, $MoSe_2$ and WSe_2 monolayers

Materials	The surface potential difference compared to the unrubbed area	Time constant (h)	Work function (eV)
MoS_2	~20 mV lower	207.8	5.15 eV [248]
WS_2	~0.5 V higher	184.0	4.6 eV [249]
$MoSe_2$	~0.5 V higher	183.6	4.57 eV [250]
WSe_2	~0.9 V higher	164.5	4.21 eV [249]

It is noticed that the electrons are transferred from the samples to the AFM tip during triboelectrification in the case of WS_2, $MoSe_2$ and WSe_2, whereas MoS_2 exhibits an opposite transfer direction, and the amount of tribo-charges are different for all of them. The reason behind this phenomenon is the diverse work functions of these four materials.

In addition, the diffusion time constants reduce with the decrease of their work functions, since a lower work function indicates an easier electron transition from the valence band to the conductive band, making the material neutralize the abundant charges with the surrounding environment fluently. Under this circumstance, MoS_2 has the longest lifetime while WSe_2 owns the shortest among these four materials, and the diffusion processes of WS_2 and $MoSe_2$ are alike thanks to their similar work functions.

Furthermore, the density of tribo-charges is adjustable for all of these four TMDs by a bias voltage applied onto the conductive AFM tip, and the controllable range narrows down in the following rank: WSe_2, $MoSe_2$, WS_2, MoS_2 when -10 ~ +10 V biases are applied. This may be induced by the varying carrier mobility and the capacity to accept/lose charges of these materials.

As for the effect of layer number, the surface potential difference becomes smaller with the increase of layer number due to the interlayer screening effect, and a larger time constant is observed in the meantime given the poor conductivity (higher work function) as well as better protection (more layers to shield the tunneling charges from the atmosphere) of multilayers.

Considering the interaction with the environment nearby, the surface-adsorbed water molecules from the atmosphere can act as carrier trappers to affect the surface potential and charge distribution of 2D materials, but heat treatment can efficiently handle this problem.

Last but not least, there also exists the transfer of materials during the frictional process, which can be utilized for tuning the triboelectric properties of materials.

Chapter 6 Transition metal dichalcogenides-based applicable triboelectrification

Based on the previously discussed triboelectrification of transition metal dichalcogenides, applicable fields consisting of bandgap modification as well as tunable antenna will be introduced in this chapter.

6.1 Bandgap modification

6.1.1 Introduction

MoS_2, WS_2, $MoSe_2$, and WSe_2 are potential for a range of applications such as optical electronics due to their adjustable bandgap, which experiences an indirect-to-direct transition when the thickness is thinned to monolayer and can be tuned under strain [261]. Taking MoS_2 for instance, the bandgap of its single-layer and bilayer can be decreased for strain levels at 10% and 6%, respectively; the energy of direct gap is only slightly lower than the indirect one for single-layer MoS_2, making the bandgap very responsive to strain [262], [263].

Although experimental investigations on the bandgap modification have been conducted [188], [264], the selected substrates are insulating materials and there may exist triboelectric charges at the interlayer, so the study of strain-induced bandgap modification is not in situ since the tribo-charges may act as a bias to affect. Under this circumstance, a paradigm is presented here to observe the in situ strain-dependent bandgap modulation, and the effect of underlying tribo-charges is also provided. The samples used here are the MoS_2 nanoflakes deposited on different substrates (SiO_2/Si, gold, sapphire, and polyimide), the same as the ones observed in Chapter 5.

6.1.2 In situ strain-dependent bandgap modulation

Due to the different work functions between the Pt-coated conductive tip and single-layer MoS_2, there is a charge transfer between them during the triboelectric process and the generated tribo-charges can tunnel to the underlying substrate and localize there. To avoid the generation of triboelectric charges, the surface potential difference was negated with a bias voltage when rubbing the 1×1 μm^2 region, and different normal forces were applied to

induce various strains on the nanoflakes in the meantime. Afterward, Raman spectroscopy was performed to obtain the PL spectra.

Figure 91 shows the PL spectra of MoS_2 monolayer on SiO_2/Si, gold, sapphire and polyimide substrates with different applied normal forces. It is noteworthy that the PL peak redshifts when a larger normal force is applied in all cases, which is consistent with the results obtained by first-principles calculations regardless of the details and magnitude of their predictions [186], [263], [265]. This phenomenon can be explained by the reduction of MoS_2 bandgap under mechanical strain [266]. In addition, a slight difference for the strain-induced bandgap energy shifts of these four cases can be seen, since the bandgap of atomically thin 2D semiconductors is strongly dependent on the dielectric environments around [267].

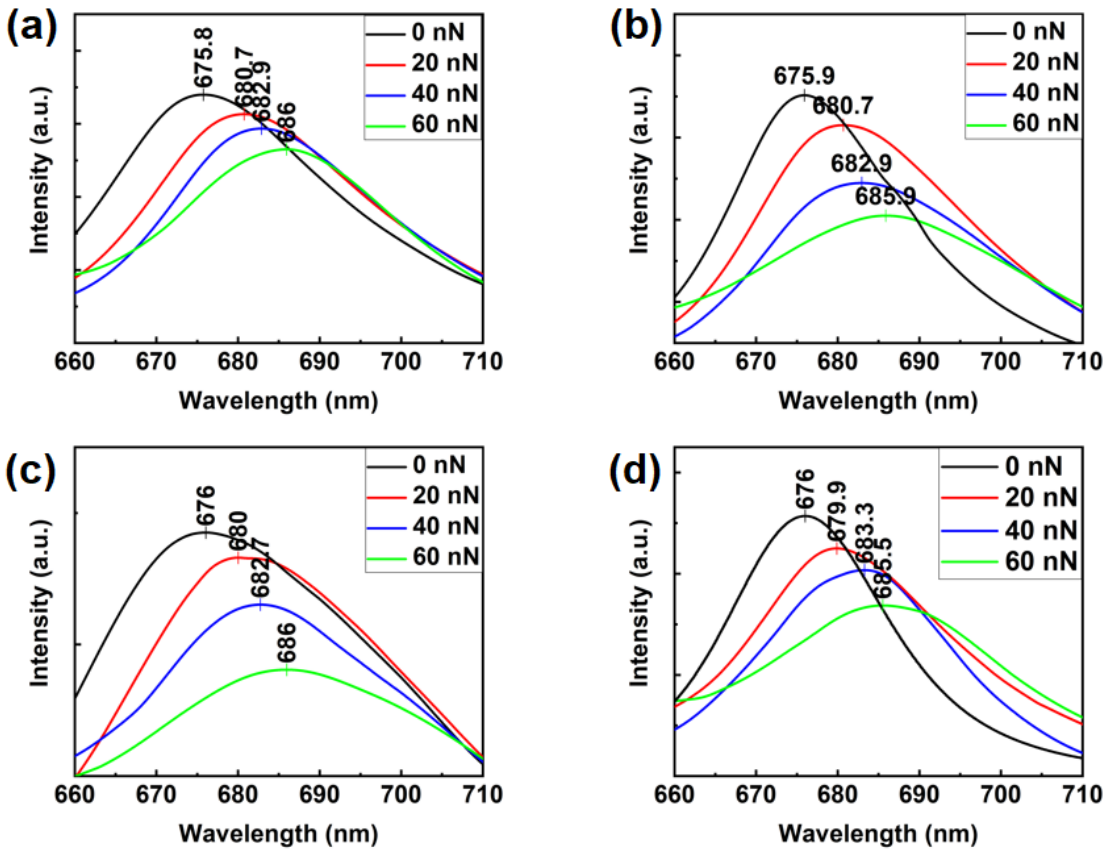

Figure 91 – PL spectra of MoS_2 monolayer on different substrates rubbed with 0, 20, 40 and 60 nN normal force applied: (a) SiO_2/Si, (b) gold, (c) sapphire and (d) polyimide.

6.1.3 Bandgap modification by tribo-charges

To evaluate the modification of bandgap via tribo-charges, the PL maps of MoS_2 nanoflakes on SiO_2/Si, gold, sapphire and polyimide substrates with different bias voltages during the frictional process were scanned as well (20 nN normal force was applied). As demonstrated

for single-layer MoS_2 in Figure 92, the variation of PL peaks is very subtle for all the cases, and the reason behind is the slight band structure deformation for MoS_2 monolayer under an electric field perpendicular to the nanoflakes.

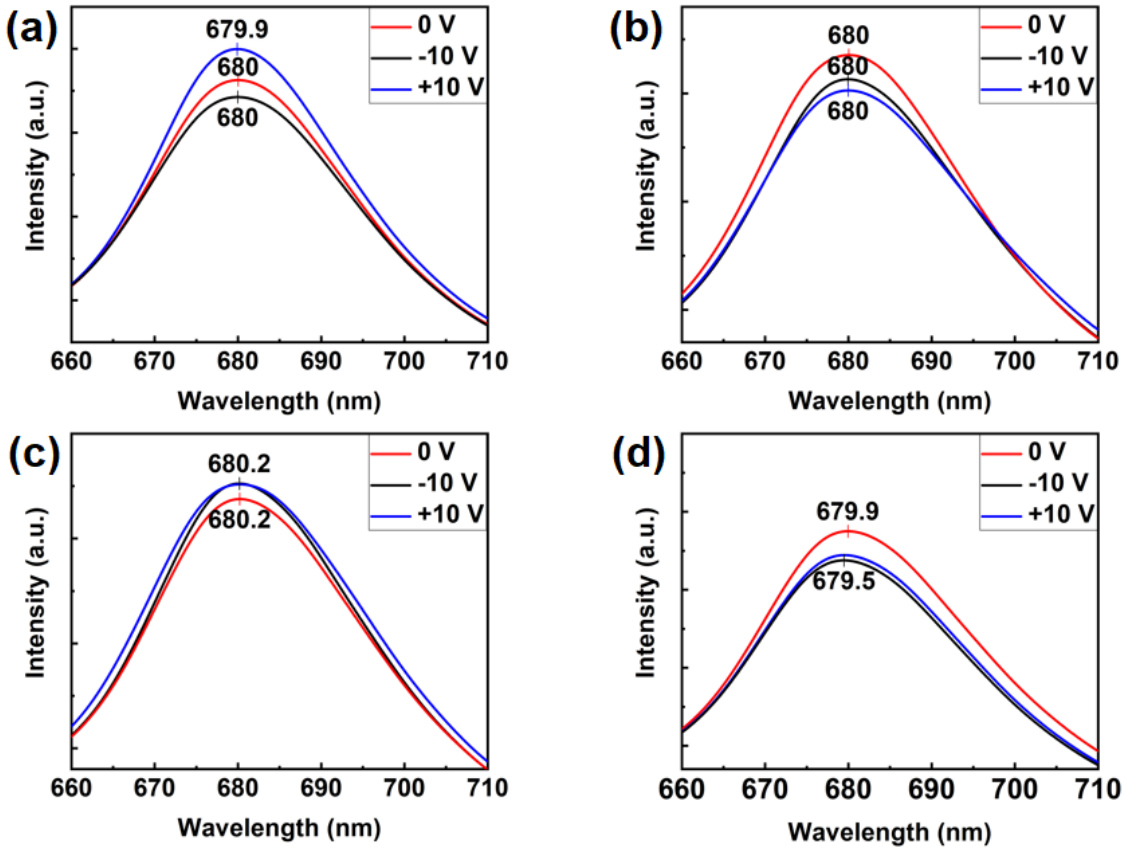

Figure 92 – PL spectra of MoS_2 monolayer on different substrates rubbed with -10, 0 and +10 V bias voltages applied: (a) SiO_2/Si, (b) gold, (c) sapphire and (d) polyimide.

However, there is an obvious redshift of the PL peaks for bilayer MoS_2 on SiO_2/Si, sapphire and polyimide substrates when bias voltages are applied during the rubbing process (Figure 93). Considering the insulating properties of these three substrates, the triboelectric charges can tunnel through the MoS_2 nanoflakes and act as a localized bias underneath, so the bandgap of MoS_2 can be modulated by these underlying tribo-charges. To specify, the bandgap decreases with the increase of the local electric field, therefore a higher wavelength can be expected with a bias voltage applied. But in the case of the gold substrate, the signal peaks are quite similar for different biases, since the generated tribo-charges cannot survive on the substrate due to the excellent conductivity of gold.

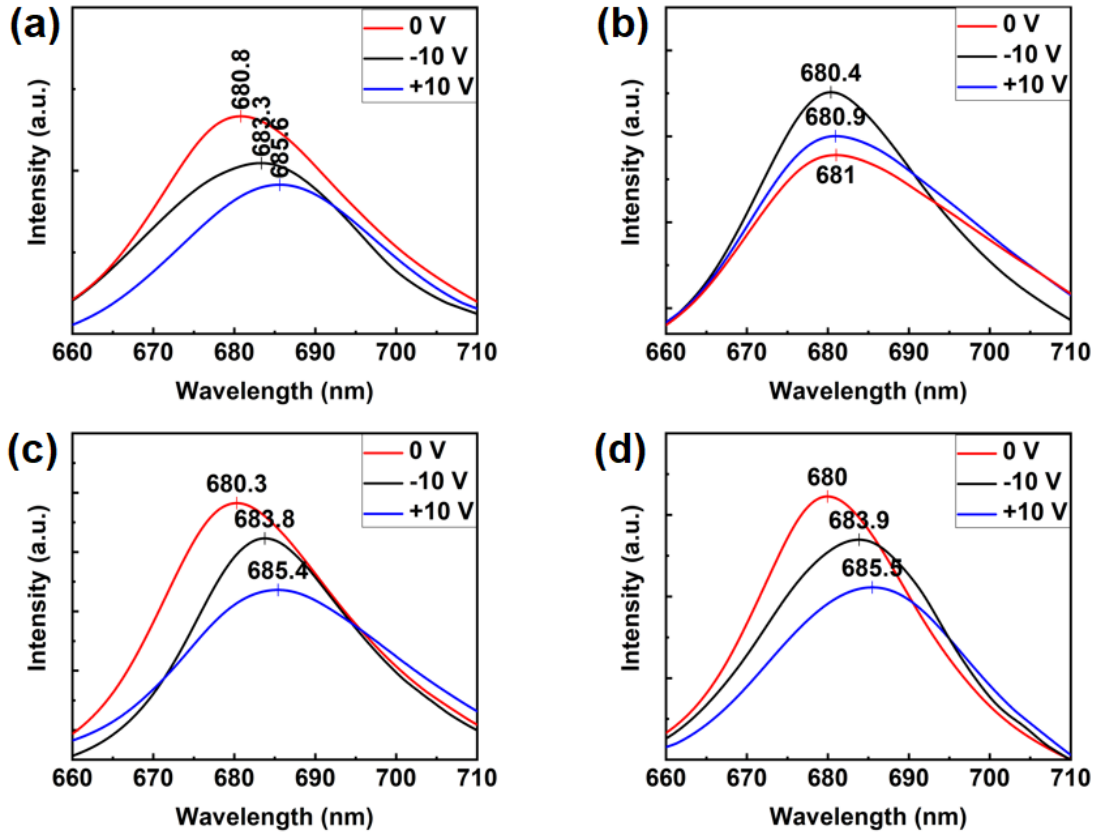

Figure 93 – PL spectra of MoS_2 bilayer on different substrates rubbed with -10, 0 and +10 V bias voltages applied: (a) SiO_2/Si, (b) gold, (c) sapphire and (d) polyimide.

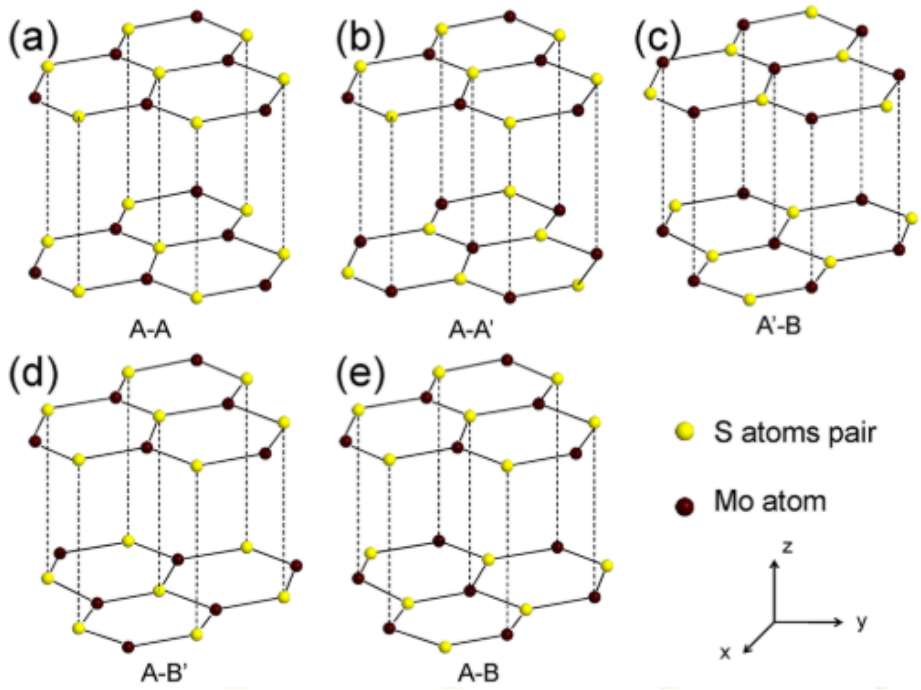

Figure 94 – Drawing schemes of five bilayer MoS_2 stacking structures: (a) A-A, (b) A-A', (c) A'-B, (d) A-B' and (e) A-B. Here, one pair of S atoms is represented by one yellow circle for a concise scheme [268].

Interestingly, the -10 and +10 V bias voltages lead to a different signal peak shift though their magnitudes are identical. As previously reported in [268], there are five stacking structures for bilayer MoS_2: A-A, A-A',A'-B, A-B' and A-B (Figure 94), and A-B structure is the only one owing spontaneous polarization among them. On the zero-bias condition, the S atoms of the top monolayer and the Mo atoms of the bottom monolayer are superimposed, but the Mo atoms of the top monolayer and the S atoms of the bottom monolayer are not, so a spontaneous polarization along the z direction is formed, and the bandgap of this structure will respond differently to the +z and –z electric fields though the same magnitude is applied.

As the tribo-charges can modify the bandgap of TMDs, it can pave a new path for the optical applications such as optical modulator, single-photon emitter and so forth, where the working states can be tuned via triboelectrification.

6.2 Triboelectrically-tunable antenna for 5G base station

As the tribo-charges can localize at the interlayer between TMDs nanoflakes and the underlying insulator, and they can act as a bias voltage to control the conductive/insulating state of TMDs, tunable antennas with omnidirectional and unidirectional radiations have been proposed for 5G base station application in this section.

6.2.1 Introduction

An antenna can realize the conversion between radio waves in space and electric currents within conductors when electrically connected with the receiver or transmitter. For transmission, the antenna is supplied with an electric current by a radio transmitter, and it can radiate the energy from the current as electromagnetic waves (radio waves). When working for reception, an antenna is capable of collecting some power of a radio wave to produce an electric current, which can be subsequently amplified by a receiver. Consequently, antennas are one of the indispensable components for radio systems and wireless communication.

Nowadays, more and more attention has been paid to the upcoming 5G wireless communication systems, which exhibit a higher speed rate and lower latency compared with the currently used 4G networks. In this case, the millimeter wave band has been considered as a suitable candidate, and new rules (FCC 15138) for wireless wideband of 28 GHz, 37 GHz, 39 GHz and 64 - 71 GHz have been proposed [269]–[272]. In this section, a tunable antenna based on the triboelectrification of $MoSe_2$ is presented.

There are two key parameters to evaluate the quality of antennas: return loss (S_{11}) and gain. The return loss reflects the working frequency of the designed antenna, and the S_{11}<-10 dB range is commonly used, which means that the frequency within this band can be radiated. Gain exhibits the power transmitted in the peak-radiation direction with respect to an isotropic antenna, which radiates energy in all directions. For the radiation patterns, they are generally illustrated in E-plane (the plane parallel to the electric field) and H-plane (the plane parallel to the magnetic field).

Generally, antennas can be designed to transmit and receive radio waves in all horizontal directions equally (omnidirectional antennas), or preferentially in a particular direction (unidirectional antennas). So these two types of tunable antennas have been designed and simulated with the help of commercial software CST Microwave Studio.

6.2.2 Omnidirectional antennas

The structure of $MoSe_2$-based triboelectrically-controlled tunable 5G omnidirectional antenna is shown in Figure 95. A Teflon substrate with a dielectric constant of 2.2 and a thickness of 1 mm is selected due to its low cost and stability. The dipole, containing two metal arms and $MoSe_2$ sheets attached on both ends, is etched on the substrate; a transition structure is adopted to achieve the impedance match between the dipole and feed network (a 50 Ohm coaxial cable whose outer conductor is soldered to one arm of the dipole, and the inner conductor is connected to the other one).

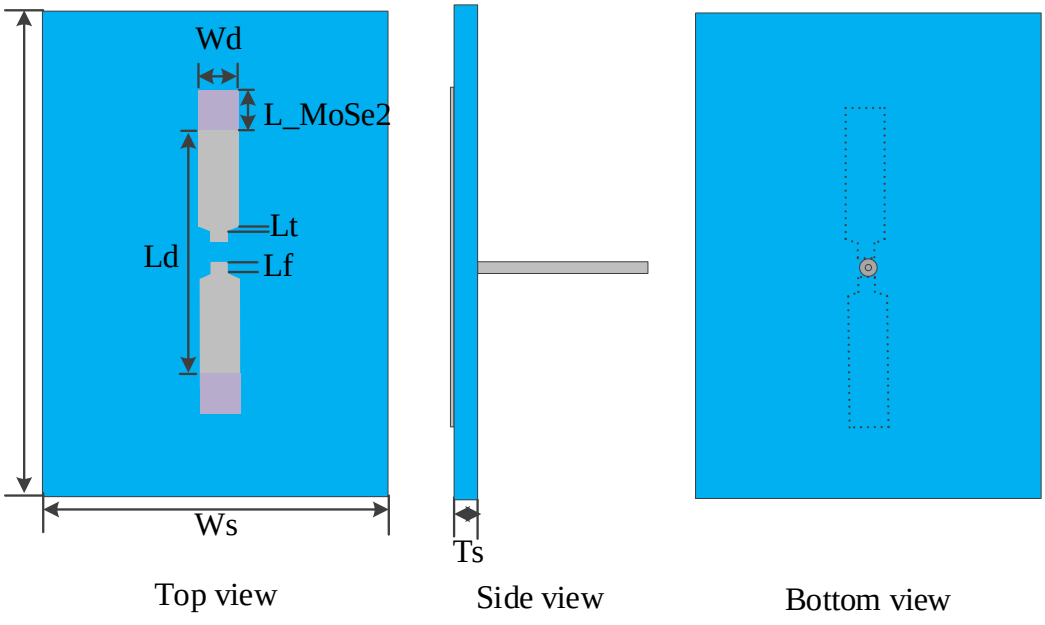

Figure 95 – Structure of tunable 5G omnidirectional antenna.

To realize the desirable characteristics, it is of necessity to determine the effects of various parameters in this structure. Here, the total length $Ld+L_{MoSe2}$ (including metallic and $MoSe_2$ parts), width *Wd*, length of feeding parts *Lf* and *Lt*, were studied as demonstrated in Figure 96. It is noteworthy that the resonant frequency shifts from 27 to 37 GHz when the total length of the dipole is shortened from 3.5 to 2 mm, since the resonant frequency is proportional to the length of the antenna to some degree (Figure 96a). In addition, the width of dipole affects the bandwidth of the antenna, and the resonant frequency is also moved to the higher end with a smaller width (Figure 96b). Moreover, there is only a slight variation of the return loss with the varying lengths of feeding parts, but they are responsible for the impedance match, so the value of return loss can be tuned by these two parameters (Figure 96c and d).

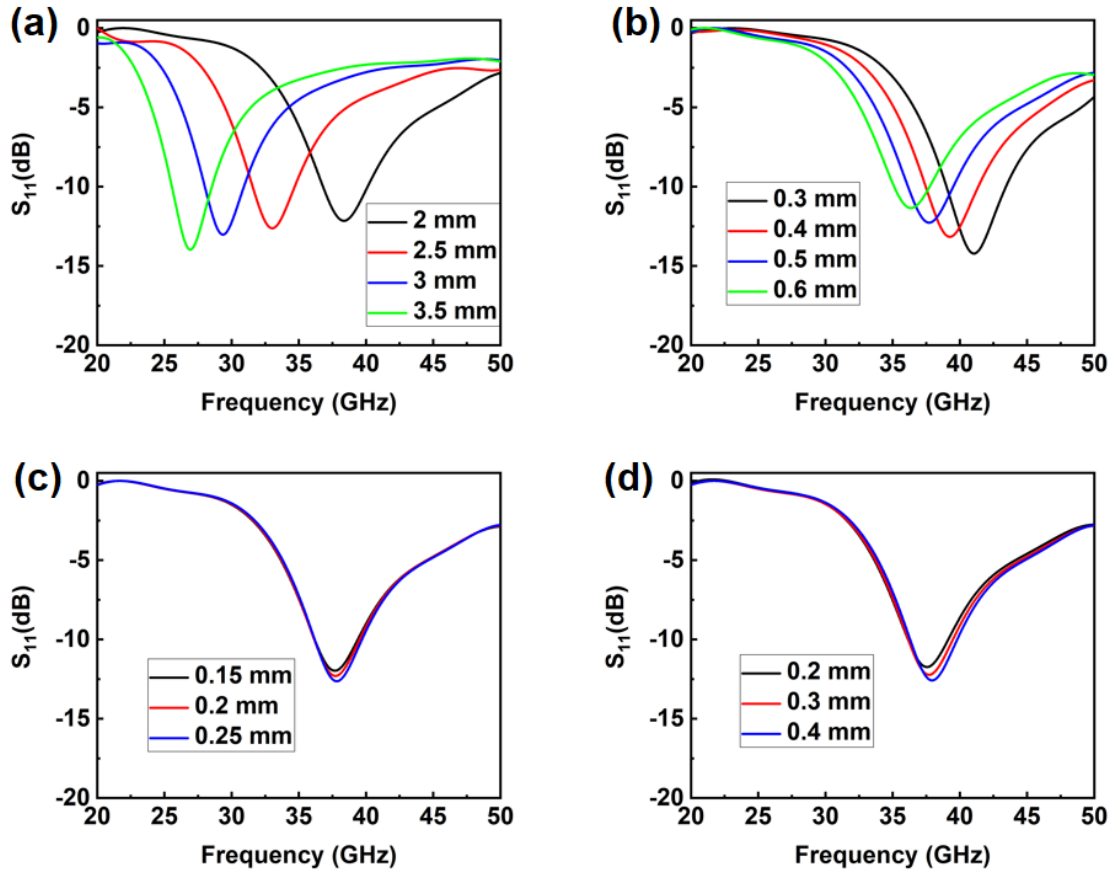

Figure 96 – Return loss characteristic of proposed antenna with (a) total length *Ld+ L_MoSe2* and (b) width *Wd* of dipole, length of feeding parts (c) *Lf* and (d) *Lt*.

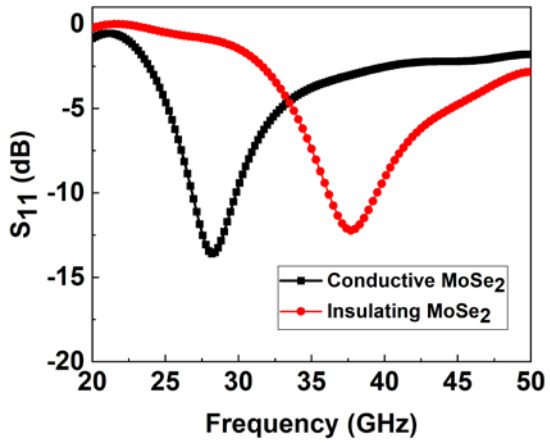

Figure 97 – Return loss of tunable 5G omnidirectional antenna when $MoSe_2$ is in conducting and insulating states.

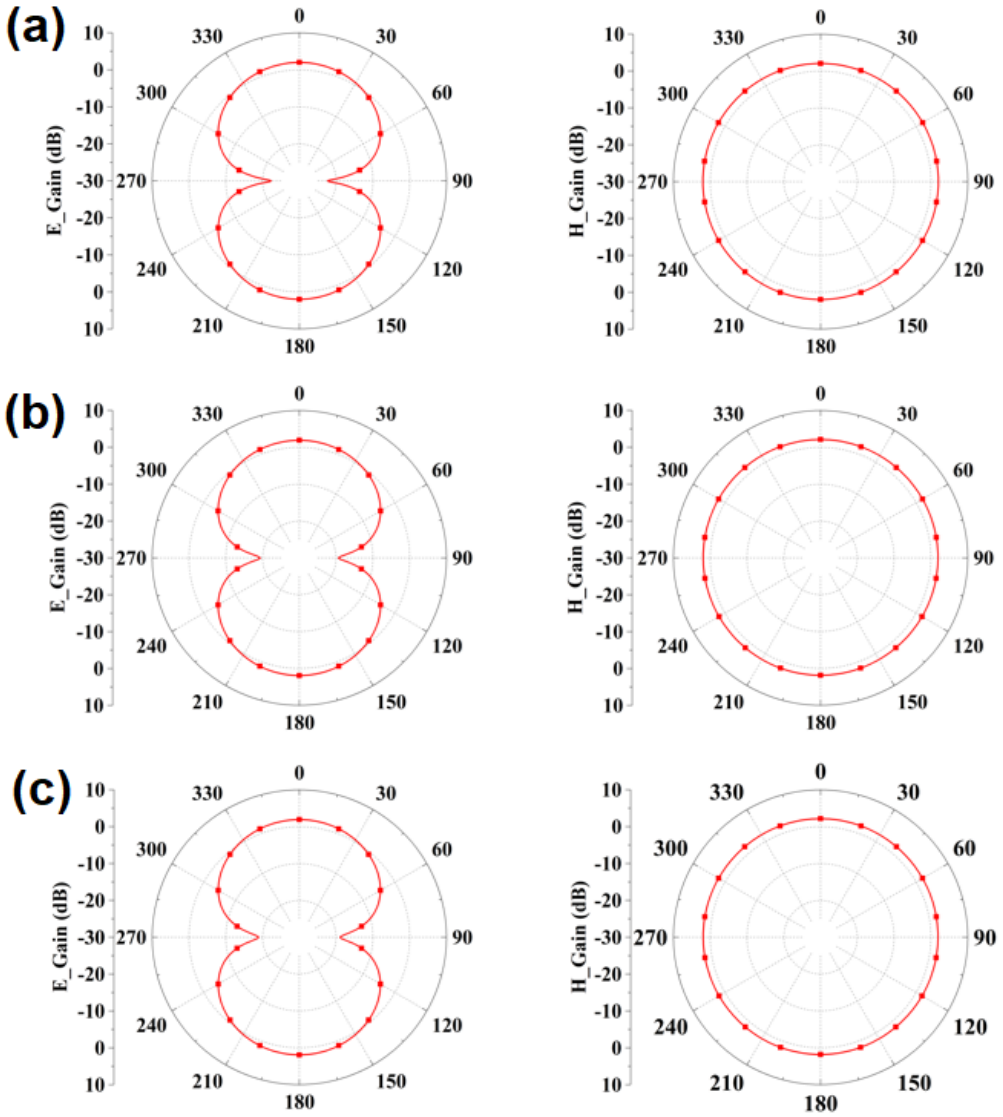

Figure 98 – Radiation patterns (E-plane and H-plane) of tunable 5G unidirectional antenna working at (a) 28 GHz (b) 37 GHz and (c) 39 GHz.

Here, it should be mentioned that the size of $MoSe_2$ (575×500 μm^2) is much larger than the $MoSe_2$ nanoflakes (lateral size of ~10 μm) for triboelectric characterization. However, it would be feasible to convert large-scale MoS_2 to $MoSe_2$ with Se and H_2 [273].

Table 10 – Parameters for tunable 5G omnidirectional antenna

Parameters	Description	Value (mm)
Ld	Length of dipole	2.05
Lf	Length of feeding part	0.195
Ls	Length of substrate	3.5
Lt	Length of taper line	0.3
L_MoSe2	Length of $MoSe_2$	0.575
Wd	Width of dipole	0.5
Ws	Width of substrate	1.75
Ts	Thickness of substrate	0.5

As investigated in Chapter 5, the tribo-charges initiated by frictional process can tunnel through the $MoSe_2$ nanoflakes and localize at the interlayer between $MoSe_2$ and the underlying substrate. In this situation, these well-preserved tribo-charges can act as a bias voltage to control the conductivity of $MoSe_2$ above. Resultantly, when the triboelectrically-controllable $MoSe_2$ sheets work at the conductive state, the return loss, as displayed in Figure 97, is lower than -10 dB from 26.8 to 29.8 GHz, which covers the 28 GHz resonant frequency for 5G base station, and a ~3 GHz bandwidth is obtained. When the $MoSe_2$ sheets are switched to the insulating state, the frequency band is shifted to the 36.8~40.2 GHz range to attain the radiation at 37 and 39 GHz [269]–[272]. Meanwhile, a symmetrical radiation is realized in the H-plane, and a stable gain ranging from 2.06 to 2.16 dBi is achieved as well (Figure 98).

6.2.3 Unidirectional antennas

To realize the unidirectional radiation, a metallic reflector can be placed at the back of the substrate since electromagnetic waves can be reflected, as illustrated in XXXX, and the optimized parameters are listed in Table 11.

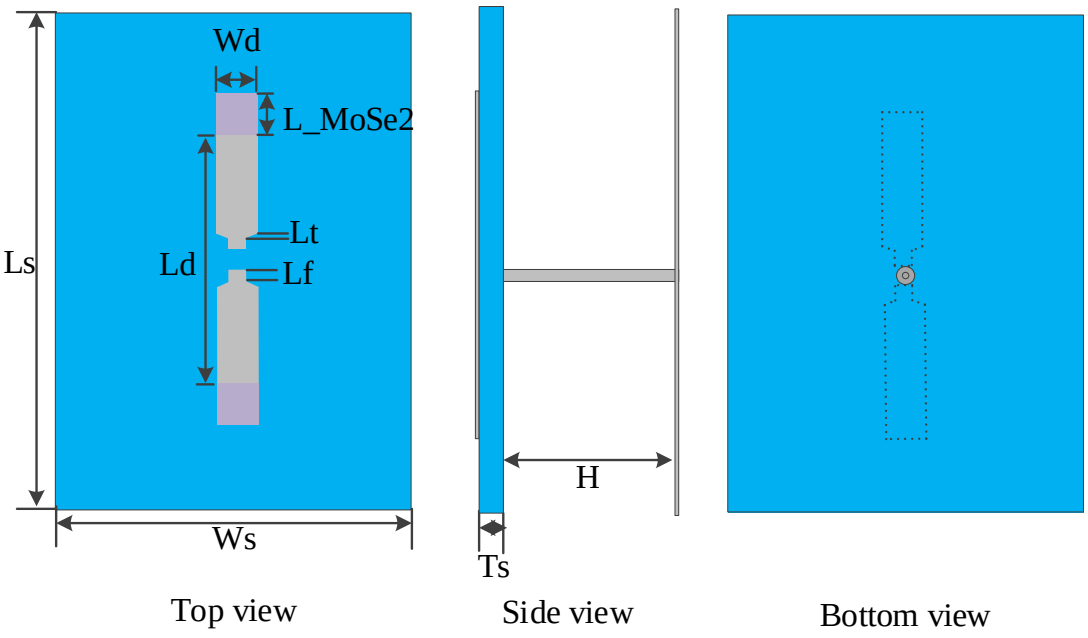

Figure 99 – Structure of tunable 5G unidirectional antenna.

As evident from the return loss in Figure 100, the antenna is still tunable from 27~29.7 GHz range to 34.5~41.2 GHz when the $MoSe_2$ sheets are switched from conductive to insulating state. In addition, the radiation patterns in Figure 101 indicate a unidirectional radiation, and the gain has been enhanced to 6.53 dBi at 28 GHz, 5.63 dBi at 37 GHz and 5.39 dBi at 39 GHz. A broad beamwidth over 120° can be reached for these three working frequencies: 123.4° at 28 GHz, 153.1° at 37 GHz and 160.4° at 39 GHz. Therefore, three of this antenna element can be arrayed to realize a gain over 5.39 dBi in all horizontal directions, which is more favorable for 5G base station application.

Table 11 – Parameters for tunable 5G unidirectional antenna

Parameters	Description	Value (mm)
Ld	Length of dipole	2.1
Lf	Length of feeding part	0.195
Ls	Length of substrate	3.5
Lt	Length of taper line	0.3
L_MoSe2	Length of $MoSe_2$	0.5
Wd	Width of dipole	0.5
Ws	Width of substrate	1.75
Ts	Thickness of substrate	0.5
H	Distance between substrate and reflector	2

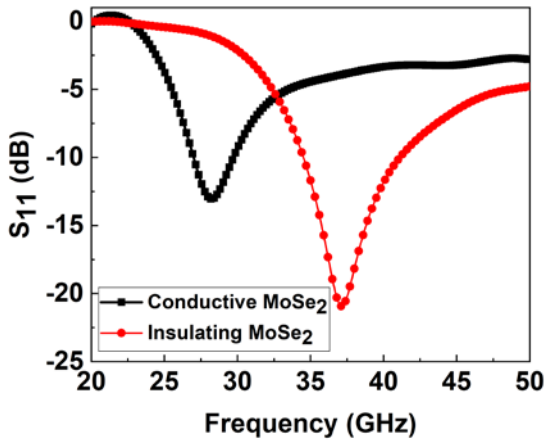

Figure 100 – Return loss of tunable 5G unidirectional antenna when $MoSe_2$ is in conducting and insulating states.

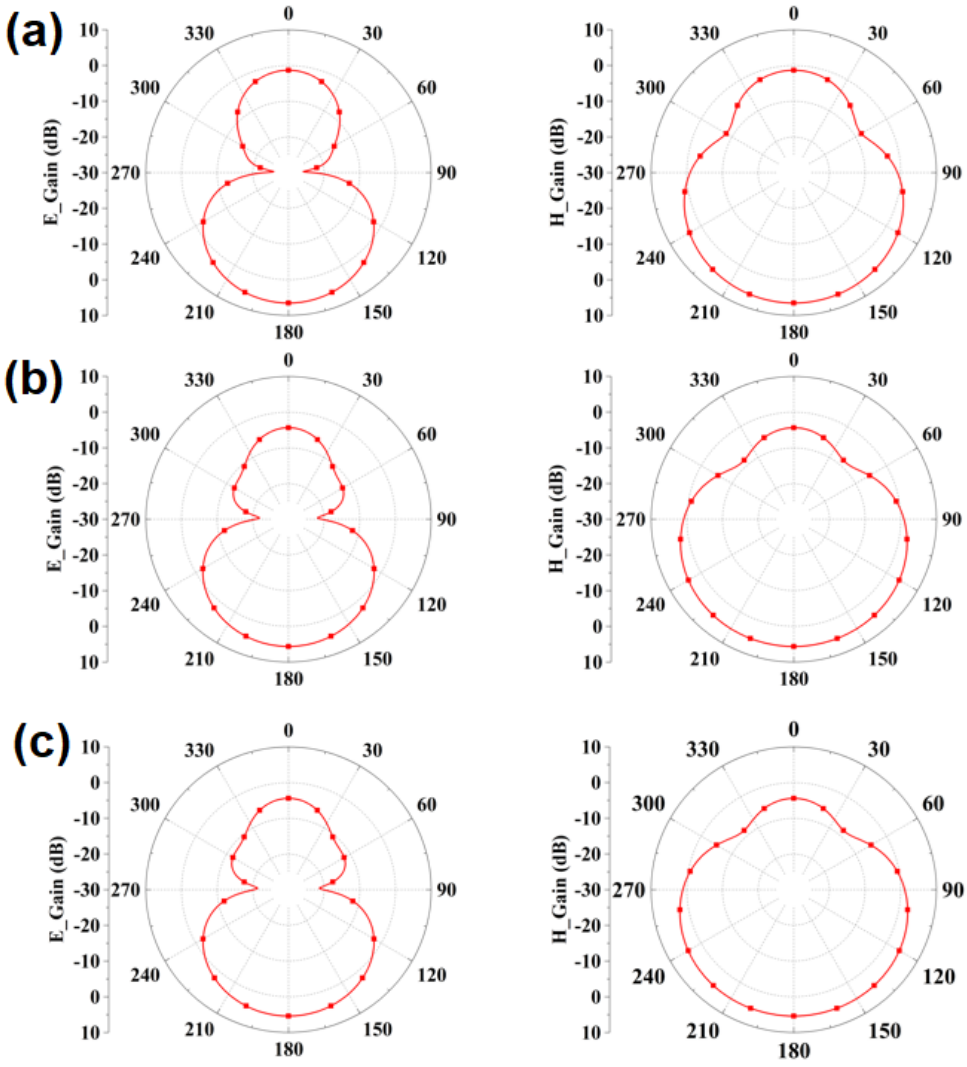

Figure 101 – Radiation patterns (E-plane and H-plane) of tunable 5G unidirectional antenna working at (a) 28 GHz (b) 37 GHz and (c) 39 GHz.

6.3 Summary

TMDs-based applicable triboelectric investigation containing the bandgap modification and the tunable antenna, have been discussed in this chapter.

For the bandgap modification, the in situ effect of strain was investigated by rubbing the sample with appropriate bias, which can negate the surface potential difference between the conductive Pt-coated tip and the sample. It exhibits that the bandgap decreases monotonically with the increase of applied force. The reason behind is the reduction of orbital overlapping and hybridization due to the weakened atomic bonds when localized strain appears. As the bandgap of MoS_2 nanoflakes strongly depends on the dielectric environments, the strain-induced bandgap energy shifts differently for MoS_2 on various substrates. In addition, while the bandgap of MoS_2 is almost unchanged when an external perpendicular electric field is applied because of the very subtle band structure deformation, the bandgap of bilayer MoS_2 can be modified via the electric field generated by the underlying tribo-charges, and applying positive and negative biases has different effects on the bandgap thanks to the spontaneous polarization along the direction perpendicular to the nanoflakes plane. This finding can pave a new path for the optical applications such as optical modulator, single-photon emitter and so forth, where the working states can be tuned via triboelectrification.

A $MoSe_2$-based triboelectrically-controlled tunable antenna was proposed to apply to the upcoming 5G base station. As the tribo-charges can tunnel through the $MoSe_2$ nanoflakes and localize at the interlayer to act as a bias voltage, the conductive/insulating states $MoSe_2$ can be controlled, which results in the adjustable working frequency band from 28 GHz to around 38 GHz. In the meantime, a stable gain (less than 0.1 dBi variation in the whole range) is achieved for this omnidirectional antenna. Additionally, a unidirectional radiation can be reached with a metallic reflector placed at the back of the tunable antenna, and a broad beamwidth can still remain. Due to the long-term preservation of the tribo-charges, no extra bias is needed in this case and the energy can be saved to a large extent.

Chapter 7 Conclusions and future work

7.1 Conclusions

To overcome the huge energy consumption on the globe, triboelectrification emerges as a readily available, stable and efficient mechanical-to-electrical energy conversion approach. In this study, we have focused on this topic and, after a detailed review of the literature, 2D chemical vapor deposited transition metal dichalcogenides including MoS_2, WS_2, $MoSe_2$, and WSe_2 were selected for the triboelectric investigation.

- Effects of parameters in CVD process have been studied for the successful synthesis of TMDs. Amongst, a stoichiometric ratio of sources (Mo/W, S/Se) is necessary for the growth, otherwise reaction may be incomplete and defects can arise. Other parameters (temperature, gas flow and substrate cleanness) can affect the amount of vaporized precursors to control the qualities of products. Importantly, as all these TMDs materials were synthesized in the same CVD system in this thesis, the rules obtained are more instructive for future deposition.

The triboelectric properties of MoS_2, WS_2, $MoSe_2$, and WSe_2 were characterized after the confirmation of their high-quality.

- Due to the diverse work functions, the electrons are transferred between the samples and the AFM tip during triboelectrification, and the generated amount of tribo-charges are different.
- The diffusion time constants reduce with the decrease of work functions, since a lower work function indicates an easier electron transition from the valence band to the conductive band, making the material neutralize the abundant charges with the surrounding environment fluently.
- The density of tribo-charges is adjustable by a bias applied onto the conductive AFM tip, and the controllable range may be affected by the varying carrier mobility and the capacity to accept/lose charges of these materials.
- As for the effect of layer number, the surface potential difference becomes smaller with the increase of layer number due to the interlayer screening effect, and a larger time constant is observed in the meantime given the poor conductivity (higher work function) as well as better protection (more layers to shield the tunneling charges from the atmosphere) of multilayers.

- Considering the interaction with the environment nearby, the surface-adsorbed water molecules from the atmosphere can act as carrier trappers to affect the surface potential and charge distribution of 2D materials, but heat treatment can efficiently handle this problem.
- There exists the transfer of materials during the frictional process, which can be utilized for tuning the triboelectric properties of materials.

TMDs-based applicable triboelectric investigation containing the bandgap modification and the tunable antenna, have been discussed.

- For the bandgap modification, the bandgap decreases monotonically with the increase of applied force due to the reduction of orbital overlapping and hybridization from the weakened atomic bonds, and the bandgap of MoS_2 nanoflakes strongly depends on the dielectric environments. In addition, while the bandgap of MoS_2 is almost unchanged when an external perpendicular electric field is applied because of the very subtle band structure deformation, the bandgap of bilayer MoS_2 can be modified via the electric field generated by the underlying tribo-charges, and applying positive and negative biases has different effects on the bandgap thanks to the spontaneous polarization along the direction perpendicular to the nanoflakes plane. This finding can pave a new path for the optical applications such as optical modulator, single-photon emitter and so forth, where the working states can be tuned via triboelectrification.
- A $MoSe_2$-based triboelectrically-controlled tunable antenna was proposed to apply to the upcoming 5G base station. As the tribo-charges can tunnel through the $MoSe_2$ nanoflakes and localize at the interlayer to act as a bias voltage, the conductive/insulating states $MoSe_2$ can be controlled, which results in the adjustable working frequency band from 28 GHz to around 38 GHz. In the meantime, a stable gain (less than 0.1 dBi variation in the whole range) is achieved for this omnidirectional antenna. Additionally, a unidirectional radiation can be reached with a metallic reflector placed at the back of the tunable antenna, and a broad beamwidth can still remain. Due to the long-term preservation of the tribo-charges, which work as a bias under the nanoflakes to control the state of $MoSe_2$, no extra bias is needed in this case and the energy can be saved to a large extent.

7.2 Future work

- 2D transition metal dichalcogenides-based van der Waals stacked heterostructures

2D transition metal dichalcogenides-based van der Waals stacked heterostructures have recently been paid much more attention thanks to their broad applications in transistors [274], [275], optical sensors [276], [277], light-emitting diodes [278], [279], photovoltaics [280], [281] and catalysts [282], [283]. Their unique optical and electronic properties have overcome some of the challenges encountered by graphene-based heterostructures, so many advanced functionalities such as a tunable optical band gap, enhanced photon absorption, significant exciton creation and ultrafast and high-efficiency charge transfer have been offered.

Hitherto, most researchers used mechanical exfoliation or chemical vapor deposition method followed by transfer and annealing to synthesize stacked 2D heterostructures. In fact, the transfer process can induce inevitable interfacial contamination like organic residuals. It has been reported that the interaction between layers is very sensitive to the lattice alignment, and the interaction can be deteriorated by the presence of foreign substances or variations in distance between neighboring layers [284]. For example, the distortions or gaps at the atomic level can weaken or even decouple the interlayer interactions in these stacked structures. Despite the fact that adsorbates can be removed by a post-annealing process, the annealing environment, like temperature and time, has a significant effect on the interlayer coupling and exciton transitions [285], and chemical reaction between neighboring layers may appear and unfavorable alloys can be formed [281], making the interaction more complicated.

Here, the WS_2/MoS_2 heterostructure has been successfully prepared by two-step chemical vapor deposition methods. MoS_2 was deposited onto SiO_2/Si substrate and it was followed by the growth of another WS_2 layer on the top. The characterizations of prepared WS_2/MoS_2 heterostructure are provided in the Appendix, which indicates its excellent quality. However, the evaluation of its triboelectric properties is still unfulfilled, so it needs to be characterized in the near future.

- Modulation of triboelectrification

Fundamentally, the performance of triboelectrification-based applications is mainly determined by the triboelectric charge density, so the modulation of charge density plays an important role in making improvements. Aside from the control via bias voltage during triboelectrification, physical surface engineering and chemical surface functionalization can

be employed to boost the tribo-charge density, as reviewed in Chapter 2. In the case of TMDs, various surface morphologies will be created and appropriate chemicals will be selected to dope for the triboelectric enhancement.

- More 2D TMDs-based applications

Apart from the bandgap modification and tunable antenna proposed in Chapter 6, more applications like a switch, power divider, frequency selective surface, optical antenna, non-volatile multi-valued memory can be tried based on the triboelectric properties of TMDs.

- More theory and modelling work

Apparently, almost all of the work completed in my PhD period is experimental. But to understand the mechanism of triboelectrification better, some modeling and theory digging-up are indispensable and they will be scheduled in the near future.

- A profound understanding of nanotribology affected by triboelectrification

Triboelectrification, during which charges are transferred and accumulated on materials via frictional process, can occur during sliding, leading to a perturbation of the charge neutrality of materials. In this case, charges may move through the material freely or be localized in specific atomic sites, thereby attractive or repulsive Columbic forces can arise, which can alter the frictional properties [286]. The experimental data in this study are valuable for the computational works of nanotribology, and there is close cooperation with computational researchers in our group.

Appendix

- Transfer of MoS_2 nanoflakes onto various substrates and their characterizations

The CVD-grown MoS_2 on SiO_2/Si was spin-coated with polystyrene (PS, Sigma-Aldrich) at the speed of 1000 rpm for 50 s, and then cured on a hot plate at 90 °C for 15 min. The coated sample was subsequently covered with thermal release tape (from Nitto) and floated in deionized water. Once the MoS_2/PS/tape stack detached from the substrate, it was transferred to the target substrates (gold, sapphire and polyimide), and the tape was peeled off when dry. The transferred sample was then immersed in chloroform ($CHCl_3$) solvent until the PS film was fully dissolved. Finally, solvent residues of the successfully transferred MoS_2 samples were rinsed off by deionized water. It should be mentioned that insulating sapphire and polyimide are attached to the top of a gold layer which can be grounded for the KFM measurement.

MoS_2 on gold, sapphire and polyimide substrates were then characterized by optical microscope, AFM, Raman spectroscopy as well as XPS to evaluate their quality. As evident in Figure 102, Figure 103 and Figure 104, the results are quite similar to the characterization of MoS_2 on SiO_2/Si substrate in Figure 64, so the high-quality can be confirmed for transferred single-layer MoS_2 on gold, sapphire and polyimide substrates.

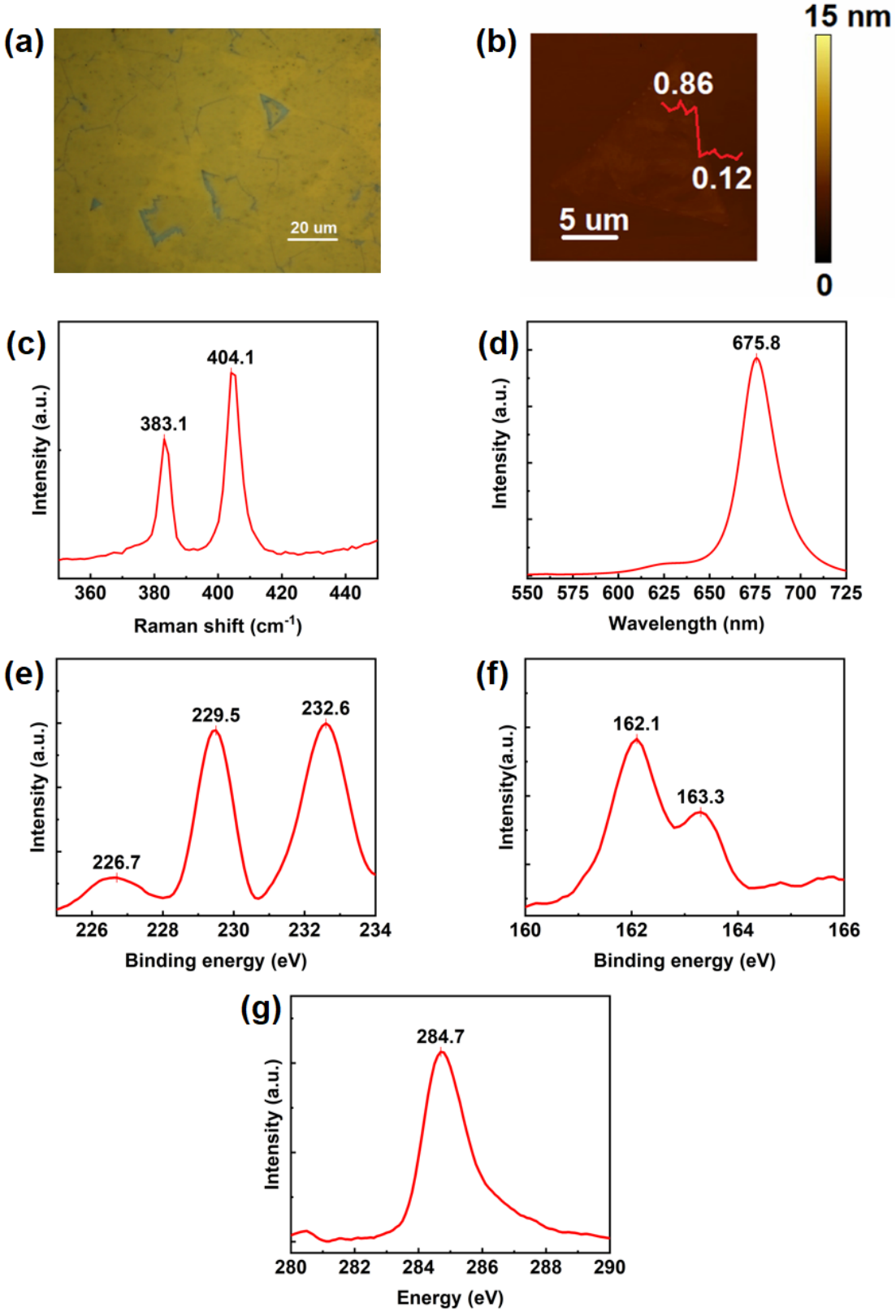

Figure 102 – Characterization of MoS_2 transferred on gold substrate. (a) Optical image. (b) Surface topography by AFM in tapping mode. (c) Raman spectrum and (d) PL spectrum excited by 532 nm laser. (e) Mo 3d, S 2s (f) S 2p and (g) C 1s orbitals demonstrated by XPS spectra.

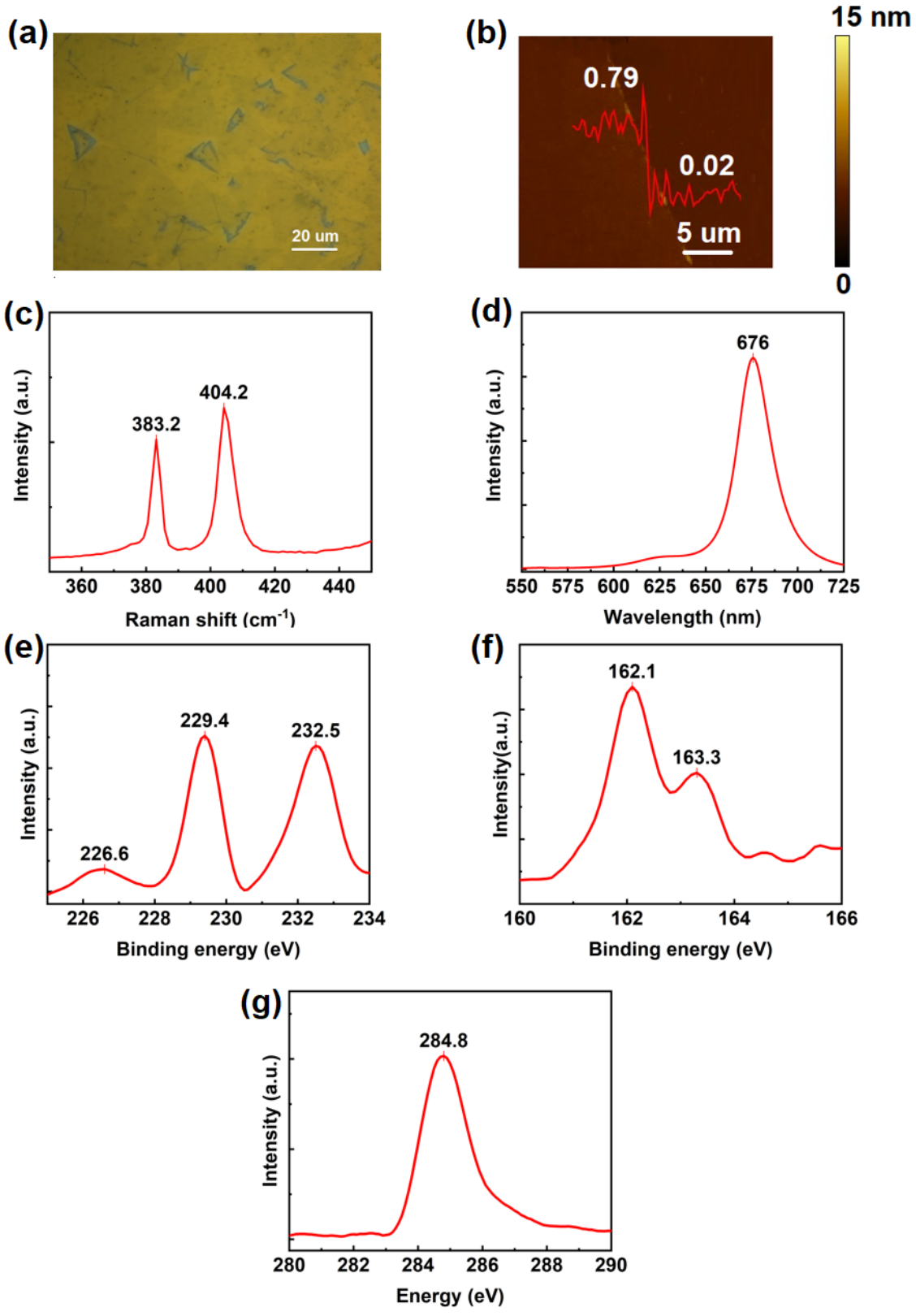

Figure 103 – Characterization of MoS_2 transferred on sapphire substrate. (a) Optical image. (b) Surface topography by AFM in tapping mode. (c) Raman spectrum and (d) PL spectrum excited by 532 nm laser. (e) Mo 3d, S 2s (f) S 2p and (g) C 1s orbitals demonstrated by XPS spectra.

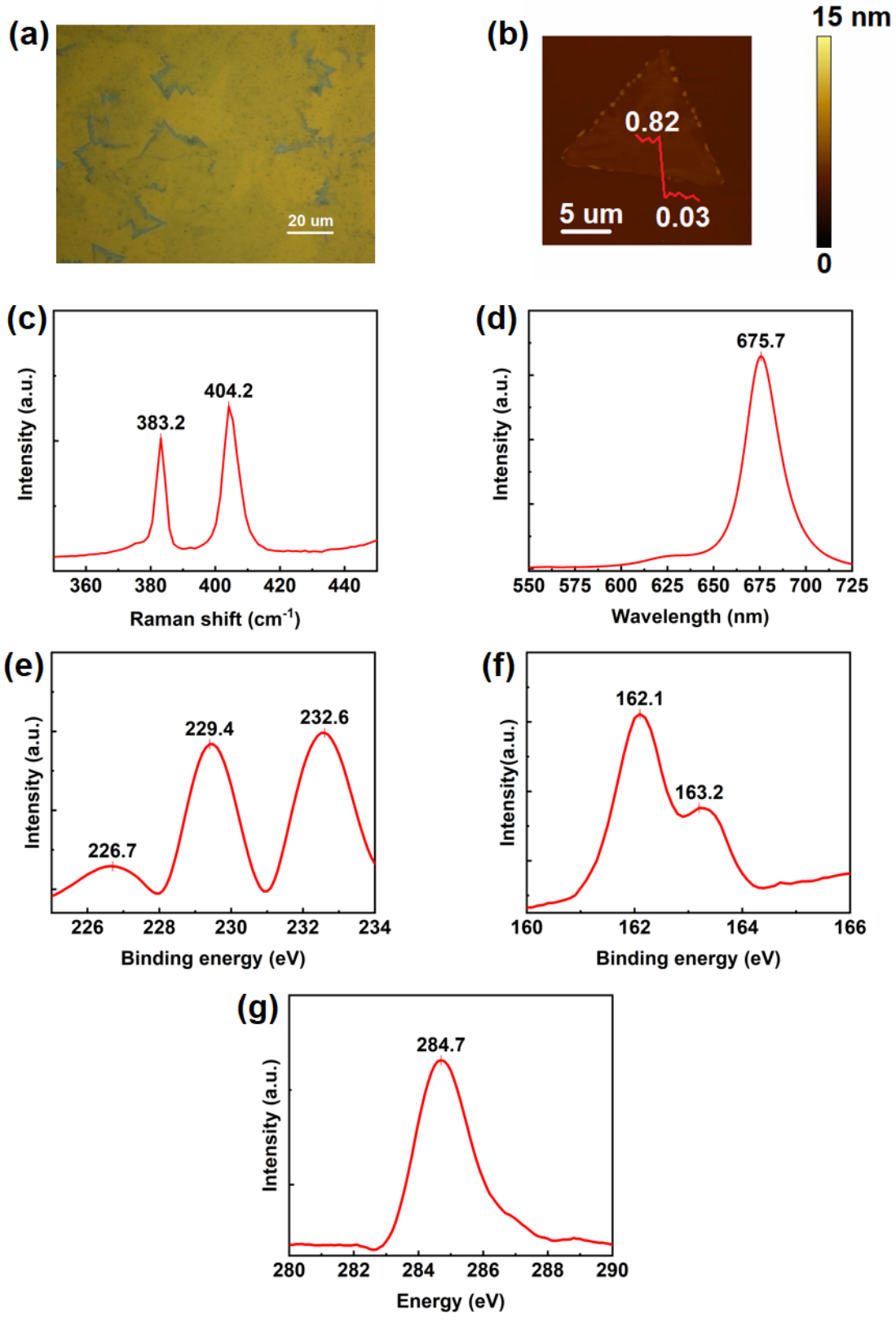

Figure 104 – Characterization of MoS_2 transferred onto polyimide substrate. (a) Optical image. (b) Surface topography by AFM in tapping mode. (c) Raman spectrum and (d) PL spectrum excited by 532 nm laser. (e) Mo 3d, S 2s (f) S 2p and (g) C 1s orbitals demonstrated by XPS spectra.

- XPS spectra of C 1s orbital for MoS_2, WS_2, $MoSe_2$ and WSe_2

Prior to the triboelectric characterization, the XPS spectrum of C 1s orbital is scanned for MoS_2, WS_2, $MoSe_2$ and WSe_2. As shown in Figure 105. The peak at ~284.6 eV corresponds to the C-C bond, which is expected due to the utilization of carbon tapes for fixing the sample. However, there is no obvious C-S bond (in the 285-287.5 eV range) found in the spectrum [287], indicating that there is no significant chemisorption of C. Although physisorption could happen, contact-mode AFM would remove adsorbed molecules at the side of tested areas or even wear materials [288]. In the meantime, the surface topographic images in Figure 74b, Figure 75a, Figure 76a, and Figure 77a show no accumulation of materials at the side, so it is not expected to have significant contamination on the sample surface.

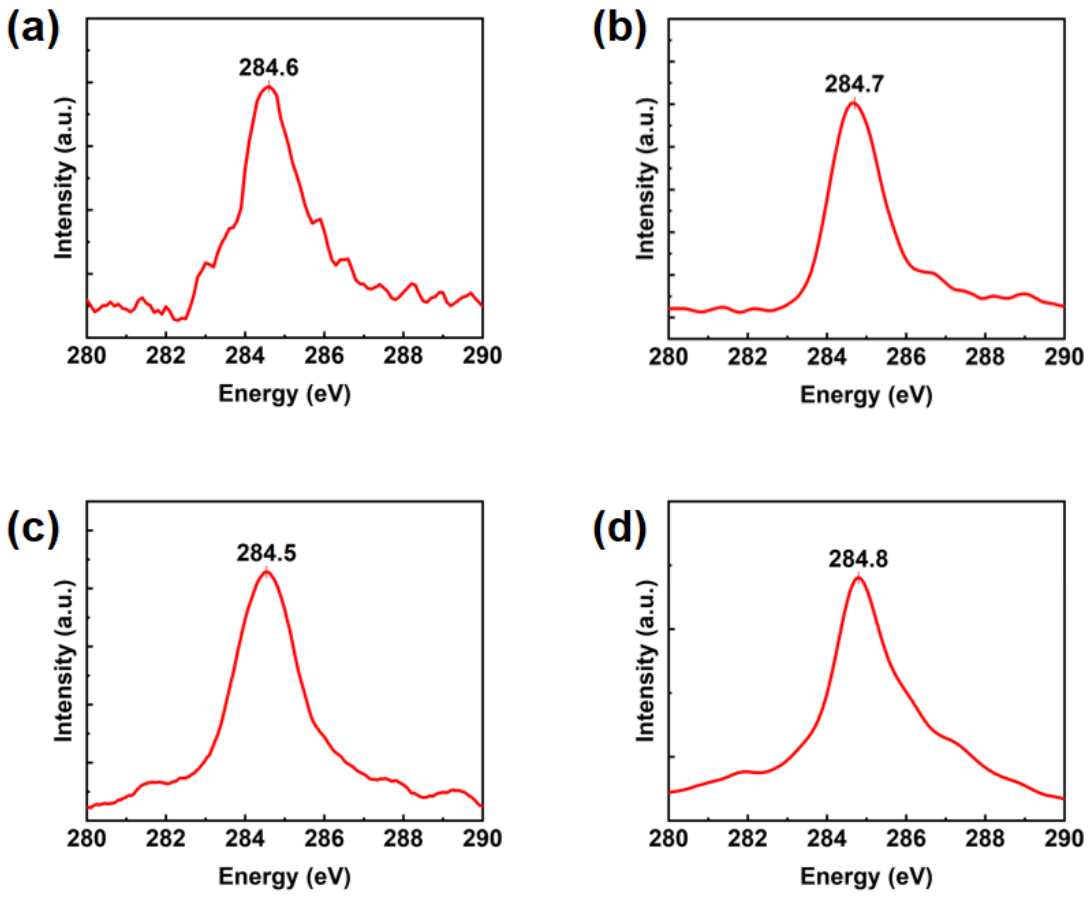

Figure 105 – XPS spectra of C 1s orbital for (a) MoS_2, (b) WS_2, (c) $MoSe_2$ and (d) WSe_2.

- Characterization of WS_2/MoS_2 heterostructure

Aside from the growth of MoS_2, WS_2, $MoSe_2$ and WSe_2, the synthesis of WS_2/MoS_2 heterostructure has been tried with a new facility (the tube furnace glovebox in Figure 106) due to the use of H_2S as a carrier gas. Before the reaction, chemical vapor deposited MoS_2 on SiO_2/Si substrate was loaded on the cleaned boat which was then placed into the tube. The tube was subsequently pushed into the glovebox and put down on the furnace. When the gas inlet and the exhaust extract system were connected, Ar flow was introduced to purge the system for 10 minutes. Afterward, the tube furnace was programed to 900 ℃ at 10 ℃/min ramping rate. Once the target temperature was reached, the pressure was set to be 30 mbar and precursors (WCl_6, H_2S) were introduced. When the 5-minute deposition was completed, the valves for both precursors were shut and the furnace was switched off.

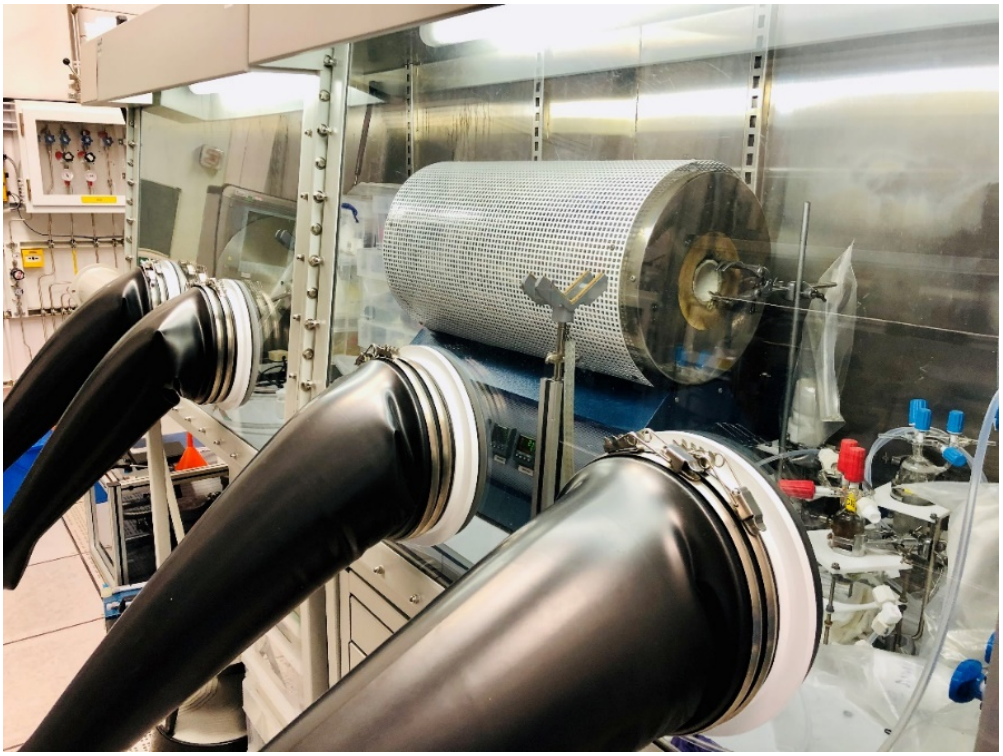

Figure 106 – CVD tube furnace glovebox.

Figure 107a demonstrates the optical image of WS_2/MoS_2 heterostructure deposited on SiO_2/Si substrate by CVD method. Although the triangular nanoflakes can be seen apparently, their nature needs to be characterized further. According to the surface topographic image scanned by tapping mode AFM (Figure 107b), the step height of nanoflake marked in Figure 107a is ~1.62 nm, indicating the thickness of bi-layer. As evident from Figure 107c and d, the overall Raman and PL signals of the WS_2/MoS_2 heterostructure are independently contributed by MoS_2 (383.2 and 404.2 cm^{-1}, frequency difference is 21.0

cm^{-1}) and WS_2 (350.2 and 419.9 cm^{-1}, frequency difference is 69.7 cm^{-1}). Compared with the frequency differences between E_{2g} and A_{1g} modes for single-layer MoS_2 (20.6 cm^{-1}) and WS_2 (67.2 cm^{-1}) provided in Figure 64 and Figure 66, these values are larger in the case of heterostructure, which can be ascribed to the stacked bilayer structure. A similar phenomenon can be noticed from the PL spectrum: the emission peaks for WS_2/MoS_2 heterostructure are shifted to the higher wavelength end in contrast to MoS_2 (676 nm) and WS_2 (620.2 nm) monolayer due to the interactions between these two layers.

Moreover, the XPS scan was performed for the WS_2/MoS_2 heterostructure to confirm its elemental compositions. As displayed in Figure 107e-h, the peaks at 226.4, 229.1, 232.3, 32.3, 34.5, 162.1, 163.2 eV correspond to the S 2s, Mo $3d_{5/2}$, Mo $3d_{3/2}$, W $4f_{7/2}$, W $4f_{5/2}$, S $2p_{3/2}$ and S $2p_{1/2}$ orbits, and the carbon 1s peak at 284.7 eV indicates that there is no significant chemisorption of carbon.

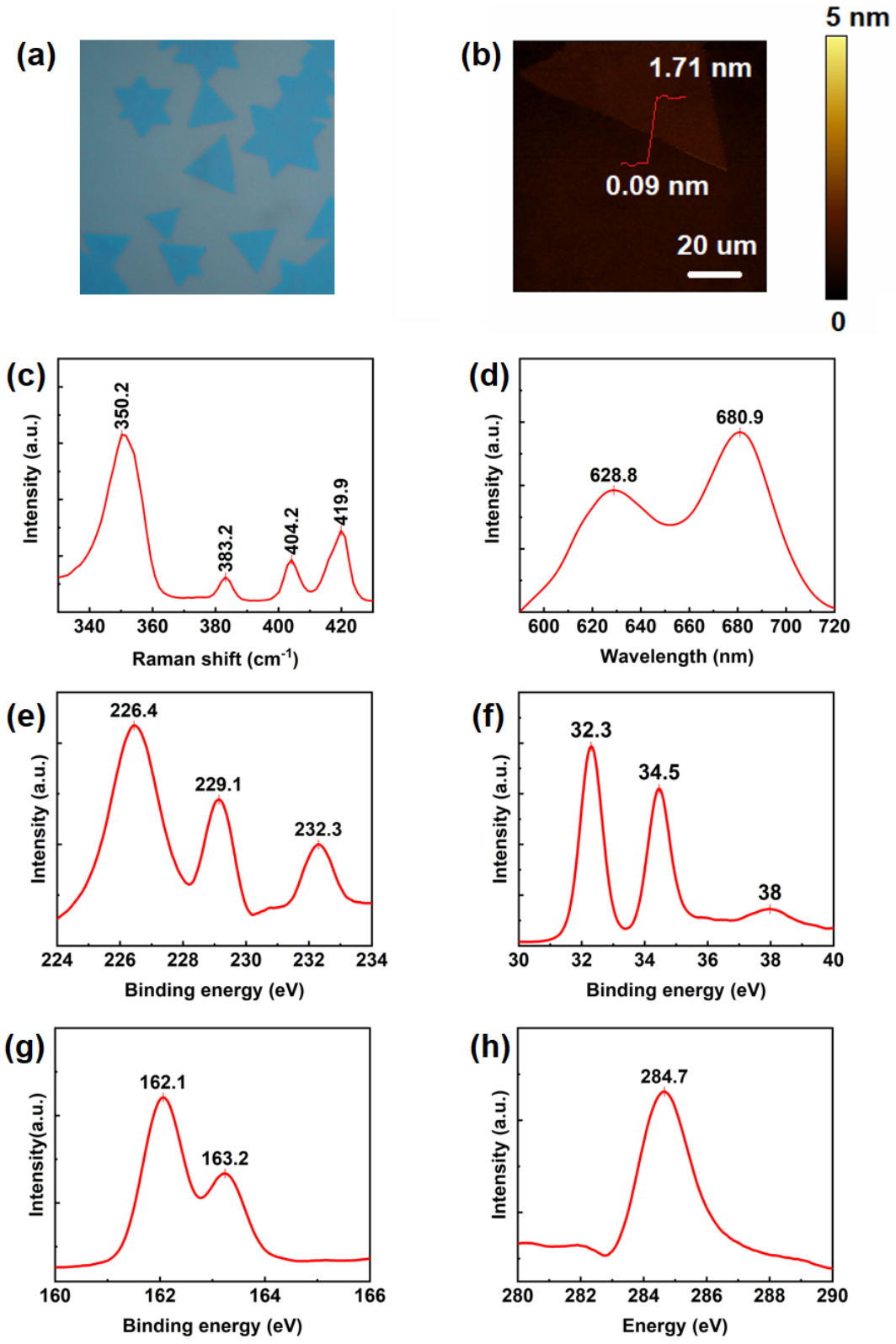

Figure 107 – Characterization of WS_2/MoS_2 heterostructure deposited on SiO_2/Si substrate by CVD method. (a) Optical image. (b) Surface topography by AFM in tapping mode. (c) Raman spectrum and (d) PL spectrum excited by 532 nm laser. (e) Mo 3d, S 2s, (f) W 4f, (g) S 2p as well as (h) C 1s orbitals demonstrated by XPS spectra.

Bibliography

[1] Z. L. Wang, “Triboelectric nanogenerators as new energy technology for self-powered systems and as active mechanical and chemical sensors,” *ACS Nano*, vol. 7, no. 11, pp. 9533–9557, 2013.

[2] C. Wu *et al.*, “Enhanced Triboelectric Nanogenerators Based on MoS2 Monolayer Nanocomposites Acting as Electron-Acceptor Layers,” *ACS Nano*, p. acsnano.7b03657, 2017.

[3] Z. L. Wang and W. Wu, “Nanotechnology-enabled energy harvesting for self-powered micro-/nanosystems,” *Angewandte Chemie - International Edition*, vol. 51, no. 47. pp. 11700–11721, 2012.

[4] H. Zeng, J. Dai, W. Yao, D. Xiao, and X. Cui, “Valley polarization in MoS2 monolayers by optical pumping,” *Nat. Nanotechnol.*, vol. 7, no. 8, pp. 490–493, 2012.

[5] S. Wi, M. Chen, D. Li, H. Nam, E. Meyhofer, and X. Liang, “Photovoltaic response in pristine WSe2 layers modulated by metal-induced surface-charge-transfer doping,” *Appl. Phys. Lett.*, vol. 107, no. 6, 2015.

[6] B. Radisavljevic, A. Radenovic, J. Brivio, V. Giacometti, and A. Kis, “Single-layer MoS2 transistors,” *Nat. Nanotechnol.*, vol. 6, no. 3, pp. 147–150, 2011.

[7] A. Castellanos-Gomez, M. Poot, G. a Steele, H. S. J. van der Zant, N. Agraït, and G. Rubio-Bollinger, “Elastic Properties of Freely Suspended MoS2 Nanosheets.,” *Adv. Mater.*, vol. 24, no. 6, pp. 772–5, 2012.

[8] S. Bertolazzi, J. Brivio, and A. Kis, “Stretching and breaking of ultrathin MoS2,” *ACS Nano*, vol. 5, no. 12, pp. 9703–9709, 2011.

[9] S. A. Han, R. Bhatia, and S.-W. Kim, “Synthesis, properties and potential applications of two-dimensional transition metal dichalcogenides,” *Nano Converg.*, vol. 2, no. 1, p. 17, 2015.

[10] H. S. Lee *et al.*, “MoS2 nanosheet phototransistors with thickness-modulated optical energy gap,” *Nano Lett.*, vol. 12, no. 7, pp. 3695–3700, 2012.

[11] Z. Wang *et al.*, “Comparative studies on single-layer reduced graphene oxide films

obtained by electrochemical reduction and hydrazine vapor reduction," *Nanoscale Res. Lett.*, vol. 7, no. 1, p. 161, 2012.

[12] H. Li *et al.*, "Fabrication of single- and multilayer MoS2 film-based field-effect transistors for sensing NO at room temperature," *Small*, vol. 8, no. 1, pp. 63–67, 2012.

[13] Y. Zhang, J. Ye, Y. Matsuhashi, and Y. Iwasa, "Ambipolar MoS2 thin flake transistors," *Nano Lett.*, vol. 12, no. 3, pp. 1136–1140, 2012.

[14] H. Wang *et al.*, "Integrated circuits based on bilayer MoS2 transistors," *Nano Lett.*, vol. 12, no. 9, pp. 4674–4680, 2012.

[15] K. Chang and W. Chen, "L-Cysteine-assisted synthesis of layered MoS2/graphene composites with excellent electrochemical performances for lithium ion batteries," *ACS Nano*, vol. 5, no. 6, pp. 4720–4728, 2011.

[16] M. Acerce, D. Voiry, and M. Chhowalla, "Metallic 1T phase MoS2 nanosheets as supercapacitor electrode materials," *Nat. Nanotechnol.*, vol. 10, no. 4, pp. 313–8, 2015.

[17] H. Zou *et al.*, "Quantifying the triboelectric series," *Nat. Commun.*, vol. 10, no. 1, pp. 1–9, 2019.

[18] A. R. Akande and J. Lowell, "Contact electrification of polymers by metals," *J. Electrostat.*, vol. 16, no. 2–3, pp. 147–156, 1985.

[19] B. A. Grzybowski, M. Fialkowski, and J. A. Wiles, "Kinetics of contact electrification between metals and polymers," *J. Phys. Chem. B*, vol. 109, no. 43, pp. 20511–20515, 2005.

[20] C. yang Liu and A. J. Bard, "Electrons on dielectrics and contact electrification," *Chem. Phys. Lett.*, vol. 480, no. 4–6, pp. 145–156, 2009.

[21] J. Lowell, "The electrification of polymers by metals," *J. Phys. D. Appl. Phys.*, vol. 9, pp. 1571–1585, 2001.

[22] J. Lowell, "Contact electrification of metals," *J. Phys. D. Appl. Phys.*, vol. 8, no. 1, pp. 53–63, 1975.

[23] J. Lowell and a. C. Rose-Innes, "Contact electrification," *Adv. Phys.*, vol. 29, no. 6,

pp. 947–1023, 1980.

[24] A. Wåhlin and G. Bäckström, “Sliding electrification of Teflon by metals,” *J. Appl. Phys.*, vol. 45, no. 5, pp. 2058–2064, 1974.

[25] Y. Zhang and T. Shao, “Contact electrification between polymers and steel,” *J. Electrostat.*, vol. 71, no. 5, pp. 862–866, 2013.

[26] D. K. Davies, “Charge generation on dielectric surfaces,” *J. Phys. D. Appl. Phys.*, vol. 2, no. 11, p. 1533, 1969.

[27] J. W. Peterson, “Contact charging between nonconductors and metal,” *J. Appl. Phys.*, vol. 25, no. 7, pp. 907–915, 1954.

[28] W. D. Greason, “Investigation of a test methodology for triboelectrification,” *J. Electrostat.*, vol. 49, no. 3–4, pp. 245–256, 2000.

[29] W. D. Greason, “Triboelectrification of wood with PTFE,” *J. Electrostat.*, vol. 71, no. 2, pp. 140–144, 2013.

[30] Y. S. Zhou *et al.*, “In situ quantitative study of nanoscale triboelectrification and patterning,” *Nano Lett.*, vol. 13, no. 6, pp. 2771–2776, 2013.

[31] W. Melitz, J. Shen, A. C. Kummel, and S. Lee, “Kelvin probe force microscopy and its application,” *Surf. Sci. Rep.*, vol. 66, no. 1, pp. 1–27, 2011.

[32] S. Kim *et al.*, “Rewritable ghost floating gates by tunnelling triboelectrification for two-dimensional electronics,” *Nat. Commun.*, vol. 8, no. May, p. 15891, 2017.

[33] F. R. Fan, L. Lin, G. Zhu, W. Wu, R. Zhang, and Z. L. Wang, “Transparent triboelectric nanogenerators and self-powered pressure sensors based on micropatterned plastic films,” *Nano Lett.*, vol. 12, no. 6, pp. 3109–3114, 2012.

[34] G. Zhu *et al.*, “Toward large-scale energy harvesting by a nanoparticle-enhanced triboelectric nanogenerator,” *Nano Lett.*, vol. 13, no. 2, pp. 847–853, 2013.

[35] Y. S. Zhou *et al.*, “Manipulating Nanoscale Contact Electrification by an Applied Electric Field,” vol. 14, no. 3, pp. 1567–1572, 2014.

[36] S. Wang *et al.*, “Molecular surface functionalization to enhance the power output of triboelectric nanogenerators,” *J. Mater. Chem. A*, vol. 4, no. 10, pp. 3728–3734, 2016.

[37] L. Kómorowski, J. Lipiński, and M. J. Pyka, “Electronegativity and hardness of chemical groups,” *J. Phys. Chem.*, vol. 97, no. 13, pp. 3166–3170, 1993.

[38] H. Y. Li, L. Su, S. Y. Kuang, C. F. Pan, G. Zhu, and Z. L. Wang, “Significant Enhancement of Triboelectric Charge Density by Fluorinated Surface Modification in Nanoscale for Converting Mechanical Energy,” *Adv. Funct. Mater.*, vol. 25, no. 35, pp. 5691–5697, 2015.

[39] J. H. Kim, B. K. Yun, J. H. Jung, and J. Y. Park, “Enhanced triboelectrification of the polydimethylsiloxane surface by ultraviolet irradiation,” *Appl. Phys. Lett.*, vol. 108, no. 13, 2016.

[40] H. Zhu *et al.*, “Triboelectric Nanogenerators Based on Melamine and Self-Powered High-Sensitive Sensors for Melamine Detection,” *Adv. Funct. Mater.*, vol. 26, no. 18, pp. 3029–3035, 2016.

[41] G. Zhu *et al.*, “Triboelectric-generator-driven pulse electrodeposition for micropatterning,” *Nano Lett.*, vol. 12, no. 9, pp. 4960–4965, 2012.

[42] S. Wang, L. Lin, Y. Xie, Q. Jing, S. Niu, and Z. L. Wang, “Sliding-triboelectric nanogenerators based on in-plane charge-separation mechanism,” *Nano Lett.*, vol. 13, no. 5, pp. 2226–2233, 2013.

[43] B. Meng *et al.*, “A transparent single-friction-surface triboelectric generator and self-powered touch sensor,” *Energy Environ. Sci.*, vol. 6, no. 11, pp. 3235–3240, 2013.

[44] S. Wang, Y. Xie, S. Niu, L. Lin, and Z. L. Wang, “Freestanding triboelectric-layer-based nanogenerators for harvesting energy from a moving object or human motion in contact and non-contact modes,” *Adv. Mater.*, vol. 26, no. 18, pp. 2818–2824, 2014.

[45] Z. L. Wang, J. Chen, and L. Lin, “Progress in triboelectric nanogenerators as a new energy technology and self-powered sensors,” *Energy Environ. Sci.*, vol. 8, no. 8, pp. 2250–2282, 2015.

[46] W. Tang *et al.*, “Liquid-metal electrode for high-performance triboelectric nanogenerator at an instantaneous energy conversion efficiency of 70.6%,” *Adv. Funct. Mater.*, vol. 25, no. 24, pp. 3718–3725, 2015.

[47] Y. Xie *et al.*, “Grating-Structured Freestanding Triboelectric-Layer Nanogenerator

for Harvesting Mechanical Energy at 85% Total Conversion Efficiency," *Adv. Mater.*, vol. 26, no. 38, pp. 6599–6607, 2014.

[48] C. Zhang, W. Tang, L. Zhang, C. Han, and Z. L. Wang, "Contact electrification field-effect transistor," *ACS Nano*, vol. 8, no. 8, pp. 8702–8709, 2014.

[49] S. Kim *et al.*, "Rewritable ghost floating gates by tunnelling triboelectrification for two-dimensional electronics," *Nat. Commun.*, vol. 8, 2017.

[50] M. Tortonese, R. C. Barrett, and C. F. Quate, "Atomic resolution with an atomic force microscope using piezoresistive detection," *Appl. Phys. Lett.*, vol. 62, no. 8, pp. 834–836, 1993.

[51] G. Binnig and C. F. Quate, "Atomic Force Microscope," *Phys. Rev. Lett.*, vol. 56, no. 9, pp. 930–933, 1986.

[52] C. R. Dean *et al.*, "Boron nitride substrates for high-quality graphene electronics," *Nat. Nanotechnol.*, vol. 5, no. 10, pp. 722–726, 2010.

[53] K. S. Novoselov *et al.*, "Electric Field Effect in Atomically Thin Carbon Films," *Science (80-.).*, vol. 306, no. 5696, pp. 666–669, 2004.

[54] H. Gleiter, "Nanostructured materials: basic concepts and microstructure," *Acta Mater.*, vol. 48, no. 1, pp. 1–29, 2000.

[55] V. V. Pokropivny and V. V. Skorokhod, "Classification of nanostructures by dimensionality and concept of surface forms engineering in nanomaterial science," *Mater. Sci. Eng. C*, vol. 27, no. 5-8 SPEC. ISS., pp. 990–993, 2007.

[56] Y. T. Kim, J. H. Han, B. H. Hong, and Y. U. Kwon, "Electrochemical Synthesis of CdSe quantum-Dot arrays on a graphene basal plane using mesoporous silica thin-film templates," *Adv. Mater.*, vol. 22, no. 4, pp. 515–518, 2010.

[57] J. Wang, M. Lin, Y. Yan, Z. Wang, P. C. Ho, and P. L. Kian, "CdSe/AsS core-shell quantum dots: Preparation and two-photon fluorescence," *J. Am. Chem. Soc.*, vol. 131, no. 32, pp. 11300–11301, 2009.

[58] V. Wood and V. Bulović, "Colloidal quantum dot light-emitting devices," *Nano Rev.*, vol. 1, no. 5202, pp. 1–7, 2010.

[59] Z. Lu, Z. Zhu, X. Zheng, Y. Qiao, J. Guo, and C. M. Li, “Biocompatible fluorescence-enhanced ZrO2-CdTe quantum dot nanocomposite for in vitro cell imaging,” *Nanotechnology*, vol. 22, no. 15, 2011.

[60] N. N. Ledentsov, “Long-wavelength quantum-dot lasers on GaAs substrates: From media to device concepts,” *IEEE J. Sel. Top. Quantum Electron.*, vol. 8, no. 5, pp. 1015–1024, 2002.

[61] X.-F. Guan *et al.*, “Front-side illuminated CdS/CdSe quantum dots co-sensitized solar cells based on TiO_2 nanotube arrays.,” *Nanotechnology*, vol. 22, no. 46, p. 465402, 2011.

[62] G. Zhang and D. Wang, “Colloidal lithography - The art of nanochemical patterning,” *Chemistry - An Asian Journal*, vol. 4, no. 2. pp. 236–245, 2009.

[63] D. Deng and J. Y. Lee, “Hollow core-shell mesospheres of crystalline SnO2 nanoparticle aggregates for high capacity Li+ ion storage,” *Chem. Mater.*, vol. 20, no. 5, pp. 1841–1846, 2008.

[64] T. Leshuk, S. Linley, G. Baxter, and F. Gu, “Mesoporous hollow sphere titanium dioxide photocatalysts through hydrothermal silica etching,” *ACS Appl. Mater. Interfaces*, vol. 4, no. 11, pp. 6062–6070, 2012.

[65] N. A. Dhas and K. S. Suslick, “Sonochemical preparation of hollow nanospheres and hollow nanocrystals,” *J. Am. Chem. Soc.*, vol. 127, no. 8, pp. 2368–2369, 2005.

[66] S. V. N. T. Kuchibhatla, A. S. Karakoti, D. Bera, and S. Seal, “One dimensional nanostructured materials,” *Progress in Materials Science*, vol. 52, no. 5. pp. 699–913, 2007.

[67] N. Li, K. Yanagisawa, and N. Kumada, “Facile hydrothermal synthesis of yttrium hydroxide nanowires,” *Cryst. Growth Des.*, no. 110, pp. 2–5, 2009.

[68] R. Shi, P. Yang, X. Dong, Q. Ma, and A. Zhang, “Growth of flower-like ZnO on ZnO nanorod arrays created on zinc substrate through low-temperature hydrothermal synthesis,” *Appl. Surf. Sci.*, vol. 264, pp. 162–170, 2013.

[69] X. Chen *et al.*, “Silica nanotubes by templated thermolysis of silicon tetraacetate,” *Chem. Mater.*, vol. 23, no. 13, pp. 3129–3131, 2011.

[70] S. Liang *et al.*, “Ultrathin Na1.1V3O7.9 nanobelts with superior performance as cathode materials for lithium-ion batteries,” *ACS Appl. Mater. Interfaces*, vol. 5, no. 17, pp. 8704–8709, 2013.

[71] Y. S. Hor *et al.*, “Nanowires and nanoribbons of charge-density-wave conductor NbSe3,” *Nano Lett.*, vol. 5, no. 2, pp. 397–401, 2005.

[72] J. Y. Lao, J. G. Wen, and Z. F. Ren, “Hierarchical ZnO Nanostructures,” *Nano Lett.*, vol. 2, no. 11, pp. 1287–1291, 2002.

[73] D. Pradhan and K. T. Leung, “Vertical growth of two-dimensional zinc oxide nanostructures on ITO-coated glass: Effects of deposition temperature and deposition time,” *J. Phys. Chem. C*, vol. 112, no. 5, pp. 1357–1364, 2008.

[74] T. Karakouz, D. Holder, M. Goomanovsky, A. Vaskevich, and I. Rubinstein, “Morphology and refractive index sensitivity of gold island films,” *Chem. Mater.*, vol. 21, no. 24, pp. 5875–5885, 2009.

[75] A. Kargar, Y. Jing, S. J. Kim, C. T. Riley, X. Pan, and D. Wang, “ZnO/CuO heterojunction branched nanowires for photoelectrochemical hydrogen generation,” *ACS Nano*, vol. 7, no. 12, pp. 11112–11120, 2013.

[76] L. Cheng *et al.*, “High curie temperature Bi1.85Mn0.15Te3 nanoplates,” *J. Am. Chem. Soc.*, vol. 134, no. 46, pp. 18920–18923, 2012.

[77] R. Gao *et al.*, “High-yield synthesis of boron nitride nanosheets with strong ultraviolet,” *J. Phys. Chem. C*, vol. 113, no. 34, pp. 15160–15165, 2009.

[78] T. Premkumar, Y. S. Zhou, Y. F. Lu, and K. Baskar, “Optical and field-emission properties of ZnO nanostructures deposited using high-pressure pulsed laser deposition.,” *ACS Appl. Mater. Interfaces*, vol. 2, no. 10, pp. 2863–2869, 2010.

[79] X. Zhang *et al.*, “Synthesis of a highly efficient BiOCl single-crystal nanodisk photocatalyst with exposing {001} facets,” *ACS Appl. Mater. Interfaces*, vol. 6, no. 10, pp. 7766–7772, 2014.

[80] M. Toma, G. Loget, and R. M. Corn, “Flexible teflon nanocone array surfaces with tunable superhydrophobicity for self-cleaning and aqueous droplet patterning,” *ACS Applied Materials and Interfaces*, vol. 6, no. 14. pp. 11110–11117, 2014.

[81] L. Wang and Y. Yamauchi, “Facile synthesis of three-dimensional dendritic platinum nanoelectrocatalyst,” *Chem. Mater.*, vol. 21, no. 15, pp. 3562–3569, 2009.

[82] J. Liu, J. Essner, and J. Li, “Hybrid Supercapacitor Based on Coaxially Coated Manganese Oxide on Vertically Aligned Carbon Nanofiber Arrays,” *Chem. Mater.*, vol. 22, no. 17, pp. 5022–5030, 2010.

[83] J. N. Wang, L. F. Su, and Z. P. Wu, “Growth of highly compressed and regular coiled carbon nanotubes by a spray-pyrolysis method,” *Cryst. Growth Des.*, vol. 8, no. 5, pp. 1741–1747, 2008.

[84] D. Liu, G. Zou, J. Zhang, P. Zhu, Q. Cui, and W. Lei, “Direct Synthesis, Growth Mechanism, and Optical Properties of 3D AlN Nanostructures with Urchin Shapes,” *Cryst. Growth Des.*, vol. 9, no. 3, pp. 1489–1493, 2009.

[85] K. S. Novoselov *et al.*, “Electric Field Effect in Atomically Thin Carbon Films,” *Science (80-.).*, vol. 306, no. 5696, pp. 666–669, 2004.

[86] K. S. Novoselov, V. I. Fal’Ko, L. Colombo, P. R. Gellert, M. G. Schwab, and K. Kim, “A roadmap for graphene,” *Nature*, vol. 490, no. 7419, pp. 192–200, 2012.

[87] D. S. L. Abergel, V. Apalkov, J. Berashevich, K. Ziegler, and T. Chakraborty, “Properties of graphene: a theoretical perspective,” *Adv. Phys.*, vol. 59, no. 4, pp. 261–482, 2010.

[88] K. I. Bolotin *et al.*, “Ultrahigh electron mobility in suspended graphene,” *Solid State Commun.*, vol. 146, no. 9–10, pp. 351–355, 2008.

[89] K. S. Novoselov *et al.*, “Two-dimensional gas of massless Dirac fermions in graphene,” *Nature*, vol. 438, no. 7065, pp. 197–200, 2005.

[90] K. I. Bolotin, F. Ghahari, M. D. Shulman, H. L. Stormer, and P. Kim, “Observation of the fractional quantum Hall effect in graphene.,” *Nature*, vol. 462, no. 7270, pp. 196–199, 2009.

[91] L. Wang *et al.*, “One-dimensional electrical contact to a two-dimensional material.,” *Science*, vol. 342, no. 6158, pp. 614–7, 2013.

[92] K. K. Kim *et al.*, “Synthesis of monolayer hexagonal boron nitride on Cu foil using chemical vapor deposition,” *Nano Lett.*, vol. 12, no. 1, pp. 161–166, 2012.

[93] K. Watanabe, T. Taniguchi, and H. Kanda, “Direct-bandgap properties and evidence for ultraviolet lasing of hexagonal boron nitride single crystal,” *Nat. Mater.*, vol. 3, no. 6, pp. 404–409, 2004.

[94] A. K. Geim and I. V Grigorieva, “Van der Waals heterostructures,” *Nature*, vol. 499, no. 7459, pp. 419–425, 2014.

[95] A. Kumar, A. Khosla, J. S. Saini, and S. Singh, “Meta-heuristic range based node localization algorithm for Wireless Sensor Networks,” *2012 Int. Conf. Localization GNSS, ICL-GNSS 2012*, pp. 1–7, 2012.

[96] M. Chhowalla, H. S. Shin, G. Eda, L.-J. Li, K. P. Loh, and H. Zhang, “The chemistry of two-dimensional layered transition metal dichalcogenide nanosheets,” *Nat. Chem.*, vol. 5, no. 4, pp. 263–275, 2013.

[97] C. Ataca, H. Şahin, and S. Ciraci, “Stable, single-layer MX 2 transition-metal oxides and dichalcogenides in a honeycomb-like structure,” *J. Phys. Chem. C*, vol. 116, no. 16, pp. 8983–8999, 2012.

[98] R. Kappera *et al.*, “Phase-engineered low-resistance contacts for ultrathin MoS2 transistors,” *Nat. Mater.*, vol. 13, no. 12, pp. 1128–1134, 2014.

[99] Y. C. Lin, D. O. Dumcenco, Y. S. Huang, and K. Suenaga, “Atomic mechanism of the semiconducting-to-metallic phase transition in single-layered MoS2,” *Nat. Nanotechnol.*, vol. 9, no. 5, pp. 391–396, 2014.

[100] R. Kappera *et al.*, “Metallic 1T phase source/drain electrodes for field effect transistors from chemical vapor deposited MoS2,” *APL Mater.*, vol. 2, no. 9, 2014.

[101] K. A. N. Duerloo, Y. Li, and E. J. Reed, “Structural phase transitions in two-dimensional Mo-and W-dichalcogenide monolayers,” *Nat. Commun.*, vol. 5, 2014.

[102] Q. WANG, H. LI, and Z. ZHOU, “Hausdorff measure and its algorithm of conformal image,” *Sci. Sin. Math.*, vol. 42, no. 7, pp. 699–709, 2012.

[103] G. H. Lee *et al.*, “Highly Stable, Dual-Gated MoS2 Transistors Encapsulated by Hexagonal Boron Nitride with Gate-Controllable Contact, Resistance, and Threshold Voltage,” *ACS Nano*, vol. 9, no. 7, pp. 7019–7026, 2015.

[104] S. Das, H. Y. Chen, A. V. Penumatcha, and J. Appenzeller, “High performance

multilayer MoS2 transistors with scandium contacts," *Nano Lett.*, vol. 13, no. 1, pp. 100–105, 2013.

[105] S. Bertolazzi, J. Brivio, and A. Kis, "Stretching and breaking of ultrathin MoS2," *ACS Nano*, vol. 5, no. 12, pp. 9703–9709, 2011.

[106] Q. H. Wang, K. Kalantar-Zadeh, A. Kis, J. N. Coleman, and M. S. Strano, "Electronics and optoelectronics of two-dimensional transition metal dichalcogenides," *Nat. Nanotechnol.*, vol. 7, no. 11, pp. 699–712, 2012.

[107] C. M, "Photoluminescence from Chemically Exfoliated MoS2," *Nano Lett.*, vol. 12, no. 12, p. 526, 2012.

[108] G. Eda, T. Fujita, H. Yamaguchi, D. Voiry, M. Chen, and M. Chhowalla, "Coherent atomic and electronic heterostructures of single-layer MoS2," *ACS Nano*, vol. 6, no. 8, pp. 7311–7317, 2012.

[109] E. Benavente and M. A. Santa Ana, "Intercalation chemistry of molybdenum disulfide," *Coordination Chemistry Reviews*, vol. 224, no. 1–2. pp. 87–109, 2002.

[110] A. S. Golub, Y. V Zubavichus, Y. L. Slovokhotov, and Y. N. Novikov, "Single-layer dispersions of transition metal dichalcogenides in the synthesis of intercalation compounds," *Russ. Chem. Rev.*, vol. 72, no. 2, pp. 123–141, 2007.

[111] J. N. Coleman *et al.*, "Two-dimensional nanosheets produced by liquid exfoliation of layered materials.," *Science*, vol. 331, no. 6017, pp. 568–571, 2011.

[112] Z. Zeng *et al.*, "Single-layer semiconducting nanosheets: High-yield preparation and device fabrication," *Angew. Chemie - Int. Ed.*, vol. 50, no. 47, pp. 11093–11097, 2011.

[113] K. G. Zhou, N. N. Mao, H. X. Wang, Y. Peng, and H. L. Zhang, "A mixed-solvent strategy for efficient exfoliation of inorganic graphene analogues," *Angew. Chemie - Int. Ed.*, vol. 50, no. 46, pp. 10839–10842, 2011.

[114] G. Cunningham *et al.*, "Solvent exfoliation of transition metal dichalcogenides: Dispersibility of exfoliated nanosheets varies only weakly between compounds," *ACS Nano*, vol. 6, no. 4, pp. 3468–3480, 2012.

[115] R. J. Smith *et al.*, "Large-scale exfoliation of inorganic layered compounds in aqueous surfactant solutions," *Adv. Mater.*, vol. 23, no. 34, pp. 3944–3948, 2011.

[116] P. May, U. Khan, J. M. Hughes, and J. N. Coleman, “Role of solubility parameters in understanding the steric stabilization of exfoliated two-dimensional nanosheets by adsorbed polymers,” *J. Phys. Chem. C*, vol. 116, no. 20, pp. 11393–11400, 2012.

[117] P. Joensen, R. F. Frindt, and S. R. Morrison, “Single-layer MoS2,” *Mater. Res. Bull.*, vol. 21, no. 4, pp. 457–461, 1986.

[118] Z. Yin *et al.*, “Single-layer MoS2 phototransistors,” *ACS Nano*, vol. 6, no. 1, pp. 74–80, 2012.

[119] T. Mos, S. Ghatak, A. N. Pal, and A. Ghosh, “Nature of Electronic States in Atomically,” *ACS Nano*, vol. 5, no. 10, pp. 7707–7712, 2011.

[120] A. Castellanos-Gomez, M. Barkelid, A. M. Goossens, V. E. Calado, H. S. J. Van Der Zant, and G. A. Steele, “Laser-thinning of MoS2: On demand generation of a single-layer semiconductor,” *Nano Lett.*, vol. 12, no. 6, pp. 3187–3192, 2012.

[121] G. H. Han *et al.*, “Laser thinning for monolayer graphene formation: Heat sink and interference effect,” *ACS Nano*, vol. 5, no. 1, pp. 263–268, 2011.

[122] Y. Zhou *et al.*, “Microstructuring of graphene oxide nanosheets using direct laser writing,” *Adv. Mater.*, vol. 22, no. 1, pp. 67–71, 2010.

[123] M. Currie *et al.*, “Quantifying pulsed laser induced damage to graphene,” *Appl. Phys. Lett.*, vol. 99, no. 21, 2011.

[124] A. Castellanos-Gomez, N. Agrat, and G. Rubio-Bollinger, “Optical identification of atomically thin dichalcogenide crystals,” *Appl. Phys. Lett.*, vol. 96, no. 21, 2010.

[125] S. Kim *et al.*, “Effects of plasma treatment on surface properties of ultrathin layered MoS2,” *2D Mater.*, vol. 3, no. 3, p. 035002, 2016.

[126] E. a. Gulbransen, K. F. Andrew, and F. a. Brassart, “Oxidation of Molybdenum 550° to 1700°C,” *J. Electrochem. Soc.*, vol. 110, no. 10, p. 952, 1963.

[127] M. R. Islam *et al.*, “Tuning the electrical property via defect engineering of single layer MoS2 by oxygen plasma.,” *Nanoscale*, vol. 6, no. 17, pp. 10033–9, 2014.

[128] M. B. Dines, “Lithium intercalation via n-Butyllithium of the layered transition metal dichalcogenides,” *Mater. Res. Bull.*, vol. 10, no. 4, pp. 287–291, 1975.

[129] R. A. Gordon, D. Yang, E. D. Crozier, D. T. Jiang, and R. F. Frindt, “Structures of exfoliated single layers of WS2, MoS2, and MoSe2 in aqueous suspension,” *Phys. Rev. B - Condens. Matter Mater. Phys.*, vol. 65, no. 12, pp. 1254071–1254079, 2002.

[130] H. L. Tsai, J. Heising, J. L. Schindler, C. R. Kannewurf, and M. G. Kanatzidis, “Exfoliated-restacked phase of WS2,” *Chem. Mater.*, vol. 9, no. 4, pp. 879–882, 1997.

[131] A. Gupta, T. Sakthivel, and S. Seal, “Recent development in 2D materials beyond graphene,” *Prog. Mater. Sci.*, vol. 73, pp. 44–126, 2015.

[132] Y. Peng *et al.*, “Hydrothermal Synthesis and Characterization of Single-Molecular-Layer MoS2 and MoSe2,” *Chem. Lett.*, vol. 30, no. 8, pp. 772–773, 2001.

[133] J. G. Song *et al.*, “Layer-controlled, wafer-scale, and conformal synthesis of tungsten disulfide nanosheets using atomic layer deposition,” *ACS Nano*, vol. 7, no. 12, pp. 11333–11340, 2013.

[134] D. J. Late *et al.*, “Pulsed laser-deposited MoS2 thin films on W and Si: Field emission and photoresponse studies,” *ACS Appl. Mater. Interfaces*, vol. 6, no. 18, pp. 15881–15888, 2014.

[135] G. Siegel, Y. P. Venkata Subbaiah, M. C. Prestgard, and A. Tiwari, “Growth of centimeter-scale atomically thin MoSfilms by pulsed laser deposition,” *APL Mater.*, vol. 3, no. 5, pp. 0–7, 2015.

[136] C. Muratore *et al.*, “Continuous ultra-thin MoS2 films grown by low-temperature physical vapor deposition,” *Appl. Phys. Lett.*, vol. 104, no. 26, 2014.

[137] B. Zhou *et al.*, “Growth of single crystal WS2 thin films via atmospheric pressure CVD,” *Conf. Progr. Dig. - 7th Int. Conf. Manip. Manuf. Meas. Nanoscale, IEEE 3M-NANO 2017*, vol. January, pp. 379–383, 2018.

[138] M. Monolayer and W. S. Mos, “Atomically Resolved Observation of Continuous Interfaces between As-grown MoS2 Monolayer and WS2/MoS2 Heterobilayer on SiO2,” *ACS Appl. Nano Mater.*, vol. 1, no. 5, pp. 2041–2048, 2018.

[139] K. L. Choy, “Chemical vapour deposition of coatings,” *Prog. Mater. Sci.*, vol. 48, no. 2, pp. 57–170, 2003.

[140] Y. Lv, F. Huang, L. Zhang, J. Weng, S. Zhao, and Z. Ji, “Preparation and

Photoluminescence of Tungsten Disulfide Monolayer," *Coatings*, vol. 8, no. 6, p. 205, 2018.

[141] Z. Yao, J. Liu, K. Xu, E. K. C. Chow, and W. Zhu, "Material Synthesis and Device Aspects of Monolayer Tungsten Diselenide," *Sci. Rep.*, vol. 8, no. 1, pp. 1–8, 2018.

[142] H. Kim, "Characteristics and applications of plasma enhanced-atomic layer deposition," in *Thin Solid Films*, 2011, vol. 519, no. 20, pp. 6639–6644.

[143] H. Kim, H. B. R. Lee, and W. J. Maeng, "Applications of atomic layer deposition to nanofabrication and emerging nanodevices," *Thin Solid Films*, vol. 517, no. 8. pp. 2563–2580, 2009.

[144] Y. H. Lee *et al.*, "Synthesis of large-area MoS2 atomic layers with chemical vapor deposition," *Adv. Mater.*, vol. 24, no. 17, pp. 2320–2325, 2012.

[145] H. Liu *et al.*, "Statistical Study of Deep Submicron Dual-Gated Field-Effect Transistors on Monolayer Chemical Vapor Deposition Molybdenum Disulfide Films," *Nano Lett.*, vol. 13, no. 6, pp. 2640–2646, 2013.

[146] S. Najmaei *et al.*, "Vapour phase growth and grain boundary structure of molybdenum disulphide atomic layers," *Nat. Mater.*, vol. 12, no. 8, pp. 754–759, 2013.

[147] W. Li *et al.*, "Broadband optical properties of large-area monolayer CVD molybdenum disulfide," *Phys. Rev. B - Condens. Matter Mater. Phys.*, vol. 90, no. 19, 2014.

[148] J. Wang *et al.*, "Direct growth of molybdenum disulfide on arbitrary insulating surfaces by chemical vapor deposition," *RSC Adv.*, vol. 5, no. 6, pp. 4364–4367, 2015.

[149] I. Bilgin *et al.*, "Chemical Vapor Deposition Synthesized Atomically-Thin Molybdenum Disulfide with Optoelectronic-Grade Crystalline Quality," *ACS Nano*, vol. 10, no. 1021, p. 5b02019, 2015.

[150] A. Alharbi and D. Shahrjerdi, "Electronic properties of monolayer tungsten disulfide grown by chemical vapor deposition (SI)," *Appl. Phys. Lett.*, vol. 109, no. 19, p. 193502, 2016.

[151] A. Thangaraja, "Chemical vapor deposition of tungsten disulfide (WS2) crystals on graphene and hexagonal boron nitride (h-BN)," 2016.

[152] Y. Zhang *et al.*, "Controlled Growth of High-Quality Monolayer WS2 Layers on Sapphire," *ACS Nano*, vol. 7, no. 10, pp. 8963–8971, 2013.

[153] W. Zhang, J. K. Huang, C. H. Chen, Y. H. Chang, Y. J. Cheng, and L. J. Li, "High-gain phototransistors based on a CVD MoS2 monolayer," *Adv. Mater.*, vol. 25, no. 25, pp. 3456–3461, 2013.

[154] N. Peimyoo *et al.*, "Nonblinking, intense two-dimensional light emitter: Monolayer WS2 Triangles," *ACS Nano*, vol. 7, no. 12, pp. 10985–10994, 2013.

[155] J. C. Shaw *et al.*, "Chemical vapor deposition growth of monolayer MoSe2 nanosheets," *Nano Res.*, vol. 7, pp. 1–62, 2014.

[156] X. Wang *et al.*, "Chemical vapor deposition growth of crystalline monolayer MoSe2," *ACS Nano*, vol. 8, no. 5, pp. 5125–5131, 2014.

[157] R. Ghosh *et al.*, "Large area chemical vapor deposition growth of monolayer MoSe2 and its controlled sulfurization to MoS2," *J. Mater. Res.*, pp. 1–6, 2016.

[158] B. B. Wang, K. Zheng, X. X. Zhong, D. Gao, and B. Gao, "Synthesis and structure of molybdenum diselenide nanosheets produced from MoO3 and Se powders," *J. Alloys Compd.*, vol. 695, pp. 27–34, 2017.

[159] D. R. Tobergte and S. Curtis, "Chemical Vapor Deposition Growth of Monolayer WSe2 with Tunable Device Characteristics and Growth Mechanism Study," *J. Chem. Inf. Model.*, vol. 53, no. 9, pp. 1689–1699, 2013.

[160] J. K. Huang *et al.*, "Large-area synthesis of highly crystalline WSe2 monolayers and device applications," *ACS Nano*, vol. 8, no. 1, pp. 923–930, 2014.

[161]F. Wang *et al.*, "Synthesis, properties and applications of 2D non-graphene materials," *Nanotechnology*, vol. 26, no. 29, p. 292001, 2015.

[162] S. J. Yun, S. M. Kim, K. K. Kim, and Y. H. Lee, "A systematic study of the synthesis of monolayer tungsten diselenide films on gold foil," *Curr. Appl. Phys.*, vol. 16, no. 9, pp. 1216–1222, 2016.

[163] S. K. Kim *et al.*, "Directional dependent piezoelectric effect in CVD grown monolayer MoS2 for flexible piezoelectric nanogenerators," *Nano Energy*, vol. 22, pp. 483–489, 2016.

[164] X. Wang, H. Feng, Y. Wu, and L. Jiao, “Controlled Synthesis of Highly Crystalline MoS2 Flakes by Chemical Vapor Deposition,” *J Am Chem Soc*, vol. 135, no. 14, pp. 5304–5307, 2013.

[165] A. M. Van Der Zande *et al.*, “Grains and grain boundaries in highly crystalline monolayer molybdenum disulphide,” *Nat. Mater.*, vol. 12, no. 6, pp. 554–561, 2013.

[166] H. Fang, S. Chuang, T. C. Chang, K. Takei, T. Takahashi, and A. Javey, “High-performance single layered WSe2 p-FETs with chemically doped contacts,” *Nano Lett.*, vol. 12, no. 7, pp. 3788–3792, 2012.

[167] W. Liu, J. Kang, D. Sarkar, Y. Khatami, D. Jena, and K. Banerjee, “Role of metal contacts in designing high-performance monolayer n-type WSe2 field effect transistors,” *Nano Lett.*, vol. 13, no. 5, pp. 1983–1990, 2013.

[168] J. Zhou *et al.*, “A library of atomically thin metal chalcogenides,” *Nature*, vol. 556, no. 7701, pp. 355–359, 2018.

[169] H. Li, J. Wu, X. Huang, Z. Yin, J. Liu, and H. Zhang, “A universal, rapid method for clean transfer of nanostructures onto various substrates,” *ACS Nano*, vol. 8, no. 7, pp. 6563–6570, 2014.

[170] Y. H. Lee *et al.*, “Synthesis and transfer of single-layer transition metal disulfides on diverse surfaces,” *Nano Lett.*, vol. 13, no. 4, pp. 1852–1857, 2013.

[171] D. Ma *et al.*, “A universal etching-free transfer of MoS2 films for applications in photodetectors,” *Nano Res.*, vol. 8, no. 11, pp. 3662–3672, 2015.

[172] A. Gurarslan *et al.*, “Surface-energy-assisted perfect transfer of centimeter-scale monolayer and few-layer MoS2films onto arbitrary substrates,” *ACS Nano*, vol. 8, no. 11, pp. 11522–11528, 2014.

[173] D. B. Moore *et al.*, “Synthesis, structure, and properties of turbostratically disordered (PbSe)1.18(TiSe2)2,” *Chem. Mater.*, vol. 25, no. 12, pp. 2404–2409, 2013.

[174] Y. H. Huang, C. C. Peng, R. S. Chen, Y. S. Huang, and C. H. Ho, “Transport properties in semiconducting NbS2 nanoflakes,” *Appl. Phys. Lett.*, vol. 105, no. 9, 2014.

[175] C. D. Layered, “Well-Defined Colloidal 2D Layered Transition-Metal Chalcogenide

Nanocrystals via Generalized Synthetic Protocols," pp. 1–4, 2012.

[176] S. S. Varghese, S. H. Varghese, S. Swaminathan, K. K. Singh, and V. Mittal, "Two-dimensional materials for sensing: Graphene and beyond," *Electronics (Switzerland)*, vol. 4, no. 3. pp. 651–687, 2015.

[177] N. Choudhary, M. D. Patel, J. Park, B. Sirota, and W. Choi, "Synthesis of large scale MoS2 for electronics and energy applications," *Journal of Materials Research*, vol. 31, no. 7. pp. 824–831, 2016.

[178] J. Lee *et al.*, "Two-dimensional layered MoS2 biosensors enable highly sensitive detection of biomolecules," *Sci. Rep.*, vol. 4, p. 7352, 2014.

[179] C. H. Lee *et al.*, "Atomically thin p-n junctions with van der Waals heterointerfaces," *Nat. Nanotechnol.*, vol. 9, no. 9, pp. 676–681, 2014.

[180] N. Choudhary, M. R. Islam, N. Kang, L. Tetard, Y. Jung, and S. I. Khondaker, "Two-dimensional lateral heterojunction through bandgap engineering of MoS2 via oxygen plasma," *J. Phys. Condens. Matter*, vol. 28, no. 36, 2016.

[181] W. Wu *et al.*, "Piezoelectricity of single-atomic-layer MoS2 for energy conversion and piezotronics," *Nature*, vol. 514, no. 7253, pp. 470–474, 2014.

[182] D. Sarkar, W. Liu, X. Xie, A. C. Anselmo, S. Mitragotri, and K. Banerjee, "MoS2 field-effect transistor for next-generation label-free biosensors," *ACS Nano*, vol. 8, no. 4, pp. 3992–4003, 2014.

[183] N. Choudhary *et al.*, "Directly deposited MoS2 thin film electrodes for high performance supercapacitors," *J. Mater. Chem. A*, vol. 3, no. 47, pp. 24049–24054, 2015.

[184] S. Lin *et al.*, "Interface designed MoS 2 /GaAs heterostructure solar cell with sandwich stacked hexagonal boron nitride," *Sci. Rep.*, vol. 5, no. October, pp. 1–9, 2015.

[185] X. Cui *et al.*, "Multi-terminal transport measurements of MoS2 using a van der Waals heterostructure device platform," *Nat. Nanotechnol.*, vol. 10, no. 6, pp. 534–540, 2015.

[186] T. Li, "Ideal strength and phonon instability in single-layer MoS2," *Phys. Rev. B - Condens. Matter Mater. Phys.*, vol. 85, no. 23, 2012.

[187] H. Shi, H. Pan, Y. W. Zhang, and B. I. Yakobson, “Quasiparticle band structures and optical properties of strained monolayer MoS2 and WS2,” *Phys. Rev. B - Condens. Matter Mater. Phys.*, vol. 87, no. 15, 2013.

[188] K. He, C. Poole, K. F. Mak, and J. Shan, “Experimental demonstration of continuous electronic structure tuning via strain in atomically thin MoS2,” *Nano Lett.*, vol. 13, no. 6, pp. 2931–2936, 2013.

[189] I. Aharonovich, D. Englund, and M. Toth, “Solid-state single-photon emitters,” *Nat. Photonics*, vol. 10, no. 10, pp. 631–641, 2016.

[190] M. R. Rosenberger *et al.*, “Quantum Calligraphy: Writing Single-Photon Emitters in a Two-Dimensional Materials Platform,” *ACS Nano*, vol. 13, no. 1, pp. 904–912, 2019.

[191] M. Aldrigo, M. Dragoman, and D. Masotti, “Metal-Insulator Transition in Monolayer MoS2 for Tunable and Reconfigurable Devices,” *2018 Int. Semicond. Conf.*, pp. 101–104, 2018.

[192] M. Dragoman, A. Cismaru, M. Aldrigo, A. Radoi, and D. Dragoman, “Switching microwaves via semiconductor-isolator reversible transition in a thin-film of MoS2,” *J. Appl. Phys.*, vol. 118, no. 4, 2015.

[193] W. A. Bryant, “The fundamentals of chemical vapour deposition,” *Journal of Materials Science*, vol. 12, no. 7. pp. 1285–1306, 1977.

[194] S. Motojima, N. Iwamori, T. Hattori, and K. Kurosawa, “Deposition and microhardness of SiC from the Si2Cl6-C3H8-H2-Ar system,” *J. Mater. Sci.*, vol. 21, no. 4, pp. 1363–1367, 1986.

[195] T. Goto, J. Tsuneyoshi, K. Kaya, and T. Hirai, “Preferred orientation of AlN plates prepared by chemical vapour deposition of AlCl3+NH3 system,” *J. Mater. Sci.*, vol. 27, no. 1, pp. 247–254, 1992.

[196] C. W. Lee, S. W. Nam, and J. S. Chun, “A phenomenological study of the nucleation and growth of chemically vapour-deposited TiC coatings on cemented carbide,” *Thin Solid Films*, vol. 86, no. 1, pp. 63–71, Nov. 1981.

[197] Y. Saito, K. Sato, and H. Tanaka, “Diamond synthesis from methane-hydrogen-water mixed gas using a microwave plasma,” *Microwaves*, vol. 23, pp. 842–846, 1988.

[198] H. O. Pierson, “Handbook of Carbon, Graphite, Diamond and Fullerenes,” *Handb. Carbon, Graph. Diam. Fullerenes*, pp. 25–69, 1993.

[199] J. Butler and R. Woodin, “Thin film diamond growth mechanisms,” *Thin Film Diam.*, vol. 342, no. 1664, pp. 209–224, 1994.

[200] B. Lux, C. Colombier, H. Altena, and K. Stjernberg, “Preparation of alumina coatings by chemical vapour deposition,” *Thin Solid Films*, vol. 138, no. 1. pp. 49–64, 1986.

[201] Y. Sato and M. Kamo, “Texture and some properties of vapor-deposited diamond films,” *Surf. Coatings Technol.*, vol. 39–40, no. C, pp. 183–198, 1989.

[202] E. Lassner and W.-D. Schubert, *Tungsten*, vol. 37, no. 05. 1999.

[203] W. Zhou, R. Apkarian, Z. L. Wang, and D. Joy, “Fundamentals of scanning electron microscopy (SEM),” *Scanning Microsc. Nanotechnol. Tech. Appl.*, pp. 1–40, 2007.

[204] E. Smith and G. Dent, *Modern Raman Sectroscopy - A Practical Approach*. 2005.

[205] C. Lee, H. Yan, L. Brus, T. Heinz, J. Hone, and S. Ryu, “Anomalous lattice vibrations of single-and few-layer MoS2,” *ACS Nano*, vol. 4, no. 5, pp. 2695–700, 2010.

[206] C. Lee, H. Yan, L. E. Brus, T. F. Heinz, J. Hone, and S. Ryu, “Anomalous lattice vibrations of single- and few-layer MoS2,” *ACS Nano*, vol. 4, no. 5, pp. 2695–2700, 2010.

[207] T. Han *et al.*, “Probing the optical properties of MoS2 on SiO2/Si and sapphire substrates,” *Nanomaterials*, vol. 9, no. 5, 2019.

[208] H. Li *et al.*, “From bulk to monolayer MoS2: Evolution of Raman scattering,” *Adv. Funct. Mater.*, vol. 22, no. 7, pp. 1385–1390, 2012.

[209] P. Tonndorf *et al.*, “Photoluminescence emission and Raman response of MoS2, MoSe2, and WSe2 nanolayers,” *Opt. Express*, vol. 21, no. 4, pp. 4908–4916, 2013.

[210] L. Yuanzheng *et al.*, “Accurate identification of layer number for few-layer WS2 and WSe2 via spectroscopic study,” *Nanotechnology*, vol. 29, no. 12, p. 124001, 2018.

[211] A. Berkdemir *et al.*, “Identification of individual and few layers of WS2 using Raman spectroscopy.,” *Sci. Rep.*, vol. 3, p. 1755, 2013.

[212] B. Bhushan, *Nanotribology and Nanomechanic-Measurement Techniques and Nanomechanics*. 2011.

[213] J. J. De Yoreo, "Principles of Crystal Nucleation and Growth," *Rev. Mineral. Geochemistry*, vol. 54, no. 1, pp. 57–93, 2003.

[214] S. S. Wang *et al.*, "Shape Evolution of Monolayer MoS2 Crystals Grown by Chemical Vapor Deposition," *Chem. Mater.*, vol. 26, no. 22, pp. 6371–6379, 2014.

[215] S. Park *et al.*, "Direct determination of monolayer MoS2 and WSe2 exciton binding energies on insulating and metallic substrates," *2D Mater.*, vol. 5, no. 2, 2018.

[216] H. Wang, C. C. Huang, and T. Polcar, "Triboelectrification of Two-Dimensional Chemical Vapor Deposited WS2 at Nanoscale," *Sci. Rep.*, vol. 9, no. 1, pp. 1–8, 2019.

[217] Y. Kim, H. Bark, G. H. Ryu, Z. Lee, and C. Lee, "Wafer-scale monolayer MoS2 grown by chemical vapor deposition using a reaction of MoO3 and H2S," *J. Physics-Condensed Matter*, vol. 28, no. 18, p. 6, 2016.

[218] H. Liu *et al.*, "Role of the carrier gas flow rate in monolayer MoS2 growth by modified chemical vapor deposition," *Nano Res.*, vol. 10, no. 2, pp. 1–9, 2016.

[219] C. Nie *et al.*, "Ultrafast growth of large-area monolayer MoS2 film via gold foil assistant CVD for a highly sensitive photodetector," *Nanotechnology*, vol. 28, no. 27, 2017.

[220] V. Senthilkumar, L. C. Tam, Y. S. Kim, Y. Sim, M. J. Seong, and J. I. Jang, "Direct vapor phase growth process and robust photoluminescence properties of large area MoS2 layers," *Nano Res.*, vol. 7, no. 12, pp. 1759–1768, 2014.

[221] Y. Yu, C. Li, Y. Liu, L. Su, Y. Zhang, and L. Cao, "Controlled scalable synthesis of uniform, high-quality monolayer and few-layer MoS2 films.," *Sci. Rep.*, vol. 3, p. 1866, 2013.

[222] X. Zhang *et al.*, "Raman spectroscopy of shear and layer breathing modes in multilayer MoS2," *Phys. Rev. B - Condens. Matter Mater. Phys.*, vol. 87, no. 11, 2013.

[223] Q. Ji *et al.*, "Epitaxial monolayer MoS2 on mica with novel photoluminescence," *Nano Lett.*, vol. 13, no. 8, pp. 3870–3877, 2013.

[224] K. K. Liu *et al.*, “Growth of large-area and highly crystalline MoS2 thin layers on insulating substrates,” *Nano Lett.*, vol. 12, no. 3, pp. 1538–1544, 2012.

[225] C. Chen *et al.*, “Growth of large-area atomically thin MoS2 film via ambient pressure chemical vapor deposition,” *Photonics Res.*, vol. 3, no. 4, pp. 110–114, 2015.

[226] C. A. Papageorgopoulos and W. Jaegermann, “Li intercalation across and along the van der Waals surfaces of MoS2 (0001),” *Surf. Sci.*, vol. 338, no. 1–3, pp. 83–93, 1995.

[227] C. Altavilla, M. Sarno, and P. Ciambelli, “A novel wet chemistry approach for the synthesis of hybrid 2D free-floating single or multilayer nanosheets of MS2@oleylamine (M=Mo, W),” *Chem. Mater.*, vol. 23, no. 17, pp. 3879–3885, 2011.

[228] K. C. Wong, X. Lu, J. Cotter, D. T. Eadie, P. C. Wong, and K. A. R. Mitchell, “Surface and friction characterization of MoS2 and WS2 third body thin films under simulated wheel/rail rolling-sliding contact,” *Wear*, vol. 264, no. 7–8, pp. 526–534, 2008.

[229] P. Liu *et al.*, “Large-Area WS2 Film with Big Single Domains Grown by Chemical Vapor Deposition,” *Nanoscale Res. Lett.*, vol. 12, no. 1, p. 558, 2017.

[230] A. M. Hussain, G. A. T. Sevilla, K. R. Rader, and M. M. Hussain, “Chemical vapor deposition based tungsten disulfide (WS2) thin film transistor,” *2013 Saudi Int. Electron. Commun. Photonics Conf. SIECPC 2013*, 2013.

[231] Q. Fu, W. Wang, L. Yang, J. Huang, J. Zhang, and B. Xiang, “Controllable synthesis of high quality monolayer WS2 on a SiO2/Si substrate by chemical vapor deposition,” *RSC Adv.*, vol. 5, no. 21, pp. 15795–15799, 2015.

[232] S. Qiao, H. Yang, Z. Bai, G. Peng, and X. Zhang, “Identifying the number of WS2 layers via Raman and photoluminescence spectrum,” vol. 141, no. Icmmcce, pp. 1408–1413, 2017.

[233] H. Martinez, A. Benayad, D. Gonbeau, P. Vinatier, B. Pecquenard, and A. Levasseur, “Influence of the cation nature of high sulfur content oxysulfide thin films MO y S z (M = W, Ti) studied by XPS,” *Appl. Surf. Sci.*, vol. 236, no. 1–4, pp. 377–386, 2004.

[234] M. Cattelan *et al.*, “New Strategy for the Growth of Complex Heterostructures Based on Different 2D Materials,” *Chem. Mater.*, vol. 27, no. 11, pp. 4105–4113, 2015.

[235] F. Reale, “Chemical Vapour Deposition of Atomically Thin Tungsten Disulphide,” 2017.

[236] Y. Chang *et al.*, “Monolayer MoSe2 Grown by Chemical Vapor Deposition for Fast Photodetection,” *ACS Nano*, vol. 8, no. 8, pp. 8582–8590, 2014.

[237] J. C. Shaw *et al.*, “Chemical vapor deposition growth of monolayer MoSe2 nanosheets,” *Nano Res.*, vol. 7, no. 4, pp. 1–7, 2014.

[238] J. Xia *et al.*, “CVD synthesis of large-area, highly crystalline MoSe2 atomic layers on diverse substrates and application to photodetectors,” *Nanoscale*, vol. 6, no. 15, pp. 8949–8955, 2014.

[239] Y. Zhao, H. Lee, W. Choi, W. Fei, and C. J. Lee, “Large-area synthesis of monolayer MoSe2 films on SiO2/Si substrates by atmospheric pressure chemical vapor deposition,” *RSC Adv.*, vol. 7, no. 45, pp. 27969–27973, 2017.

[240] B. B. Wang *et al.*, “Growth and photoluminescence of oriented MoSe2 nanosheets produced by hot filament CVD,” *RSC Adv.*, vol. 6, no. 43, pp. 37236–37245, 2016.

[241] A. Roy *et al.*, “Structural and Electrical Properties of MoTe2 and MoSe2 Grown by Molecular Beam Epitaxy,” *ACS Appl. Mater. Interfaces*, vol. 8, pp. 7396–7402, 2016.

[242] J. K. Huang *et al.*, “Large-area synthesis of highly crystalline WSe2 monolayers and device applications,” *ACS Nano*, vol. 8, no. 1, pp. 923–930, 2014.

[243] W. Liu, J. Kang, D. Sarkar, Y. Khatami, D. Jena, and K. Banerjee, “Role of metal contacts in designing high-performance monolayer n-type WSe2 field effect transistors,” *Nano Lett.*, vol. 13, no. 5, pp. 1983–1990, 2013.

[244] H. Li *et al.*, “Mechanical exfoliation and characterization of single- and few-layer nanosheets of WSe2, TaS2, and TaSe2,” *Small*, vol. 9, no. 11, pp. 1974–1981, 2013.

[245] J. Huang *et al.*, “Large-area synthesis of monolayer WSe2 on a SiO2/Si substrate and its device applications,” *Nanoscale*, vol. 7, no. 9, pp. 4193–4198, 2015.

[246] M. Nonnenmacher, M. P. O’Boyle, and H. K. Wickramasinghe, “Kelvin probe force microscopy,” *Appl. Phys. Lett.*, vol. 58, no. 25, pp. 2921–2923, 1991.

[247] J. R. Rumble, *Handbook of Chemistry and Physics 99th Edition - NaCl*. 2018.

[248] S. Choi, Z. Shaolin, and W. Yang, “Layer-number-dependent work function of MoS2 nanoflakes,” *J. Korean Phys. Soc.*, vol. 64, no. 10, pp. 1550–1555, 2014.

[249] L. Britnell *et al.*, “Strong Light-Matter Interactions in Heterostructures of Atomically Thin Films,” *Science (80-.).*, vol. 340, no. June, pp. 1311--1314, 2013.

[250] C. Gong, H. Zhang, W. Wang, L. Colombo, R. M. Wallace, and K. Cho, “Band alignment of two-dimensional transition metal dichalcogenides: Application in tunnel field effect transistors,” *Appl. Phys. Lett.*, vol. 103, no. 5, 2013.

[251] A. Cammarata and T. Polcar, “Tailoring Nanoscale Friction in MX2 Transition Metal Dichalcogenides,” *Inorg. Chem.*, vol. 54, no. 12, pp. 5739–5744, 2015.

[252] B. J. Irving, P. Nicolini, and T. Polcar, “On the lubricity of transition metal dichalcogenides: An: ab initio study,” *Nanoscale*, vol. 9, no. 17, pp. 5597–5607, 2017.

[253] P. Nicolini and T. Polcar, “A comparison of empirical potentials for sliding simulations of MoS2,” *Comput. Mater. Sci.*, vol. 115, pp. 158–169, 2016.

[254] R. Addou, L. Colombo, and R. M. Wallace, “Surface Defects on Natural MoS2,” *ACS Appl. Mater. Interfaces*, vol. 7, no. 22, pp. 11921–11929, 2015.

[255] S. Matsusaka, H. Maruyama, T. Matsuyama, and M. Ghadiri, “Triboelectric charging of powders: A review,” *Chem. Eng. Sci.*, vol. 65, no. 22, pp. 5781–5807, 2010.

[256] M. W. Williams, “Triboelectric charging of insulating polymers-some new perspectives,” *AIP Adv.*, vol. 2, no. 1, 2012.

[257] N. J. Lee *et al.*, “The interlayer screening effect of graphene sheets investigated by Kelvin probe force microscopy,” *Appl. Phys. Lett.*, vol. 95, no. 22, 2009.

[258] Y. Li, C. Y. Xu, and L. Zhen, “Surface potential and interlayer screening effects of few-layer MoS2 nanoflakes,” *Appl. Phys. Lett.*, vol. 102, no. 14, 2013.

[259] D. Ziegler *et al.*, “Variations in the work function of doped single- and few-layer graphene assessed by Kelvin probe force microscopy and density functional theory,” *Phys. Rev. B - Condens. Matter Mater. Phys.*, vol. 83, no. 23, 2011.

[260] C. K. Oliveira, M. J. S. Matos, M. S. C. Mazzoni, H. Chacham, and B. R. A. Neves, “Anomalous response of supported few-layer hexagonal boron nitride to DC electric

fields: A confined water effect?," *Nanotechnology*, vol. 23, no. 17, 2012.

[261] W. S. Yun, S. W. Han, S. C. Hong, I. G. Kim, and J. D. Lee, "Thickness and strain effects on electronic structures of transition metal dichalcogenides: 2H-MX2 semiconductors (M = Mo, W; X = S, Se, Te)," *Phys. Rev. B - Condens. Matter Mater. Phys.*, vol. 85, no. 3, 2012.

[262] E. Scalise, M. Houssa, G. Pourtois, V. V. Afanasev, and A. Stesmans, "First-principles study of strained 2D MoS2," *Phys. E Low-Dimensional Syst. Nanostructures*, vol. 56, pp. 416–421, 2014.

[263] P. Lu, X. Wu, W. Guo, and X. C. Zeng, "Strain-dependent electronic and magnetic properties of MoS 2 monolayer, bilayer, nanoribbons and nanotubes," *Phys. Chem. Chem. Phys.*, vol. 14, no. 37, pp. 13035–13040, 2012.

[264] A. Castellanos-Gomez *et al.*, "Local strain engineering in atomically thin MoS2," *Nano Lett.*, vol. 13, no. 11, pp. 5361–5366, 2013.

[265] H. Shi, H. Pan, Y. W. Zhang, and B. I. Yakobson, "Quasiparticle band structures and optical properties of strained monolayer MoS2 and WS2," *Phys. Rev. B - Condens. Matter Mater. Phys.*, vol. 87, no. 15, 2013.

[266] S. Manzeli, A. Allain, A. Ghadimi, and A. Kis, "Piezoresistivity and Strain-induced Band Gap Tuning in Atomically Thin MoS2," *Nano Lett.*, vol. 15, no. 8, pp. 5330–5335, 2015.

[267] A. A. Avetisyan, B. Partoens, and F. M. Peeters, "Electric-field control of the band gap and Fermi energy in graphene multilayers by top and back gates," *Phys. Rev. B - Condens. Matter Mater. Phys.*, vol. 80, no. 19, 2009.

[268] Q. Liu, L. Li, Y. Li, Z. Gao, Z. Chen, and J. Lu, "Tuning electronic structure of bilayer MoS2 by vertical electric field: A first-principles investigation," *J. Phys. Chem. C*, vol. 116, no. 40, pp. 21556–21562, 2012.

[269] M. El Shorbagy, R. M. Shubair, M. I. Alhajri, and N. K. Mallat, "On the design of millimetre-wave antennas for 5G," *Mediterr. Microw. Symp.*, pp. 7–10, 2017.

[270] J. Lota, S. Sun, T. S. Rappaport, and A. Demosthenous, "5G uniform linear arrays with beamforming and spatial multiplexing at 28, 37, 64, and 71 GHz for outdoor

urban communication: A two-level approach," *IEEE Trans. Veh. Technol.*, vol. 66, no. 11, pp. 9972–9985, 2017.

[271] D. Psychoudakis, H. Zhou, B. Biglarbegian, T. Henige, and F. Aryanfar, "Mobile station radio frequency unit for 5G communications at 28GHz," *IEEE MTT-S Int. Microw. Symp. Dig.*, vol. 2016-Augus, pp. 1–3, 2016.

[272] M. Saiful, F. Reyhan, Y. Rahayu, and F. Muhammadsyah, "The Design of Broadband 8x2 Phased Array 5G Antenna MIMO 28 GHz for Base Station," vol. 12, no. 11, pp. 840–843, 2018.

[273] M. Mahjouri-Samani *et al.*, "Patterned arrays of lateral heterojunctions within monolayer two-dimensional semiconductors," *Nat. Commun.*, vol. 6, no. July, 2015.

[274] N. Huo, J. Kang, Z. Wei, S. S. Li, J. Li, and S. H. Wei, "Novel and enhanced optoelectronic performances of multilayer MoS2 -WS2 heterostructure transistors," *Adv. Funct. Mater.*, vol. 24, no. 44, pp. 7025–7031, 2014.

[275] X. Qian, J. Liu, L. Fu, and J. Li, "Quantum spin hall effect in two - Dimensional transition metal dichalcogenides," *Science (80-.).*, vol. 346, no. 6215, pp. 1344–1347, 2014.

[276] M. Massicotte *et al.*, "Picosecond photoresponse in van der Waals heterostructures," *Nat. Nanotechnol.*, vol. 11, no. 1, pp. 42–46, 2016.

[277] Y. Yu *et al.*, "Equally efficient interlayer exciton relaxation and improved absorption in epitaxial and nonepitaxial MoS2/WS2 Heterostructures," *Nano Lett.*, vol. 15, no. 1, pp. 486–491, 2015.

[278] Z. Yin *et al.*, "Preparation of MoS2-MoO3 hybrid nanomaterials for light-emitting diodes," *Angew. Chemie - Int. Ed.*, vol. 53, no. 46, pp. 12560–12565, 2014.

[279] F. Withers *et al.*, "Light-emitting diodes by band-structure engineering in van der Waals heterostructures," *Nat. Mater.*, vol. 14, no. 3, pp. 301–306, 2015.

[280] Y. C. Lin *et al.*, "Atomically thin heterostructures based on single-layer tungsten diselenide and graphene," *Nano Lett.*, vol. 14, no. 12, pp. 6936–6941, 2014.

[281] M. Y. Li *et al.*, "Epitaxial growth of a monolayer WSe2-MoS2 lateral p-n junction with an atomically sharp interface," *Science (80-.).*, vol. 349, no. 6247, pp. 524–528,

2015.

[282] J. Kibsgaard, Z. Chen, B. N. Reinecke, and T. F. Jaramillo, “Engineering the surface structure of MoS 2 toÂ preferentially expose active edge sites forÂ electrocatalysis,” *Nat. Mater.*, vol. 11, no. 11, pp. 963–969, 2012.

[283] T. F. Jaramillo, K. P. Jørgensen, J. Bonde, J. H. Nielsen, S. Horch, and I. Chorkendorff, “Identification of active edge sites for electrochemical H2 evolution from MoS2 nanocatalysts,” *Science (80-.).*, vol. 317, no. 5834, pp. 100–102, 2007.

[284] Y. Yoo, Z. P. Degregorio, and J. E. Johns, “Seed Crystal Homogeneity Controls Lateral and Vertical Heteroepitaxy of Monolayer MoS2 and WS2,” *J. Am. Chem. Soc.*, vol. 137, no. 45, pp. 14281–14287, 2015.

[285] S. Tongay *et al.*, “Tuning interlayer coupling in large-area heterostructures with CVD-grown MoS2 and WS2 monolayers,” *Nano Lett.*, vol. 14, no. 6, pp. 3185–3190, 2014.

[286] A. Cammarata and T. Polcar, “Vibrational contributions to intrinsic friction in charged transition metal dichalcogenides,” *Nanoscale*, vol. 9, no. 32, pp. 11488–11497, 2017.

[287] A. Bratt and A. R. Barron, “XPS of Carbon Nanomaterials,” *Measurement*, pp. 1–16, 2011.

[288] J. Zekonyte and T. Polcar, “Friction Force Microscopy Analysis of Self-Adaptive W-S-C Coatings: Nanoscale Friction and Wear,” *ACS Appl. Mater. Interfaces*, vol. 7, no. 38, pp. 21056–21064, 2015.